Development of Clinically-Viable Applications of MR Elastography

---

A thesis submitted in fulfilment
of the requirements for the
Degree of

Master of Science in Physics

at the University of Canterbury

---

by

James L. Flewellen

University of Canterbury,
Christchurch, New Zealand

May 2008

Abstract

Magnetic Resonance Elastography is a method of imaging the elasticity of soft tissues through measurement of small motions induced into a sample. It shows great promise in the detection of a wide variety of pathologies, especially tumours.

An imaging protocol was developed to acquire MR elastography data for use in a clinical setting. A 3D gradient echo sequence was modified to allow for the detection of harmonic motion and tested on silicone phantoms and *ex-vivo* muscle and brain samples. The time for acquiring a high resolution, quantitative dataset of 3D motions was about 45 minutes. Our imaging method included motion encoding along all three coordinate axes and at several time points along the motion cycle. This time could be easily be reduced by more than half for future clinical use, while still retaining full quantitative data. A modified EPI sequence shows promise for even faster acquisition.

The ability to detect the mechanical anisotropy of brain and muscle tissue in *ex-vivo* samples was also investigated. Initial results from the muscle data indicate a change in shear wavelength is observed for actuation along orthogonal axes. This is a strong indicator of anisotropy detection. Further work needs to be done to improve results from the brain sample as preliminary results are inconclusive.

Contents

List of Figures

List of Tables

List of Abbreviations

AP:	Anterior-Posterior
bpm:	beats per minute
CT:	Computed Tomography
CV:	Control Variable
DMA:	Dynamic Mechanical Analysis
DTI:	Dial Test Indicator
ECG:	ElectroCardioGram
EM:	ElectroMagnetic
EPI:	Echo Planar Imaging
FID:	Free Induction Decay
FOV:	Field of View
FSE:	Fast Spin Echo
GRE:	Gradient Recalled Echo
IR:	Inversion Recovery
MEG:	Motion Encoding Gradient
MR:	Magnetic Resonance
MRE:	Magnetic Resonance Elastography
MRI:	Magnetic Resonance Imaging
NMR:	Nuclear Magnetic Resonance
RF:	RadioFrequency
RL:	Right-Left
ROI:	Region(s) of Interest
SE:	Spin Echo
SI:	Superior-Inferior
SNR:	Signal-to-Noise Ratio
TE:	Echo Time
TI:	Inversion Time
TR:	Repetition Time

Chapter 1

Introduction

The centuries-old technique of palpation to assess physiological change or damage demonstrates that physicians have known, for a long time, that many diseases cause a change in the mechanical properties of soft tissues. Even today, a physician's first approach to assessing an ailment will often be manual palpation. The importance of self-examination of the breast to detect potential cancers has received increasing attention, especially over the last two decades, to such an extent where it is now well in the public consciousness [1]. Surgeons will also often palpate tumours uncovered in surgery that had been previously undetected by conventional medical imaging modalities to assess the need for removal [2].

Due to the subjective nature of manual palpation, and its relatively low sensitivity, recent times have seen an increasing interest in quantifying the mechanical properties of various soft tissues, and documenting the mechanisms through which different diseases cause change in these properties, for diagnostic purposes. Although there was initially limited data on the *ex-vivo* mechanical properties of tissue (due to the technical difficulty of applying conventional material load-cell devices to biological tissue) let alone information on the even more difficult-to-obtain *in-vivo* properties, there was enough in the literature to suggest that the measurement of mechanical properties of different tissues would be clinically beneficial [2]. Some studies into the mechanical properties of soft tissues have revealed that the elastic moduli of soft tissues in the human body varies over four orders of magnitude [3]. It is also generally agreed that the elasticity of a tissue is the parameter most greatly changed by alterations in its physiological state [4], with variations in the elastic modulus of up to an order of magnitude from the healthy to the diseased state [5]. Over the last decade, the clinical importance of measuring the changes in mechanical properties of tissues has become more widely recognised and some very recent studies have made some ground in making independent *ex-vivo* measurements of the elastic modulus [6]. The technique of Magnetic Resonance Elastography (MRE) has huge potential to 'unlock' these hard-to-measure properties from within the body; to effectively allow us to 'see' elasticity *in-vivo* and to determine quantitative values of these unchartered properties of the human anatomy.

MRE is a phase-contrast based Magnetic Resonance Imaging (MRI) technique that can directly visualise propagating acoustic strain waves in a soft medium. In this study, these mechanical waves are induced into the medium through an actuator providing harmonic oscillation. The resulting displacement field can then be imaged. The detectable shift in displacement is on the order of microns. From this mapping, mechanical properties such as the shear modulus, Young's modulus, bulk modulus and Poisson's ratio can be determined.

MRE has been applied to imaging of the liver [7], [8], lung [9], heel [10], [11] (for studies into diabetes), kidneys [12], skeletal muscle [13], [14], [15], [16], vascular wall [17], and even the brain [18], [19], [20]. One area currently receiving a lot of attention is the field of breast cancer detection [21], [22], [23], [24], [25], [26], [27]. It has been observed that the mechanical properties of healthy breast tissue differ significantly to those of malignant tumours, and again to those of benign fibroadenomas [28]. One potential of MRE is to detect variations in stiffness on a minute scale, eventually leading to the detection of smaller, less developed tumours, and tumours found far from the breast surface. Any one of these would be a significant improvement over current imaging standards. It is well known that the earlier a cancer can be detected, the greater the chances are of successful treatment.

One focus of this study is to develop a robust system for MRE imaging which could eventually be used in a clinical setting. Key to this is the development of new pulse sequences to allow for feasible scan times and moving toward the testing of more realistic phantoms.

A second focus is in the area of soft tissue anisotropy. The anisotropy of muscle is widely known and there is a great potential in MRE anisotropy analysis of skeletal muscle in, for instance, sports medicine and rehabilitation. Anisotropy could also play an important role in the analysis of breast tumours, as it has been observed that although in some cases malignant tumours may exhibit similar isotropic stiffnesses to a benign growth, the two may be differentiable through observation of the levels of anisotropy [23]. Attention in elastography has recently turned to the brain. The brain is known to contain highly oriented white matter tracts. This anisotropy is used in diffusion tensor imaging and tractography [29], [30], [31]. However, it is unknown whether the mechanical anisotropy of these structures reflects the diffusion anisotropy. Work undertaken by Kruse *et al.* [18] and McCracken *et al.* [32] would also suggest that such mechanical measurements might be useful in determining changes due to injury or disease.

Chapter 2

Background and Theory

2.1 Magnetic Resonance Imaging

Magnetic Resonance Imaging (MRI) is a technique by which images are produced using the properties of nuclear spin, and the associated magnetic moment, of atomic nuclei, principally hydrogen in clinical applications. The images are obtained tomographically and can reveal internal physical and chemical properties of an object through measurement of returned radiofrequency (RF) signals. One of the chief advantages of MRI over other imaging modalities is excellent soft-tissue contrast, which is based on magnetic relaxation times that vary over almost an order of magnitude between tissue types, giving intrinsically high contrast. This level of contrast is significantly higher than x-ray based techniques, such as CT, which has very poor soft tissue contrast. Images are also obtained non-invasively and without ionising radiation, using signals generated from within the patient itself. In addition, tomographic images can be generated along any direction without changing the orientation of the patient or mechanically adjusting the machine.

The most effective discussion of the theory of MRI incorporates both a classical and quantum mechanical approach to the physics. Classical mechanics is adequate for most areas of MRI theory; however, a brief foray into quantum mechanics is required to understand the fundamentals at the microscopic scale.

As hydrogen is the element predominantly used in clinical applications of MRI, due to its high concentration in the body and strong nuclear magnetic moment, the theory outlined below will deal mainly with ^{1}H nuclei, that is, proton MRI.

2.1.1 Requirements for MRI

The fundamental requirements for MRI are essentially quite simple:

- A large external static magnetic field. Typical field strengths for current clinical use are 1.5 to 3.0T.
- A transmit coil allowing for transmission of RF pulses to the subject within the magnetic field.
- Receive coils. Both transmit and receive coils are tuned to the proton resonance frequency (64MHz for a 1.5T scanner).

- Gradient coils to produce a linear variation in magnetic field strength with position for spatial encoding along the three orthogonal axes: $\hat{\boldsymbol{x}}$, $\hat{\boldsymbol{y}}$, and $\hat{\boldsymbol{z}}$.

2.1.2 Origins in Nuclear Magnetic Resonance

MRI has its foundations in Nuclear Magnetic Resonance (NMR), a physical phenomenon based fundamentally on the spin angular momentum in certain nuclei. Protons and neutrons both possess an intrinsic spin angular momentum quantum number of $\pm\frac{1}{2}$. Nuclei with unpaired protons and neutrons will have a net spin angular momentum, $\boldsymbol{J}$. As the nucleus possesses a charge, it also has an associated magnetic dipole moment $\boldsymbol{\mu}$, proportional to $\boldsymbol{J}$:

$$\boldsymbol{\mu} = \gamma \boldsymbol{J} \tag{2.1}$$

The constant of proportionality, γ, is known as the *gyromagnetic ratio* and is a quantity specific to each isotope.

Ordinarily, in non-magnetic materials, these magnetic moments are oriented randomly, meaning there is no net magnetic moment. However, in the presence of a strong external magnetic field, $\boldsymbol{B_0}$, the moments will attempt to align themselves either ‘parallel’ (paramagnetic) or ‘anti-parallel’ (diamagnetic) to the direction of the field (by convention taken to be $\hat{\boldsymbol{z}}$). Due to the constraints of quantisation of angular momentum, a magnetic moment will not align exactly along the direction of the external field. In fact, what is known as ‘parallel’ and ‘anti-parallel’ is really a description of two quantum states of a nucleus, known also as ‘spin-up’ and ‘spin-down’ respectively. As the moment cannot align itself exactly along the external magnetic field, it will experience a torque, causing it to precess about the direction of the field [33, ch. 8].

Classical electromagnetism describes the torque on a magnetic moment, $\boldsymbol{\mu}$, in a magnetic field, $\boldsymbol{B}$:

$$\boldsymbol{\tau} = \boldsymbol{\mu} \times \boldsymbol{B} \tag{2.2}$$

Mechanically, torque ($\boldsymbol{\tau}$) is also the rate of change of angular momentum:

$$\frac{\mathrm{d}\boldsymbol{J}}{\mathrm{d}t} = \boldsymbol{\tau} \tag{2.3}$$

The classical equation of motion for a magnetic moment in a magnetic field can thus be derived, via substitution of (2.1):

$$\frac{\mathrm{d}\boldsymbol{\mu}}{\mathrm{d}t} = \gamma \boldsymbol{\mu} \times \boldsymbol{B} \tag{2.4}$$

Quantum mechanical effects prevent this equation from being applied accurately to individual protons; however, examination of a bulk quantity of protons, such as that used in MR imaging purposes, reveals the classical description is adequate. In the macroscopic case, a magnetisation vector, $\boldsymbol{M}$, is introduced, which is simply the local magnetic moment per unit volume. Thus for a volume, V, containing a bulk quantity of protons, but assumed to be small enough to have a constant external magnetic field, the magnetisation is given by [34, ch. 4.1]:

$$\boldsymbol{M} = \frac{1}{V}\sum_i \boldsymbol{\mu}_i \tag{2.5}$$

Summing over the equations of motion for individual spins (ignoring individual proton-proton interaction) yields:

$$\frac{1}{V}\sum_i \frac{\mathrm{d}\boldsymbol{\mu}_i}{\mathrm{d}t} = \frac{\gamma}{V}\sum_i \boldsymbol{\mu} \times \boldsymbol{B}$$

or:

$$\frac{\mathrm{d}\boldsymbol{M}}{\mathrm{d}t} = \gamma \boldsymbol{M} \times \boldsymbol{B} \tag{2.6}$$

This equation is the bulk analogue of (2.4) and is known as the *Bloch equation* (with no relaxation effects) [34, ch. 4.1].

The concept of a net magnetisation vector can also be arrived at through quantum mechanics. In the quantum formulation, there are two populations of spin-states, as mentioned earlier. Protons receive thermal energy from their surrounding environment, thus are constantly changing between spin-up and -down states. Boltzmann statistics show, that for a large number of protons with two possible energy states, the proportion of spins in the two levels is given by:

$$\frac{N_{up}}{N_{down}} = \mathrm{e}^{\frac{\Delta E}{kT}} = \mathrm{e}^{\frac{\gamma \hbar B_0}{kT}} \tag{2.7}$$

(See [33, ch. 8.3], and A.2) where k is the Boltzmann constant, T is temperature, $\hbar$ is Planck's constant, and B_0 is the magnitude of the external magnetic field.

At room temperature, thermal energy (kT) is much greater than the proton spin energy ($\gamma \hbar B_0$) [34, ch. 4.2] so there is little energetic preference for spins to align with the external magnetic field. The magnitude of the net magnetisation, M_0 (where the subscript indicates thermal equilibrium), is determined by the net difference between the two spin-states. With this in mind, equation (2.7) can be expressed as Curie's law, in which the constants are simplified into the Curie constant, C:

$$M_0 = C\frac{B_0}{T} \tag{2.8}$$

It is clear that the only two variables that affect M_0 are temperature and magnetic field strength. As it is unfeasible to change body temperature greatly, the only way to increase magnetisation and improve MR signal is with a higher field strength. Even in a 1.5T magnetic field, Boltzmann statistics give an anti-parallel:parallel ratio of $1 : 1.000004$ [33, ch. 8]. While this seems an insignificant ratio, Avogadro's number ensures there is a measurable excess of spin-up states; the sheer number of protons in a sample means that the small proportion that does align still results in a measurable net magnetisation, In the classical formulation, the individual magnetic moments of protons precessing about $\hat{\boldsymbol{z}}$ can be represented by vectors, known as *spins*. These spins are all at random phases, creating two 'cones' of vectors, one parallel (spin-up) and one anti-parallel (spin-down) to $\hat{\boldsymbol{z}}$ (figure 2.1). Due to the slight energetic favouring of the spin-up state, the vector sum of these spins results in the macroscopic magnetisation vector, $\boldsymbol{M_0}$, aligned along the direction of the external magnetic field. The order of magnitude for $\boldsymbol{M_0}$ is microAmpères per metre.

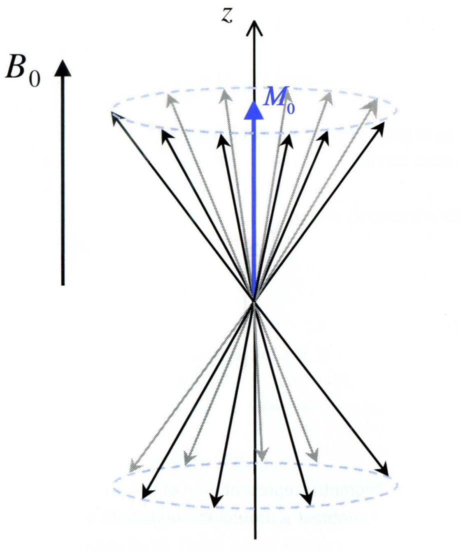

Figure 2.1: Vectors representing classical spins create two 'cones'; the net magnetisation vector, $\boldsymbol{M_0}$, is aligned along the direction of the external magnetic field. Source: [33]

In solving the Bloch equation (2.6) for a classical magnetisation vector, it is noticed that we arrive at a simple harmonic motion solution with a resonant frequency of:

$$\omega = \gamma B \tag{2.9}$$

See A.1 for derivation. 2.9 is known as the *Larmor equation.*

In the quantum mechanical formulation, a proton can change its state from spin-up to spin-down, or vice versa, by gaining or losing a prescribed amount of energy via a photon; this energy difference is directly proportional to the external magnetic field strength. Knowing the energy difference means the photon frequency required to enact a state change can be determined. The subsequent derivation (see A.2) also results in the Larmor frequency found from the classical picture. The Larmor equation is perhaps the most fundamental in MRI, and shows the link between the classical and quantum pictures: the precession frequency of a proton in an external magnetic field is the same as the frequency of a photon required to enact a change between quantum mechanical spin-states.

It would be expected that a time-varying magnetic field perpendicular to $\boldsymbol{B_0}$, such as that found in electromagnetic radiation, will have an effect on the magnetisation vector. What allows for manipulation of the spins in a material is the concept of resonance, the fact the spins will only interact with electromagnetic radiation of the same frequency at which they are precessing, in other words, their resonant, or Larmor frequency. For a proton, with $\gamma = 42.58\text{MHz/T}$, in a clinical field of 1.5 to 3.0T, this frequency is within the radiofrequency range. Fortunately, electromagnetic radiation at these frequencies is not substantially absorbed by human tissue or bone (although, as absorption increases with frequency, power deposition from EM radiation can be an issue in high-field scanners). It is the application of sequences of RF pulses at the Larmor frequency that, in part, allows for manipulation of the alignment of spins in order to return a measurable signal from which an image can be generated.

2.1.3 Generating Signals

In order to generate a measurable signal, the magnetisation vector, $\boldsymbol{M_0}$, must be perturbed from its equilibrium position. Application of a secondary magnetic field, $\boldsymbol{B_1}$, which is perpendicular to the external field, and rotating about the direction of $\boldsymbol{B_0}$ at the resonance frequency, ω_0, will cause $\boldsymbol{M_0}$ to move away from $\hat{\boldsymbol{z}}$ in a spiral path (figure 2.2). Such a field is provided by an RF pulse at the resonance frequency. A typical RF pulse has the form: $\boldsymbol{B_1} = B_1(t)\mathrm{e}^{-i\omega_0 t+\phi}$ where ϕ is an arbitrary phase, generally assumed to be zero, ω_0 is resonance frequency and $B_1(t)$ is known as the envelope function. The envelope function determines the shape and length of the RF pulse and thus the extent to which it excites the system.

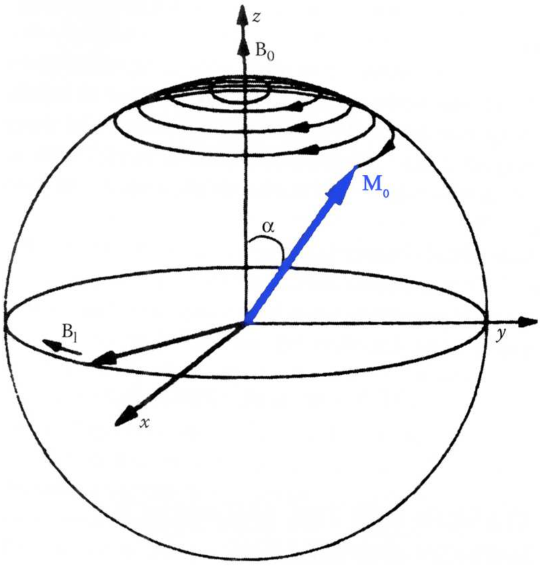

Figure 2.2: During application of the RF pulse, $\boldsymbol{B}_1$, the net magnetisation vector, $\boldsymbol{M_0}$ spirals down from its equilibrium position towards the transverse plane. Source: [35].

One particular conceptual tool useful in visualising the fundamentals of MR physics is the *rotating frame of reference* (figure 2.3). In the classical formulation, it is helpful to consider the reference frame of the magnetisation vector; that is, considering the observer to be on a transverse plane rotating about $\hat{\boldsymbol{z}}$ at the Larmor frequency.

In its equilibrium position, $\boldsymbol{M_0}$ is directed along $\hat{\boldsymbol{z}}$. In the rotating frame, the RF field appears to be stationary and the magnetisation precesses about $\boldsymbol{B}_1$ (along $\hat{\boldsymbol{x}}$ in figure 2.4). For a square wave envelope, where $B_1(t) = B_1$, in the presence of an RF field, the

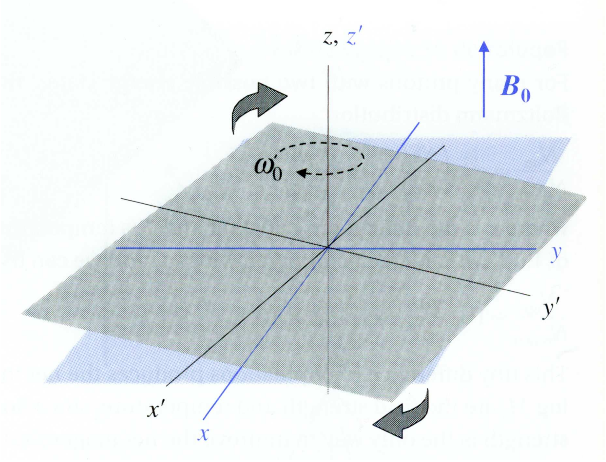

Figure 2.3: In the rotating frame of reference, the primed coordinates are considered to be rotating about $\hat{z}$ at the Larmor frequency, in the same direction as the spins. The rotating spins thus appear to be stationary. Source: [33].

precession frequency of the net magnetisation vector in the rotation frame is:

$$\omega = \gamma B_1 \tag{2.10}$$

The angle through which the spins rotate, α, is given by the integral of ω over time:

$$\begin{aligned}\alpha = \int_0^\tau \omega \mathrm{d}t &= \gamma \int_0^\tau B_1 \mathrm{d}t \\ &= \gamma B_1 \tau \end{aligned} \tag{2.11}$$

In general the amplitude function will be more complicated. The angle, α, is known as the *flip angle* (figure 2.4).

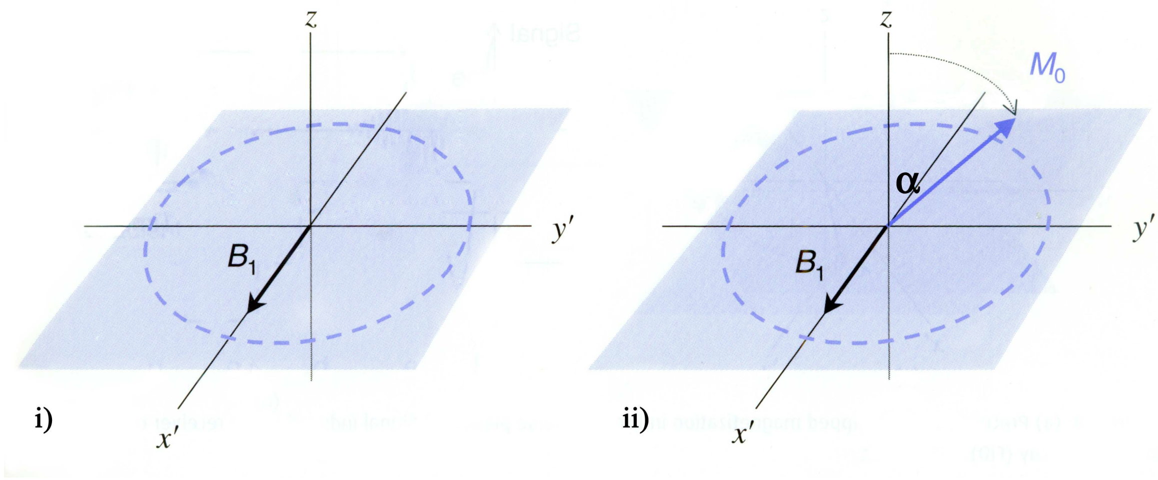

Figure 2.4: i) An RF field produces the $\boldsymbol{B_1}$ magnetic field vector, which appears as fixed in the rotating frame. ii) The net magnetisation vector then precesses about $\boldsymbol{B_1}$ until the RF pulse is switched off. $\boldsymbol{M_0}$ is left at angle α to the external field, aligned along $\hat{z}$. This angle is known as the flip angle. Source: [33].

The flip angle can be altered in two ways: changing the amplitude of the B_1 envelope function, and/or changing the length of time the pulse is held on for. The linear relationship between α and t is apparent in equation (2.11) above. Two common pulses are: a 90° pulse, where the RF signal is turned off once the magnetisation vector is entirely in the transverse plane; and a 180° pulse, of either double the length of time (2τ), or twice the amplitude ($2B_1$), which has the effect of inverting the longitudinal magnetisation.

Once moved out of alignment, the magnetisation vector experiences a torque from the external field and precesses about $\hat{\boldsymbol{z}}$ at the Larmor frequency. A receive coil tuned to this frequency will register an alternating voltage induced due to the oscillating magnetic field of the component of $\boldsymbol{M_0}$ in the transverse (xy) plane ($\boldsymbol{M}_T$). The longitudinal component of the magnetisation varies very slowly with time (on the order of seconds compared to tens of nanoseconds for the period of precession) and will thus not cause any significant induction. This analogue signal undergoes signal demodulation, which converts the frequency from 64MHz to around 250kHz, and then passes through an analogue-digital converter whereby the signal is processed by a computer. A variety of relaxation mechanisms (see 2.1.4) returns the magnetisation to its equilibrium position. The decay of transverse magnetisation means the voltage signal received has the form of a damped oscillator: the oscillation occurs at the Larmor frequency, but with an amplitude that decays exponentially. This type of signal is known as Free Induction Decay (FID) (see figure 2.7).

2.1.4 Image Contrast

Contrast in MR images is observed through exploitation of the characteristic relaxation times of spins following initial RF excitation. Once excited by an RF pulse, spins return to their equilibrium through a number of mechanisms. The difference in relaxation properties of hydrogen atoms in different tissues is what causes the intrinsic contrast between tissues and results in the clinical practicality of MRI.

Bloch was the first to observe two distinct and independent methods of relaxation [36]. These two fundamental processes are: *spin-lattice* interaction, also known as T_1 recovery, and *spin-spin* interaction, also known as T_2 relaxation. T_1 recovery occurs as a result of interaction of the spins with the surrounding environment, transferring energy to the 'lattice'. T_2 relaxation results from a loss of coherence between spins; this occurs through local inhomogeneities in the magnetic field. T_2 relaxation is due to time-varying effects intrinsic to the imaged subject. A third process, T_2', can be classified as relaxation due to static extrinsic effects caused by small inhomogeneities of the applied B_0 field. What is known as T_2^* is the combination of these T_2 effects. T_1 and T_2 are characteristic time constants which vary in different biological tissues.

When considering the bulk magnetisation vector, $\boldsymbol{M}$, it is useful to introduce two components: the longitudinal magnetisation, M_L, aligned along the direction of the external field, and the transverse magnetisation, $\boldsymbol{M}_T$, in the xy-plane (adapting the notation used in [34]. In its equilibrium position, $\boldsymbol{M}$ consists entirely of longitudinal magnetisation. In the rotating frame of reference introduced earlier, a 90° RF pulse excites $\boldsymbol{M}$ from its equilibrium position into the transverse plane. As the spins return to equilibrium position, two independent exponential effects are observed: the recovery of longitudinal magnetisation, and the decay of transverse magnetisation. These effects occur simultaneously, however T_2

decay occurs a lot faster, in general, than T_1 recovery (figure 2.5).

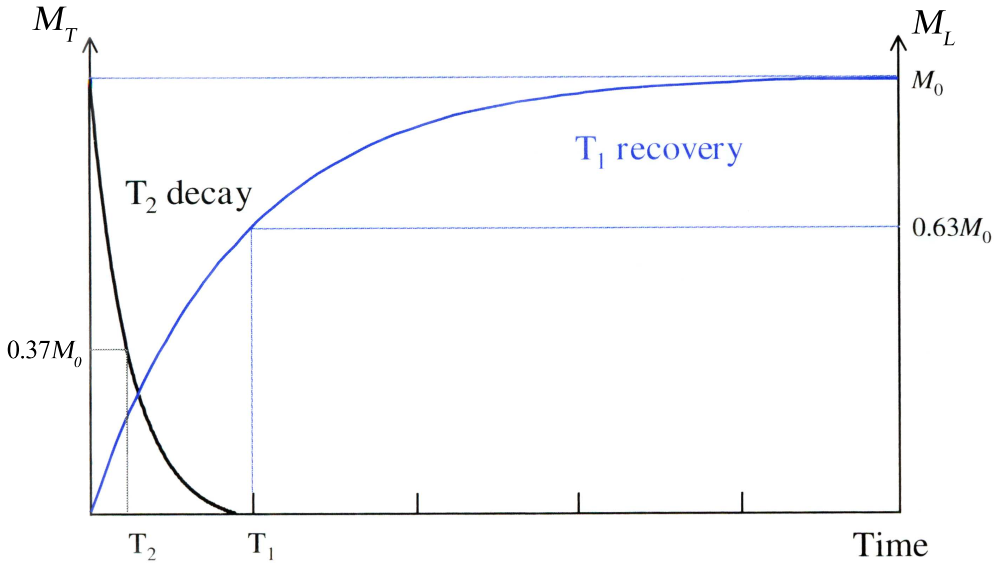

Figure 2.5: T_1 recovery and T_2 decay are relaxation processes occurring simultaneously. In general T_2 occurs faster than T_1. The T_1 time constant is the time value for longitudinal magnetisation to recover to 63% $(1-\mathrm{e}^{-1})$ of the equilibrium value; the T_2 time constant is the time taken for transverse magnetisation to decay to 37% (e^{-1}) of its initial value. Source: [33].

T_1 Relaxation

The longitudinal magnetisation recovers through the interaction of spins with the surrounding lattice. The application of an RF pulse promotes spins from a low-energy state to a high-energy state: energy is absorbed. T_1 relaxation releases this absorbed energy to the surrounding environment. As the high-energy state is still a relatively stable state for the spins, they require a stimulating magnetic field to return them to equilibrium. Stimulating fields occur through *intra-molecular dipole-dipole interaction*: through its thermal jostling, a spin will experience a fluctuating, magnetic field from the dipoles of neighbouring molecules (which are also in thermal motion). These microscopic local fields lead to the transfer of energy from the excited spins to the proximate local environment. However, for an effective transfer of energy, the molecules are required to have vibrational modes in the range of the spin precession frequency (the Larmor frequency). In general, molecules have a range of motional frequencies known as the *spectral density function* (see [33, ch. 8.6]), which means their magnetic dipoles will also have a frequency distribution. The difference in these distributions for different molecules influences the efficacy of energy transfer from the spin system and thus the T_1 characteristic time value of the tissue. The correlation time, τ_c, of the molecules also plays a part; liquids such as water and cerebrospinal fluid are less effective at absorbing energy than solid tissues, leading to a longer T_1 value. As energy is transferred from the spins to the lattice, the spin system returns to its equilibrium, low-energy state and what is called longitudinal magnetisation recovers. The T_1

characteristic time value represents the time required for longitudinal magnetisation to regain 63.2% ($1 - \mathrm{e}^{-1}$) of its equilibrium value.

The equation governing recovery of M_L following a 180° RF pulse is:

$$M_L(t) = M_L(0)[1 - 2\mathrm{e}^{-t/T_1}] \tag{2.12}$$

where $M_L(0)$ is the initial value of longitudinal magnetisation.

T_2 Relaxation

Transverse magnetisation decays, in general, faster than longitudinal magnetisation recovers. Unlike the T_1 process, no energy is lost through the decay of $\boldsymbol{M}_T$; rather, the effect is due to the dephasing of spins in the transverse plane. This loss of phase coherence is due to what is termed 'spin-spin interactions'. Intrinsic local inhomogeneities in the magnetic field are set up through protons 'seeing' not only the external magnetic field but also the localised fields produced by its neighbours. Variations in these local fields lead to small differences in precession frequencies, thus, in the rotating frame, the transverse spin vectors appear to 'fan out' or, dephase. The overall effect is that the vector sum of these individual spin vectors, $\boldsymbol{M}_T$, decreases. The decay of transverse magnetisation is dependent on another characteristic time constant, T_2. The T_2 of a tissue represents the time required for the transverse magnetisation to decay to 36.7% (e^{-1}) of its initial value. The equation governing the dephasing of transverse magnetisation is:

$$\boldsymbol{M}_T(t) = M_T(0)\mathrm{e}^{-t/T2} \tag{2.13}$$

These dephasing effects are due to random spin fluctuations causing time-varying changes in the local magnetic field seen by a spin. As such, the signal decay caused by T_2 dephasing is irreversible. Figure 2.6 summarises the T_1 and T_2 relaxation processes.

There is another cause of loss of phase coherence in the transverse plane. Imperfections in the external magnetic field, on the microscopic scale, lead to T_2' effects. These variations cause a dephasing in the same way as the T_2 effects described above. The difference between T_2 and T_2' is that the extrinsic T_2' effects are constant, non-time-varying, and thus the dephasing effect can be reversed through specially designed pulse sequences (see 2.1.7) thus cancelling out the loss of signal. The 'observed' decay rate of transverse magnetisation is known as T_2^* (see figure 2.7) and is given by combining the T_2 and T_2' decay rates:

$$\frac{1}{T_2^*} = \frac{1}{T_2} + \frac{1}{T_2'} \tag{2.14}$$

Net Relaxation Effect

Bloch's equation (2.6) can now be rewritten to include these relaxation effects:

$$\frac{\mathrm{d}\boldsymbol{M}}{\mathrm{d}t} = \gamma \boldsymbol{M} \times \boldsymbol{B} + \frac{1}{T_1}(M_0 - M_L)\hat{\boldsymbol{z}} - \frac{1}{T_2}\boldsymbol{M}_T \tag{2.15}$$

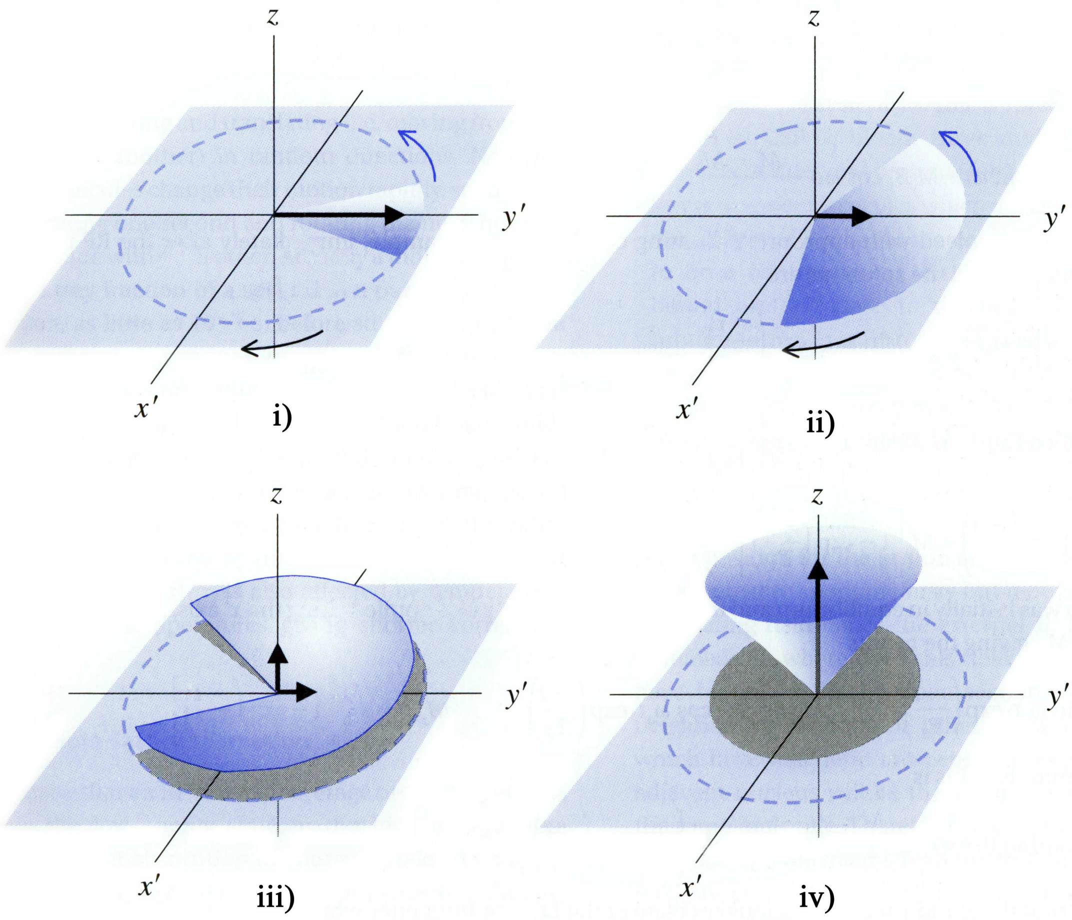

Figure 2.6: In the rotating frame, T_2 relaxation appears as a dephasing of spin coherence leading to a net loss of transverse magnetisation (i and ii). The slower (in general) process of T_1 recovery can be thought of, in this analogy, as an umbrella closing up; the net magnetisation recovers, shown by the bold arrow (iii and iv) as the individual spin vectors form a closing cone precessing, out of phase, around $\hat{\boldsymbol{z}}$. Source: [33].

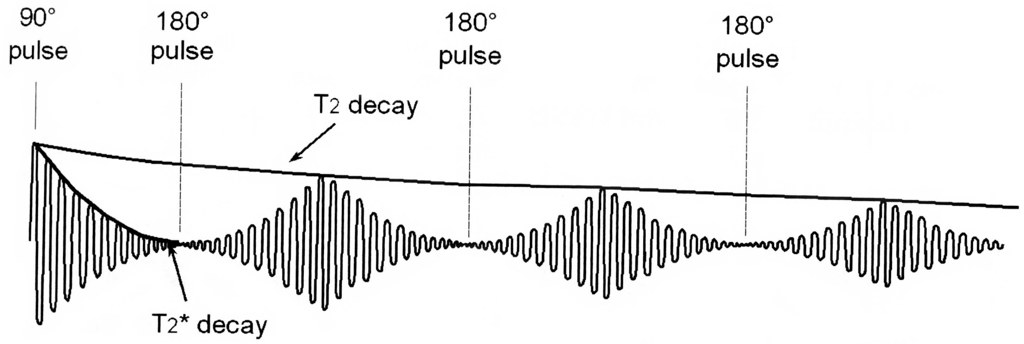

Figure 2.7: Application of a multiple spin echo pulse sequence consisting of multiple 180° refocusing pulses produces the above signal. T_2^* decay is responsible for the initial dephasing of spins and the Free Induction Decay signal. The signal pattern can be recovered following a 180° RF pulse. The recovered 'echoes' however are not at the same amplitude as the original signal; the signal decays exponentially with time. This loss in amplitude is due to irreversible, time-varying T_2 effects. Source: [37].

and the resulting constant-field solutions are [34, ch. 4.4]:

$$M_x(t) = \mathrm{e}^{-t/T_2}(M_x(0)\cos\omega_0 t + M_y(0)\sin\omega_0 t) \tag{2.16}$$

$$M_y(t) = \mathrm{e}^{-t/T_2}(M_y(0)\cos\omega_0 t + M_x(0)\sin\omega_0 t) \tag{2.17}$$

$$M_L(t) = M_L(0)\mathrm{e}^{-t/T_1} + M_0(1 - \mathrm{e}^{-t/T_1}) \tag{2.18}$$

where ω_0 is the resonance frequency, x and y constitute the transverse plane, and $M(0)$ is the equilibrium value of the magnetisation.

Different combinations of RF and magnetic field gradient pulses, known as pulse sequences (see 2.1.7) are employed to enhance or reduce these intrinsic tissue properties and generate images of different contrasts.

2.1.5 Spatial Encoding

The ability to spatially encode data in three dimensions is what distinguishes MRI from NMR and allows for the generation of images. The spins in the imaging target are excited through an RF pulse, and as they return to equilibrium, the returned signal is measured. This signal is a superposition of spin signals from throughout the imaging target that are precessing at different frequencies and at different phases. The key to acquiring spatial information is how spins at different positions are encoded with different frequency and phase information. The encoded spatial information is then extracted from the received signal and processed to form meaningful images. Small volumes in which the phase and frequency of the spins are taken to be constant are known as *voxels*.

In general, the excitation RF pulse cannot be spatially directed (there are some exceptions, for instance, the SMASH [38], SENSE [39], and TSENSE [40] techniques, which use multiple RF coils in parallel), thus what provides the position encoding are three pairs of *gradient coils* engineered into the scanner. These gradient coils produce magnetic field gradients along the three orthogonal directions. A gradient, in the MRI context, is an additional magnetic field superimposed on the main uniform field that varies linearly with position. In the simplest case (along the bore of the scanner, $\hat{\boldsymbol{z}}$), a gradient is formed by a pair of coils with opposing currents (known as a Maxwell configuration). Gradients along $\hat{\boldsymbol{x}}$ and $\hat{\boldsymbol{y}}$ are formed by a Golay configuration of four coils (figure 2.8). The strength of the gradient field is determined by the current applied through the coil.

A spatial variation can be induced along any one of the orthogonal directions, or at an oblique angle through the simultaneous activation of more than one gradient coil. Gradient field strength has an order of magnitude of mT/m ; the *rise time* is the time it takes to achieve this peak amplitude of the gradient field from zero. Another technical consideration is the *slew rate* which is the maximum rate of change of the magnetic gradient fields and the limiting factor behind how fast gradient fields can be switched. The slew rate has an order of magnitude of mT/m/msec.

In general, the total magnetic field strength with a gradient switched on is given by:

$$\boldsymbol{B} = (B_0 + G_x x + G_y y + G_z z)\hat{\boldsymbol{z}} \tag{2.19}$$

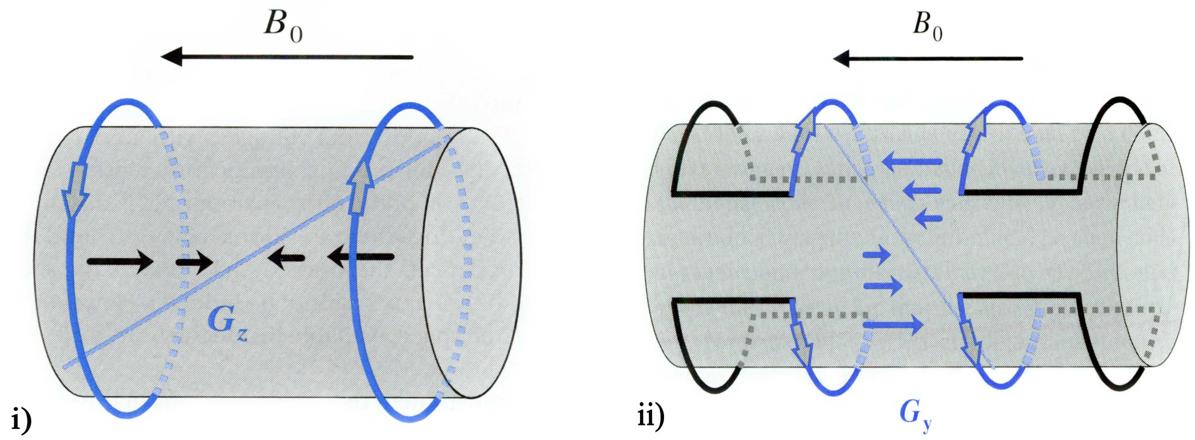

Figure 2.8: i) The Maxwell configuration of coils produces a linear variation in magnetic field along the bore of the scanner. ii) The Maxwell configuration is not practicable along $\hat{\boldsymbol{x}}$ and $\hat{\boldsymbol{y}}$. Instead a Golay configuration, consisting of four coils, produces a quadrupolar magnetic field when a current is applied. Only the innermost arcs of the coils are responsible for producing the transverse gradient field. G_y is shown here; for a gradient field along $\hat{\boldsymbol{x}}$, the same configuration is used, rotated about the bore by 90°. Source: [33].

where B_0 is the magnitude of the external field, G_x, G_y and G_z are magnetic field gradients in their respective directions, and $G_i = \frac{\partial B_z}{\partial i}; i = x, y, z$. Positions x, y, and z are relative to the iso-centre of the magnet. It should be stressed here that while variations in the magnetic field can occur in any direction, the field is always oriented in $\hat{\boldsymbol{z}}$. (Maxwell's equation, $\nabla \cdot \boldsymbol{B} = 0$, means undesirable fields are inevitably set up along $\hat{\boldsymbol{x}}$ and $\hat{\boldsymbol{y}}$; these are *generally* small enough to be ignored, but not always.)

As spin precession frequency is dependent on magnetic field strength, by spatially varying the magnetic field, the precession frequency is made a function of position, from the Larmor equation (2.9):

$$\omega = \gamma(B_0 + \boldsymbol{r} \cdot \boldsymbol{G}) \tag{2.20}$$

where $\boldsymbol{r} = \begin{pmatrix} x \\ y \\ z \end{pmatrix}$ and $\boldsymbol{G} = \begin{pmatrix} G_x \\ G_y \\ G_z \end{pmatrix}$. Applying a gradient along a certain direction has the effect of causing protons to precess at a higher frequency where the magnetic field strength is greater than B_0, and at a lower frequency where B is less than B_0 (figure 2.9). This difference in precession speeds results in different frequencies detected by the receive coil, which are in turn used to differentiate MR signals at different spatial positions. The point in the centre where spins experience only B_0 and the precession frequency is the Larmor frequency is known as the *iso-centre*.

Slice Selection

The first step in creating an MR image is *slice selection*, which involves selecting a two-dimensional slice through the target. This is controlled by applying a gradient along the direction orthogonal to the plane of the desired slice in order to restrict RF excitation of protons only in that slice. The excitation pulse is executed simultaneously with the slice-select gradient and is amplitude-modulated to contain a narrow bandwidth of frequencies,

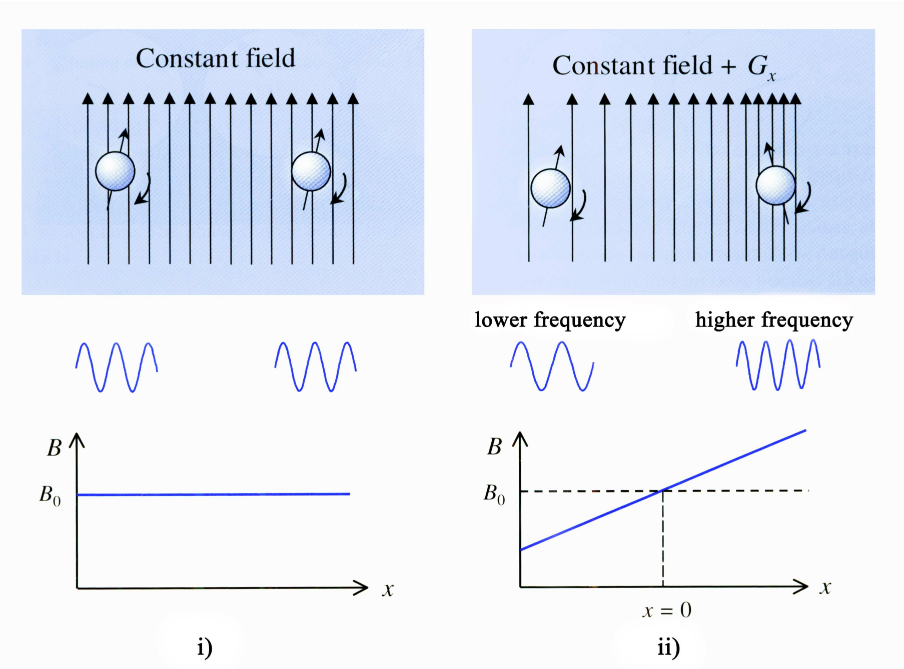

i)

ii)

Figure 2.9: The effect of a gradient field on precessing spins. i) shows that in a constant magnetic field, all spins precess at the same frequency. ii) With a gradient field applied, precession frequency now depends upon position, with protons experiencing a lower field precessing at a lower frequency, and similarly for protons in a higher field. Source: [33].

$\Delta\omega$, corresponding to the thickness of the slice and the precession frequencies of the spins within that slice affected by the gradient (figure 2.10). With $\hat{\boldsymbol{z}}$ as the slice-select direction, the width of a slice in the xy-plane is given by $\Delta z = \frac{\Delta\omega}{\gamma G_z}$. This relation comes from the Larmor equation (2.9) with $\Delta B = G_z \Delta z$, thus $\Delta\omega = \gamma(G_z \Delta z)$. The *slice profile*, or shape of the slice, is given by the Fourier transform of the amplitude envelope of the applied RF pulse; thus, for an approximately rectangular slice, a sinc function RF pulse may be used (figure 2.11). Exciting thin slices requires either a long RF pulse or strong gradients. It should be noted that to produce a perfectly rectangular slice profile, an infinite sinc pulse is required. In reality, the truncation of the sinc pulse results in some deviation from a true rectangular slice profile, experienced at the edge of the slice.

Once the spins in a two-dimensional slice through the target have been excited, the spatial information within this slice can be encoded before the spins return to equilibrium. This is achieved through *phase* and *frequency encoding.*

Phase and Frequency Encoding

Following slice selection, a gradient on an orthogonal axis (by convention, $\hat{\boldsymbol{y}}$) is turned on. As stated earlier, this has the effect of increasing or decreasing the precession frequencies of spins, depending upon their position in space. Over a short period of time this causes a phase change, varying linearly along the y-axis (figure 2.12). Once the gradient is switched off, spins return to their original precession frequency, however, the relative phase differences between spins remains: phase is now a function of position along $\hat{\boldsymbol{y}}$. Phase information is not unique, however: it is a cyclical function. For instance, a phase of 0 is

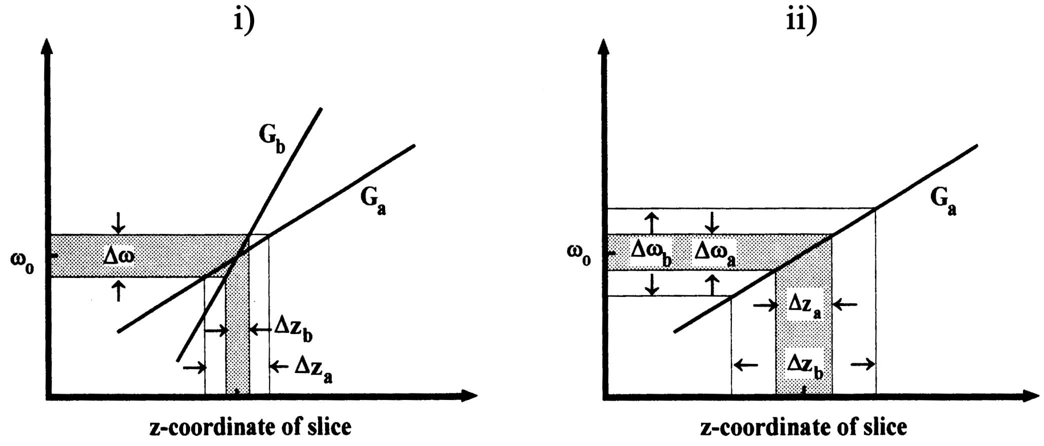

Figure 2.10: i) shows the effect of gradient field strength on slice thickness. The stronger the gradient, the thinner the slice. ii) shows the effect of having a constant magnetic gradient field strength, but varying the bandwidth of the slice select RF pulse. The narrower the bandwidth, the thinner the slice selected. Source: [41].

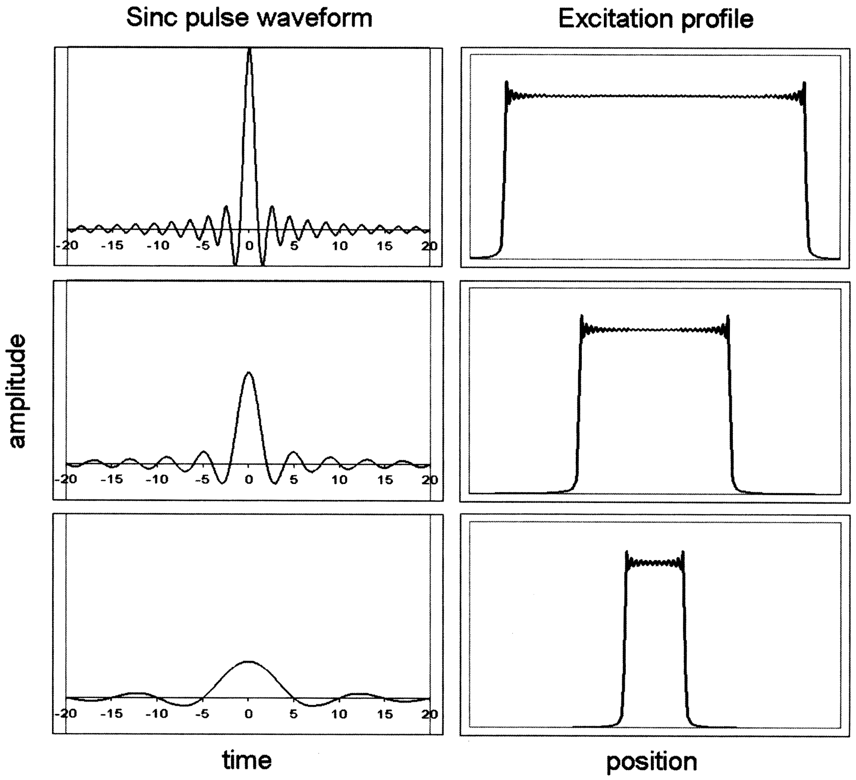

Figure 2.11: This figure shows the relationship between the RF sinc pulse and the 'top-hat' shaped rectangular slice; the two functions are a Fourier pair. The width of the sinc pulse lobes determines the RF bandwidth, which in turn affects the width of the slice. Narrow lobes produce a wide bandwidth, and thus a thick slice (top pair of images). Conversely, wider lobes produce narrower bandwidth, and thus thinner slices. Source: [37].

equivalent to a phase of 2π. Therefore, this process must be repeated for phase encoding gradients of different strengths in order to obtain enough information to uniquely define spatial coordinates in $\hat{\boldsymbol{y}}$.

Each phase encoding gradient is turned on for a very short time before a frequency encoding gradient is activated along the third orthogonal axis ($\hat{\boldsymbol{x}}$). Frequency encoding involves application of a continuous gradient, known as the 'read-out' gradient, during which the signal is sampled by the receive coil over time. This gradient has the effect of altering the frequency of the spins along $\hat{\boldsymbol{x}}$ (figure 2.12); the combined signal of these different frequencies is picked up by the receive coil.

The signal received by the pickup coil is now a summation of sinusoids at different frequencies and phases. A discrete Fourier transform (as the analogue RF signal is sampled through an analogue-digital converter) is applied to convert the signal from a function of time to a function of frequency. As, through equation (2.9), $\Delta\omega$ is proportional to ΔB, and, through equation (2.19), ΔB is proportional to position, this frequency information leads to the spatial location of the spins. [42] contains an excellent analogy between the process described above for MR imaging, and the processing of superimposed sound waves by the human ear into recognisable frequencies.

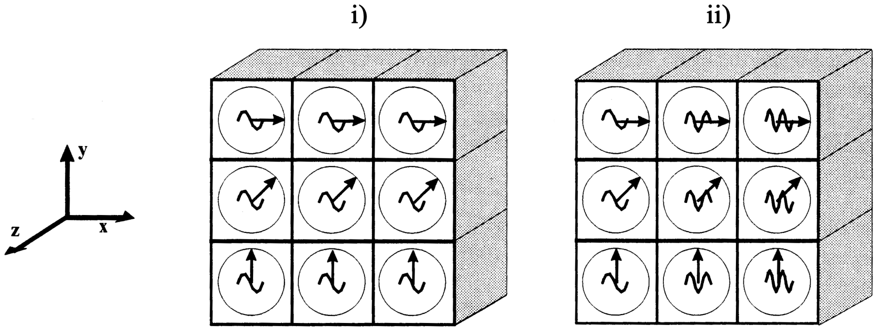

Figure 2.12: i) Following application of a phase encoding pulse on G_y, spins in all voxels are precessing at the same frequency (represented by the sinusoid) but with different phases (represented by the arrow), depending on their position along $\hat{\boldsymbol{y}}$. ii) During application of the read-out (frequency encoding) gradient, G_x, spins retain the same phase offset, but precess at different frequencies, depending on their position along $\hat{\boldsymbol{x}}$. Source: [41].

2.1.6 *k*-space

An alternative way to look at phase and frequency encoding following slice selection is to consider the Fourier domain of the signals.

Mathematically, the total signal received can be represented by:

$$S_{tot} = \int S(\boldsymbol{r}) \mathrm{e}^{i\phi(\boldsymbol{r})} \mathrm{d}\boldsymbol{r} \tag{2.21}$$

which consists of a summation of the signal at each point in space multiplied by a phase factor. Each spin has a intrinsic signal magnitude, $S(\boldsymbol{r})$, and phase factor, $\phi(\boldsymbol{r})$. The phase is given by the integral of the angular frequency; using this and equation (2.20):

$\phi = \int \omega \mathrm{d}t = \gamma \int (B_0 + \boldsymbol{G} \cdot \boldsymbol{r})\mathrm{d}t$. The external magnetic field is not relevant when looking at *relative* phase accrued, thus the B_0 term can be removed from the preceding expression and the phase factor becomes $\phi = \gamma \int \boldsymbol{G} \cdot \boldsymbol{r}\mathrm{d}t$. As above, $\boldsymbol{G} = \begin{pmatrix} G_x \\ G_y \\ G_z \end{pmatrix}$ and $\boldsymbol{r} = \begin{pmatrix} x \\ y \\ z \end{pmatrix}$.

For the 2D case, we define $k_x = \frac{\gamma}{2\pi} \int G_x \mathrm{d}t$, and similarly $k_y = \frac{\gamma}{2\pi} \int G_y \mathrm{d}t$. Generalising to three dimensions, equation (2.21) becomes:

$$S_{tot} = \int S(\boldsymbol{r}) e^{2\pi i \boldsymbol{k} \cdot \boldsymbol{r}} \mathrm{d}\boldsymbol{r} \tag{2.22}$$

where $\boldsymbol{k} = \frac{\gamma}{2\pi} \int \boldsymbol{G} \mathrm{d}t$. This mathematical formulation reveals the dependence of the spatial frequency coordinates, k_x, k_y, k_z, on the magnetic field gradients, G_x, G_y, G_z. The signal picked up by the receive coil can now be described as a function of $\boldsymbol{k}$:

$$F(\boldsymbol{k}) = \int S(\boldsymbol{r}) e^{2\pi i \boldsymbol{k} \cdot \boldsymbol{r}} \mathrm{d}\boldsymbol{r} \tag{2.23}$$

and $F(\boldsymbol{k})$ can be recognised as the Fourier transform of $S(\boldsymbol{r})$. Taking an inverse Fourier transform of this expression yields the spatial information:

$$S(\boldsymbol{r}) = \int F(\boldsymbol{k}) e^{-2\pi i \boldsymbol{k} \cdot \boldsymbol{r}} \mathrm{d}\boldsymbol{k} \tag{2.24}$$

Thus, given the definition $\boldsymbol{k} = \frac{\gamma}{2\pi} \int \boldsymbol{G} \mathrm{d}t$, by varying $\boldsymbol{G}$, one can sample the spatially-encoded signals in the Fourier domain, $F(\boldsymbol{k})$. These signals received from the imaging target are stored in an array, known as *k-space*. k-space represents the spatial frequency, or time-dependent, domain of the image slice, and is the raw data acquired before a Fourier transform generates the familiar MR image. A k-space array has the same dimensions as the final image generated; by convention, phase encoding is used to locate signals along the vertical axis (k_y), and frequency encoding is used to locate signals along the horizontal axis (k_x). Values in k-space are complex, with both magnitude and phase.

As mentioned above, the scanner receives a summation of RF signals at many different frequencies from spins at different positions within the imaging target. This is facilitated through the receive coil registering oscillating voltages over time. These signals are stored in a k-space array as functions of the time-dependent coordinates, k_x and k_y. Each data entry along a row of k-space corresponds to a different spatial frequency in the object acquired during data acquisition with a frequency-encode gradient activated. The received signal is a function of time. Moving down the rows in k-space relates to a new value of the phase encode gradient strength. A 2D Fourier transform of this array generates an image as a function of the spatial position coordinates x and y. The magnitude of the complex data yields to what extent a particular spatial frequency is represented in the imaging target; the phase of the data reveals how the particular spatial frequency wave is positioned in image space.

Whilst these magnetic field gradients cause continuous changes in the position of k-space, the MR signal must be sampled discretely in order for the digital computer processing. Therefore, the data must be sampled at an appropriate rate to preserve information. This rate is known as the *Nyquist frequency* (see [42]).

The actions of gradient pulses can be mapped out on a k-space array. For instance, a negative gradient lobe on the x-axis will move the voxel position in k-space to the left of the origin; a positive gradient lobe on the y-axis will move the voxel position up from the origin. The application of different pulse sequences (see 2.1.7) where different combinations of gradients are used, has the effect of 'filling' k-space in a different manner. A conventional sequence will fill k-space one row at a time; however, pulse sequences have been designed with the intent of filling k-space in a particular fashion, for example, radial acquisition ([42] has a good table outlining different k-space filling trajectories).

k-space and image-space are a Fourier pair; they are related by a Fourier transform. A k-space image is typically bright near the origin and darker the further along the axes (figure 2.13). As it is a map of spatial frequencies, what is being represented here is the rate at which image features change relative to their position. MR signals from a uniform object do not vary much over a range of spatial positions; therefore the spatial frequency signal will be low, i.e. near the origin. At the boundary between two types of tissue, say, the image signal changes significantly within a small spatial position; thus edges are represented by high spatial frequencies. In general, contrast information and the general shape of an object are contained within the low-spatial-frequency information, whereas the spatial resolution (fine detail of boundaries and edges) is contained within the high-spatial-frequency information.

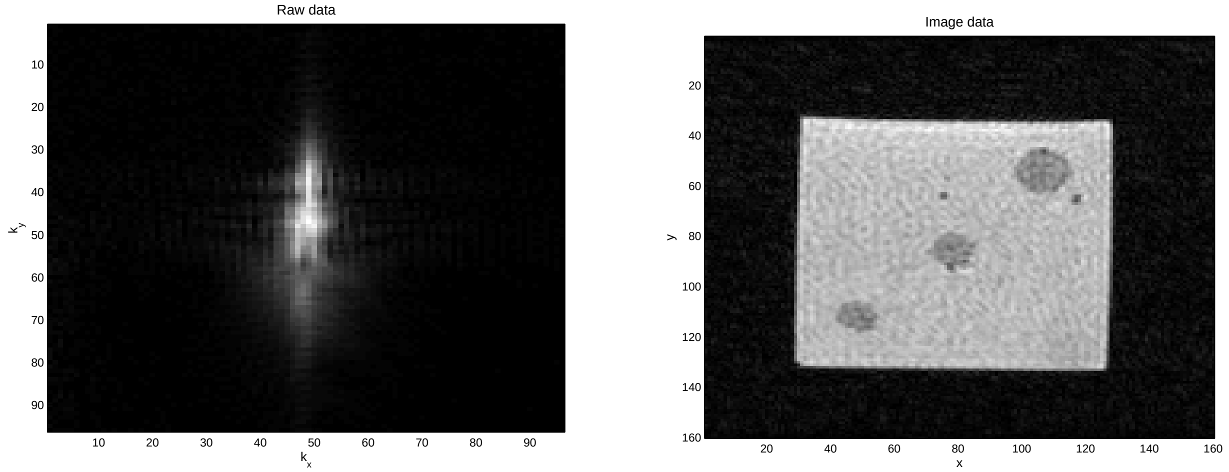

Figure 2.13: *Left:* The raw data in k-space of a silicone phantom with cylindrical inclusions used in this project. *Right:* The corresponding data in image space, following interpolation. In both cases the origin is at the centre and the magnitude of the data is displayed. Note the dimensions of the raw data (96×96) and the zero-fill interpolated image space data (160×160). See 4.2 for further details on data interpolation .

2.1.7 Some Basic Pulse Sequences

Combinations of multiple RF pulses and magnetic field gradients are known as *pulse sequences*. Applications of different pulse sequences are used to exploit the differences in values of T_1, T_2 and proton density (literally the density of hydrogen) between tissues, and thus generate image contrast.

One of the concepts crucial to RF manipulation of spins and thus the pulse sequences built upon it, is the ability to apply pulses of arbitrary angle. The 90° RF pulse discussed earlier results in a 'tipping' of the bulk magnetisation vector, $\boldsymbol{M}$, 90° from its equilibrium position into the transverse plane. Another fundamental RF pulse is a 180° pulse, which has the effect of inverting the magnetisation. In general, an RF pulse of an arbitrary flip angle, α, (figure 2.4) can be applied to $\boldsymbol{M}$, and different flip angles are used in different MR contexts.

'Echoes' are another concept fundamental to signal generation. An echo refers to an MR signal that is acquired through dephasing the spins, then inducing them to rephase. Following tipping of the net magnetisation into the transverse plane through a 90° pulse, a signal is generated with a peak a certain time value after the centre of the pulse. This value is known as the *echo time* (TE). There are a number of different ways to induce rephasing of the spins and thus produce echoes; there are also methods of deliberately dephasing the spins, known as *spoiling*, to accelerate the data acquisition.

All pulse sequences have in common the *repetition time* (TR). As mentioned in 2.1.5, different phase encoding values have to be applied to the system in order to fill the whole of k-space due to the non-uniqueness of phase data. This is achieved through repeating the sequence, after a time parameter of TR, with different gradient strengths on the phase-encoding axis. For example, in a conventional 256 × 256 acquisition, 256 different phase encode values are required, thus there will be 256 TRs per slice.

There are many pulse sequences available to MR radiographers. Four fundamental pulse sequences, upon which many others are based, are discussed below.

Gradient Recalled Echo

In a gradient recalled echo (GRE) sequence (often known as 'gradient echo'), an echo is formed by application of magnetic gradient pulses (figure 2.14). Spins are initially excited by an RF pulse, followed by a negative-amplitude magnetic gradient (or negative *lobe*). The effect of this negative lobe is to dephase the spins much more quickly than they would naturally. A positive gradient is then applied in order to reverse the magnetic field gradient and thus rephase the spins. Spins precessing at a higher frequency due to the effect of the negative lobe on their position will precess at a lower frequency due to the positive lobe, and vice versa. Eventually the previously dephased spins will come back in phase generating the echo signal. If the positive gradient remains on, the spins will again dephase. The positive lobe will only counteract the dephasing effects of the initial negative gradient pulse. Dephasing effects due both to local inhomogeneities in the external field and random time-varying effects due to spin-fluctuations are not recovered, hence the GRE sequence is dependent on the T_2^* relaxation parameter. Changing the echo time will vary the dependence of the signal on the T_2^* value of the tissue:

$$S_{GE} = S_0 \mathrm{e}^{-TE/T_2^*} \tag{2.25}$$

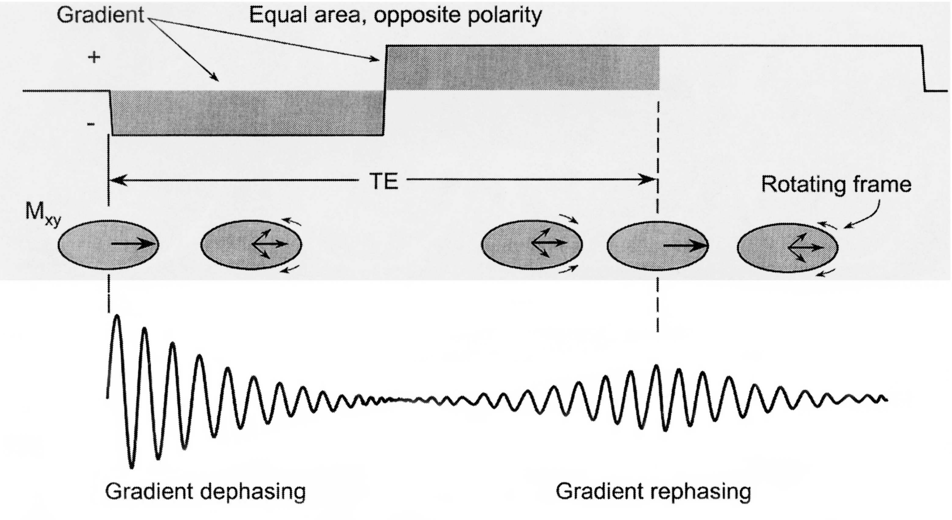

Figure 2.14: Following initial excitement by an RF pulse, the transverse component of the magnetisation is dephased through application of a negative polarity magnetic field gradient. The spins are brought back into phase through a gradient pulse applied at the opposite polarity. Hence the term 'gradient *recalled* echo'. The returned signal reaches a maximum at the point where the second gradient pulse has reached an area equal to that of the first pulse. Source: [37].

Spin Echo

A spin echo sequence creates an echo through application of multiple RF pulses (figure 2.15). After an initial 90° pulse to excite the magnetisation into the transverse plane, the spins are left to dephase naturally for a short time before a 180° pulse is applied. This pulse has the effect of reversing the phases of the spins, so those previously dephasing clockwise will now appear to have already dephased anticlockwise. These spins will continue a clockwise phase-shift, however they are now coming back into phase. The opposite applies for spins originally dephasing anticlockwise. After a time interval equal to that between the initial 90° and 180° pulses (TE), the spins rephase, generating the echo signal. One advantage of the spin echo sequence, over the gradient echo sequence, is that it eliminates dephasing effects due to static magnetic field inhomogeneities and thus the echo peak amplitude depends only on T_2 and diffusion effects. Assuming the spins have not moved significantly during the sequence, diffusion can be discounted and the signal generated is given by:

$$S_{SE} = S_0 \mathrm{e}^{-TE/T_2} \tag{2.26}$$

Spin echo is the sequence used for determining T_2 values of samples.

Inversion Recovery

In order to measure the T_1 value of a sample, a sequence known as inversion recovery is used (figure 2.16). An initial 180° pulse is applied in order to invert the longitudinal magnetisation. Following a time interval, known as the *inversion time* (TI), to allow the spins to regain some longitudinal magnetisation, a spin echo sequence is applied. First, a 90° pulse rotates the remaining M_L into the transverse plane; then a second 180° pulse

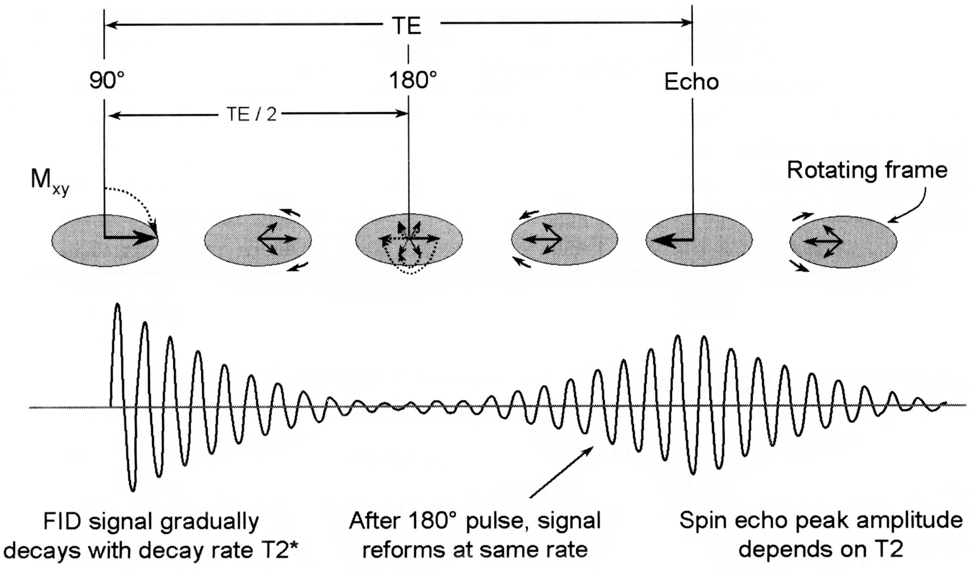

Figure 2.15: Schematic of a spin echo pulse sequence. Following the initial 90° pulse, the spins dephase according to T_2^* relaxation producing the characteristic FID signal. After time TE/2 a 180° pulse is applied which refocuses spins and produces an echo at time TE after the initial pulse. Source: [37].

rephases the spins to generate an echo signal. The signal received is proportional to M_L at time TI following the initial 180° pulse:

$$S_{IR} = S_0 \left| 1 - 2\mathrm{e}^{-TI/T_1} \right| \tag{2.27}$$

If TI is chosen to match $\ln 2 \times$the T_1 value for a particular sample, no signal will be returned, as there will be no longitudinal component of the magnetisation to flip into the transverse plane with the 90° pulse. This is the basis of techniques for nulling out the signal from particular tissue types such as FLAIR (FLuid Attenuation by Inversion Recovery), which removes the signal from fluid, and STIR (Short Tau Inversion Recovery), which removes the signal from fat (see [33, ch. 12]).

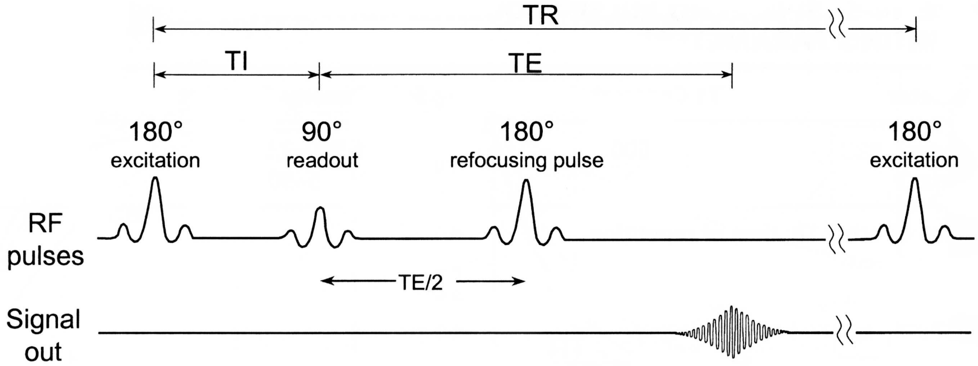

Figure 2.16: An inversion recovery sequence is simply a spin echo sequence with a 180° excitation placed in front. This initial pulse 'inverts' the longitudinal magnetisation, which then 'recovers' until time TI after the first pulse. At this stage a 90° pulse converts remaining longitudinal magnetisation into transverse magnetisation, which can then be picked up by the receive coil through the spin echo approach. The sequence is repeated after time TR between initial 180° excitation pulses. Source: [37].

Echo Planar Imaging

Echo planar imaging (EPI) is a technique whereby several lines of k-space are sampled from a single RF excitation. As such it provides a very fast method of MR imaging. EPI can be spin echo and gradient echo based. Each sequence begins with the standard way of applying spin or gradient echo: spins, having been excited into the transverse plane, are induced to rephase either through a 180° RF pulse (spin echo), or through positive and negative magnetic gradients (gradient echo).

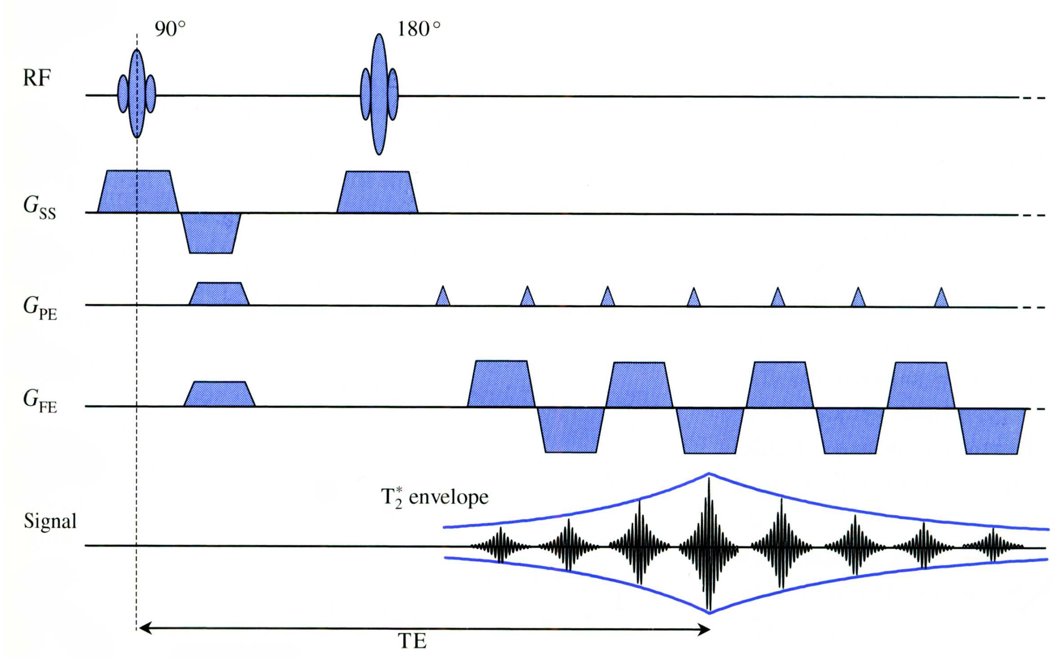

Figure 2.17: A schematic of a 'blipped' spin echo EPI pulse sequence. In this figure, SS stands for slice select, PE for phase encoding and FE for frequency encoding. Following the initial RF excitation and the slice select pulse, a 180° RF pulse starts to bring the spins back into phase. Immediately following this pulse, the *readout train*, consisting of oscillating gradients along the frequency encode gradient and phase encoding 'blips', begins producing signal echoes. The signal strength of the echoes is governed by the T_2^* envelope. Only 8 echoes are shown here; in practice, the sequence would acquire 64 to 128 echoes. Source: [33].

In an EPI sequence, the signal is sampled continuously following the initial excitation. In what is known as 'blipped' EPI, an oscillating readout gradient is applied along the frequency encode axis immediately following the refocusing RF or gradient pulse. This occurs simultaneously with phase encoding 'blips' (figure 2.17). The blips are of a constant size and have the effect of adding further phase encoding to the spins. This effectively traverses k-space line by line: for each phase encode blip, the k-space trajectory moves to another phase value, and the readout gradient traverses the frequency encode axis (figure 2.18). This combination of pulses is known as a readout train. A 'nonblipped' EPI sequence has a continuous phase encoding gradient switched on simultaneously with the oscillating readout gradients, and results in a zigzag pattern to fill k-space, rather than the square filling of the blipped sequence. This is sometimes known as 'ramp sampling' and requires data to be regridded to a Cartesian grid before Fourier processing to image space. Other k-space trajectories for EPI also exist, such as circular and square spiral filling.

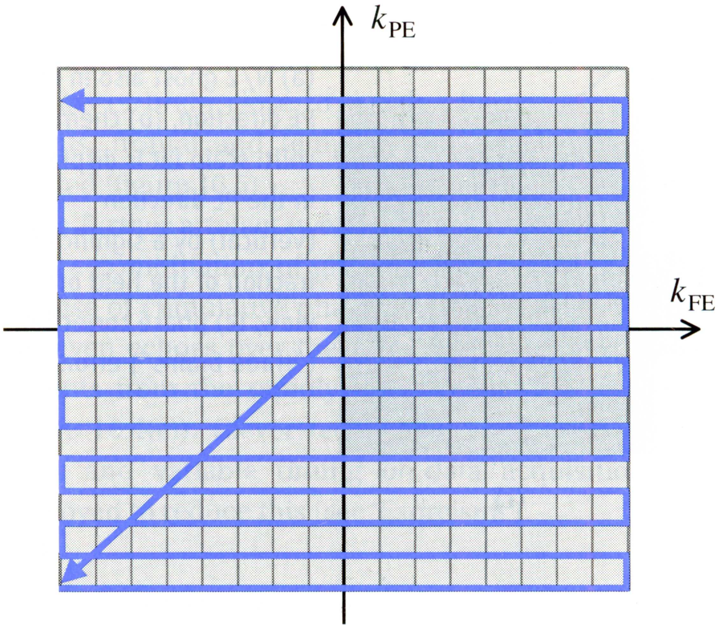

Figure 2.18: Figure 2.17 details the phase encoding 'blips' and oscillating frequency encoding pulses of the EPI readout train. This diagram shows the effects of these pulses on how data in k-space is acquired. Following initial magnetic gradient pulses along the phase and frequency encode axes, the phase and frequency values of the spins are taken to a corner of the k-space data array. This is shown by the diagonal arrow from the centre of the array to the lower left corner. During the readout train, a positive lobe pulse along the frequency encode axis fills a line of k-space from left to right. A phase encode blip following this adds further phase to the spins and has the effect of going up a line in k-space. A negative lobe frequency encode gradient then fills k-space from right to left. This process continues until the entire k-space array is filled. Source: [33].

EPI sequences can be *single-shot* or *multi-shot*. In the single-shot case, the whole of k-space is acquired within a single TR. In multi-shot EPI, multiple acquisitions are interleaved, using several RF excitations to cover k-space. In this project, four-shot EPI was used to reduce artifacts. Typically, 20 slices can be obtained in about 30 seconds [33, ch. 16.2].

The T_2^* decay envelope (figure 2.17) limits EPI resolution to, typically, 64×64 or 128×128. In general, echo times are limited to no shorter than 30 to 60ms [33, ch. 16.2], thus it may be difficult imaging tissues with a short T_2. EPI is also susceptible to artifacts. These are primarily due to 'phase ghosting', caused by imperfections in the rapidly-switching frequency encoding gradients, and consequences of high signal bandwidth and low sampling rate along k_y, which leave the acquisition susceptible to chemical-shift artifacts and small variations in the magnetic field. See [33, ch. 16.2] and [34, ch 19.5] for more details.

2.2 Magnetic Resonance Elastography

Magnetic Resonance Elastography (MRE) is an MRI-based technique through which the elastic properties of soft materials (for instance, tissue or tissue-mimicking phantoms) can be determined quantitatively. Research into elastography was first conducted into this area using ultrasound techniques [43], [44], [45] , however, interest in MRE has increased over the last decade, since the development of phase-contrast MRI techniques allowing for measurement of static and cyclic displacement. The chief advantage over ultrasound techniques is that MRE experiences none of the limitations in selecting acoustic windows throughout the body [46].

MRE uses an MRI phase contrast technique to measure the displacement of voxels due to propagating mechanical shear waves in a soft tissue medium. Current MRE techniques are capable of detecting motion on the range of microns through a full three-dimensional imaging volume. This is achieved through measurements of the relative phase change in the MR signal of a moving sample. The limiting factor on the size of motion able to be detected is thus the phase resolution of the MR scan, not the wavelength of the propagating waves (figure 2.19). The promise that MRE can be used to detect stiffness abnormalities on a much smaller scale than can be currently detected generates great excitement over developing MRE technologies.

A method of actuation is required to induce these acoustic shear waves in the medium [47]. A number of ways of achieving this has been demonstrated, including impulse, quasi-static [28], transient [20], or dynamic mechanical actuation [48], [49]. Within these methods, a number of approaches has been used (for instance, pneumatic [13], electromechanical [50], and piezoelectric drivers [51]). The displacement data recorded can then be processed to reconstruct quantitative values for the elastic properties of the sample, over the entire volume [52], [53], [54], [55]. Images known as *elastograms* [56] can be produced that show tissue stiffness or elasticity.

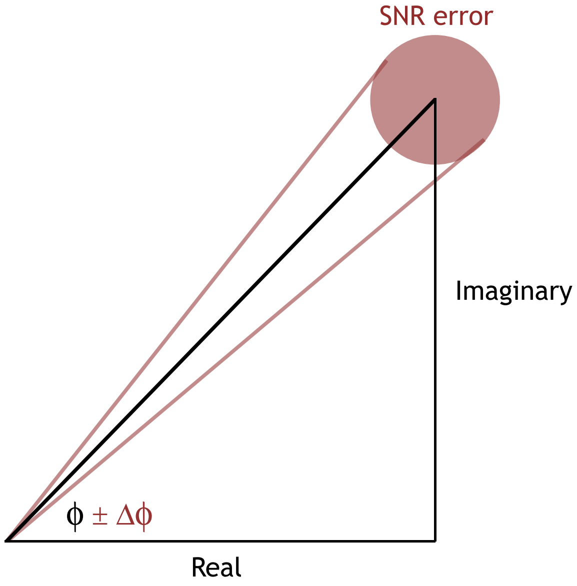

Figure 2.19: As MRE is a phase contrast technique, the phase resolution is the limiting factor on the size of motion able to be detected. The data generated by the phase contrast MRI scan is complex; the phase of this signal, ϕ, is recorded. Poor signal-to-noise ratio (SNR) leads to an error in the phase, $\Delta\phi$, as shown here.

2.2.1 Elastic Properties of Soft Tissue

The current reconstruction model used in our research treats tissue as an incompressible, isotropic, linear elastic material [26]. In this simplification, the material satisfies Hooke's law in three dimensions [57]:

$$\sigma = 2\mu\epsilon + \lambda tr(\epsilon)I \tag{2.28}$$

where I is the standard identity matrix, σ is the stress tensor, ϵ is the strain tensor, thus defined in terms of displacements, $\boldsymbol{u}$:

$$\epsilon = \frac{\nabla\boldsymbol{u} + \nabla\boldsymbol{u}^T}{2} \tag{2.29}$$

μ and λ are known as *Lamé's parameters*, and serve as constants describing a given material. λ does not have a physical interpretation, but μ is also known as the *shear modulus* which relates the amount of transverse strain observed given an applied transverse stress.

Two other common properties used in describing linear elastic materials are the *Young's modulus* (E), which relates the amount of longitudinal strain observed in response to an applied longitudinal stress, and *Poisson's ratio* (ν), which is a measure of compressibility describing the displacement in a particular direction as a result of an applied, orthogonal displacement. These parameters are all related such that from any two known parameters, the other two may be determined [26]:

$$E = \frac{\mu(3\lambda + 2\mu)}{\lambda + \mu} \tag{2.30}$$

and

$$\nu = \frac{\lambda}{2(\lambda + \mu)} \tag{2.31}$$

In general, the mechanical properties of tissues are somewhat between those of fluids and solids. The typical value of Poisson's ratio for most soft tissues is 0.499999 [4], indicating a very nearly incompressible material. The Young's and shear moduli can vary by orders of magnitude for different tissue types, which is important for MRE, as it can be used to distinguish regions of different tissues: tumours within the breast, for instance [3], [5], [28], [43].

2.2.2 Actuation

Dynamic, or harmonic, mechanical excitation is the method of interest in this study. The dynamic approach is to generate shear waves of frequencies in the range of 50 to 1000 Hz; shear waves at these frequencies are much less attenuated than those at higher frequencies and their wavelengths in tissue range in order of magnitude from 10^{-3} to 10^{-2} m, which is a practicable size for measuring with MRI over a conventional field of view [4]. Low frequency longitudinal waves, for instance, have an impractically long wavelength in soft tissue media (on the order of metres for frequencies below 1000 Hz); while high frequency longitudinal waves are not suitable as their propagation is determined by the *bulk modulus*, a mechanical property which does not vary much between tissues. Longitudinal waves within the medium are not redundant, as they generate shear waves through mode conversion at boundaries.

As a comparison, the approach of the static method is to image the sample before and after a known stress load is applied. In comparing the two approaches, one particular advantage of the harmonic method of acquisition is that it relies only on the wave equation [55]:

$$\nabla \cdot \mu \nabla \boldsymbol{u} + \nabla(\lambda + \mu)\nabla \cdot \boldsymbol{u} = \rho \frac{\partial^2 \boldsymbol{u}}{\partial t^2} \tag{2.32}$$

where ρ is the density of the material and $\boldsymbol{u}$ is the 3D displacement vector. Because the elastic forces (LHS of (2.32)) are compared to the inertial forces (RHS), solving for the material properties does not require knowledge of the material-property boundary conditions of the imaged sample. Rather, absolute estimates of the imaged tissue or phantom can be generated with only local knowledge of displacement, $\boldsymbol{u}$, providing ρ is known. So measurement of a propagating shear wave in a small region is enough to determine the shear modulus of the tissue in that region.

This is in comparison to the static technique, where the boundary conditions of the material are also required to be known [4], as the material properties can only be determined relative to other values in the material. Calculations of elasticity are usually of a global nature, and can thus be more computationally intensive [4], [52].

2.2.3 General Experimental Setup

While a number of different mechanisms can be used to induce harmonic shear waves to the imaged medium, some elements are common in the dynamic actuation approach.

Firstly, an oscillator and amplifier drive the actuation device at the desired frequency. The actuator must be coupled well to the surface of the object under investigation.

Secondly, a means of synchronising the actuation to the motion encoding gradients of the pulse sequence (see 2.2.4 and 3.2) is essential. This study uses a trigger pulse generated at the same frequency as the driving sinusoid for the actuator (figure 2.20). The signal generator is thus required to be connected directly to the scanner to input the triggering signal.

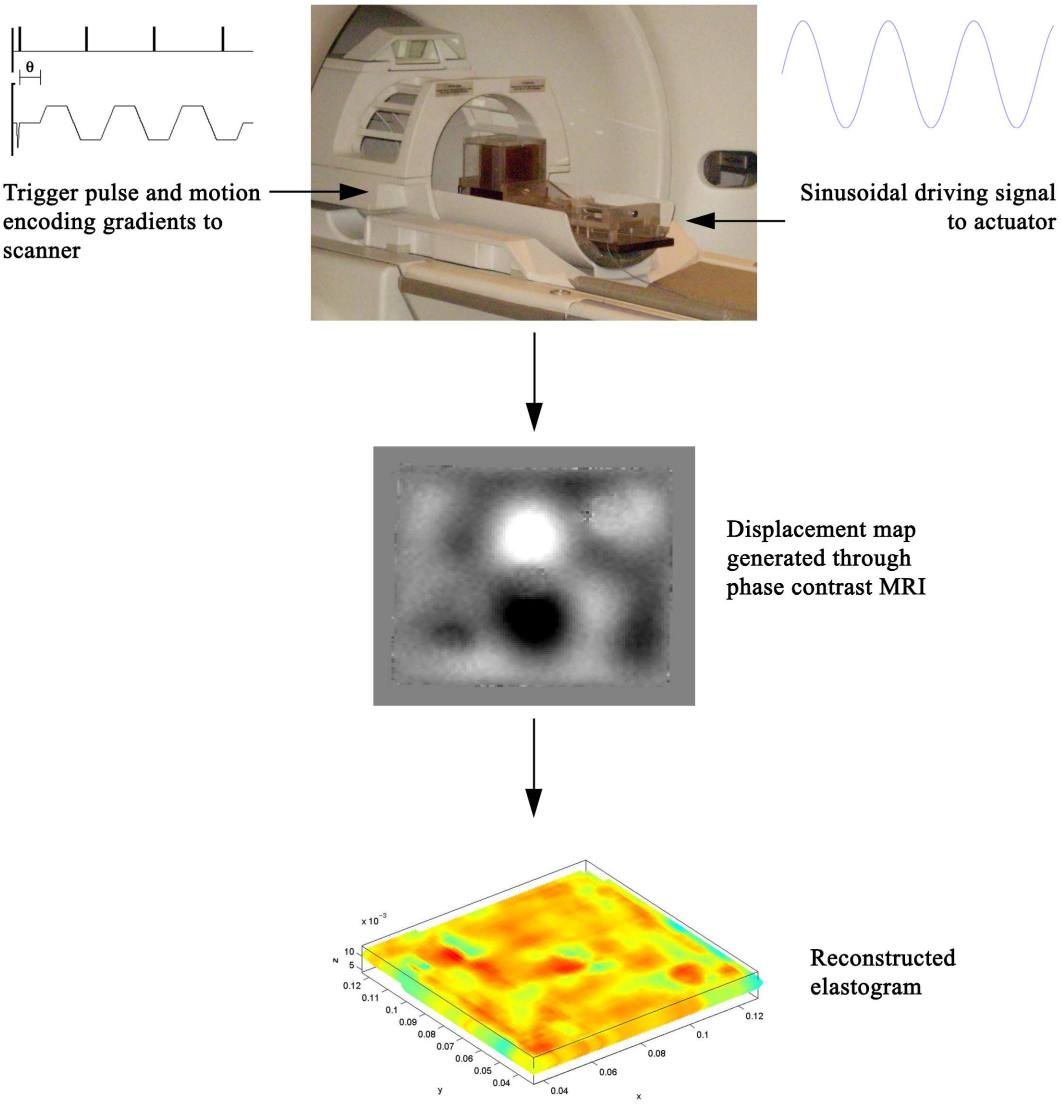

Figure 2.20: Shown is a schematic of the general experimental procedure. Motion encoding gradients are applied to the scanner, along with a trigger pulse (top left). The trigger pulse is synchronised to the sinusoidal driving signal input to the piezoelectric actuator (top right). A phase contrast MRI technique allows for the measurement of 3D displacements at every point in space (centre). From these data, the elasticity of the sample can be reconstructed, generating images known as elastograms (bottom).

2.2.4 Motion Encoding in Pulse Sequences

A brief introduction to phase contrast MRI is outlined here using a common example of this technique, before progressing to the specific case of MRE.

Phase Contrast MRI

MR phase contrast techniques are commonly used in imaging blood flow. Rather than relying on inherent T_1 or T_2 properties for contrast, this technique uses difference in phase to provided image contrast. Phase contrast angiography is a technique that relies on the signal phase; blood, in this case, and its constituent spins are assumed to be moving at a constant velocity [58, ch. 34].

Consider applying a magnetic field gradient G_x after the slice select gradient. Phase will accumulate in the spins over time (refer to 2.1.5). For instance, protons within the slice selected at $t = 0$ will experience the magnetic field gradient for a longer period of time and thus accumulate more phase. The phase shift between voxels, rather than the net magnitude of the magnetisation, is used to generate images. Thus the signal phase at each location is related to the velocity of the flow in the direction of the motion encoding gradient.

Mathematically, consider a simple step function gradient of the form:

$$G_x = \begin{cases} 0 & t < 0;\ \mathrm{t} \geq \tau \\ G_0 & 0 \leq t < \tau \end{cases} \tag{2.33}$$

Thus for the time the gradient is on, the magnitude of the total magnetic field experienced by spins in the selected slice will be $B = B_0 + G_0 x$. With the assumption that spins are moving at a constant velocity, v_0, the position is given by $x = x_0 + vt$. From (2.20), we obtain:

$$\omega = \gamma B_0 + G_0(x_0 + v_0 t) \tag{2.34}$$

The accumulated phase, ϕ, is given by the integral of the above equation, over the length of time the gradient is switched on:

$$\phi = \gamma \int_0^\tau B_0 + G_0(x_0 + v_0 t)\mathrm{d}t \tag{2.35}$$

To look at the *relative phase* accumulated, we can ignore the effects of the constant external magnetic field. Thus the expression becomes:

$$\Delta\phi = \gamma \int_0^\tau G_0(x_0 + v_0 t)\mathrm{d}t \tag{2.36}$$

This equation reveals the dependence on both initial position and velocity of the spins.

If, however, a bipolar gradient pulse is used (figure 2.21), consisting of equal and opposite lobes, the position dependence can be removed (see figure 2.22).

For

$$G_x = \begin{cases} G_0 & 0 \leq t < \tau \\ -G_0 & \tau \leq t < 2\tau \end{cases} \tag{2.37}$$

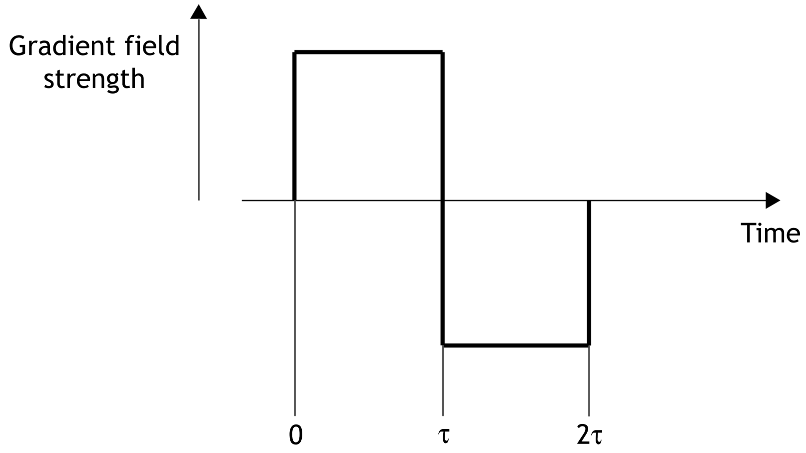

Figure 2.21: A square wave magnetic gradient pulse consisting of two lobes of equal and opposite areas.

The expression for relative phase accumulated becomes:

$$\begin{aligned} \Delta\phi &= \gamma\int_0^{\tau} G_0(x_0+v_0t)\mathrm{d}t - \gamma\int_0^{2\tau} G_0(x_0+v_0t)\mathrm{d}t \\ &= -2\gamma G_0 v_0 \tau^2 \end{aligned} \tag{2.38}$$

This reveals that the bipolar gradient pulse has no effect on a stationary spin ($v_0 = 0$). However, a moving spin will be in a different position when the negative lobe is applied and thus experience a net effect of phase accumulation.

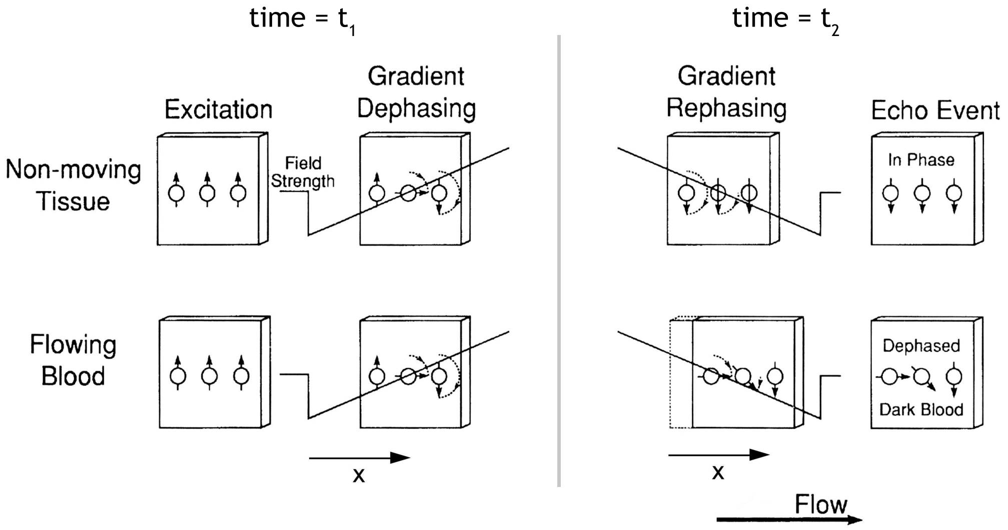

Figure 2.22: A schematic of the effect a motion encoding gradient pulse has on the phase of stationary and moving spins, in the context of imaging blood flow. The first sequence of images reveals the cancelling effect of positive and negative magnetic gradients on stationary tissue. The second sequence shows a net dephasing of the constituent spins of flowing blood. Source: adapted from [58].

Motion Encoding in MRE

A similar approach is used for motion encoding in MR elastography. A conventional MRI pulse sequence (spin echo, gradient echo, echo planar imaging, for instance) is used, with additional bipolar motion encoding gradients switched on along a specified direction (see figure 2.23). These gradients have the same period as the signal driving the actuator; the two are synchronised by a trigger pulse (see 3.2). Thus, shear waves are induced into the medium, via the actuator, at the same frequency as the motion encoding gradients.

The harmonic motion of spins at this frequency causes a measurable phase shift in the returned RF signal. Consider a full three-dimensional treatment of spins undergoing simple harmonic motion. Instead of the linear velocity from the preceding equations, let $\boldsymbol{\xi}$ represent the displacement of the spin from its mean position, $\boldsymbol{r}$:

$$\boldsymbol{\xi}(\boldsymbol{r},\theta) = \boldsymbol{\xi}_0 \cos(\boldsymbol{k}\cdot\boldsymbol{r} - \Omega t + \theta) \tag{2.39}$$

where $\boldsymbol{\xi}_0$ is the amplitude of displacement, $\boldsymbol{k}$ is the wave vector, Ω is the angular frequency of the harmonic excitation, and θ is an initial phase offset ([47]. We assume a bipolar magnetic field gradient pulse, $\boldsymbol{G}(t)$, initiated at the same frequency as the mechanical excitation of the spins, either of the square-wave form described in (2.37), or perhaps a sinusoid or a trapezoidal waveform. The accumulated phase then becomes:

$$\begin{aligned} \Delta\phi &= \gamma \int_0^{NT} \boldsymbol{G}(t)\cdot\boldsymbol{\xi}_0 \cos(\boldsymbol{k}\cdot\boldsymbol{r} - \Omega t + \theta)\mathrm{d}t \\ &= \frac{2\gamma NT(\boldsymbol{G}\cdot\boldsymbol{\xi}_0)}{\pi}\sin(\boldsymbol{k}\cdot\boldsymbol{r} + \theta) \end{aligned} \tag{2.40}$$

where T is the period of the harmonic motion (and of the gradient pulse) and N is the number of gradient cycles applied. The relationship $\Omega = \frac{2\pi}{T}$ has been used. This equation is arrived at in 3.5.1 for different cases of magnetic gradient pulse waveforms used in this project.

Spins with the maximum phase shift are those whose components of motion along the direction of the gradient vector are exactly in phase or in anti-phase with the oscillations in the magnetic field; similarly, spins with no net phase shift are those whose components of motion along the direction of the gradient vector are 90° out of phase with the magnetic field variations.

Equation (2.40) also shows that the observed phase shift is directly proportional to the number of cycles of the motion encoding gradient. Thus, a greater phase shift can be observed simply by including more motion encoding gradients in the pulse sequence. The accumulated phase shift is also proportional to the relative phase of the magnetic and mechanical oscillations. In general, several scans will be taken varying the phase offset between these two signals. In this manner, a more complete picture of the motion may be obtained [4].

Each scan is sensitive to motion in a single direction; thus, multiple scans are performed, placing the motion encoding gradient along a different gradient axis for each scan. Thus, a dataset is acquired containing three-dimensional cyclic displacement data throughout a full 3D volume at the specified MR voxel resolution.

From the dataset of displacement information, the elasticity throughout the imaged volume can be reconstructed. This is discussed in 2.3.

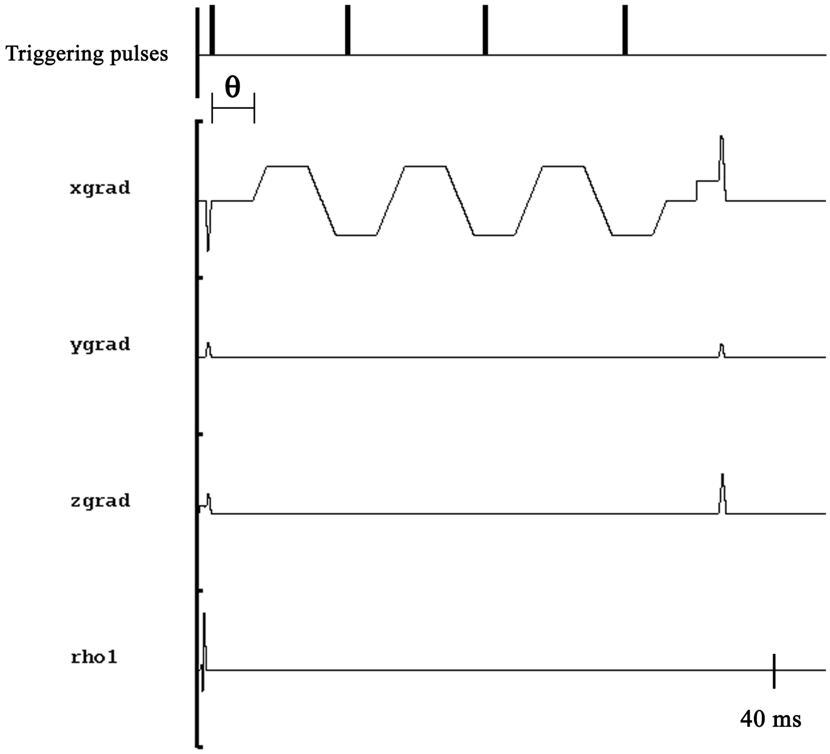

Figure 2.23: Output from a 3D gradient echo pulse sequence used in this project. In this example, three trapezoidal motion encoding gradients are applied along the $\hat{\boldsymbol{x}}$ gradient. The trapezoids have a period of 10ms. Synchronised to the start-point of each trapezoid is a triggering pulse setting the motion of the mechanical actuator to the motion encoding gradients. The phase offset between the trigger pulse and the start of a gradient pulse, θ, can be controlled and in practice is varied between scans to produce data at different relative phases.

2.3 Data Processing Using Finite Elements

This section provides a basic introduction to the processing of displacement data acquired by the MR scanner, through the phase contrast technique outlined in the previous section, into a reconstructed set of elastic properties for the volume via the subzone based finite element method. Only a simple case is presented here, with a number of assumptions made. For a more detailed treatment, see [53], [54], [55]. For cases that deal with more complex initial assumptions, such as anisotropy and viscoelasticity, see [23], [24], [25]. Manduca [4] also gives a useful overview of a number of different processing techniques.

The essential problem in MRE reconstruction that we are concerned with here can be expressed as: given a set of measured displacements in a 3D volume, find the elastic properties μ and λ. While any two of the four mechanical properties described in 2.2.1 could be used, μ and λ are chosen as they appear in this formulation of the wave equation (2.32). If necessary, once Lamé's parameters have been determined, the Young's modulus and Poisson's ratio can be calculated through equations (2.30) and (2.31).

2.3.1 Relationship of Elastic Properties to Measured Displacements

This section deals with the simple example of an isotropic, linearly elastic medium for illustrative purposes. The assumptions of a Hookean medium are valid to a certain extent through the very small-scale motion (tens of microns) induced into the medium, however, viscoelastic and anisotropic models have also been developed [24], [25].

The elastic properties of the soft tissue medium are related to the measured displacements through the velocity of the transverse and longitudinal shear waves thus:

$$v_t = \sqrt{\frac{\mu}{\rho}} \quad = \quad f_t u_t \tag{2.41}$$

$$v_l = \sqrt{\frac{\mu(4\mu - E)}{\rho(3\mu - E)}} \quad = \quad f_l u_l \tag{2.42}$$

where ρ is the density of the medium, the value of which is either known or assumed to be that of water. u corresponds to displacement; $_t$ represents transverse and $_l$ longitudinal. Equation (2.41) can be arranged thus: $\mu = \rho(f_t u_t)^2$ and substituted into equation (2.42) to result in:

$$E = \frac{\rho[3\rho\mu(f_l u_l)^2 - 4\mu^2]}{\rho\mu(f_l u_l)^2 - \mu} \tag{2.43}$$

Thus, through equations (2.30) and (2.31) any of the mechanical properties of the sample can be related to the measured displacements.

2.3.2 Equations of Motion

In general, the motion must satisfy Newton's laws for equilibrium of forces:

$$\nabla \cdot \sigma + \boldsymbol{b} = \rho \frac{\partial^2 \boldsymbol{u}}{\partial t^2} \tag{2.44}$$

where $\boldsymbol{b}$ represents the internal body force of the object. Substituting Hooke's law (2.28) into (2.44) results in:

$$\nabla \cdot (2\mu\epsilon + \lambda tr(\epsilon)I) + \boldsymbol{b} = \rho \frac{\partial^2 \boldsymbol{u}}{\partial t^2} \tag{2.45}$$

From this equation, the wave equation (2.32) follows. This is known as *Navier's equation* and can be expressed thus:

$$\mathcal{L}_F(\boldsymbol{u}(x, y, z)) = \nabla \cdot \mu \nabla \boldsymbol{u} + \nabla(\lambda + \mu)\nabla \cdot \boldsymbol{u} - \rho \frac{\partial^2 \boldsymbol{u}}{\partial t^2} = \mathbf{0} \tag{2.46}$$

where $\mathcal{L}$ is a differential operator, and $_F$ stands for the *forward problem.* $\boldsymbol{u}$ is the measured data; for the time-harmonic situation of the dynamic approach, $\boldsymbol{u}$ could be represented as $\boldsymbol{u} = \boldsymbol{u}_0 \sin \omega t$, giving $\partial^2 \boldsymbol{u}/\partial t^2 = -\omega^2 \boldsymbol{u}$. μ, λ and ρ are the unknowns of the equation.

2.3.3 The Reconstruction Scheme

In order to computationally solve for the unknowns in equation (2.46), it must be discretised. That is to say, a known basis function must be incorporated. The unknowns can then be expressed thus:

$$\begin{pmatrix} \mu(x,y,z) \\ \lambda(x,y,z) \\ \rho(x,y,z) \end{pmatrix} = \sum_{k=1}^{N} \begin{pmatrix} \mu_k \\ \lambda_k \\ \rho_k \end{pmatrix} \phi_k(x,y,z) \tag{2.47}$$

In our work, ϕ_k is a known *finite element* basis function [55].

By substituting (2.47) into (2.46) and taking the inner product with ϕ_k over all k, the Navier equation can be written in matrix form:

$$A(\boldsymbol{\mu}, \boldsymbol{\lambda}, \boldsymbol{\rho})\boldsymbol{u} = \boldsymbol{f} \tag{2.48}$$

where $\boldsymbol{\mu} = [\mu_1, \mu_2, ..., \mu_i]$ and similarly for $\boldsymbol{\lambda}$ and $\boldsymbol{\rho}$. A is a matrix with elements linear in μ_k, λ_k and ρ_k, and $\boldsymbol{f}$ contains the (known) forcing terms or boundary conditions.

Typically, the evaluation of $\boldsymbol{\mu}$, $\boldsymbol{\lambda}$ and $\boldsymbol{\rho}$ from the measured displacements $\boldsymbol{u}^m$ is set up as the solution of the following nonlinear optimisation problem, with $\boldsymbol{\zeta} = \begin{pmatrix} \boldsymbol{\mu} \\ \boldsymbol{\lambda} \\ \boldsymbol{\rho} \end{pmatrix}$:

$$\boldsymbol{\zeta} = arg_{\boldsymbol{\zeta}} min \parallel \boldsymbol{u}^m - \boldsymbol{u} \parallel_2^2 \tag{2.49}$$

where $\boldsymbol{u} = A^{-1}(\boldsymbol{\mu}, \boldsymbol{\lambda}, \boldsymbol{\rho})$

Any scheme to solve this nonlinear optimisation requires the evaluation of what is known as the *forward problem.* This involves calculating the displacement fields, $\boldsymbol{u}$, at each iteration, along with its Frechet derivatives, giving the variation of the measured displacements with respect to the change in the unknown elasticity parameters, $\boldsymbol{\zeta}$. The solution to the forward problem is then used in a suitable “inversion” strategy to determine updates on the elasticity parameters. Such inversion schemes could be Quasi-Newton or Conjugate-Gradient, for instance, although there are numerous others (see, for instance, [59], [60] for adjoint methods to treat inverse problems in elasticity; also, [61], [62], [63], [64] contain computational approaches to inversion schemes for a number of different contexts).

The forward problem is well-posed; one may wonder why a direct approach could not be taken to determine the elasticity parameters. To solve for $\boldsymbol{\mu}$, $\boldsymbol{\lambda}$ and $\boldsymbol{\rho}$, the inverse problem can be expressed as a direct conversion:

$$C(\boldsymbol{u})\boldsymbol{\zeta} = \boldsymbol{g} \tag{2.50}$$

where C is a matrix with elements depending upon the measured displacements. Like $\boldsymbol{f}$, $\boldsymbol{g}$ consists of known boundary terms. However, this direct approach of solving the inverse problem has disadvantages due to noise in the measured data. Compounding the problem, the second partial derivatives in the elasticity equation (2.46) amplify the noise. In addition, the inversion of the matrix C is not trivial simply because of the sheer size of the dataset (even at a 2 mm MR resolution throughout a typical volume, the number of datapoints in C could number in the millions); this also has a bearing on the regularisation of the data. Regularisation methods such as the Tikhonov, L-curve, and Truncated Singular Value Decomposition approaches will not be discussed in this document; the interested reader is referred to [61], [64], [65].

2.3.4 Subzone Based Reconstruction

The subzone-based finite element approach to solving the inverse problem involves breaking up the volume undergoing reconstruction into small, overlapping subzones for processing. The reconstructions of each of these subzones can be handled by different processors on a parallel computing system. This enables the computational load to be shared through a relatively simple macro-parallelisation scheme. The choice of geometry of these subzones and the number of nodes included will dictate the size of the optimisation problem each processor must solve. There are typically several thousand nodes in each subzone, and perhaps 20 to 30 subzones for a 16cm ×16cm ×2cm imaged volume. The overall solution is iteratively refined, subzone by subzone, based on solving the nonlinear optimisation problem for the difference between the measured and calculated displacement data.

A forward problem for an estimated set of mechanical properties is solved on a particular subzone, the error between that and the measured data is determined and the solution is updated accordingly. As one subzone is updated, the subzone with the greatest residual error is determined and then that subzone is updated. This process continues until the total sum of the reconstructed subzones encompasses the entire volume, and the solution has converged to the material properties of the imaged sample. One current issue with this type of optimisation based reconstruction is that it is very computationally intensive. However, this approach has the potential to lead to accurate *quantitative* values for the reconstructed elasticity of the imaged domain without the need for regularisation or filtering of the motion data.

Chapter 3

Materials and Methods

3.1 MRI Scanner

The MRI scanner used for all testing was a GE Signa 1.5T MRI scanner (GE Medical Systems, Waukesha, WI) located at St George's Hospital, Christchurch. The scanner had a maximum gradient strength of 33mT/m, and a slew rate of 120mT/m/ms. The software ran was EPIC (Environment for Pulse programming In C) version 14.0 m4.

3.2 Actuation Device

An apparatus developed in a previous project [66] was used for actuating gel phantoms. Gel phantoms were made inside cuboid Perspex boxes which were coupled to a specially-fabricated non-magnetic preloaded piezoelectric actuator (P-842K022, Physik Instrumente, GmbH Co. KG). The specifications of the actuator give a 90μm travel range and a push/pull force capacity of 800/300N.

This setup was affixed to a heavy Perspex base. Teflon pads were placed between the base and the box, and Teflon-coated vertical guides protected the actuator from excess lateral force. When in use, the whole apparatus was placed on a rubber grip surface to reduce movement of the base (figure 3.1). Electronics were also developed in the previous project to deliver a sinusoidal signal of variable amplitude. The maximum output was -2 to 12V to match the specification of the amplifier unit (E505.00, Physik Instrumente, GmbH Co. KG). The amplifier was to drive the actuator at 10 times the input voltage provided, resulting in a maximum peak-to-peak output of 140V. The actuator was driven at 100Hz, and with an input voltage of 9V.

A trigger pulse (see figure 2.23) was included in the electronics to synchronise the sinusoidal driving signal to the MR motion encoding. The electronics box was connected to the MRI scanner through the cardiac gating leads usually used to synchronise acquisition to the cardiac cycle. Code was included in the pulse sequence to sensitise the sequence to triggering in this manner.

Originally, a piezoelectric actuator with a stainless steel casing was ordered. Despite being nominally non-magnetic, this actuator produced a significant artifact on phantoms

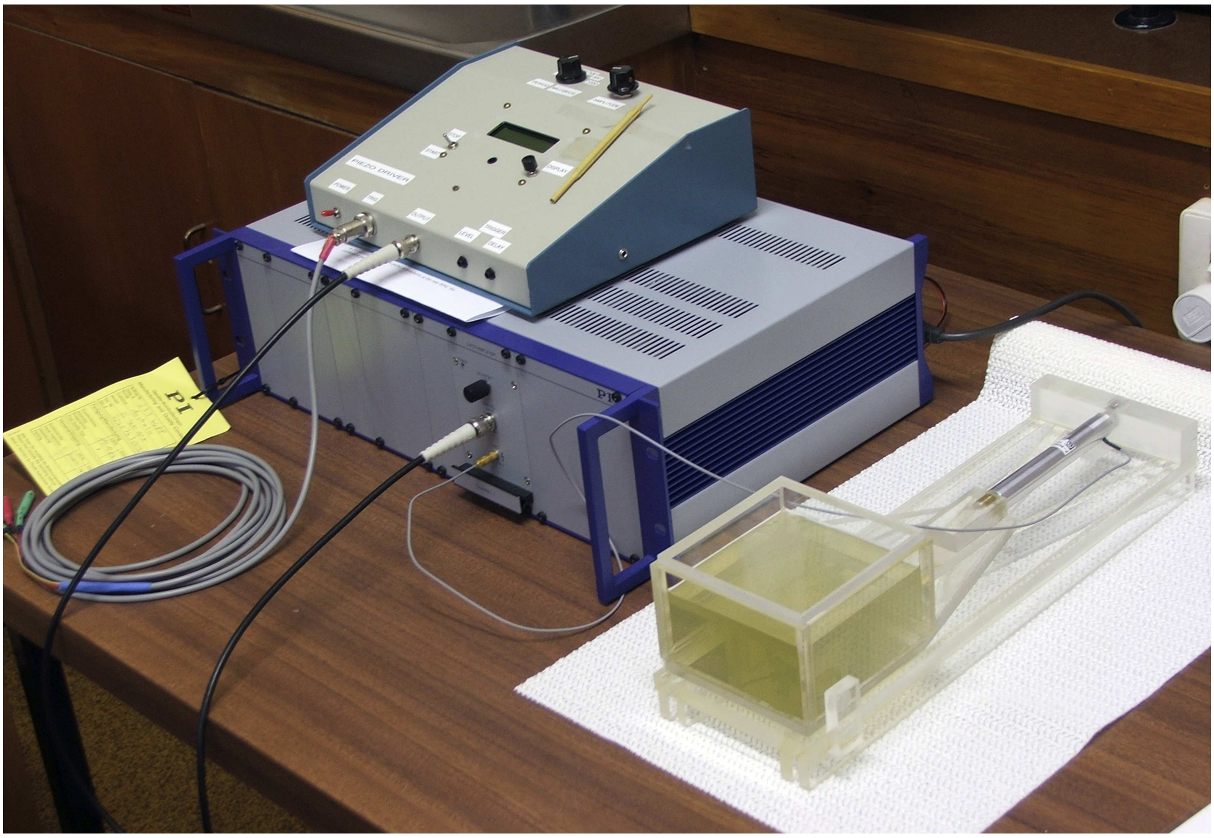

Figure 3.1: The assembled apparatus. The custom-designed piezo driver and trigger pulse signal generator sits atop the piezo amplifier. One lead from the signal generator goes to the amplifier, which in turn is connected to the actuator. A second lead is connected to the ECG (electrocardiogram) sensors on the MR scanner during scanning. This provides the synchronising trigger pulse. The phantom actuator apparatus in made almost entirely from Perspex. The non-magnetic actuator is bolted to a supporting wall strut, which is in turn cemented to the base. The other end of the actuator is connected to a Perspex spacer via a wide-thread brass screw. The spacer was included to distance the metal actuator from the phantom being imaged to minimise potential artifacts. The phantom box is at the end of the spacer and in this image contains a homogeneous gelatine phantom. Teflon pads are situated between the sample box and the base, and on the side alignment guides. These guides are in place primarily to make the apparatus more robust and do not make contact with the sample box during normal operation. The base is reinforced with Perspex supports to provide extra weight and the whole apparatus sits on a rubber grip mat. The actuator device was placed in the head coil of the scanner for image acquisition (see figure 3.3).

that were spaced 15cm away from the tip. The specially-fabricated non-magnetic actuator was housed in a casing made from an aluminium alloy and produces no noticeable artifact in scans (figure 3.2). Previous work [66] generated a magnetic field phase map of this actuator and determined an extremely low magnetic susceptibility. The maximum effect on the external magnetic field due to the presence of the actuator was calculated to be less than two parts per million.

3.3 Magnetic Relaxation Measurements

Seven cylindrical samples of silicone were imaged in order to determine the suitability of silicone as a phantom for MR imaging purposes. The samples were of differing hardnesses and were imaged alongside an IV bag of saline solution as a reference. The T_1 and T_2

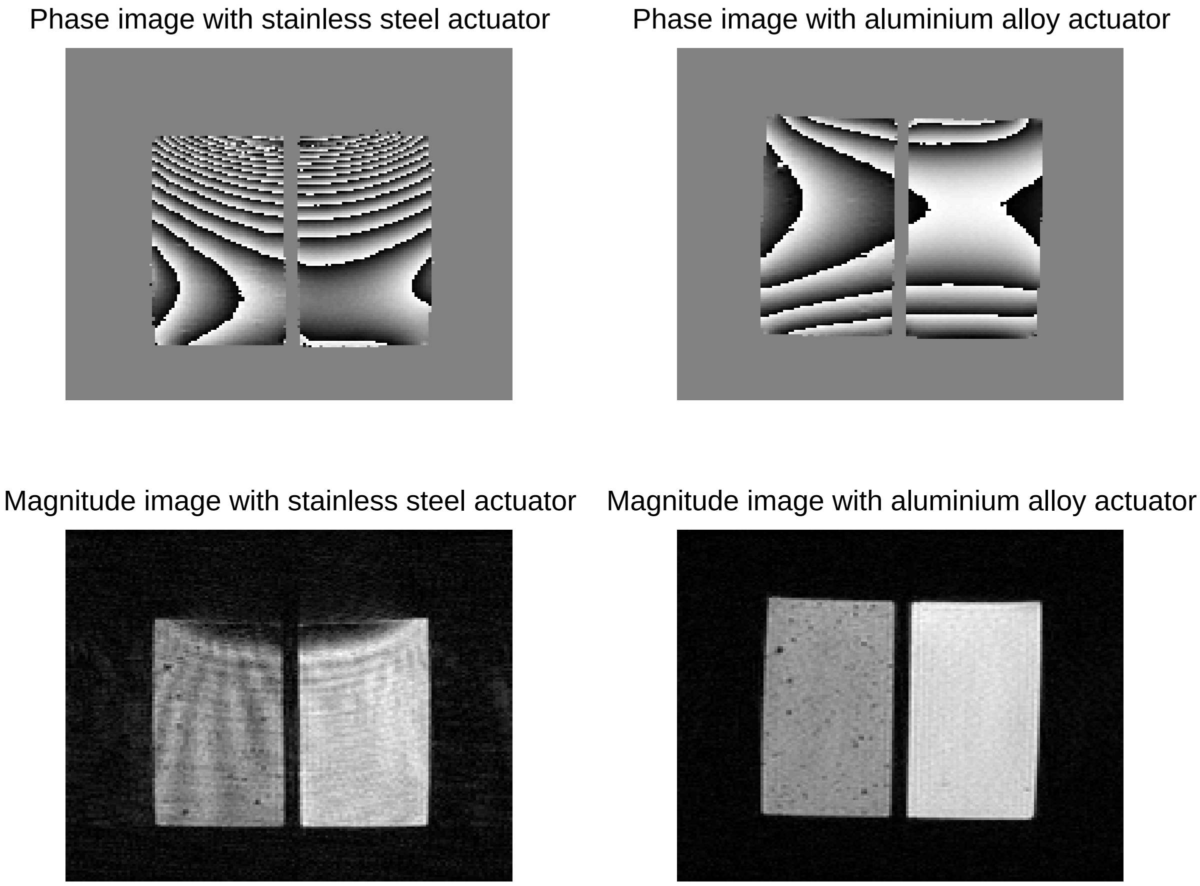
Phase image with stainless steel actuator

Phase image with aluminium alloy actuator

Magnitude image with stainless steel actuator

Magnitude image with aluminium alloy actuator

Figure 3.2: A comparison between the nominally non-magnetic stainless steel actuator and the specially-fabricated aluminium alloy actuator. A homogeneous silicone phantom is used with actuation but no motion encoding gradients activated; in each image, the actuator is at the top centre of the phantom. The phase map shows the field is not uniform close to the stainless steel actuator (top left). If there is a phase variation in the signal within a voxel, the magnitude of the total signal is reduced, as seen in the corresponding magnitude image (bottom left). This is called intravoxel dephasing. By comparison, the aluminium alloy actuator produces a slowly varying phase map of the phantom (top right) and consequently, there is no loss in signal, nor artifact within the phantom (bottom right).

values of the silicone as well as the strength of the signal were investigated.

An inversion recovery sequence was employed to determine the T_1 values of each sample with inversion times of 50, 100, 150, 200, 300, 350, 400, 450, 500, and 600 ms. A repetition time (TR) of 2000ms was used. A multiple spin echo sequence was used to determine the T_2 values. Four series each took images at four different echo times (TE): 20, 40, 60, 80ms for the first series; 40, 80, 120, 160ms for the second; 80, 160, 240, 320ms for the third; 160, 320, 480, 640ms for the fourth. The repetition time for this sequence was 1000ms.

Image data was imported into the MATLAB software package. In processing, circular regions of interest (ROI) were selected from a middle slice of each of the seven silicone samples and the sample of saline solution.

To determine the T_1 value of a particular sample, the average signal from an ROI was plotted against inversion time. The plot should reveal an initially decaying exponential until the inversion time, then a recovering exponential function. From 2.1.7, the governing equation is:

$$|S| = S_0 \left| 1 - 2\mathrm{e}^{-\frac{TI}{T_1}} \right| \tag{3.1}$$

where S_0 is the initial signal intensity.

The TI can be determined by inverting the points of the recovering exponential, then performing a linear interpolation over two points either side of the zero line to find the x-axis intercept. Equation (3.1) can then be rearranged to find T_1 in terms of the determined value for TI:

$$\begin{aligned}
1 - 2\mathrm{e}^{-\frac{TI}{T_1}} &= 0 \\
\mathrm{e}^{-\frac{TI}{T_1}} &= \frac{1}{2} \\
\frac{TI}{T_1} &= \ln 2 \\
T_1 &= \frac{TI}{\ln 2} \qquad (3.2)
\end{aligned}$$

Similarly, plotting the signal from the spin echo experiment against echo time reveals a decaying exponential as per equation (2.26):

$$S = S_0 \mathrm{e}^{-TE/T_2} \tag{3.3}$$

Determining the gradient, m, of a linear interpolation of the natural log of the data points will allow a calculation of T_2 thus:

$$m = -\frac{1}{T_2} \tag{3.4}$$

Example plots of both these methods can be seen in 5.1.

3.4 Phantoms

A number of different phantoms were designed and made for the acquisition of datasets throughout this project and to subsequently examine the efficacy of developed pulse sequences and the mechanical properties of the imaged phantom material. Silicone was used for initial testing; excised biological tissue samples were used in later experiments.

The geometry of the phantoms was chosen to be a cuboid Perspex box, filled with a soft-gel phantom material; the imaged sample was thus bound on five sides. This was developed from previous work undertaken by Weaver *et al.* [49]. The mass of a given sample undergoing actuation was approximately equivalent to that of a human breast, from which it is expected to obtain clinical data in the near future using the data acquisition methods developed in this project.

3.4.1 Silicone Phantoms

Three silicone phantoms were fabricated for initial testing of pulse sequences and data acquisition. Silicone was chosen over previously-used gelatine due to its relative ease in

Figure 3.3: The phantom actuation apparatus sitting on top of the scan table before insertion into the bore of the scanner. The head coil used is in place, but moved so the phantom can be viewed; a 3D-orientable excised muscle phantom is coupled to the actuator.

manufacturing phantoms with inclusions, and the fact that, once set, the mechanical properties remain unchanged indefinitely, whereas gelatine can dry out and go mouldy. Silicone can be moulded to fit many shapes and the manufacturing process neither requires nor generates heat. Silicone phantoms can be engineered to closely represent the mechanical properties of some tissues.

Two types of silicone were ordered from Factor II, Inc., Lakeside, AZ: ‘soft’ (known as A-341) and ‘hard’ (known as LSR-05).

Initial Silicone Phantoms

Two silicone phantoms were fabricated for initial testing with two different stiffnesses of silicone used for these phantoms. A ‘soft’ silicone material, consisting of 100% A-341, and a ‘harder’ silicone material, consisting of a mix of 50% A-341 and 50% LSR-05. Both phantoms were made and tested inside 10cm ×10cm ×10cm Perspex phantom containers.

The first phantom had a dividing wall cemented inside the container, along the direction of actuation. The right-hand side of this box (when viewed top-down from the position of the actuator) contained soft silicone; the left-hand side contained the harder mixed silicone. This phantom was to be used as a base phantom, from which the difference in wave pattern formation between the two types of silicone could be observed, and the effect of different pulse sequences could be compared to a base standard.

The second phantom consisted of a base of soft silicone, into which three cylindrical inclusions, made of the harder silicone, were set. The soft silicone in this phantom could be taken to represent a breast while the inclusions simulate harder tumours or fibroadenomas. The diameters of the inclusions were 8, 12 and 16mm; care was taken to ensure the inclusions did not rest on the bottom of the box. To manufacture this phantom, soft silicone was poured into the box as a base; plastic cylinders of the above diameters were inserted into the silicone and clamped in place; the soft silicone was allowed to set overnight; the next day, the cylinders were removed and harder silicone was made up and poured into the holes (figure 3.4).

Silicon spray ('Silicon Star', Sta-Lube, East Tamaki, NZ) was used on all surfaces to facilitate the removal of the set silicone. The silicone gels were manufactured in two stages (soft first, then harder) to ensure that the concentrations of silicone gels in both phantoms were identical.

Manufacture of Silicone Gel Phantoms

- The approximate mass of required silicone was determined by measuring the volume of the phantom box and using the density of water as an approximate density for the silicone gel.
- Both the A-341 and the LSR-05 silicone required the mixing of two parts before setting would occur. Following the manufacturer's instructions, the appropriate proportions of each part were weighed using electronic scales and mixed together. When the harder phantom was made up, a $1:1$ ratio by mass of A-341 and LSR-05 was mixed together.
- The phantom box was lubricated with silicon spray and the gel was poured into the mould.
- The box was placed into a Venturi vacuum system to allow the gel to de-gas for about 25 minutes.
- The phantom was allowed to set overnight.
- The soft gel was made first. The process was repeated the next day, mixing up the harder gel for the inclusions and the left-hand side of the homogeneous phantom. However, three drops of colourant ('FI-200, white', Factor II, Inc., Lakeside, AZ) were also added to the harder phantom in order to visibly distinguish it from the soft phantom.

It was very important to minimise the presence of air bubbles within the phantom. An air bubble will produce no signal in an MR scan, resulting in a null area in both the phase and magnitude images. This can potentially lead to susceptibility artifacts as $\chi_{silicone} \neq \chi_{air}$. This can also result in phase wrapping artifacts in the processing of the MR phase data, and, if significant, can prevent an effective elasticity reconstruction. These phantoms, made soon after delivery of the silicone, had few issues with the de-gassing process. The homogeneous phantom set very well. However, despite the lubricating silicon

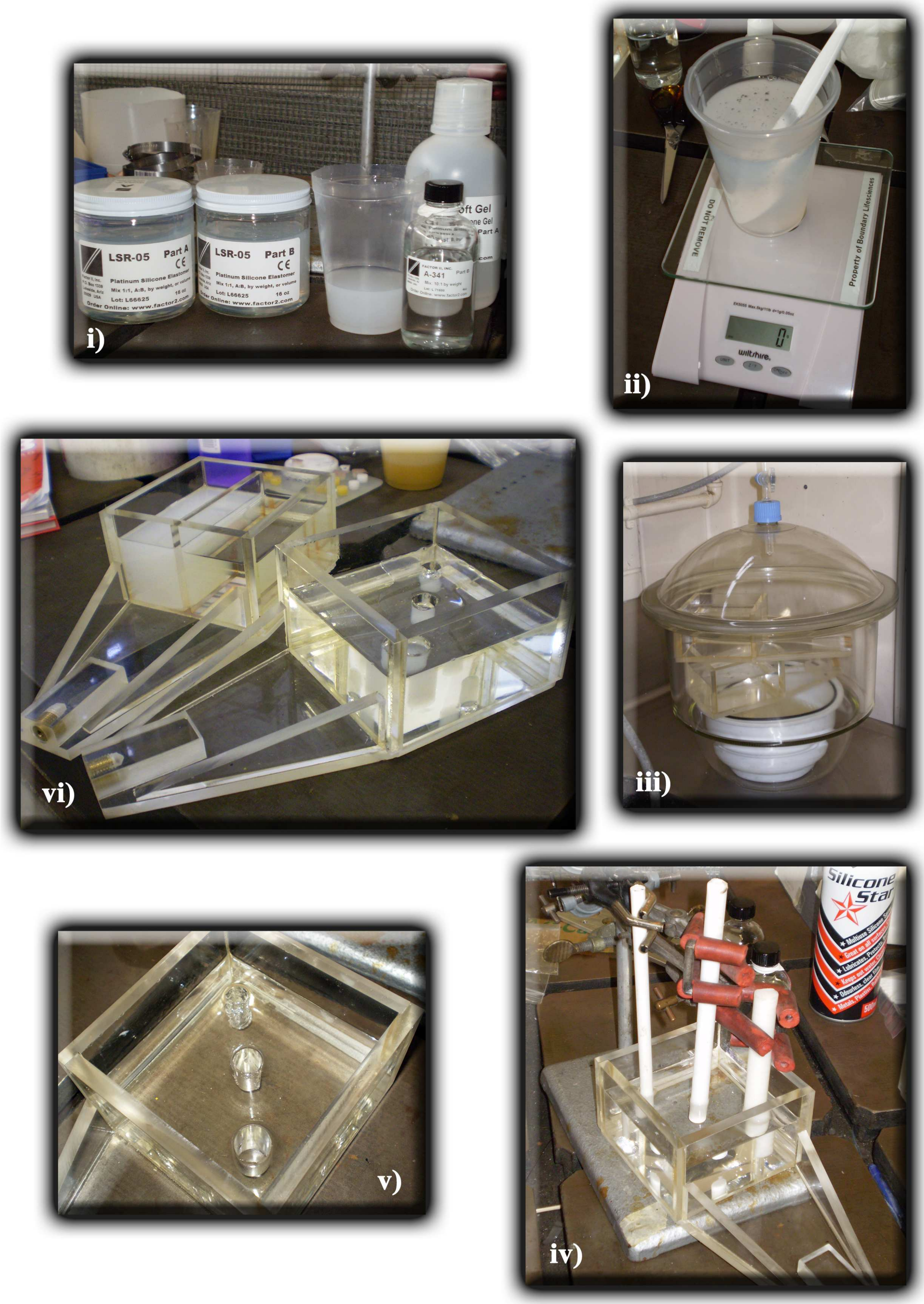

Figure 3.4: Clockwise from top left: i) Silicone gel materials. ii) Weighing appropriate masses of gel parts and mixing. iii) Boxes with silicone were placed into a Venturi vacuum system to de-gas. iv) The phantom with inclusions was left to set with three plastic cylinders, coated in silicon spray, suspended in the silicone. v) The set silicone following removal of the cylinders. vi) The set phantoms. The harder silicone can be distinguished by the white colourant added during mixing.

spray, issues were found with removal of the cylindrical spacers in the inclusions phantom. This led to an uneven surface of some soft silicone, and some air bubbles set around the inclusions. This caused a problem with subsequent elasticity reconstruction creating artifacts that were difficult to bypass.

Silicone Wedge Phantom

To look at the effect of actuating the same phantom along different orthogonal axes, a phantom box was made that could be oriented in three different directions. The premise behind this apparatus was to look for anisotropy within biological samples, however a silicone phantom was first made up for testing, using a well-defined, mechanically isotropic medium.

Whereas the earlier phantom boxes consisted of a box mounted on a Perspex spacer, this new setup consisted of a Perspex 'tray' and a removable box (see figure 3.6, left). The tray continued to act as a spacer, into which the actuator was screwed with the familiar brass screw coupling. At either end of the tray were cemented Perspex walls (running perpendicular to the axis of actuation). On top of this tray, and held in place by the walls, a cube box, of external side 10.5cm, could be placed in three different orientations (see figure 3.9) and secured by nylon screws.

Due to difficulties in accurately determining the orientation of phantoms following data processing (see 4.2.7), an innovation was undertaken in the orientable phantom setup to provide a unambiguous method of determining direction. Four markers, consisting of cod liver oil capsules were arranged such that the three orthogonal directions could be determined from examination of these markers (which appear as bright spots) in the MR image (figures 3.6, right, and 3.11). While these markers were very successful in helping accurately determine the orientation of phantoms, they have the undesired byproduct of causing phase wrapping artifacts during data processing, especially if the markers are close to the region of interest of the phantom (see figure 4.6).

For this silicone phantom, a design of a body of soft silicone with a wedge-shaped inclusion of harder silicone was adopted. The idea behind the wedge was to enable testing of the limits of resolution of the MRE setup.

The method of manufacture has similarities to the method described above. Firstly, a base of soft silicone was mixed, de-gassed, and allowed to set for 6 hours. The second stage consisted of placing a rectangular placeholder on the base and surrounding it with more soft silicone. At this stage the directional markers were included. Once this had set, some harder silicone, made to the same concentrations as for earlier phantoms, was mixed, de-gassed and poured into the resulting rectangular hole. The phantom box was rested at an angle to create the wedge, and the harder silicone was allowed to set. Finally, the phantom was filled in with a further mix of soft silicone (figure 3.5).

A significant number of air bubbles formed in the uppermost layer of silicone. In this particular case, the gel started to harden during the de-gassing process. It would appear that the raw silicone materials have a certain shelf life once the bottle has been opened; a notably shorter curing time resulted in bubbles solidifying within the material, partway

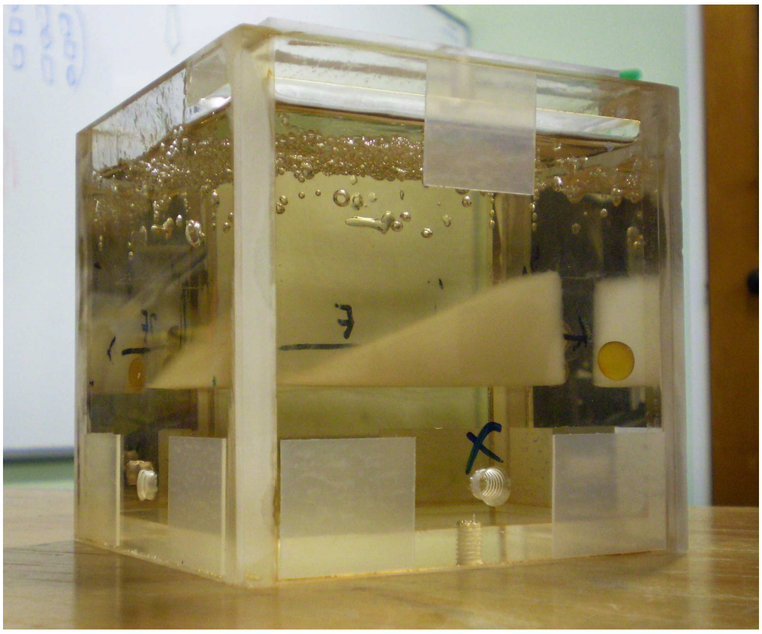

Figure 3.5: The stiffer wedge is visible embedded in softer silicone. Directional markers are also visible. Issues with silicone curing resulted in air bubbles forming in the upper layer of softer silicone.

through the de-gassing stage. Unfortunately, with the cost of shipping making up the majority of the financial expense of acquiring the silicone, it is unfeasible to order smaller batches at a time. In the future, it may be that several phantoms have to be planned in advance and all made up around the same time to make best use of the silicone.

Following imaging of the phantom within the Perspex container with actuation along the three orthogonal axes, the phantom was removed and re-imaged. This time, the now free-standing block of silicone rested on the tray while actuation proceeded in the usual manner. Despite the silicon lubrication spray, it was very difficult to extract the phantom in one piece, and required patience and a certain ingenuity. In the future, a collapsible mould approach would be beneficial for phantoms that are to be free-standing. If the mould were made out of lighter material and able to be destroyed, it would be easier to prise the silicone phantom from out of it.

3.4.2 Biological Sample Phantoms

While silicone phantoms are useful as a well-controlled and understood uniform material for determining and overcoming limitations of the MRE setup, the study of excised biological tissue samples is of interest as it is a step closer to a realistic clinical application of our MRE techniques. Phantoms were developed to look at the anisotropy of both muscle and brain tissue. These phantoms all made use of the 3D-orientable box setup.

Excised Bovine Tissue Phantoms

The first sample to be tested in this new setup was a slab of excised beef muscle suspended in gelatine. Muscle was chosen for its strong anisotropy due to fibres running along a particular direction, but not across it. The first muscle tissue sample was embedded in

Davis gelatine (Gelita NZ Ltd, Christchurch, NZ) for imaging. The optimal concentration of gelatine had been determined in earlier work [66] to be 9.9g/100mL.

Manufacture of Excised Bovine Tissue Phantom

- All screw holes in the phantom box were sealed to prevent leakage.
- The approximate volumes of required gelatine for different stages of phantom manufacture were determined and thence volumes of water and masses of gelatine were calculated.
- The excised beef tissue sample was cut into a cuboid of base side 7cm, and height 5cm.
- The first stage of phantom preparation involved mixing gelatine for a 2cm base upon which the muscle sample could rest. The required mass of gelatine was weighed and poured into water heating on a hot plate to about 70°C.
- The mixture was agitated by means of a magnetic stirrer and once the gelatine had dissolved, was cooled in a water bath to around 35°C. This temperature was near the limit of keeping the gelatine sufficiently in solution but was also cool enough to not affect the tissue.
- The base was allowed to set in a refrigerator.
- The muscle sample was placed on the hardened base, with care taken to ensure it did not touch the sides of the box (figure 3.6, left).
- A small batch of gelatine was mixed up as described above and poured around the muscle to come halfway up the sample. This was allowed to set.
- The oil capsule spatial markers were then arranged on the new plane of set gelatine (the imaging plane) and a third batch of gelatine was made up as before and very carefully poured over the sample until the beef tissue was covered by gelatine (figure 3.6, right). Again, this was refrigerated to facilitate setting and to keep the sample in optimum condition before scanning.
- The sample was brought back to room temperature before imaging (figure 3.7).

Following an unsuccessful run with the first beef tissue phantom, a second one was made up later, in a similar fashion.

Gelatine was a relatively easy material to work with. It tended to set very quickly, even at room temperature, allowing for swift enclosure of the beef sample and accuracy in positioning the directional markers. The markers had to be within the scan plane, which was not always at the base of the tissue sample, thus several layers of gelatine had to poured, semi-enclosing the tissue in order to position the markers. Air bubbles were less of a problem, although a very few tended to appear around the markers. The warm

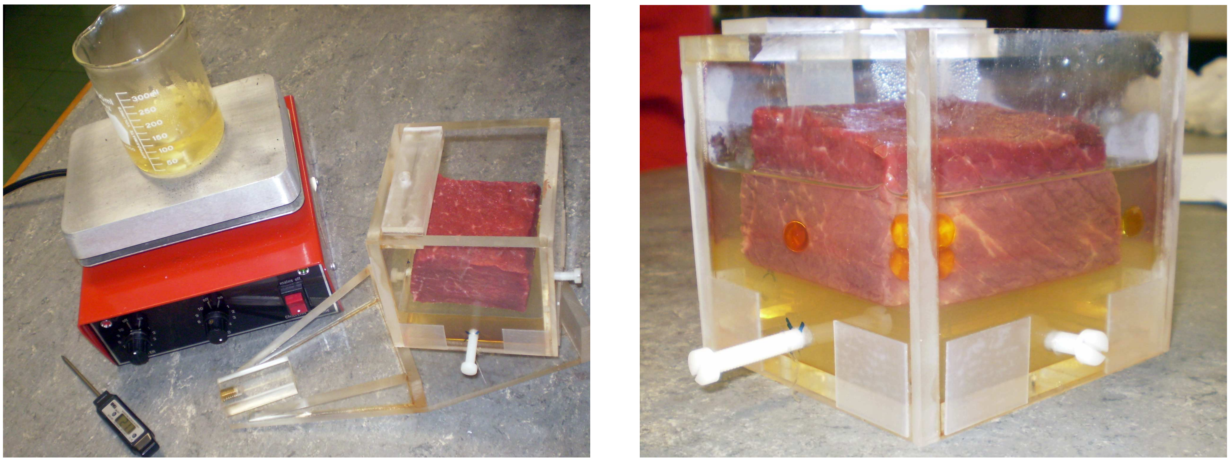

Figure 3.6: *Left:* Part of the setup used in fabricating the beef muscle phantom. A beaker containing gelatine solution is being agitated by the magnetic stirred on the hotplate. A digital thermometer was used to monitor temperature. The 3D-orientable phantom box is visible on the right with the beef sample resting on a base of set gelatine. The detachable nature of the box and the tray it is designed to rest in are apparent. *Right:* The four capsules of cod liver oil are visible, indicating the three orthogonal directions.

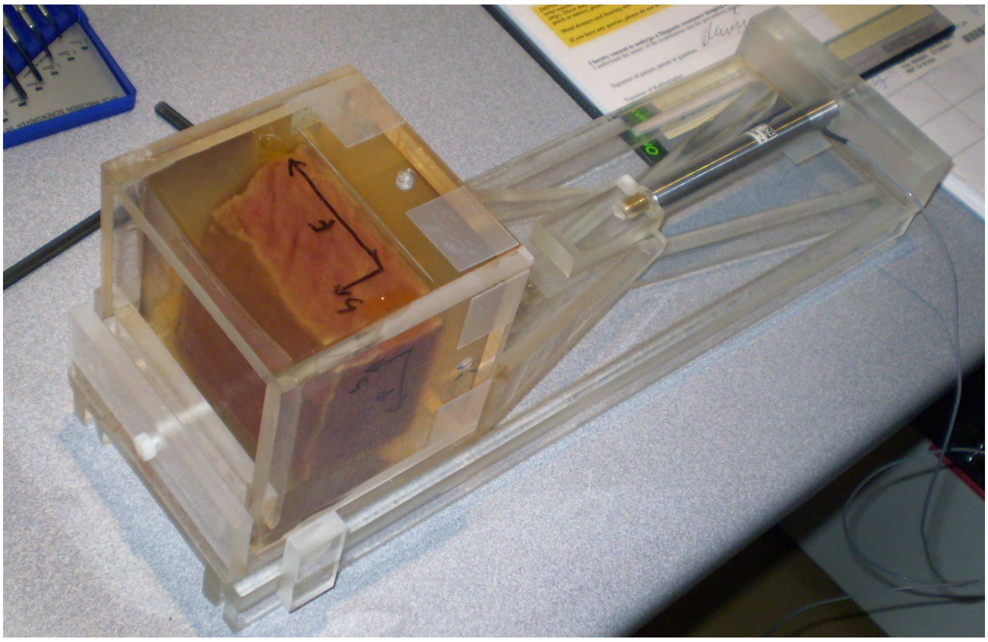

Figure 3.7: The completed beef muscle phantom before imaging. The phantom box is connected to the supporting tray in once particular orientation with nylon screws. The tray is in turn coupled to the actuator.

water, while not hot enough to affect the beef, started to dissolve the markers. Fortunately none dissolved to the extent where the oil was released into the gelatine, but they visibly deformed, which could be a cause of phase artifacts.

One potential major issue with the gelatine is its efficacy it is at transmitting shear waves to the embedded muscle tissue. It is possible that the waves reflect significantly off the denser material thus reducing the actuation of the target itself. These concerns resulted in performing a scan on a third bovine muscle phantom, which consisted of an approximately 7cm cube of excised muscle in the same orientable box apparatus without the surrounding gelatine. The comparison between the two approaches to phantoms is discussed in 6.1.1.

It was difficult to cut the muscle into a regular shape because of the very anisotropy we were trying to detect. What appeared square in one orientation would change when the sample was moved onto a different side. It was originally envisioned to rotate this third beef tissue phantom along three orientations. The inability to produce a true cube, self-supporting on three axes, meant we were limited to scanning along only two orientations.

Of course, the gelatine-tissue phantoms have a limited lifetime. They must be made up preferably no more than a day before scanning and need to be discarded after use, thus there are limitations on accurately repeating experiments on the same phantom.

Excised Ovine Brain Phantom

Finally, a brain phantom was developed using an entire sheep brain. In order to ensure effective mechanical actuation of the brain itself and to preserve the phantom for a longer period of time, the brain was set into an epoxy resin. The resin hardens clear and extremely hard, thus encasing the brain in a solid block which is actuated directly by the piezo device (see figure 3.8).

Manufacture of Ovine Brain Phantom

- A phantom box measuring the same external dimensions as before, but of thinner Perspex, to accommodate the size of the brain, was manufactured.
- An entire excised sheep brain that had been preserved in formalin was used.
- An epoxy resin ('Glass Coat', Craftsmart Australia Pty Ltd, Notting Hill, VIC) was made up in batches according to standard instructions. The reason for using batches rather than a single pour was to avoid applying too much heat to the brain, as the setting process is an exothermic reaction.
- Each batch of resin was de-gassed in a vacuum chamber for at least 20 minutes.
- The brain was suspended above the base of the box with stainless steel wire.
- The first batch of resin was poured in to provide a base for the brain to rest on. It was allowed to harden for 2 hours.

- The supporting wires were removed and a second batch of resin was poured in. A very slight vacuum was applied to the box to draw out air bubbles that had become trapped beneath the brain.

- The box was rested at an angle to ensure the entire brain was covered in order to prevent it drying out. The resin was allowed to set overnight.

- A final batch of resin was made to fill the box and allowed to set for 24 hours.

- Holes were then drilled into the box to allow for coupling to the tray of the actuator device.

Figure 3.8: From left to right: i) The brain is suspended by stainless steel wires while the first batch of epoxy resin is poured in. ii) The resin is allowed to harden, thus supporting the brain and allowing for removal of the wires. iii) Following several further resin pours, the brain is entirely encased. The epoxy resin offers excellent optical clarity.

One concern with this phantom was that the brain would dry out resulting in significantly reduced signal. A T_2 weighted scan reveals that this did not occur, with fluid still present in the ventricles, appearing bright on the image (figure 3.10).

Air bubbles were an issue with this phantom, with small bubbles appearing around the surface of the brain. Due to the viscosity of the resin, these bubbles did not rise easily to the surface. The small amount of vacuum applied to the phantom following the second resin pour appeared to help somewhat with bubble removal, however, it would unwise to continue with excessive evacuation for fear of rupturing the brain. The size of the bubbles, and the fact that they are only at the surface of the phantom means that they should not pose too big an issue with artifacts.

One final comment on the resin is that it did not appear to adhere very well to the Perspex walls. This is probably not that significant an issue for this phantom, with sufficient motion seeming to be introduced into the brain, however is a consideration for any future work with the epoxy.

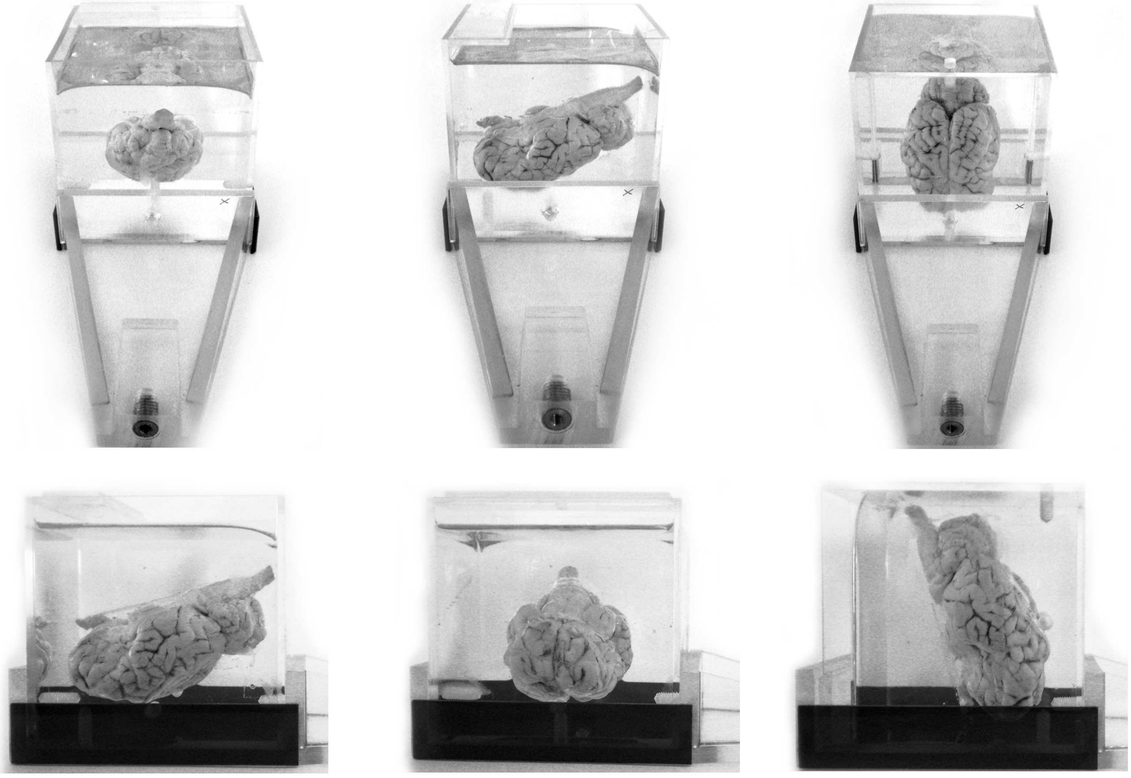

Figure 3.9: The sheep brain phantom is shown oriented along three different axes for anisotropy imaging. The top images show a view from the direction of the actuator; the bottom images show the same configuration but a side view. In the bottom images, actuation is from the right. Directional markers were affixed to the outside of the box in this case.

3.5 Initial Calculations

3.5.1 Derivation of Phase and Motion Relationships

A measurable phase change is required for successful results. Too little phase change poses difficulties in obtaining an accurate measurement, however too great a phase change can produce undesirable wraparound effects (see 4.2). This section derives the relationship between phase measured by the MRE setup and how this corresponds to the motion able to detected for three different types of motion encoding gradient pulses: square, sinusoidal and trapezoidal. The motion required for a phase change of 1 radian for different sequences using different numbers of motion encoding gradients is also calculated.

In each case, T is the period of the motion encoding gradients, N is the number of cycles applied and G_0 is the amplitude of the gradient. γ is the gyromagnetic ratio, taken to be 42.58MHz/T for protons. The displacement is assumed to have a sinusoidal motion, of the form: $x(t) = x_0 \sin \Omega t$, where x_0 is the amplitude of the motion and Ω is the angular frequency of both the motion and the gradient pulses. Given the arguments in 2.2.4, the change in phase, in general, can be expressed as:

$$\Delta\phi = \gamma \int_0^{NT} G(t)x(t)\mathrm{d}t \tag{3.5}$$

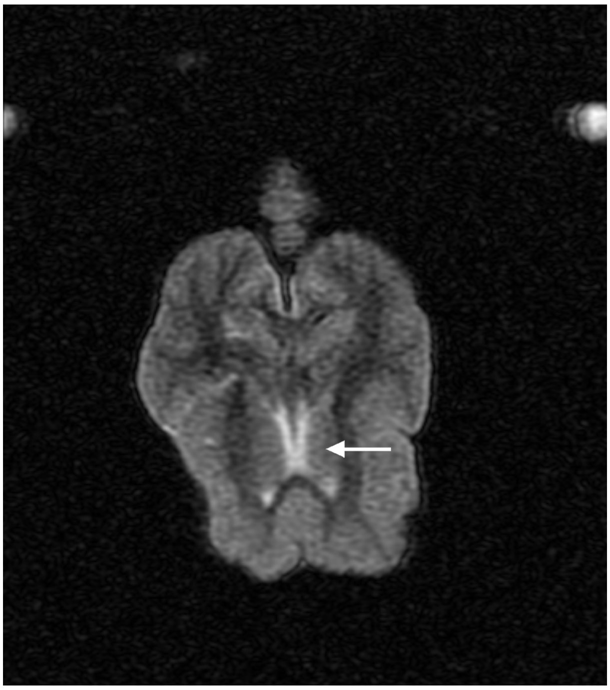

Figure 3.10: A T_2 weighted image of the excised sheep brain phantom. The bright areas indicated by the arrow are fluid-filled ventricles, indicating that the brain has not dried out substantially during the phantom manufacturing process.

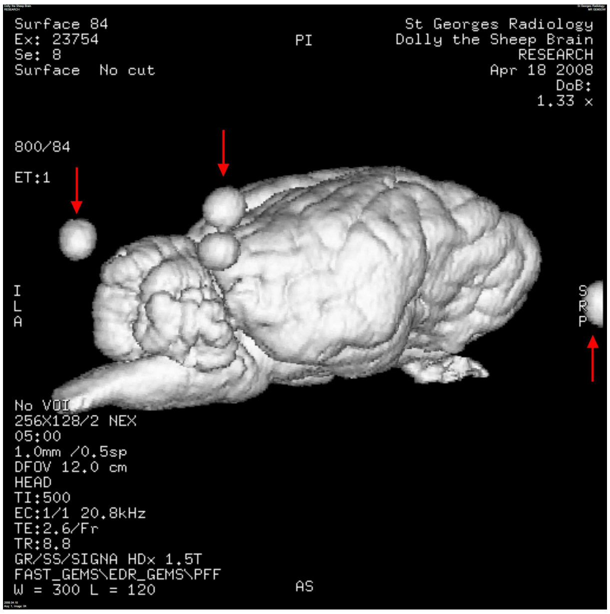

Figure 3.11: An MRI surface rendering of the excised brain phantom shows the surface structure of the brain. The directional markers, defining the three orthogonal directions are visible, indicated by the arrows.

Square Wave

The simplest case of motion encoding gradient pulse is a square wave:

$$G(t) = \begin{cases} G_0 & 0 \leq t < T/2 \\ -G_0 & \mathrm{T}/2 \leq t < T \end{cases} \tag{3.6}$$

for a single period. Thus (3.5) becomes:

$$\begin{aligned}\Delta\phi &= \gamma\int_0^{\frac{T}{2}} G_0x_0\sin\Omega t\mathrm{d}t - \gamma\int_{\frac{T}{2}}^{T} G_0x_0\sin\Omega t\mathrm{d}t \\ &= \gamma G_0x_0\left[\left[-\frac{1}{\Omega}\cos\Omega t\right]_0^{\frac{T}{2}} - \left[-\frac{1}{\Omega}\cos\Omega t\right]_{\frac{T}{2}}^{T}\right] \qquad (3.7)\end{aligned}$$

Evaluating the brackets we arrive at:

$$\begin{aligned}\Delta\phi &= \frac{\gamma G_0x_0}{\Omega}\left[(-\cos\pi+\cos 0)-(\cos 2\pi-\cos\pi)\right] \\ &= \frac{4\gamma G_0x_0}{\Omega} \qquad (3.8)\end{aligned}$$

where the relationship $\Omega = \frac{2\pi}{T}$ has been used. A linear relationship exists for the number of cycles applied, N, (see section 2.2.4). Incorporating this factor and rearranging to find the phase-dependence on motion detected, we obtain:

$$x_0 = \frac{\Delta\phi\Omega}{4N\gamma G_0} \qquad (3.9)$$

A target phase change of 1 radian over one cycle of frequency 100 Hz, with a gradient amplitude of $G_0 = 22$ mT/m, would require a motion of 26.7μm.

In reality, a square waveform is impractical due to the physical restraints of the gradient switching ability of the scanner (the slew rate).

Sinusoid

A sinusoidal waveform was also considered as a motion encoding gradient pulse, where

$$G(t) = G_0\sin\Omega t \qquad 0\leq t < NT \qquad (3.10)$$

In this case (3.5) becomes:

$$\begin{aligned}\Delta\phi &= \gamma\int_0^{NT} G_0\sin\Omega t\ x_0\sin\Omega t\mathrm{d}t \\ &= \gamma G_0x_0\int_0^{NT}\sin^2\Omega t\mathrm{d}t\end{aligned} \qquad (3.11)$$

Using the change of variable, $z = \Omega t$, and the relationship: $\sin^2 z = \frac{1}{2}(1-\cos 2z)$, the expression becomes:

$$\begin{aligned}\Delta\phi &= \gamma G_0x_0\frac{1}{\Omega}\int_0^{2N\pi}\frac{1}{2}(1-\cos 2z)\mathrm{d}z \\ &= \gamma G_0x_0\frac{1}{\Omega}\left[z-\frac{1}{2}\sin 2z\right]_0^{2N\pi} \\ &= \frac{\pi N\gamma G_0x_0}{\Omega} \qquad (3.12)\end{aligned}$$

Rearranging (3.12) and calculating for an observable phase change of 1 radian, with the same parameters as above, the motion required is 34.0μm.

Trapezoidal Waveform

While the sinusoid-based sequences passed in simulations, safety errors relating to gradient coil overheating were encountered in the scanner itself. The safety protocols could be disengaged thus allowing the sequence to work as intended, however, it was thought, in the best interests of the scanner, to try a different approach to encoding. Hence, trapezoids were used as motion encoding gradients. The trapezoidal waveform consisted of two trapeziums, each with a 1ms rise time, a 3ms plateau, and a 1ms fall time. The second trapezium was inverted in relation to the first. The motion calculation for the phase acquired with a set of trapezoids of the form seen in figure 3.12 is presented here.

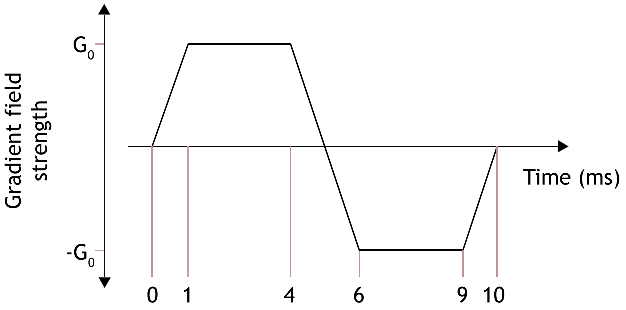

Figure 3.12: A single set of motion encoding trapezoids. The period of the waveform is 10ms; each positive and negative lobe has a plateau time of 3ms with a rise and fall time of 1ms.

The trapezoidal gradient can be expressed mathematically as:

$$G(t) = \begin{cases} 10G_0/T & 0 \leq t < T/10 \\ G_0 & \text{T}/10 \leq t < 4T/10 \\ -10G_0/T & 4\text{T}/10 \leq t < 6T/10 \\ -G_0 & 6\text{T}/10 \leq t < 9T/10 \\ 10G_0/T & 9\text{T}/10 \leq t < T \end{cases} \tag{3.13}$$

For a single period, the change in phase is:

$$\Delta\phi = \gamma \int_0^N G(t) x_0 \sin \Omega t \mathrm{d}t \tag{3.14}$$

To simplify the resulting five integrals, the result: $\int \sin \Omega t \mathrm{d}t = -\frac{1}{\Omega} \cos \Omega t$ is observed and thus (3.14) becomes:

$$\Delta\phi = \frac{\gamma G_0 x_0}{\Omega} \left[\left[-\frac{10}{T} \cos \Omega t \right]_0^{\frac{T}{10}} - \left[\cos \Omega t \right]_{\frac{T}{10}}^{\frac{4T}{10}} + \left[\frac{10}{T} \cos \Omega t \right]_{\frac{4T}{10}}^{\frac{6T}{10}} + \left[\cos \Omega t \right]_{\frac{6T}{10}}^{\frac{9T}{10}} - \left[\frac{10}{T} \cos \Omega t \right]_{\frac{9T}{10}}^{T} \right] \tag{3.15}$$

Evaluating the brackets results in:

$$\Delta\phi = \frac{\gamma G_0 x_0}{\Omega} \cos \frac{2\pi}{10} \tag{3.16}$$

upon simplification. Numerically (3.16) can be written as:

$$\Delta\phi = \frac{3.24\gamma G_0 x_0}{\Omega} \tag{3.17}$$

to three significant figures.

A calculation similar to those for the square and sinusoidal waveforms reveals that for a target phase change of 1 radian, the observed motion is 33.0μm; as expected, this is between the results for the square wave and sinusoid.

The trapezoids were confirmed as the most appropriate choice of motion encoding gradient due to a comparable sensitivity with the sinusoids, a practical ability to implement the gradients and less chance of errors when designing the pulse sequence.

The above motion sensitivity calculations have been performed for a maximum gradient amplitude of 22mT/m and a single pair of trapezoids. It was possible to include up to four pairs of trapezoids on some sequences and increase the gradient strength to 33 mT/m. With this value for G_0, the motion required for a 1 radian phase change becomes: 22.0μm for one set of trapezoids; 11.0μm for two sets; 7.3μm for three sets; and 5.5μm for four sets. More sets of trapezoids in a sequence lengthens the total time for data acquisition and increases the maximum echo time. While this offers a lot more sensitivity to motion, it also leads to a loss of signal due to either the T_2 value of the tissue (spin echo sequence), or the T_2^* value (gradient echo sequence).

A target phase change of 1 radian is quite generous; the setup should be able to detect much smaller phase changes thus increasing sensitivity even further. One point for consideration is to avoid too much phase accrual which would result in phase wrapping artifacts. Should this occur, a noise-insensitive phase unwrapping algorithm is required.

3.5.2 Force Provided by Piezoelectric Actuator

It is assumed the actuator applies simple harmonic motion to the sample, with a maximum displacement from equilibrium of ±45μm. In this project, no more than a 1.5kg mass was coupled to the actuator. With an excitation frequency of 100Hz, the maximum acceleration generated is:

$$\begin{aligned} a = \frac{\mathrm{d}^2 x}{\mathrm{d}^2 t} &= -\Omega^2 x \\ &= -17.76ms^{-2} \end{aligned} \tag{3.18}$$

Thus the maximum force required of the actuator is:

$$F = ma = 26.6N \tag{3.19}$$

The specifications of the actuator detail a push force capacity of 800N, and a pull force capacity of 300N, thus the actuator exceeds requirements by more than a factor of 10 and should provide a full displacement of the mass at 100Hz.

3.6 Pulse Sequence Programming

Work was undertaken on four different pulse sequences to include motion encoding gradients. These sequences were: a 2D gradient echo sequence (2D GRE), a fast spin echo (FSE) sequence, a 3D gradient echo (3D GRE) sequence, and a spin echo, echo planar imaging (EPI) sequence.

For reasons discussed in 3.5.1, trapezoidal motion encoding gradients (MEGs) were chosen. These trapezoids had a period of 10ms, to correspond to the period of the sinusoidal motion applied through the actuator at 100Hz. A variable *delay time* was included in all sequences to allow the phase offset between the motion encoding gradients and the actuator input to be modified. As discussed in 2.2.4, this enables a more complete picture of the motion throughout the entire time period to be built up.

What is referred to as 'negative motion encoding' in this section means inverting the amplitude of the MEGs. As the trapezoids are periodic, this has exactly the same effect as adding a delay time of half the period (5ms). This meant we needed to include a maximum delay time of only 5ms (reducing the sequence TE and TR), as the phase offset of the second half of the period could be investigated through inverting the amplitude of the motion encoding gradients.

The trigger pulse (refer to 3.2) used to synchronise the MEGs to the output of the actuator was applied through a voltage measured in the ECG input of the scanner.

The 2D GRE sequence provided a good introduction into MRE motion encoding. Only a single pair of motion encoding trapezoids was added (figure 3.13). The sequence was discontinued due to signal-to-noise (SNR) limitations in obtaining thin slices, thus restricting ability to acquire isotropic resolution.

The FSE sequence has potential to be a very fast method of acquisition. Work was not developed further on this sequence due to concerns over artifacts occurring through the refocusing of multiple echoes and affecting the motion encoding. Further details on such artifacts can be found in [33, ch. 12.3]. Other investigators have used FSE successfully [67], and it may be worth continuing the development of this sequence in the future.

The 3D GRE sequence (figure 3.14) became our standard pulse sequence against which further developments can be tested. While a number of other groups have used gradient echo techniques for MRE [68], [32], [16], [17], it is often unspecified whether a 2D or a 3D technique is used. Colleagues in 2001 claimed to be the first to acquire a full three dimensional MRE dataset [49], and it was the requirement of isotropic resolution for elasticity reconstruction that motivated our development of the 3D GRE sequence. This sequence excites the entire imaging volume as a slab, rather than individual slices within the volume, as is the case with the 2D sequence. Phase encoding is along two axes, rather than one, and the slab excitation results in high signal-to-noise, because each acquisition provides data from the entire 3D imaging volume, rather than a thin, 2D slice. It proved to be a reliable means of imaging muscle, silicone and brain tissue and allowed for acquisition of data with isotropic 2mm voxel resolution with good SNR. 3D GRE was developed with one, two, and three sets of motion encoding trapezoids.

The spin echo EPI sequence was developed as a fast method of acquiring MRE data. Its

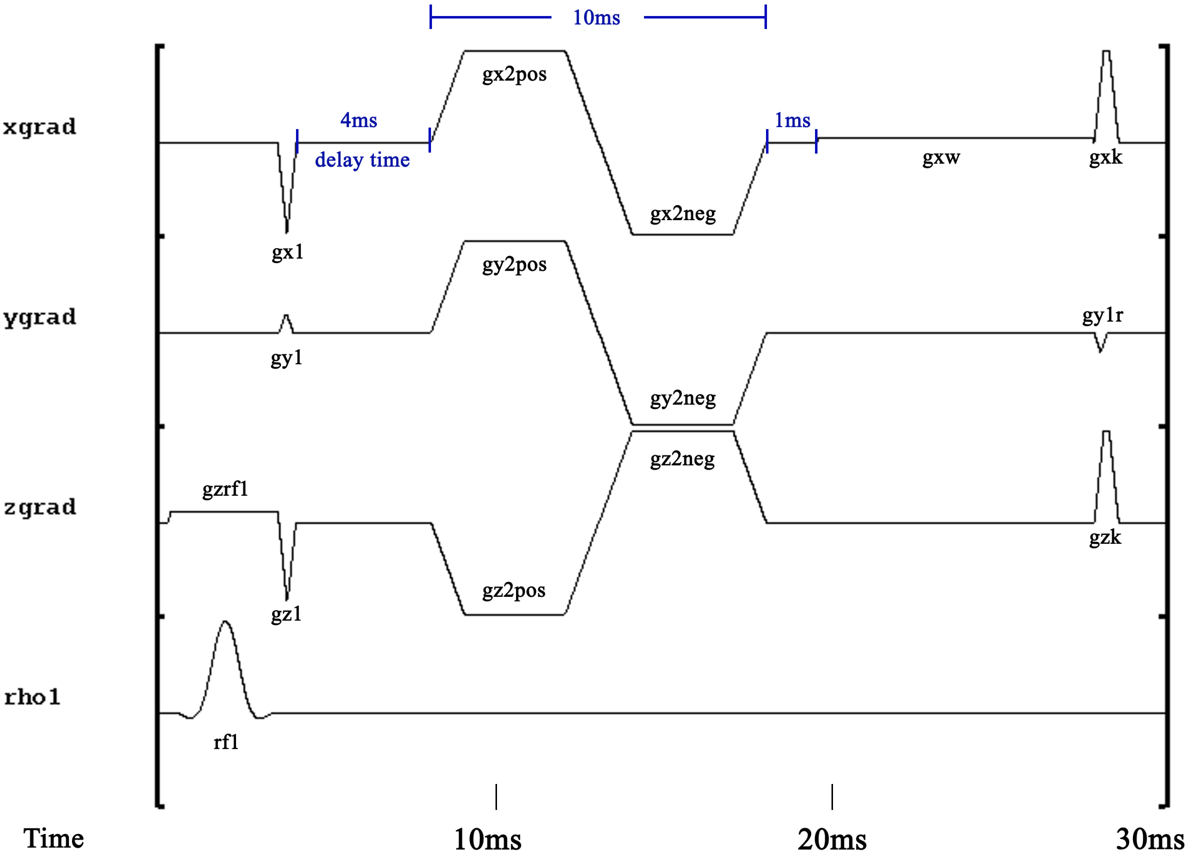

Figure 3.13: A pulse sequence diagram for the modified 2D GRE sequence used in the initial stages of this project. A single set of motion encoding trapezoids are shown on all three axes for illustrative purposes; in practice, only one axis would employ MEGs at any given time. The x and y axes show ‘positive’ trapezoids; the z axis shows ‘negative’. The period of the trapezoidal pulse is 10ms. A delay time of 4ms is shown in this image; there is thus a wait time of 1ms (the difference between the maximum delay time and the actual delay time used) following the motion encoding. This sequence required the insertion of the MEGs between the initial RF excitation (`rf1`) and the readout gradient (`gxw`). The approach used in modifying the timing of the pulses in this sequence formed the basis for developments of other sequences.

use has been shown successfully with at least one group [69]. In the sequence developed in this project, two sets of motion encoding trapezoids either side of the refocusing 180° pulse were included (figure 3.15), thus a total of four motion encoding gradients provided more sensitivity to motion than the 3D GRE sequence. The downsides to this sequence were the relatively long echo time, which meant tissues with short T_2 values, such as muscle, were unable to be effectively imaged, as well as EPI distortion artifacts due to the long echo train.

3.6.1 Programming Procedure

The following details are common to all sequences used in this project. The primary focus in modifying a sequence was to include motion encoding trapezoids along $\hat{\boldsymbol{x}}$, $\hat{\boldsymbol{y}}$ and $\hat{\boldsymbol{z}}$. New gradient waveforms had to be generated within the sequence, and it needed to be ensured that these additional pulses did not interfere with any existing pulses in the sequence. A delay time had to be added and, again, ensured that it did not coincide with existing pulses.

Additionally, code was written to allow for the synchronising triggering to be applied through the cardiac gating. A multiphase autoscan option was also included so that scans could be initiated with both positive and negative motion encoding along all three axes, without the need to define each variable between scans. In this sequence, the multiphase ran through seven options for each run: no motion encoding (to provide the reference phase data), then encoding along $+x$, $+y$, and $+z$, and finally encoding along $-x$, $-y$, and $-z$.

Control Variables

Control variables (CVs) were included in the `CVINIT` section of the code to define the amplitude and period of the motion encoding trapezoids, the maximum and variable delay time, and to switch on the ECG triggering.

`optrapamp` defined the amplitude of the motion encoding trapezoids. The MEGs were coded with a maximum and minimum gradient field strength of +40 to −40mT/m, with a default value of 33mT/m, which is the maximum value allowed by the scanner.

`optrapperiod` set the period of the motion encoding to a default value of 10ms. This CV has a minimum value of 0ms, and a maximum of 50ms.

`opmaxdelay` set the maximum delay time in the sequence to a default of 5ms. This value could be modified from 0 to 100ms.

`opdelay` was used to vary the actual phase offset between the motion output of the actuator and the MEGs. The delay could be set from 0 to 100ms, but in practice was used from 0 to 5ms.

`triggerfromecg` is the CV used to switch on the ECG triggering.

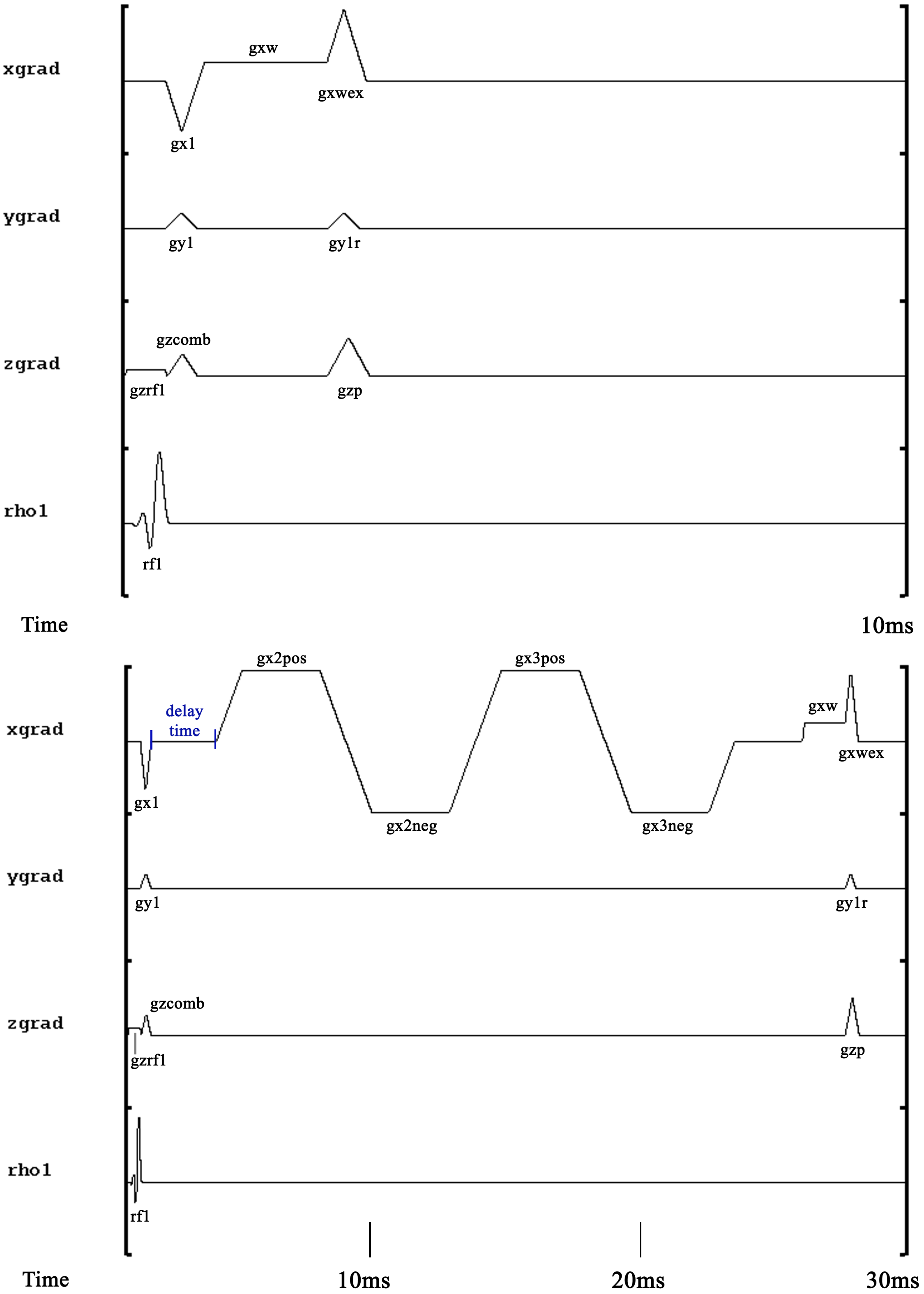

Figure 3.14: The top image shows the original 3D gradient echo sequence, labelled with the names of the pulses. The lower image shows the sequence following modification to include motion encoding. Two sets of trapezoids are in place in this sequence. This image has them on the x gradient, corresponding to the direction of frequency encoding. There is a delay time of 2.5ms, apparent between `gx1` and `gx2pos`. The space between the end of the decay ramp for `gx3neg` and `gxw` is also 2.5ms, as a result of the difference between the maximum delay time and the actual delay uses in this scan.

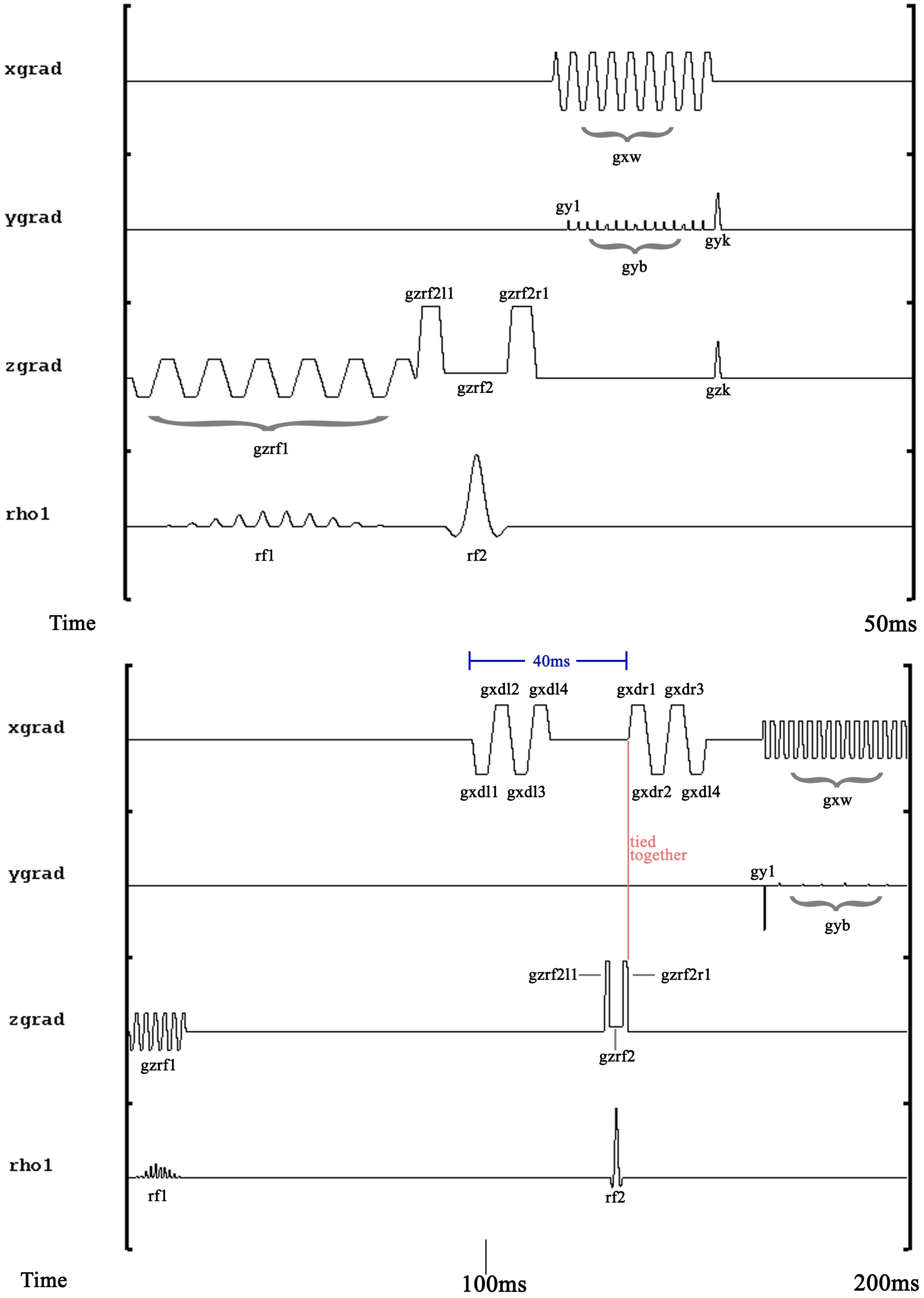

Figure 3.15: The top image shows the original spin echo EPI sequence, labelled with the names of the pulses. The lower image shows the sequence with motion encoding gradients included. The EPI sequence was modified to include four sets of motion encoding gradients, two either side of the refocusing 180° RF pulse. Positive gradients are in place along the x axis in this image. Note the polarity of each pair of trapezoids is reversed due to the 180° RF pulse flipping the phase of the spins in between each set of MEGs. There is a zero delay time in this image. `gxw` and `gyb` are pulses providing the characteristic readout train of an EPI sequence.

Pulse Generation

The `PULSEGEN` section of the code is where every magnetic gradient and RF pulse used in the sequence is defined.

Each period of a motion encoding gradient consisted of a ‘positive’ trapezium, and a ‘negative’ trapezium of the opposite polarity. These two trapeziums each consisted of a 1ms rise time, a 3ms plateau, and a 1ms fall time, and were tied together to form one cycle of the periodic motion encoding trapezoid, as can be seen in figure 3.12. This can be seen in the pulse sequence diagram of the 3D GRE sequence, where, for instance, `gx2pos` forms the positive half of the first MEG, and `gx2neg` forms the negative half (figure 3.14). The rise and fall gradients can be observed.

In this section, the scanner also runs through a calculation to determine the minimum TE and TR values of a sequence. These calculations were modified to include the periods of the MEGs and the maximum delay time.

3D GRE Sequence

In the 3D GRE sequence (refer to figure 3.14), two such pairs of trapezoids were tied together. The original sequence had to be ‘split’ after the initial excitation pulse (`rf1`) and before the readout gradient (`gxw`). In the original sequence, the `gx1` pulse was tied to the beginning of the `gxw` pulse. This was modified so that `gx1` was tied to the end of the slice select pulse, `gzrf1`, and the onset of the first MEG was tied to the end of `gx1`, `gy1` or `gzcomb`, whichever finished last, plus the delay time, which was specified as a CV. In the figure, a delay time of 2.5ms is shown.

The end pulses `gxwex`, `gy1r` and `gzp` were all tied to each other, which in turn depended on the position of `gxw`. `gxw` was set to turn on after the final MEG turned off plus an interval of the difference between the maximum delay time allowed (5ms) and the actual delay time used in a particular scan.

Spin Echo EPI Sequence

Refer to figure 3.15 for details of pulse sequence design of the motion encoding EPI sequence.

Four pairs of motion encoding trapezoids were included in the EPI sequence, two before the refocusing 180° RF pulse (`rf2`), and two after. This RF pulse has the effect of reversing the phase of the spins, thus we must take this effect into account when applying motion encoding gradients. The onset of each set of gradients must be separated by an interval of a multiple of half the period (5ms). The effect of the 180 RF pulse means that with a gap of an even multiple of 5ms (i.e. a multiple of the 10ms period), one set of MEGs must be inverted in relation to the other. This is the case in our sequence, where it was found that, within these parameters, the optimal time difference between the onset of the first set of MEGs (`gxdl1`, for instance) and the second (`gxdr1`) is 40ms.

The timing of the motion encoding gradients in this sequence was slightly different to that employed in the 3D GRE sequence. Instead of tying the first set of MEGs to after the first RF pulse, the second set of MEGs was tied to the end of the refocusing 180° pulse (`rf2`); the rest of the gradients and the delay time were calculated 'backwards' from this value. While no delay time is shown in the example figure, the delay time would be introduced after the end of `gzrf2r1`.

`gxw` and `gyb` are the pulses of the EPI readout train.

3.7 Verification of Motion

3.7.1 External Verification

Initial scans of the first excised bovine muscle phantom embedded in gelatine seemed to show a lot less motion being detected than for the initial silicone phantoms. As this was the first time the 3D-orientable box setup had been used, we needed to verify whether this setup was providing less motion to the sample than the fixed box setup. Some hypotheses behind a potential loss in motion were: reduced coupling from the actuator to the sample caused through the nylon screws, lateral motion of the sample reducing the linear actuation and mechanical coupling due to the heavier orientable phantom being of a similar mass to the apparatus base.

Some simple testing, external to the MRI, was devised to verify the motion of the newly-made silicone wedge phantom, which had a similar mass to the muscle-gelatine phantom and to compare it to the motion of the original homogeneous phantom.

Firstly a Dial Test Indicator (DTI) was set up behind the phantom apparatus. The DTI consists of a plunger against which the phantom container rested. Movement of the box registered, through the plunger, to a dial indicator, from which the amplitude of the motion could be read. The DTI setup was only effective at low frequencies (up to about 50Hz). At these frequencies, both the fixed box phantom and the orientable box phantom registered the full range of motion ($\pm 45\mu$m) with the maximum input voltage of 12V.

To investigate the motion at higher frequencies, a piezoelectric device was fitted to the wall of the phantom boxes. This device works in reverse to the actuator: a voltage is generated upon registering motion. This voltage could be observed on an oscilloscope. Unfortunately this technique could only measure relative motion. Firstly, the device was attached to the tip of the actuator, with no phantom connected. The peak voltage was recorded, and then the experiment was repeated, attaching the device to the walls of the fixed box and orientable box phantom and also the tray of the orientable box setup, which should be directly connected to the actuator output. The voltage output was investigated at a range of frequencies up to 100Hz. At 100Hz, the peak-to-peak voltage registered on the oscilloscope was 250mV for the actuator with no phantom box attached, but 120mV for when both the fixed box and the orientable box were connected.

To determine the absolute motion of the setup at higher frequencies, a more complete testing would be required, involving an accelerometer. However, this result suggests two things. Firstly, there is little difference in the motion being applied to both the fixed and orientable phantom containers: the nylon screws provide good coupling. Secondly, it would appear that only around half the motion that the actuator delivers on its own is being translated into actual motion of either box. Conversations with the piezoelectric manufacturers would suggest that damping of the actuator is an unlikely cause. The most plausible scenario is that the base of the setup is moving relative to the phantom. The base is not clamped to the scan table and indeed, vibration can be felt through the head coil during actuation. Attempting to minimise this, additional weight was added to the base of the apparatus and the input voltage was kept at 9V. Future designs may include clamping of some sort to maximise the motion input into the sample.

It is likely that a number of other, smaller factors also play a part in reducing the motion translated to the sample itself. We are dealing with significant forces over a very small range of motion, so effects such as losses through the coupling of the brass fittings, friction on the Teflon pads, flex in the Perspex at both the box and the vertical supporting wall, as well as those described above, while small, could contribute to an overall loss in phantom motion.

The result that both box setups seem to be providing a similar level of motion to the sample results in the question of why the homogeneous silicone phantom appears to be moving a lot more than the first beef tissue phantom. Qualitatively feeling the vibration of the silicone gel itself at different frequencies revealed some noticeable resonance frequencies; this was observed at different frequencies for the two gels. It is possible that resonance in the first silicone phantoms resulted in a far greater amplitude of motion of the silicone than of the containing box itself. This potential resonance effect led to a false expectation of the amplitudes we should expect to be able to detect. This resonance effect is also a possible explanation to poor reconstruction of the inclusions phantom. This is discussed in 5.4. The excised muscle phantom is a lot less likely to exhibit a similar resonance effect, thus rather than seeing a reduced motion due to a more lossy experimental setup, we were simply not sensitive enough to the motion that was there.

3.7.2 Subsequent MR Testing

The above findings led to the development of increased motion-sensitive pulse sequences, with more motion encoding gradients and stronger amplitudes. To compare the motion of the original phantom setup to that of the orientable phantom setup in the MR context, the two phantoms were imaged and the motion of voxels near the walls of the box were compared. Ideally, the box walls should be moving with the actuator, so an idea of the range of motion provided by the actuator in the MR context was able to be determined. The motion detected by the original sequence, with a single set of motion encoding trapezoids with a maximum gradient strength of 22mT/m was also compared to a newly-developed sequence with three sets of motion encoding trapezoids with an amplitude of 33mT/m.

Comparison of Motion Between Phantoms

The homogeneous silicone and the wedge phantoms were imaged with motion encoding along the direction of actuation. 16 representative voxels were selected from a slice in the middle of both the homogeneous silicone phantom, and the wedge phantom. The voxels were taken from the edge of each phantom. The measured phase in each voxel was determined, and from a rearrangement of equation (3.17), the amplitude of motion could be determined (figure 3.16).

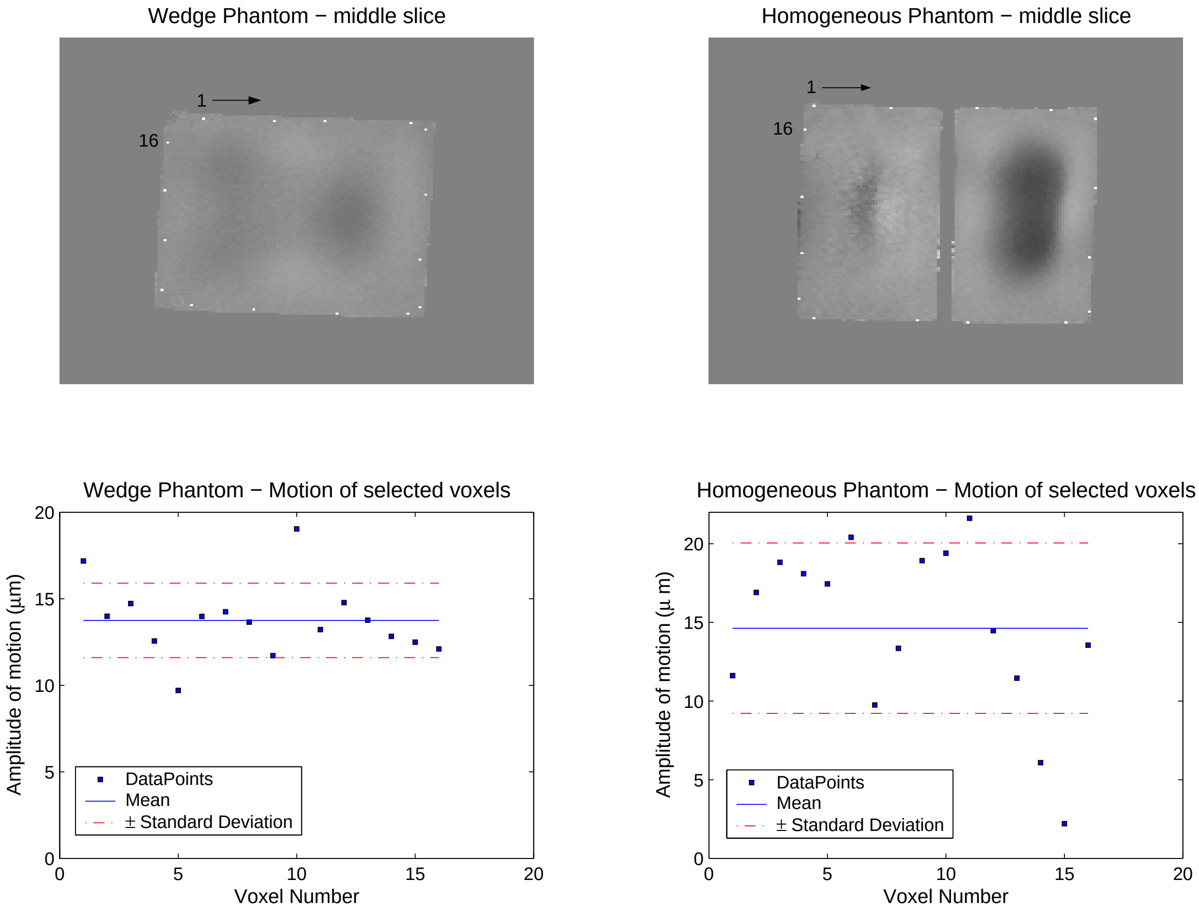

Figure 3.16: The left-hand set of images shows motion results for the silicone wedge phantom, contained within the 3D-orientable box setup. The right-hand set of images shows results for the homogeneous silicone phantom in the fixed box apparatus. The top images show the displacement of a middle slice of the phantom at a particular time. The selected voxels are highlighted. Voxel 1 is in the top left of each phantom, and the numbering continues clockwise around the edge of the phantoms as indicated. The calculated motion data is presented on the bottom figures, with the mean motion over the 16 voxels and standard deviation indicated also.

The average motion for the representative voxels from near the walls of the two different was very comparable. The mean motion of the wedge phantom was 13.7μm, with a standard deviation of 2.2; the mean of the homogeneous phantom was 14.6μm, with a standard deviation of 5.4. Only a single delay time was used in this experiment, thus, if the motion of the actuator was out of phase with the motion encoding gradients, the full amplitude of motion of the sample may not be represented here. A full range of delay times would need to be considered to determine the peak amplitude of motion over the whole cycle. This was obtained for a prior dataset of the homogeneous silicone phantom. 16 voxels were selected similarly from this dataset, and the motion of each voxel determined at delay times in intervals of 1ms from 0 to 10ms. These values were then averaged, and the results for average motion over delay time are presented in figure 3.17. This figure shows the dependence of the measured amplitude on the delay time.

The results displayed in figure 3.16 confirms that there is little difference between the

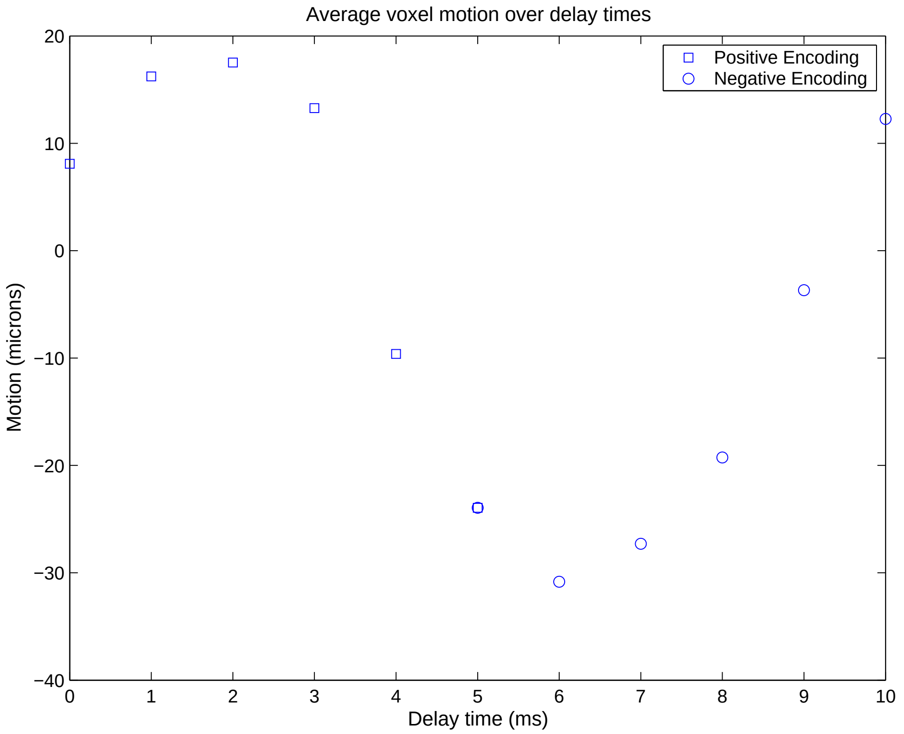

Figure 3.17: The average motion of 16 representative voxels selected from close to the sample wall of the homogeneous silicone phantom over delay times from 0 to 10ms. It is clear that for this acquisition, the peak amplitude of motion occurs at around a delay time of 2ms.

amount of motion being applied to the two different phantom setups. Error in the data most likely comes from signal-to-noise error in the MRI scan, and the fact that interfaces between different materials often produce susceptibility artifacts, thus it is difficult to get very close to the boundary of the phantom without encountering some intrinsic noise.

Increased Sensitivity in Pulse Sequences

The theoretical increase in motion sensitivity from the original sequence with a single set of trapezoids, of amplitude 22mT/m, to the sequence with three sets, of amplitude 33mT/m, is a factor of 4.5 (see 3.5.1). This was shown by imaging the wedge phantom with the two different sequences and comparing the phase detected (figure 3.18). Dividing one result by the other and averaging over all voxels, allowing for phase wrapping artifacts as much as possible, resulted in a sensitivity factor of 4.69, very close to the theoretical result. Phase wrapping artifacts, in areas where the phantom experiences a significantly greater amount of motion than neighbouring voxels, account for the degree of uncertainty.

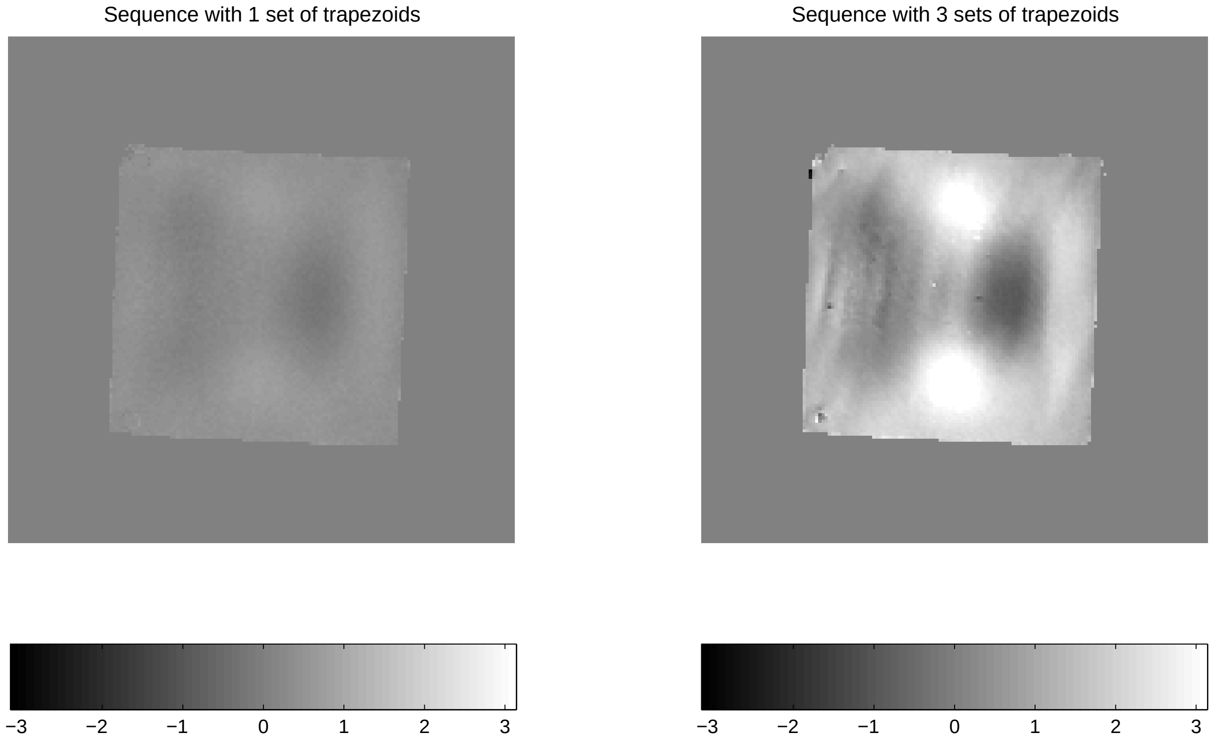

Figure 3.18: Relative phase accrual due to motion encoding data for the silicone wedge phantom is shown. The left-hand image was acquired with a single set of motion encoding gradients, of amplitude 22mT/m; the right-hand image uses three sets of motion encoding gradients, of amplitude 33mT/m. The two images are scaled to the same parameters (phase between $-\pi$ and π), and qualitatively, one can observe a dramatic increase in sensitivity in the right-hand image.

Chapter 4

Data Acquisition and Processing

4.1 MRE Dataset Acquisition

4.1.1 3D Gradient Echo Sequence

The application of the 3D gradient recalled echo (3D GRE) sequence was refined until it was a reliable, robust system that could be used to image any of the phantoms developed.

Recall, from section 3.6, that the 3D GRE sequence was developed with one, two, and three sets of motion encoding gradients. We require sufficient motion sensitivity (change in phase per micron of motion) from our sequence, and thus have the option of using any of these three sequences. As the motion encoding trapezoids have a fixed period (10ms), set by the driving frequency of the actuator, and fixed amplitude of 33mT/m, which is the maximum the scanner will allow, the only way we have of increasing motion sensitivity is to increase the number of periods of motion encoding included. Recall that the observable phase change is directly proportional to the number of motion encoding gradients (from equation (2.40)). However, increasing N increases the TE of the sequence. Equation (2.26) shows that the signal strength is dependent on e^{-TE/T_2}, thus by adding more motion encoding gradients to increase motion sensitivity, we decrease the returned signal by increasing the echo time. A compromise was made with the 3D GRE sequence by choosing to use two sets of motion encoding gradients. This gave the sequence a TE of 34ms.

A trigger pulse was sent every 100ms through the cardiac gating system, giving a ‘heart rate’ of 600bpm, the maximum available. The final scan parameters were: $TE = 34$ms; $TR = 100$ms (the interval between triggers); bandwidth = 8.06kHz. The flip angle was 45° for silicone and muscle imaging and 26° for brain imaging, which results in more signal from tissues with a long T_1. The Ernst angle (θ_E) is the name given to the flip angle used to produce the optimal signal from a given tissue. It depends on the T_1 value of the tissue being imaged, and the TR of the sequence. (θ_E) is given by [34, ch. 18]:

$$\theta_E = \cos^{-1}\left(\mathrm{e}^{-\frac{TR}{T_1}}\right) \tag{4.1}$$

For silicone, assuming a T_1 value of 600ms (see 5.1), and with a TR of 100ms, the Ernst angle is 32°. Thus a flip angle closer to this value could be used for imaging silicone phantoms in the future.

Acquisition parameters were: a 16cm field of view (FOV); excitation of a 2cm slab with ten 2mm thick slices; a 96 × 96 acquisition matrix was used. These imaging parameters gave us a 2mm isotropic resolution and allowed us to reconstruct isotropic 1mm voxels, using a data interpolation algorithm (see 4.2). Although not strictly necessary, isotropic voxels are beneficial in the elasticity reconstruction process.

Multiphase was enabled which allowed us to acquire seven sets of motion encoding data without needing to change variables between scans. In order, those sets were: no motion encoding, to be used as a reference phase; motion encoding along the positive frequency-encode (x) axis; along the positive phase-encode (y) axis; along the positive slice-select (z) axis; and then along the negative frequency, phase and slice directions. All future reference in this work to motion encoding will use these orientations. The negative encoding corresponded to changing the polarity of the motion encoding gradients. The total time to acquire these seven sets was 11 minutes.

These sets were then acquired for different delay times. The delay time alters the relative phase between the motion output of the actuator and the motion encoding gradients. Enough points are required to fully describe the motion of the phantom over the 10ms period of motion. A delay time of 5ms with positive motion encoding gradients corresponds to a 0ms delay with negative motion encoding gradients, thus delay times only up to 5ms were required. Initially six delay times were acquired: 0, 1, 2, 3, 4 and 5 ms. To reduce total acquisition time, four delay times were later employed: 0, 1.25, 2.50 and 3.75 ms. The total acquisition time for such a scan was about 45 minutes.

For anisotropy experiments, this procedure was repeated for different orientations of the box. The directional markers allowed the same slice to be selected each time, thus the effect was of imaging the same slice, but with actuation from three different directions.

Raw k-space data of the real and imaginary components of the phase information were saved.

4.1.2 EPI Sequence

The echo planar imaging (EPI) sequence was trialled on the biological samples. Due to the multiple magnetic resonances of silicone, and the susceptibility of the EPI sequence to such resonances, the silicone phantoms were not trialled. The T_2 of muscle ($\sim$ 30ms [33, ch. 8.5]) was unfortunately substantially less than the TE of the EPI sequence, thus little signal was observed from the excised beef muscle phantoms (figure 4.1). Some promising signs were exhibited with the brain phantom however (see figure 4.2).

Scan parameters used were: $TE = 91.7$ms; bandwidth = 62.50kHz. The TR depended on the triggering frequency, which was initially set to one trigger every 100ms, but then increased to a trigger every 500ms. Increasing the triggering interval in this manner improved ghosting artifacts. The acquisition was a 64×64 array, with a FOV of 16cm; sixteen 4mm slices were obtained. A four-shot sequence was used.

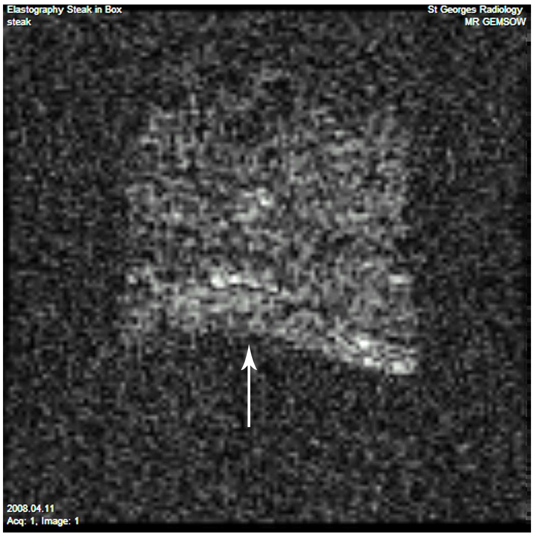

Figure 4.1: The EPI sequence was not effective at imaging muscle. This figure shows a magnitude image of a muscle phantom using the EPI sequence. The position of the muscle sample is indicated by the arrow. The short T_2 value in relation to the echo time of the sequence means very low SNR is observed.

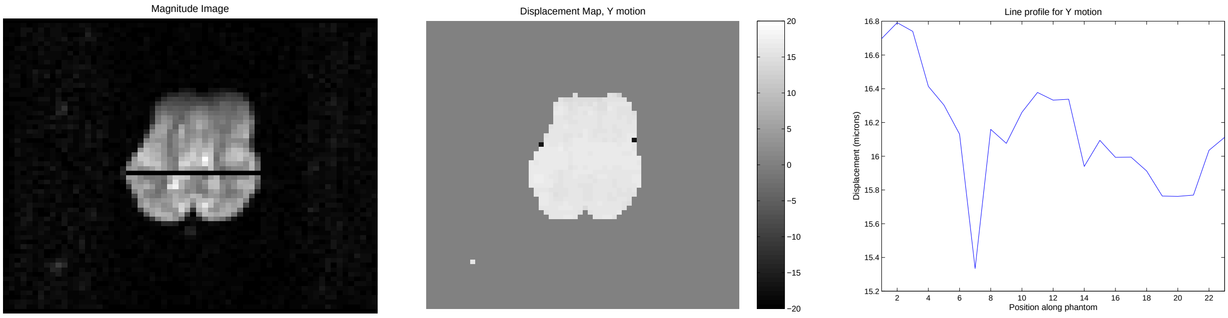

Figure 4.2: The magnitude image of the excised brain phantom acquired with the modified EPI sequence (left) shows the location of the line profile presented. The centre image shows the displacement map of motion along the ‘Y’ direction (along the vertical axis of the figure). The colourbar expresses displacement in microns. While there is little relative motion within the phantom, as confirmed by the line profile (right), the overall displacement of the phantom ($\sim 16\mu$m) is extremely comparable to results acquired with the 3D GRE sequence (see 6.2).

The scan time to acquire 8 image sets (two reference sets plus positive and negative motion encoding along $\hat{\boldsymbol{x}}$, $\hat{\boldsymbol{y}}$ and $\hat{\boldsymbol{z}}$) was 3 minutes, 20 seconds. This is significantly shorter than the 3D gradient echo sequence and thus EPI offers great potential in producing a clinically-viable MRE pulse sequence.

The modified EPI sequence was trialled on the excised brain phantom. Little motion was seen along two of the directions (which is in keeping with results found with the 3D GRE sequence), however, significant motion was observed along the direction of actuation. Given a TR of 100ms, this means that we can obtain some indication of motion (in one dimension) in 200ms per slice (one acquisition is for a reference set). The EPI sequence certainly show promise in further MRE development

Figure 4.2 shows some output from the EPI acquisition. Motion encoding is along the vertical axis of the first two images (corresponding to 'y' motion encoding), with actuation in this direction also. These data were acquired at a delay time of 2.5ms, and the acquisition is estimated to be in phase with the motion, thus near maximum amplitude of motion is detected. While little change in motion can be seen spatially throughout the phantom, the line profile indicates that at this time point, the phantom has moved about 16μm from the equilibrium position. These results are very comparable to those from the full dataset acquired with the 3D GRE sequence (see 6.2).

4.1.3 Motion Artifacts

The method of triggering used in these acquisitions appears to be susceptible to some motion artifacts. A standard ECG output is registered by the scanner. Our triggering position was set to 80% of the peak amplitude of the cardiac waveform, however, triggering did not always occur at this point. There were occasional early or late triggerings, and some triggers missed altogether. It was difficult to notice this initially, as a triggering rate of 100ms corresponds to a registered 'heartbeat' of 600bpm, however, increasing the triggering interval for the EPI sequence made the mistimed triggers more obvious.

A missed trigger does not concern us overly: it simply means the scanner will wait until the next trigger before initiating the next set of motion encoding gradients. An early or late trigger, however, will result in some motion artifacts due to a non-reproducible phase shift between the trigger and the onset of motion encoding gradients. There will always be an offset based on at which point in the cardiac cycle triggering occurs. This is one reason for needing a full range of delay times in order to observe the maximum amplitude of motion. However, if this offset varies during a scan due to inconstant triggering, an additional, random phase is accrued along the phase encoding direction in k-space, leading to motion artifacts such as can be seen in figure 4.3.

The motion artifacts are strongest when the motion encoding gradients are along the direction of actuation, and are always along the phase encode axis.

There is also some evidence to suggest that these artifacts occur when there is less relative motion of the sample. This appears to occur around a delay time of 0ms for acquisition of the brain phantom (figure 4.4). There is little change in phase between the reference image and the motion encoded image. In addition, the motion artifact along the

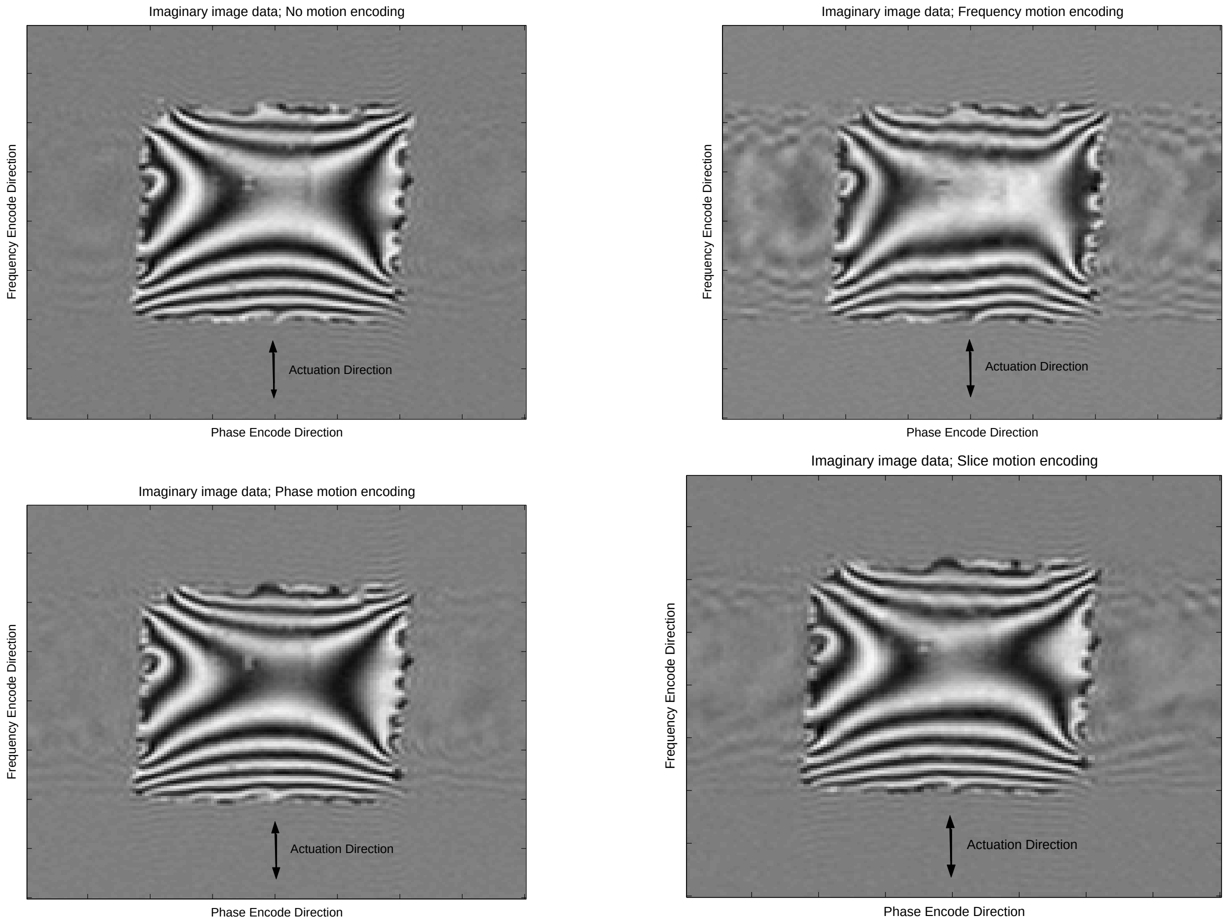

Figure 4.3: Some images of the imaginary part of complex image space data for the silicone wedge phantom are presented. The images are for the same slice of the phantom, and with acquisition at the same delay time. The direction of actuation is indicated on each image. The top left image shows data for no motion encoding enabled. The phantom is relatively free of motion artifacts. The top right image shows data for motion encoding along the frequency encode direction (the same direction as actuation). A significant motion artifact due to incorrect triggering can be seen. The bottom left image shows results for motion encoding along the phase encoding direction (horizontal axis), and the bottom right shows results for through-plane, or slice select, motion encoding. These latter two have less significant motion artifacts. In each case where artifacts are present, they extend along the phase encoding direction. This is because mistimed triggering results in an additional phase accrual which manifests itself along the phase encode axis of k-space.

phase encoding direction is significant. In comparison, when the motion and the gradients are in phase (around a delay time of 2.5ms), a large phase change within the brain indicates a large amplitude of motion detected. This also results in less motion artifact (figure 4.5).

Referring to figure 3.17, the amount of motion detected is dependent on the relative phase of the motion encoding gradient and the motion signal. The maximum motion detected occurs when the MEG and the motion are in phase, or in anti-phase. A phase jitter caused by a mistimed trigger pulse in this situation will not affect the integral in equation (3.5) greatly. However, when the motion is 90° out of phase with the motion encoding, not only is the minimum motion detected, but the motion sinusoid shown in figure 3.17 has maximum gradient, and is thus more susceptible to variations in phase.

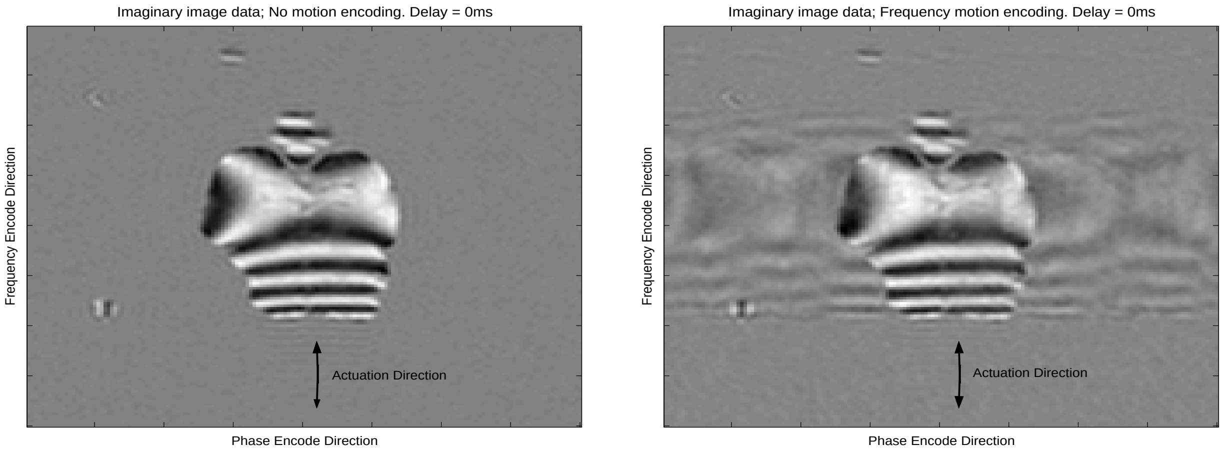

Figure 4.4: The imaginary part of complex image space data acquired for a middle slice of the brain phantom is presented. Images shown are the reference phase, with no motion encoding (left), and motion encoding activated along the frequency encode direction (right). The frequency encode direction is along the vertical axis of the image, in the same direction as the actuation. The sinusoidal motion driving signal appears to be 90° out of phase with the motion encoding gradient. This results in less observed phase shift within the phantom: qualitatively one can observe little difference in phase from the reference image to the motion encoded image. However, it is when the driving signal and the motion encoding gradients are 90° out of phase that the steepest rate of change of phase occurs. This is manifested in a far greater susceptibility to motion artifacts, as visible in the right-hand image.

4.2 Data Processing

4.2.1 Fourier Transform of k-space Data

The raw k-space data from the 3D gradient echo sequence consisted of complex data arrays of size $96 \times 96 \times 10$ (the imaged resolution). These files were imported into MATLAB, reconstructing the raw data to a complex image array of size $160 \times 160 \times 20$. This corresponds to an image resolution of isotropic 1mm voxels. This array is the complex image space data and was arrived at through a three dimensional Fourier transform of the k-space data (refer to 2.1.6). A technique known as *zero-fill interpolation processing* (ZIP) was used to interpolate the data from a 2mm voxel size to a 1mm voxel size. This technique involves increasing the k-space data matrix size to the desired image space matrix size and filling

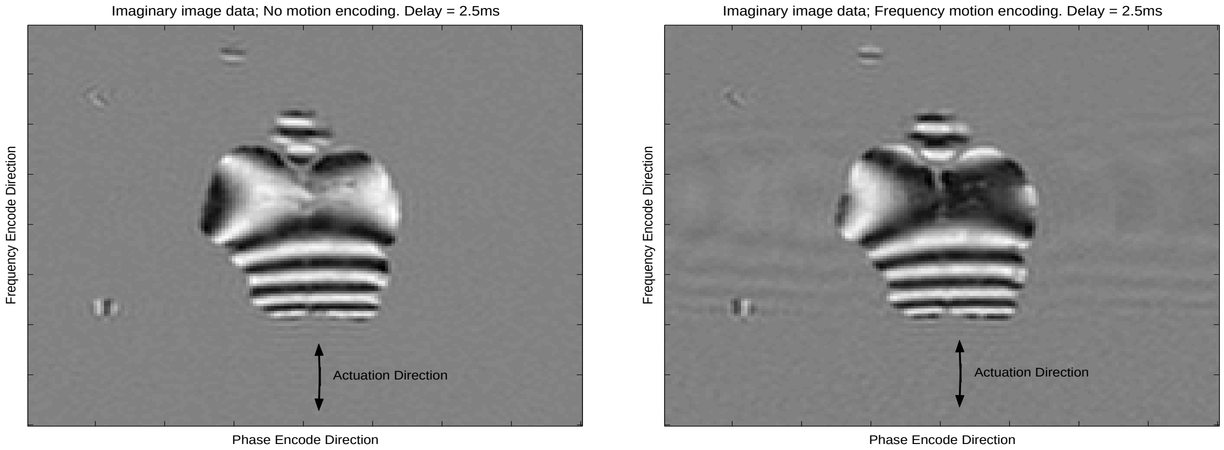

Figure 4.5: The imaginary part of complex image space data is shown for the same slice of the brain phantom as for figure 4.4 but with the motion encoding gradients in phase with the motion. As before, the left-hand image shows the reference data; the right-hand image shows motion encoding along the frequency encode direction. In comparison to figure 4.4, there is clearly a greater observable phase change within the phantom, and additionally, a significantly reduced motion artifact.

the unmeasured data points with zeros before taking the Fourier transform of the k-space data, thus resulting in a smaller voxel size in image space.

Out of the twenty slices in the complex image space data, the first and last four were discarded. This is due to the slice profile of the imaged slab not being a perfect ‘top-hat’ function (refer to 2.1.5), and thus the flip angle experienced by spins at the edges of the slab are not constant. These are slices the scanner would naturally discard, however were preserved through saving all the raw k-space data from the acquisition.

4.2.2 Mask Generation

Now using the complex image space data, a magnitude image of the reference set (no motion encoding) was determined. From this information a mask of the phantom was generated. This mask was to be overlaid on motion images to erase background noise from areas with no signal (figure 4.8).

4.2.3 Subtraction of Background Phase

All MR images have a ‘background’ phase due to spins experiencing extrinsic, local inhomogeneities in the external magnetic field. These effects are static, and thus constant to all images acquired. We are interested only in the *relative* phase of voxels within the phantom due to motion encoding (recall 2.2.4).

The phase of the reference data, from the complex image space data, was determined and stored as the reference phase data against which the motion encoded phase data could be compared.

The phase of positive and negative motion encoding along $\hat{\boldsymbol{x}}$ (frequency encode direction), $\hat{\boldsymbol{y}}$ (phase encode direction), and $\hat{\boldsymbol{z}}$ (slice select direction) was similarly determined and the reference phase data was subtracted resulting in the net phase accrued due to motion encoding. The mask was then overlaid, setting the background noise to zero (figure 4.8).

In some instances, especially with the more motion-sensitive pulse sequences, where a large phase change was detected, phase wrapping occurred, which needed to be corrected (figure 4.6). Phase wrapping is the effect of phase values in adjacent voxels 'wrapping over' from 0 to 2π, for instance, when of course, the two values are the same. Most phase images displayed in this report use a scale from $-\pi$ to π with $-\pi$ appearing dark and π appearing bright. If phase wrapping has occurred, bright voxels will be present where the surrounding area is dark, or vice versa. Initial attempts to correct this used a simple one-dimensional phase unwrapping algorithm. This proved to be mostly unsatisfactory, due to noise, and it became clear that a two- or three-dimensional phase unwrapping algorithm would be beneficial [70]. The introduction of software which could cope with this resulted in a slightly different arrangement of the data importation, although the most significant effect was felt in a greater length of time taken to process higher dimensional phase unwrapping.

4.2.4 Data Rearrangement

The above process was repeated for the different delay times acquired.

For each direction of motion encoding, the phase data were arranged in order of effective delay time. As mentioned earlier, motion encoding with reversed polarity of motion encoding gradients has the effect of shifting the delay time by half a period (5ms). Thus, negative motion encoding with a delay time of 0ms has an *effective* delay time of 5ms. Therefore, the positive and negative motion encoding data were combined to form an array that described motion in one particular direction over an entire sinusoid.

4.2.5 Fitting Motion to a Sinusoid

We expect the motion to exhibit a regular sinusoidal pattern of period 10ms, as this is the input from the actuator. A Fourier fitting was applied to the motion encoding data, decomposing the signal as a function of delay time into a set of sine waves (figure 4.7). Taking an array for a particular direction of motion encoding, a discrete fast Fourier transform was applied at each voxel over different effective delay times (adapted from [71, ch. 4]):

$$\boldsymbol{F}(k) = \sum_{j=1}^{N} \boldsymbol{f}(j) \mathrm{e}^{-\frac{2\pi i}{N}(j-1)(k-1)} \tag{4.2}$$

$\boldsymbol{f}(j)$ is the vector of phase values over effective delay times for a particular voxel; $\boldsymbol{F}(k)$ is its Fourier transform. j and k are elements in their respective vectors; N is the number of delay times; i in this case is $\sqrt{-1}$.

A plot of the magnitude of the inverse Fourier transform reveals the component frequencies making up the recorded motion signal at each voxel (figure 4.7, left). The dominant frequency (100Hz) was selected and the other components of this vector set to zero. A discrete inverse Fourier transform could then be performed to generate a Fourier fitting to the measured data:

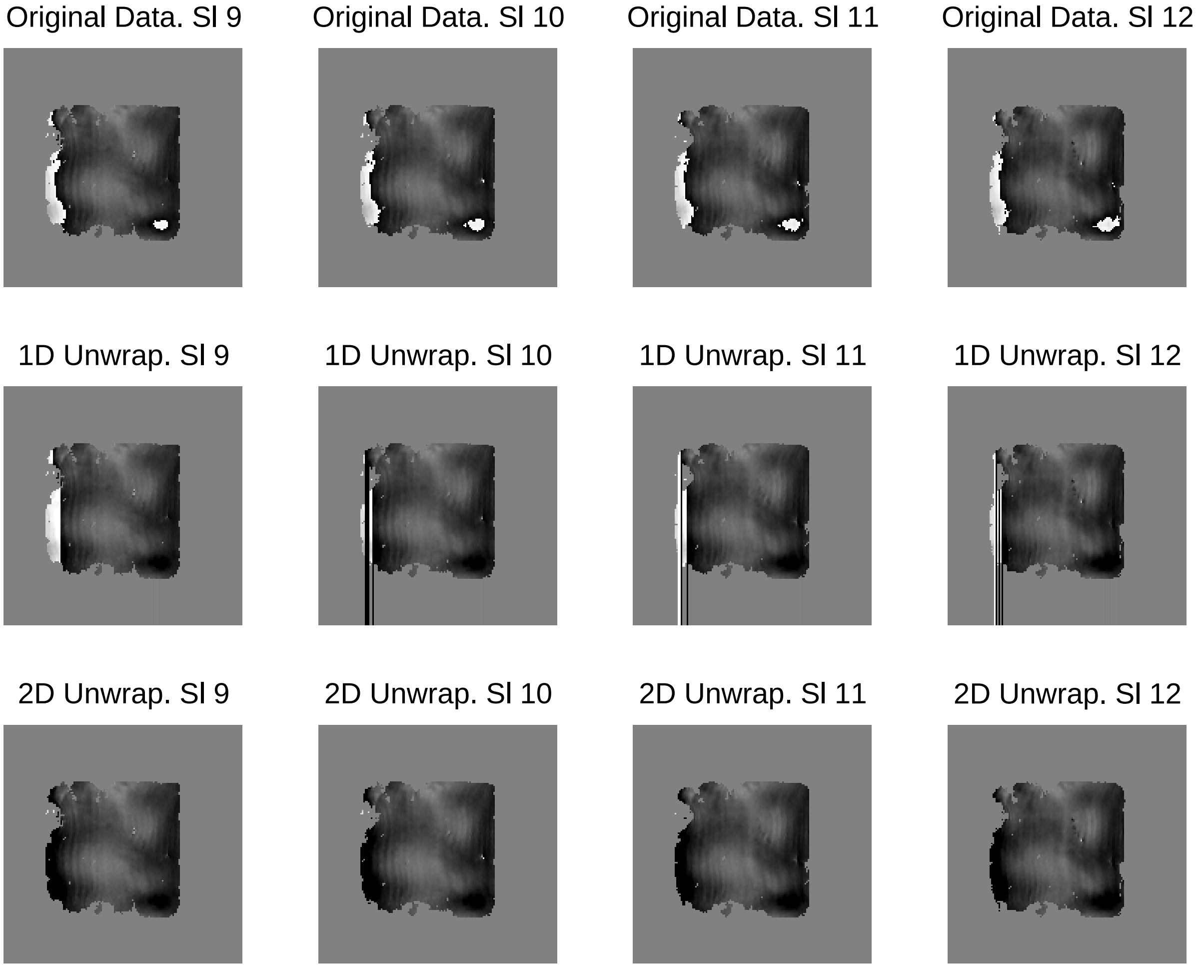

Figure 4.6: Four central slices of the excised beef tissue phantom, with no gelatine, are shown. The images are of the phantom displacement at a particular time point. Motion encoding is through-plane; the delay time selected is 1.25ms. All images have been masked to eliminate the zero-signal noise. The top set of images shows the original motion data. Some phase wrapping is visible, notably along the left-hand edge, and in the bottom right corner. This artifact is a result of a directional marker at this location. The limitations of the simple one-dimensional unwrapping approach are revealed in the second set of images, with some phase remaining unwrapped, and lines appearing in other locations. The two-dimensional approach (bottom) yields much more satisfactory results.

$$\boldsymbol{f}(j) = \frac{1}{N}\sum_{k=1}^{N}(k)\mathrm{e}^{-\frac{2\pi i}{N}[-(j-1)(k-1)]} \tag{4.3}$$

The inverse Fourier transform returns a complex value at each frequency. The magnitude and phase of this complex data is recorded for each direction of motion encoding at each voxel within the imaged volume and stored as a four dimensional array. The first three dimensions of this array contain the spatial coordinates of the imaged volume; the fourth dimension contains the magnitude and phase data.

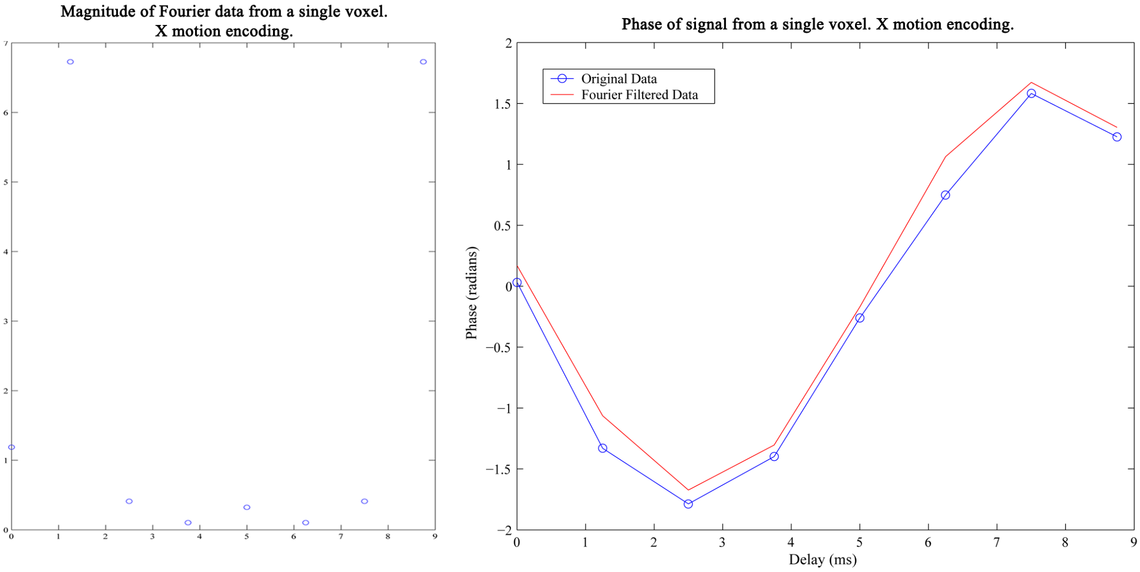

Figure 4.7: The original data is decomposed into a set of sinusoids through a Fourier transform; the magnitude of each frequency is shown for a particular voxel of the brain phantom (left). The dominant frequency (100Hz) is selected (component 2) and this sinusoid is used as a fitting to the original data (right). The phase data shown here corresponds directly to the amplitude of motion of the sample through equation (3.17). The magnitude and phase of this sinusoid, and for those of the other motion encoding directions, are stored in the final dataset for each voxel in the imaged volume.

This file, along with the reference set magnitude data, and information on the frequency of actuation, the voxel resolution and a matrix describing the rotation (see 4.2.7) required for elasticity processing is stored as a `.mat` file and delivered to engineers from the Centre of Bioengineering, University of Canterbury, for elasticity processing.

4.2.6 Ellipsoid of Motion for MRE Data

The MRE acquisition process described above generates the magnitude and phase of motion, at every point in space, along the x, y, and z directions. This describes the complete three-dimensional motion of points numbering in the hundreds of thousands for a typical dataset.

The motion of any given point can be calculated from these datasets using:

$$\begin{aligned} x &= x_0\cos(\omega t + \phi_x) \\ y &= y_0\cos(\omega t + \phi_y) \\ z &= z_0\cos(\omega t + \phi_z) \end{aligned} \tag{4.4}$$

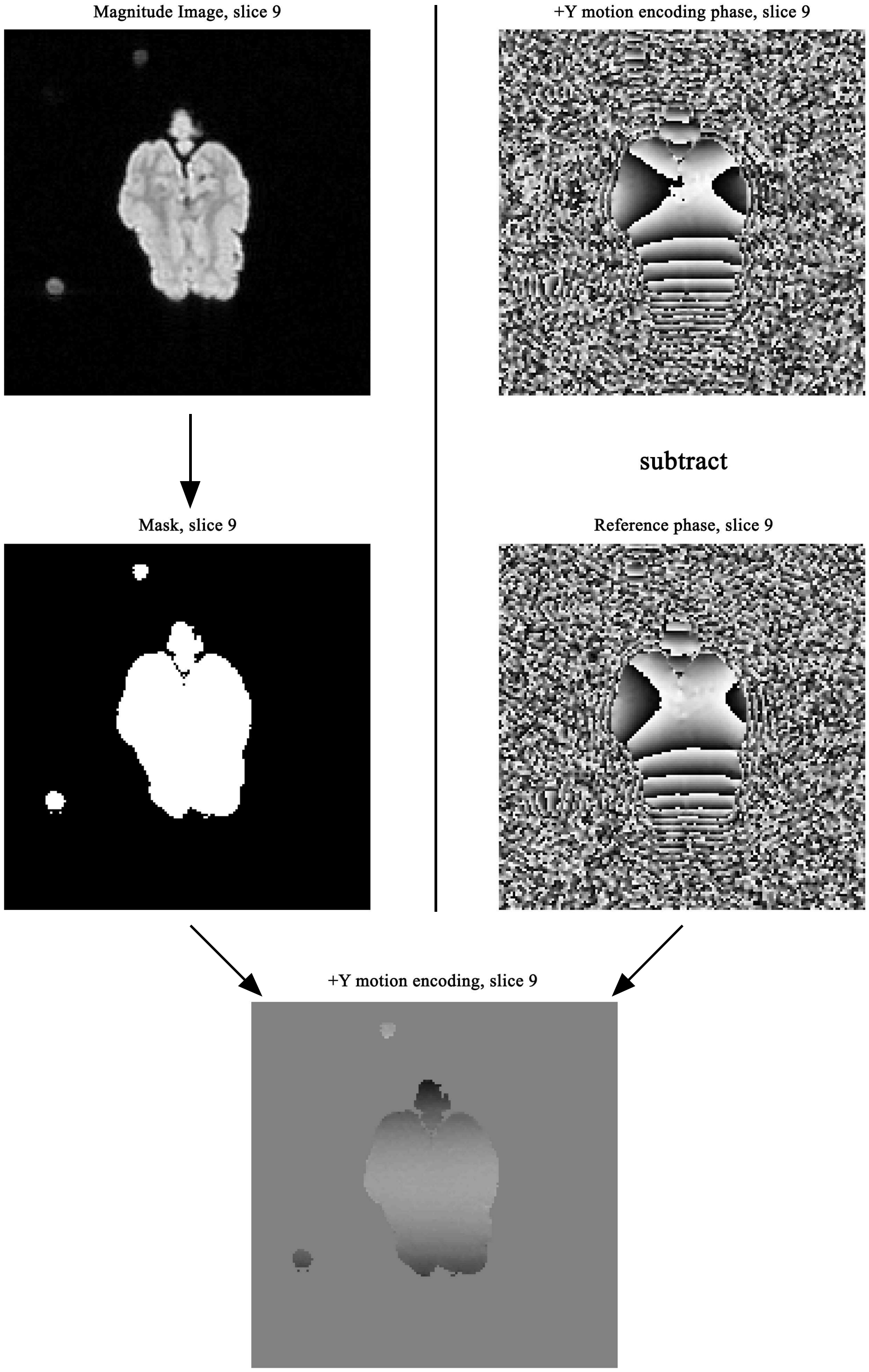

Figure 4.8: From the raw data imported into MATLAB, a magnitude image (top left) is generated. This is used to produce the mask to eliminate background noise. The reference set phase data (no motion encoding) is subtracted from phase data for motion encoding along a particular direction (top right). The mask is overlaid onto this subtracted image and the resulting figure reveals the phase due solely to motion encoding (bottom centre). These images are from the excised brain phantom. '+Y motion encoding' corresponds to motion encoding along the positive phase encoding axis (horizontal axis in these images).

where x_0, y_0 and z_0 are the amplitudes of motion along the respective axes; ϕ_x, ϕ_y and ϕ_z are the respective phases. The resultant motion is an ellipse in three dimensions. An example of one voxel has been generated in figure 4.9.

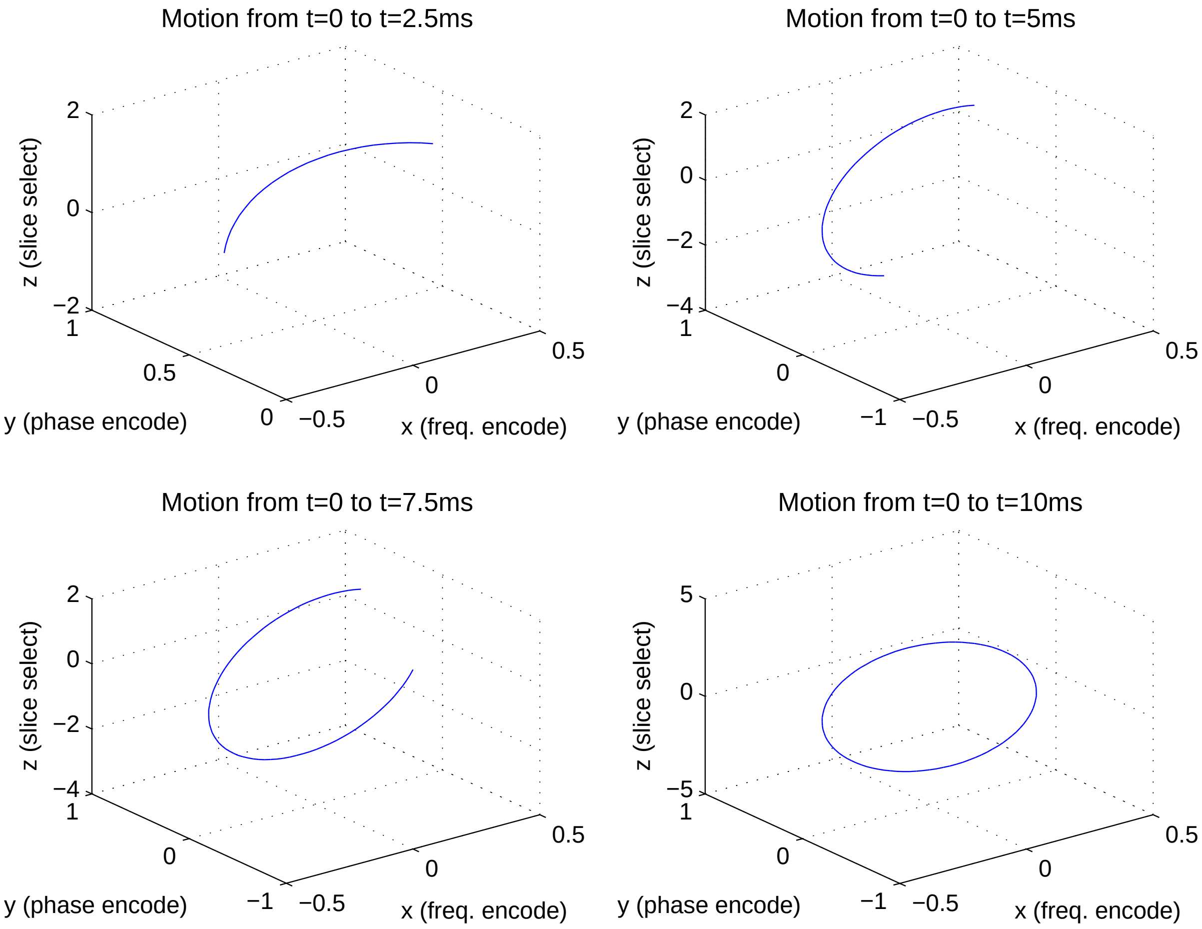

Figure 4.9: The three-dimensional motion of any voxel can be plotted from the completed MRE dataset. The resultant motion is in the form of a 3D ellipse. Here is the motion of one voxel from the silicone wedge phantom shown at four different time points along the cycle.

4.2.7 Coordinate Systems

One seemingly minor issue which required a significant effort to overcome, was determining the orientation of the processed datasets in relation to the physical orientation of the phantom. Unfortunately, there is no absolute coordinate system common to the MR scanner and the processed data. The MR scanner alone has: a *physical gradient* coordinate system, defined from the iso-centre of the magnet, with $\hat{\boldsymbol{z}}$ along the bore of the scanner; a *logical gradient* coordinate system, which defines $\hat{\boldsymbol{x}}$ as the frequency encode direction, $\hat{\boldsymbol{y}}$ as the phase encode direction, and $\hat{\boldsymbol{z}}$ as the slice select direction, no matter which direction a slice is oriented; finally there is the *anatomical location* based on the radiological view of a patient.

Data stored in our acquisitions were aligned along the logical gradient coordinates, thus there was a often a conflict with the orientation of data imported into processing software, and the physical coordinates of a phantom. In addition to this, importation into MATLAB, and Fourier processing within MATLAB have the potential to reorient certain directions.

The elasticity reconstruction requires data in a particular orientation. An incorrect orientation will not converge to a solution. Thus a rotation matrix is required to transform the processed data to the correct coordinate system for reconstruction.

Initially, the simplest solution was a trial and error approach of applying rotation matrices to data until one produced a meaningful elasticity reconstruction. As long as data is acquired with the same method, this matrix will not need to change.

The innovation of the directional markers means we can now determine unambiguously the three orthogonal directions, no matter what orientations the data processing involves.

As mentioned earlier, discussion on the motion of the sample will keep $\hat{\boldsymbol{x}}$ as the frequency encode direction, $\hat{\boldsymbol{y}}$ as the phase encode direction, and $\hat{\boldsymbol{z}}$ as the slice select direction, thus keeping with the logical gradient coordinate system.

4.3 Elasticity Reconstruction

The specifics of elasticity reconstruction are beyond the scope of this thesis, however a brief overview of the process is included here.

The saved dataset containing real-valued magnitude and phase information of the 3D motion at each voxel in space is delivered for elasticity processing. The motion at each point in space and time is given by:

$$\boldsymbol{u}(\boldsymbol{x}, t) = M(\boldsymbol{x}) \cos(\omega t + P(\boldsymbol{x})) \tag{4.5}$$

where $\boldsymbol{u}$ is the motion, M and P are the stored magnitude and phase at each voxel, and ω is the actuation frequency.

These data are converted to a *complex magnitude* of real and imaginary components:

$$\bar{\boldsymbol{u}}_r(\boldsymbol{x}) = M(\boldsymbol{x}) \cos(P(\boldsymbol{x})) \tag{4.6}$$

$$\bar{\boldsymbol{u}}_i(\boldsymbol{x}) = M(\boldsymbol{x}) \sin(P(\boldsymbol{x})) \tag{4.7}$$

before being placed onto a finite element mesh (figure 4.10). Each voxel is represented by a node and the entire volume is broken into several subzones, of a given geometry, for parallel processing. Several thousand nodes make up a subzone.

An educated, initial 'guess' is required for values of shear modulus, density, and bulk modulus. The iterative process refines these initial values into more accurate values with each progression, thus leading to a distinct stiffness value at each node. Boundaries are applied to these parameters to prevent them from attaining unreasonable values.

The number of zones per edge of the imaged sample needs to be defined, as well as the subzone overlap, to ensure that different subzones do not share a boundary.

The maximum number of iterations to be used is set and finally, the optimisation process is specified. In all reconstructions of data from this project, a conjugate gradient method was used.

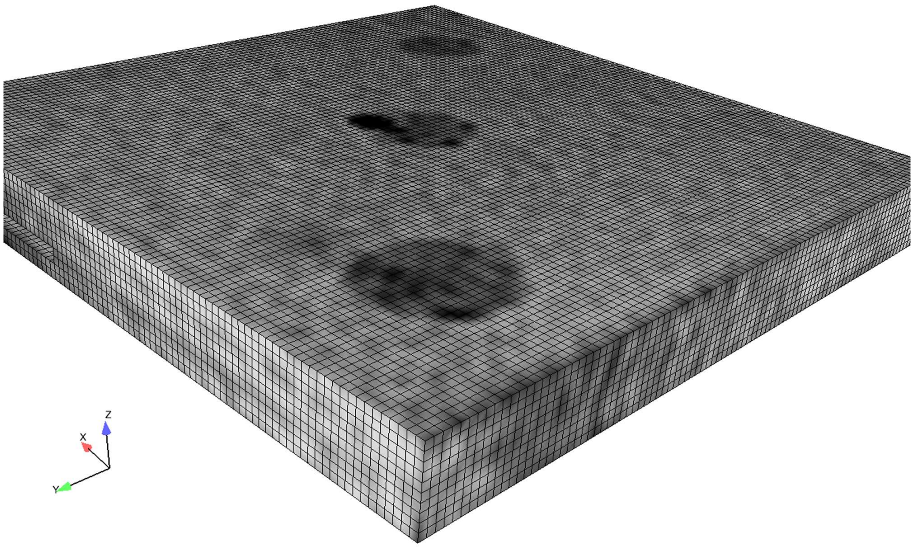

Figure 4.10: Detail of the finite element mesh is shown for the silicone inclusions phantom. The magnitude of the phantom is shown; a cylinder can be seen in the nearest corner. The mesh imposed on the data is shown by the black gridlines. The orientation of the phantom is indicated by the axes.

4.3.1 External Measurement of Shear Modulus

Externally-verified values of the shear modulus of different phantoms would be useful data to help ensure accuracy in reconstruction. Dynamic Mechanical Analysis (DMA) offers the ability to test silicone and, potentially, biological samples to determine a range of mechanical properties. DMA has been shown to be a useful comparison to MRE results [72]. The procedure, however, is not trivial. Sample preparation is important, requiring samples less than 10mm square and of about 2mm thickness; the sides must also be completely perpendicular to ensure the most accurate readings. There are also a range of calibration tests that would need to be undertaken before determining values for the shear modulus.

Chapter 5

Silicone Phantoms

5.1 Magnetic Relaxation Properties

Initial scans of silicone samples (figure 5.1) revealed that silicone did indeed produce a measurable signal, thus confirming it as a suitable material for MR imaging.

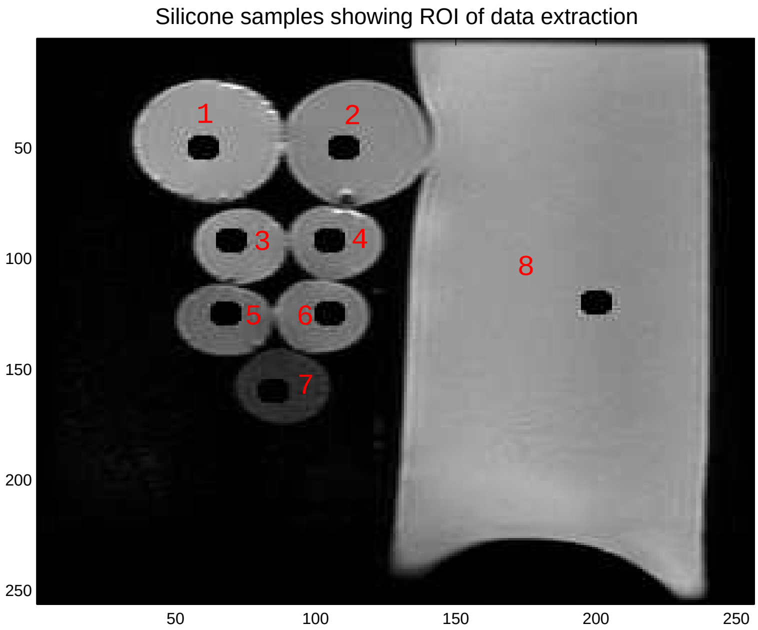

Figure 5.1: Silicone samples during a multiple spin echo scan. The bag of saline solution used as a reference is on the right. One set of regions of interest is shown here, from which T_1 and T_2 values were calculated.

T_1 and T_2 values of the seven samples were determined for three regions of interest (ROI) using the methods outlined in 3.3 (see also figures 5.2 and 5.3). These values were then averaged over the different ROI (table 5.1).

Sample 1 was qualitatively the softest sample and this appears to correspond to higher T_1 and T_2 values; conversely, the hardest sample, number 7, resulted in shorter T_1 and T_2 times. The notably stiffer samples, numbers 5 and 7, producing less signal, resulted in greater errors.

To optimise SNR, we would require a T_1 less than the sequence TR in order to maximise

Sample	T_1 (ms)	T_2 (ms)
1	617 ± 31	196 ± 8
2	612 ± 35	174 ± 6
3	611 ± 26	162 ± 7
4	611 ± 30	157 ± 9
5	590 ± 50	166 ± 11
6	601 ± 28	161 ± 10
7	558 ± 80	157 ± 24
8	1028 ± 14	515 ± 9

Table 5.1: T_1 and T_2 values for initial silicone samples. Sample 8 corresponds to saline.

longitudinal recovery; a T_2 much greater than the TE of the sequence would ensure the T_2 dephasing process has not significantly reduced the signal before data acquisition.

Overall, there is little variation in T_1 between the seven samples; T_2 would appear to be slightly more affected. The average T_1 value is 600 ± 42ms, while the average T_2 value is 168 ± 28ms. With an echo time of 34ms used in the 3D GRE sequence with two sets of MEGs, a T_2 value of ~ 168ms would mean little T_2 decay occurs before data acquisition. The effective TR of this sequence is 100ms, governed by the triggering frequency. 600ms is a rather long T_1 for a non-fluid, around the same value as white matter [33, ch. 8.5]. This resulted in T_1-weighted images.

The saline solution produced long T_1 and T_2 times as expected for a fluid.

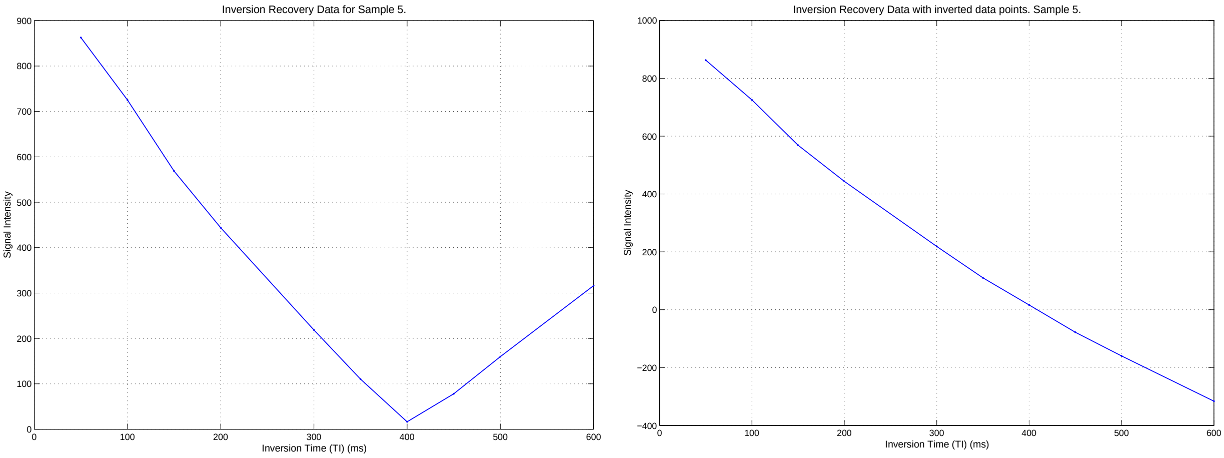

Figure 5.2: *Left:* Original inversion recovery data for silicone sample 5. The vertical axis is the *magnitude* of signal intensity. The 'bounce' in signal intensity at an inversion time of around 400ms can be observed. *Right:* The points following the 'bounce' were inverted in order to determine the inversion time at which zero signal occurs. From this point, the T_1 value can be calculated.

With a view to modelling breast tissue, both mechanically and in its magnetic relaxation properties, as mentioned above, the silicone samples did not resemble any particular biological tissue in terms of MR properties (see table 5.1). With a T_1 value of ~ 600ms, the closest tissues are perhaps white matter and liver [33, ch. 8.5] (data for measurements at 1.5T), both of which have T_2 values less than those calculated for silicone. A T_2 of ~ 168ms most closely resembles that of marrow or subcutaneous fat [73], which sounds promising, however fat has a T_1 value of less than half of 600ms. Silicone is perhaps more valuable

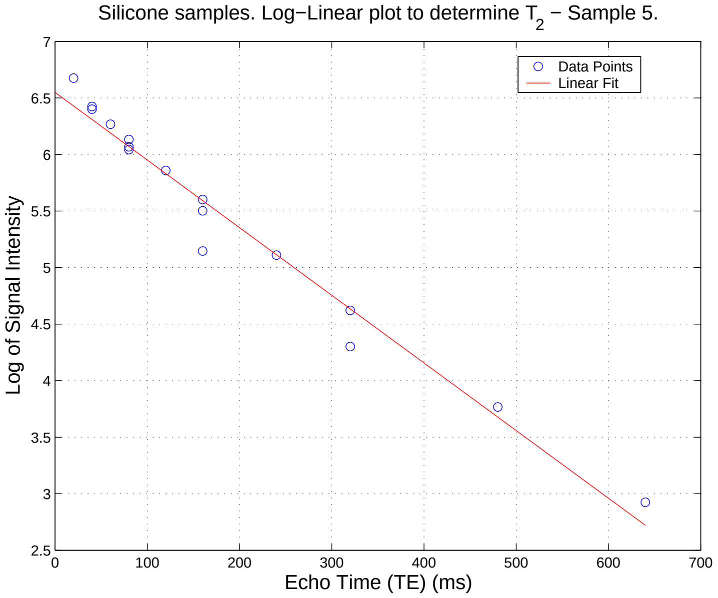

Figure 5.3: A log-linear plot of signal intensity data points against echo time and a linear interpolation for silicone sample 5. The gradient of the interpolation is used to calculate the T_2 value of the sample.

in its ability to closely mimic the *mechanical properties* of soft tissues, rather than its MR properties.

Tissue	T_1 (ms)	T_2 (ms)	Source
white matter	600	80	[34]
white matter	780	90	[37]
white matter	560	82	[33]
grey matter	950	100	[34]
grey matter	900	100	[37]
grey matter	1100	92	[33]
fatty tissue	250	60	[34]
fat	200	–	[33]
subcutaneous fat	288	165	[73]
CSF	4500	2200	[34]
muscle	870	45	[37]
muscle	1075	33	[33]
muscle	1130	35.3	[73]
liver	500	40	[37]
spleen	1025	–	[33]
cartilage	1060	42.1	[73]
marrow	288	165	[73]
synovial fluid	2850	1210	[73]

Table 5.2: T_1 and T_2 values of some tissues found in the literature. All values are reported for a 1.5T external field.

Contrast agents could potentially be added to the silicone during the phantom fabrication stage to modify the magnetic relaxation properties, if it were deemed necessary to have a phantom that mimicked both the magnetic and mechanical properties of a particular tissue type. However, matching both T_1 and T_2 can be difficult.

5.2 Wave Generation in Silicone Phantoms

The harmonic motion induced by the actuator results in a steady-state wave pattern in the imaged phantom. Due to the geometry of the phantom apparatus, the nature of these wave patterns can be rather complex, even with a simple box boundary.

Primary shear wave generation occurs at the side walls and floor of the container. Reflections of these waves, however, also lead to secondary shear wave generation from all sides. Reflections occur at the hard boundaries of a phantom enclosed by the Perspex box, but also at air-sample boundaries, for instance at the free surface of all gel-based phantoms. Internal reflections are also present, occurring, for example, at the interface between hard and soft silicone gel, or between gelatine and muscle tissue. Compressional waves (of a wavelength too long to be seen with MRE techniques) are also generated; the energy of such waves is turned into shear waves through mode conversion at solid boundaries.

Our technique images the displacement map at 8 to 10 time points throughout the actuation period. Through the Fourier fitting process detailed in 4.2.5, we can build up a three dimensional picture of the displacements within an imaged phantom at any given time.

The literature treating waves in an elastic medium, whether bounded or not, is exceedingly limited in relation to MRE. Most standard texts treat the mathematics of infinite or semi-infinite waves in elastic solids with application to earthquakes, structural beams, or crystals, for instance Chen [74], Graff [75], Main [76], and Pain [77]. There are also descriptions of two- and some three-dimensional cases of membranes, or thin plates. Very little is to be found on the nature of mechanical waves in tissue, or a tissue-resembling material. Although Fung [78] contains some discussion on the elastic properties of soft tissues.

In terms of very simple waves, we could expect to see either a standing or a travelling wave pattern.

5.2.1 Standing Wave Patterns

Standing waves would be found in a medium with low losses. Reflected waves from boundaries superimpose on the incoming wave to generate a wave with no energy transport through the medium. A simple standing wave pattern would be characterised by a node at the solid boundaries, and, assuming a progression to a simple 2D case, some form of chequerboard pattern, as can be seen in figure 5.4. This pattern would be dependent on the normal mode being excited. The phase of such a wave would be constant, as each region of the material is moving either in phase or in anti-phase with every other region [77, ch. 9].

A separation of variables approach means that in three dimensions, a simple standing

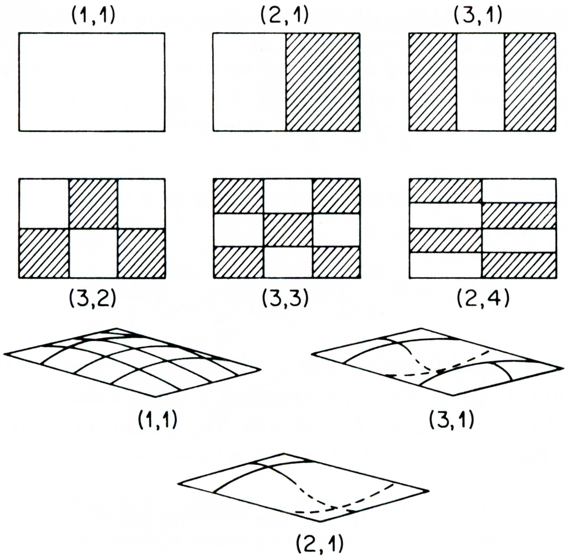

Figure 5.4: Standing wave patterns for different modes on a two-dimensional membrane. The top set of images gives a schematic representation where clear and shaded areas show opposite sinusoidal displacements. The lines indicate nodes where the surface does not move. The typical 'chequerboard' pattern can be seen. The lower images show a surface representation of the first three normal modes; the sinusoidal motion of the surface can be clearly seen. Source: [77].

wave can be written as a combination of waves along the three orthogonal axes [77, ch. 9]:

$$w = A\cos(k_x x)\cos(k_y y)\cos(k_z z)\cos(ckt) \tag{5.1}$$

where A is the amplitude, c is the wave velocity, and k_i are wave numbers such that $k^2 = k_x^2 + k_y^2 + k_z^2$.

Less simple standing waves could involve regions of maximum or minimum amplitude out of phase with one another, yet still resulting in no propagation of energy, and forming a repeating pattern over time. We could expect the phase of such a wave to be constant in the regions that move together, but perhaps varying between these regions. Another less conventional standing wave could be where the entire medium moves together sinusoidally, and within this motion, nodes and antinodes are observed.

5.2.2 Travelling Waves

The other possible type of wave observed within the phantom is a travelling wave. These waves would be expected to form in a lossy medium, with weak reflections from boundaries. Travelling waves do not form nodes at the solid boundaries, and as such, appear to move through the phantom as time progresses. Each region of the phantom will be out of phase with every other region within the span of a wavelength, as energy propagates through the medium. The phase of a travelling wave will thus be non-constant. An ideal travelling wave would have a linear change in phase over distance.

5.2.3 Simple Wave Analysis

A very simple wave analysis only requires that shear waves be generated within a medium and that the wavelength of these waves can be measured. Approximate values of the shear modulus of a sample can be determined by the wavelength of generated shear waves, providing the density of the material is known [49]. The velocity of a shear wave is given by:

$$c = \sqrt{\frac{\mu}{\rho}} \tag{5.2}$$

where μ is the shear modulus of the medium, and ρ is the density.

The velocity is, of course, the product of the wavelength (λ) and the known (linear) frequency of the shear waves (ν): $c = \nu\lambda$. Thus equation (5.2) can be rearranged to find the shear modulus:

$$\mu = \rho\nu^2\lambda^2 \tag{5.3}$$

5.3 Homogeneous Phantom

The homogeneous silicone phantom was intended to provide a reference study for the subsequent use of silicone in more complex phantoms. The nature of steady-state wave patterns set up within the phantom is discussed in this section.

Figure 5.5 shows a magnitude image of one slice through the phantom. The direction of actuation for this phantom was along the vertical axis of this image. What is referred to a x motion encoding in this discussion is also along this direction ('superior-inferior', or SI). y motion encoding is along the horizontal axis ('right-left', or RL), and z motion encoding is in the through-plane direction ('anterior-posterior', or AP). Thus, a figure that details x motion encoding, for example, shows the displacement map for motion in the superior-inferior direction of the phantom.

To investigate the motion of the phantom, line profiles were taken through the hard and soft silicone samples for different time points, for all three directions of motion encoding. Figure 5.6 shows displacement maps of the motion along $\hat{\boldsymbol{x}}$ at four time points throughout the actuation cycle. The results of line profiles are also displayed in this figure. Profiles are taken superior-inferior through each silicone sample and across the overall phantom (right-left). Figures 5.7 and 5.7 show the results of displacement maps and line profiles for motion encoding along $\hat{\boldsymbol{y}}$ and $\hat{\boldsymbol{z}}$ respectively.

To better visualise the behaviour of a line profile throughout the entire motion cycle, the results of line profiles taken at 20 time points throughout the actuation period were superimposed in a single plot. Results for AP profiles of both the hard and soft silicone for x and z motion encoding are presented in figure 5.9.

The phase of the motion along all three motion encoding directions was also investigated to determine the nature of the wave patterns generated in the phantoms. The results of phase maps and corresponding line profiles are presented in figure 5.10

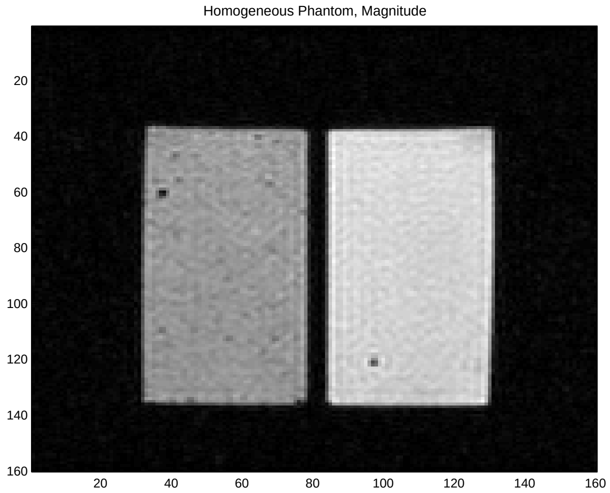

Figure 5.5: Magnitude image of homogeneous silicone phantom. The stiffer silicone is on the left of this image; the softer silicone is on the right. The direction of actuation is along the vertical axis of this image. This is the same direction as x motion encoding. y motion encoding is along the horizontal axis, and z motion encoding is through-plane.

The 3D wave mechanics of the situation are best visualised in figures 5.11 and 5.12. These figures show a reconstruction of the full 3D displacement data at each voxel and present it as a complex transient response. The amplitudes of the motion have been artificially enhanced to show the wave motion. The data is presented as a time series, with each figure showing several snapshots in time throughout the 10ms motion period. Essentially, these figures plot the ellipsoid of motion as seen in 4.2.6 for every voxel throughout the 3D volume. Superimposed on this wave function is the amplitude of motion along $\hat{\boldsymbol{x}}$ (figure 5.11) and $\hat{\boldsymbol{z}}$ (figure 5.12). The colourbars on each figure indicate the amplitude of motion along these particular directions; red indicates motion in the positive direction, blue is motion in the negative direction. The colouring can be used in conjunction with the wave pattern to better visualise the nature of the generated shear wave pattern. Motion along $\hat{\boldsymbol{y}}$ has not been presented as very little motion was seen in this direction.

In the case of the stiffer sample, the most motion was observed along the direction of actuation ($\hat{\boldsymbol{x}}$), which exhibited an amplitude of $\sim 40\mu$m, followed by the through-plane direction ($\hat{\boldsymbol{z}}$), which had an amplitude of $\sim 20\mu$m. The softer silicone had comparable motion amplitudes along both $\hat{\boldsymbol{x}}$ and $\hat{\boldsymbol{z}}$, of about 15μm. Refer to figures 5.6 and 5.8 for these data. Recall the amplitude of motion input through the actuator is about 20μm. As could be expected, both samples showed very little lateral motion (along $\hat{\boldsymbol{y}}$) (figure 5.7). Motion in this direction is only a couple of microns.

Looking at the motion across one vertical line profile at 20 time points throughout the period, a notable difference can be observed between the soft and hard phantoms (figure 5.9). For the hard phantom, encoding along both $\hat{\boldsymbol{x}}$ and $\hat{\boldsymbol{z}}$ show what is very close to a standing wave pattern (allowing for node motion due to movement of the walls of the container). The soft silicone, however, has a much more complicated wave pattern, more indicative of a travelling wave in both directions, although along $\hat{\boldsymbol{x}}$, the motion could be seen to be a more complicated standing wave pattern as discussed in 5.2.1. There is also a distinct node for motion along $\hat{\boldsymbol{z}}$ which one would not expect to find in a pure standing

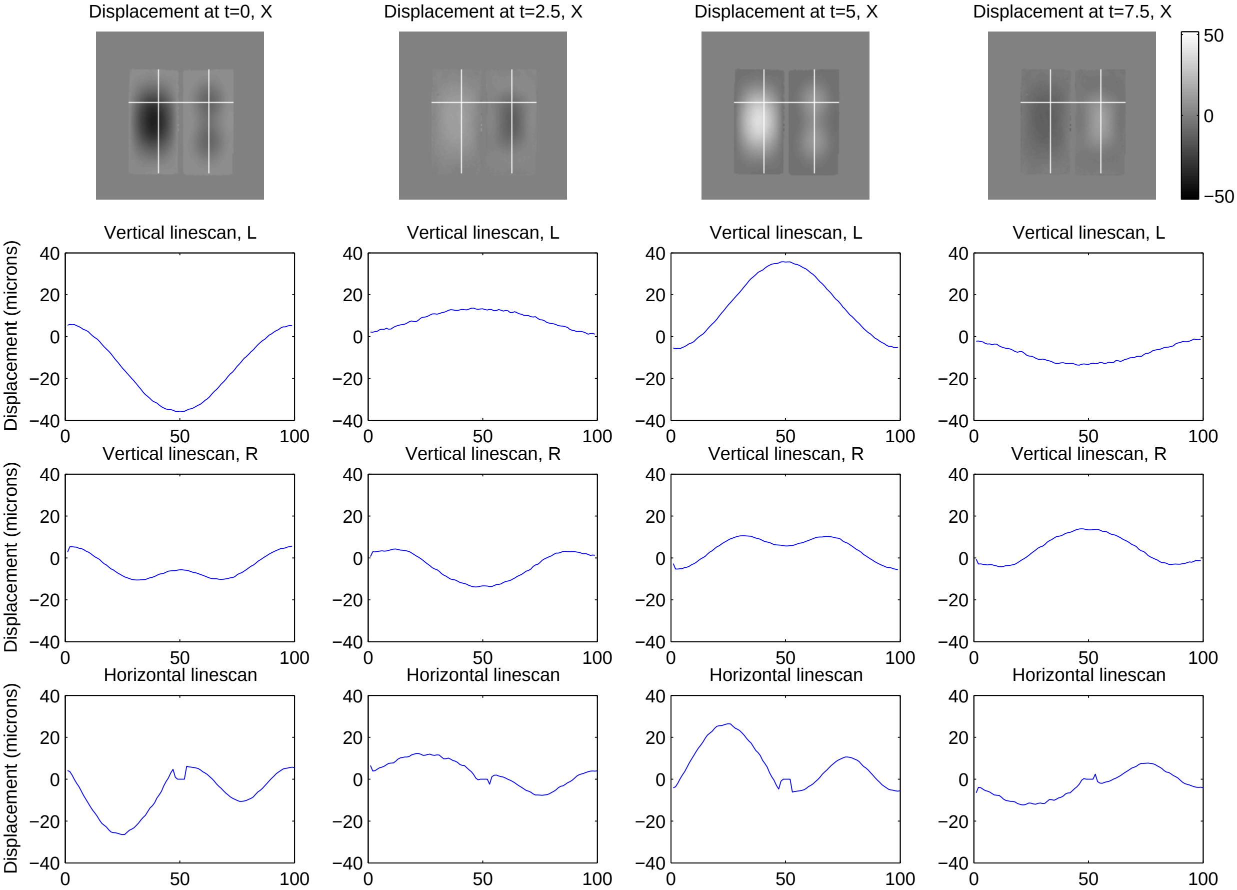

Figure 5.6: Displacement map and line profiles for x motion encoding. The top set of images shows the displacement of the phantom at four evenly-spaced time points throughout the 10ms period. The results of line profiles through the phantom are shown. ‘L’ stands for a line scan through the left-hand phantom; ‘R’ through the right. A ‘vertical’ line profile is taken vertically through the plane of the image. A regular wave pattern is seen for both silicone samples, although the two are not in phase. The maximum amplitude of motion is almost 40μm for the stiffer gel, while only just over 15μm for the softer gel. The horizontal profiles cross the Perspex boundary between the two samples, thus there is a small region of zero motion present in the middle of these profiles.

wave pattern.

The fact that the stiffer silicone has a peak amplitude greater than that of the input suggests some form of resonance phenomenon observed for this silicone at 100Hz. Investigating the phase of the motion along the same 1D profiles, we observe that phase is constant in the centre of the hard silicone phantom for $\hat{\boldsymbol{x}}$ motion encoding (figure 5.10). As discussed in 5.2.1, this is indicative of a standing wave, and indeed, nodes can be observed at the boundaries of the phantom container.

The situation is less simple for the softer phantom, where phase is non-constant. These variations in phase indicate some form of travelling wave, although for $\hat{\boldsymbol{x}}$ motion encoding the phase appears to be changing slowly through the centre of the phantom. Thus, perhaps we are observing some form of wave in between the two extremes of a travelling and standing wave. The wave motion of the gel can be best visualised in figures 5.11 and 5.12.

As there is very little motion along $\hat{\boldsymbol{y}}$, there is correspondingly very little change in phase in this direction.

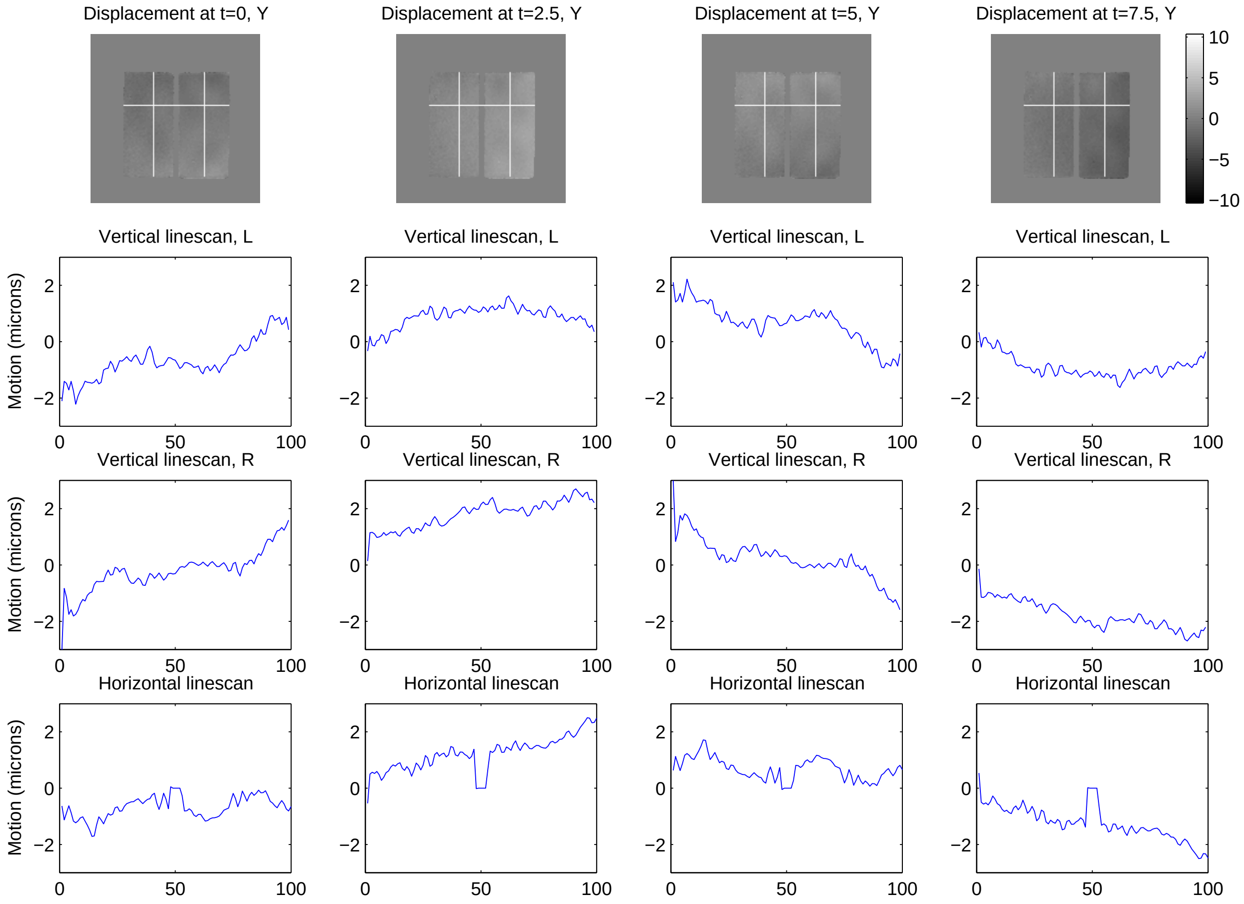

Figure 5.7: Displacement map and line profiles for y motion encoding. The same locations of line profiles as in figure 5.6 are used. Little motion is seen along this direction, in comparison to motion along $\hat{\boldsymbol{x}}$ and $\hat{\boldsymbol{z}}$. The variations seen in these figures are due to noise.

The phantom box contains an incompressible, bounded material. This means that as the gel moves along $\hat{\boldsymbol{x}}$ due to actuation, one side of it also moves up, as this is the only unbounded surface. To counteract the upward motion, another part of the gel must move down. This motion is plainly seen in figure 5.12. The effects of laminar flow are apparent in this diagram, as the gel at the sides of the container is not moving relative to the wall, whereas the centre of the phantom is moving significantly. A typical flow profile is visible, especially in the soft phantom (note, for instance $t = 2T/10$).

The x direction resonance of the stiff phantom is also visible in figure 5.11 where it can be seen that the majority of the gel phantom is moving together as a whole, indicated by the regions of blue or red.

Referring to figure 5.8, a clear wavelength can be determined from these line profiles. The stiffer silicone has a wavelength equal to the length of the box: 10cm. The softer silicone has a wavelength of half the length of the box. It is acknowledged that the geometry of the box has an effect of the wavelength. Assuming a density of silicone of 1000kgm^{-3} and using equation (5.3), we obtain shear modulus values of 100kPa for the hard silicone, and 25kPa for the soft silicone. These results are comparable to values determined by a minimum error estimation method used on surface motion data of phantoms made to the same concentrations, as found by Peters [79], [80].

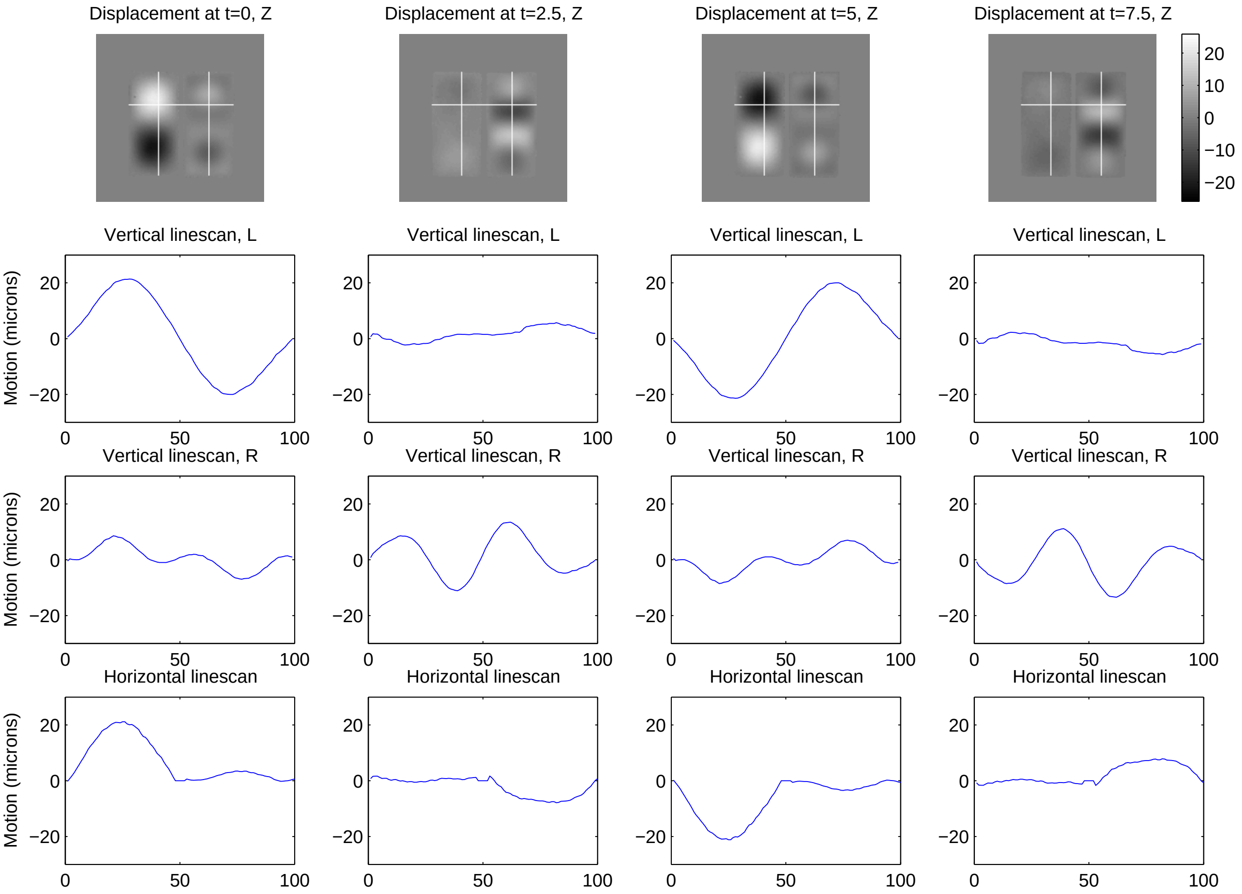

Figure 5.8: Displacement map and line profiles for z motion encoding. The same locations of line profiles as in the previous two figures are used. A regular motion pattern is seen in these images. The nodes are apparent at the boundaries with little relative motion occurring there. The vertical line scans suggest the stiffer phantom has a wavelength equal to the length of the box (10cm), while the softer sample has an additional node in the centre, thus giving a wavelength of 5cm.

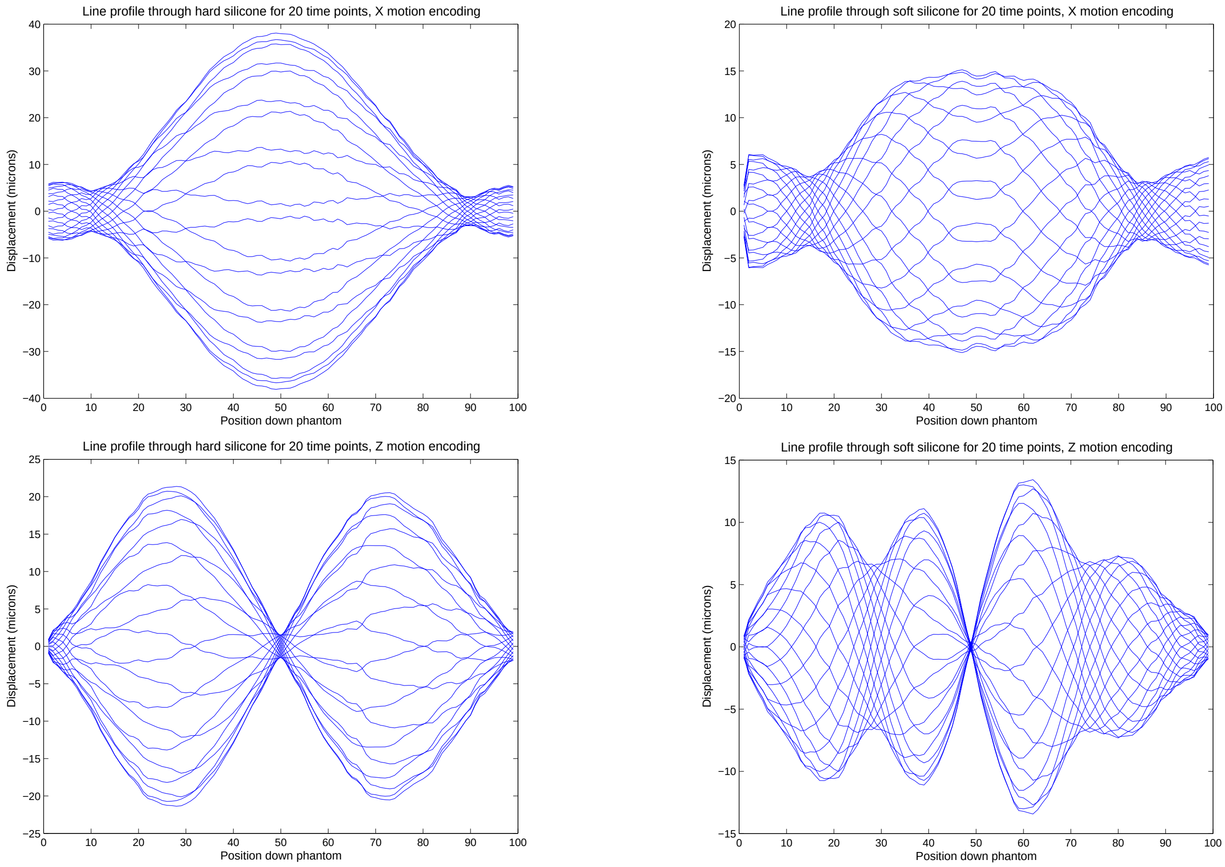

Figure 5.9: The line profiles are taken over 20 equally spaced time points throughout the actuation period for motion encoding along $\hat{\boldsymbol{x}}$ (top) and $\hat{\boldsymbol{z}}$ (bottom). The location of the profiles is the same as indicated on earlier figures. The profiles through the hard silicone (left-hand images) show a very regular standing wave pattern. The soft silicone (right-hand images) have a notably different pattern. This is indicative of a more complicated wave pattern, perhaps some combination of travelling and standing waves. Note also, the amplitude of motion is a lot less for the soft silicone, again suggesting some form of resonance might be occurring in the hard silicone that is not in the soft.

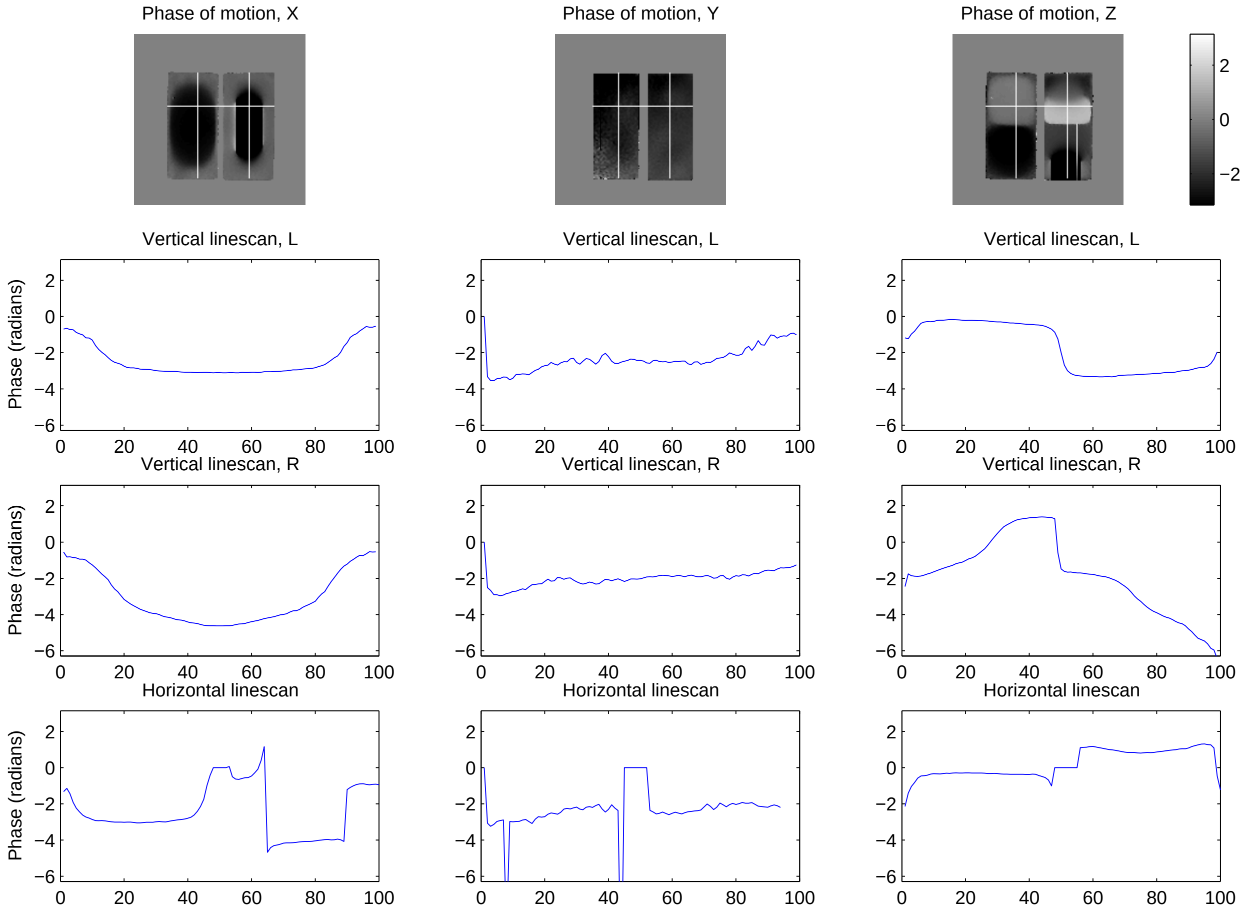

Figure 5.10: The phase in the left-hand phantom (hard silicone) does not change much within the centre of the phantom for motion encoding along either $\hat{\boldsymbol{x}}$ or $\hat{\boldsymbol{z}}$. The phase in the right-hand phantom (soft silicone) is varying, perhaps as a sinusoid, although it is a little difficult to tell from phase wrapping artifacts in the line scan for motion in the z direction. A non-zero gradient would suggest an additional factor to the standing wave pattern. There is very little phase change along $\hat{\boldsymbol{y}}$; this is to be expected as little motion occurred in this direction.

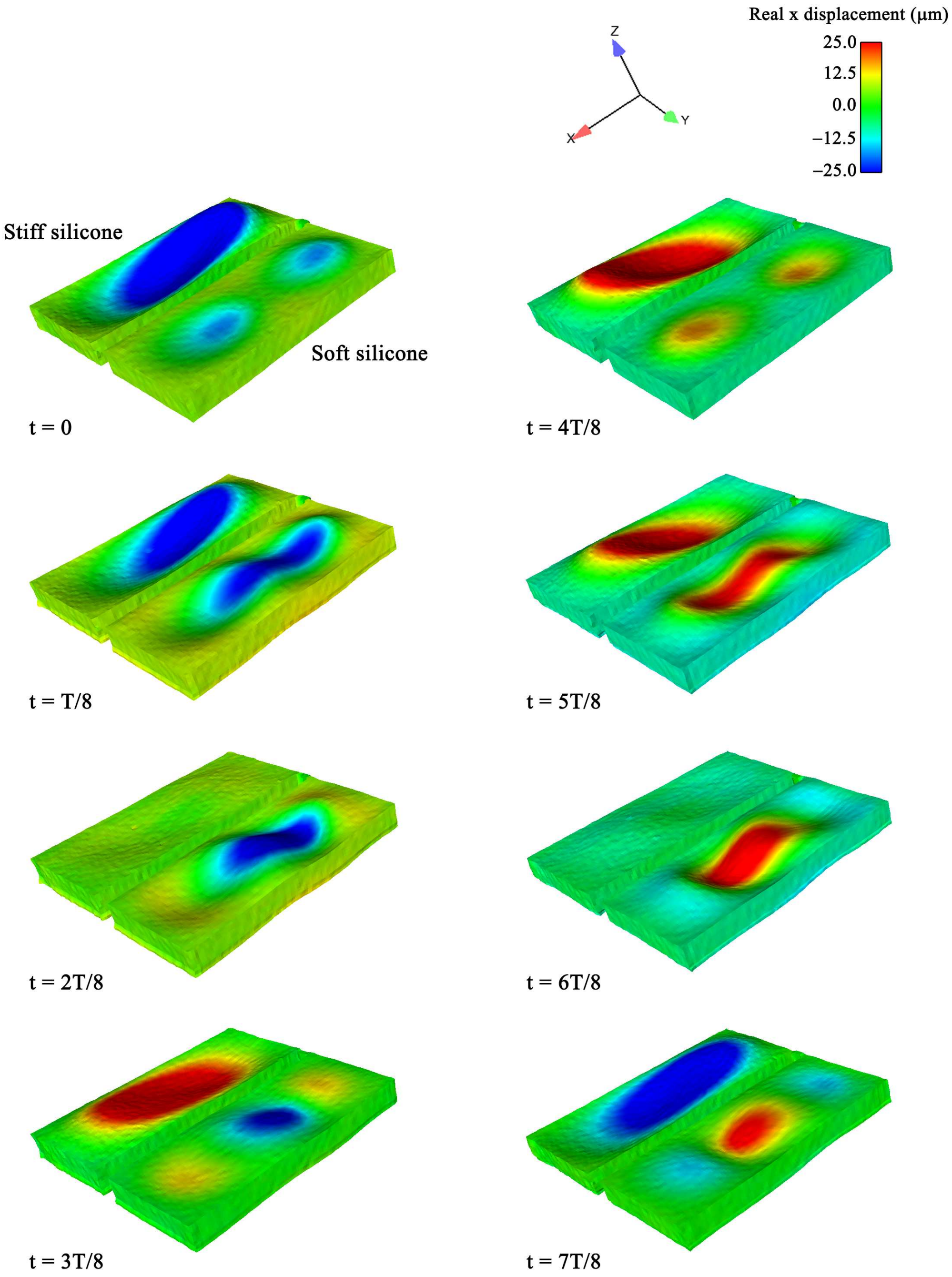

Figure 5.11: The 3D complex transient response of the motion throughout the entire imaged volume is shown. This is a plot of the motion of each voxel in three dimensions and allows for visualisation of the wave behaviour in the phantom. The amplitude of the motion has been enhanced to allow micron-sized motions to be visible. The colouring imposed on the wave pattern is that of the motion along the x direction. Red indicates where the silicone is moving in the positive x direction; blue indicates negative x motion. The standing wave pattern in the stiff silicone can be seen clearly as the majority of the phantom is moving in phase back and forth. The soft silicone has a more complicated wave pattern in this direction.

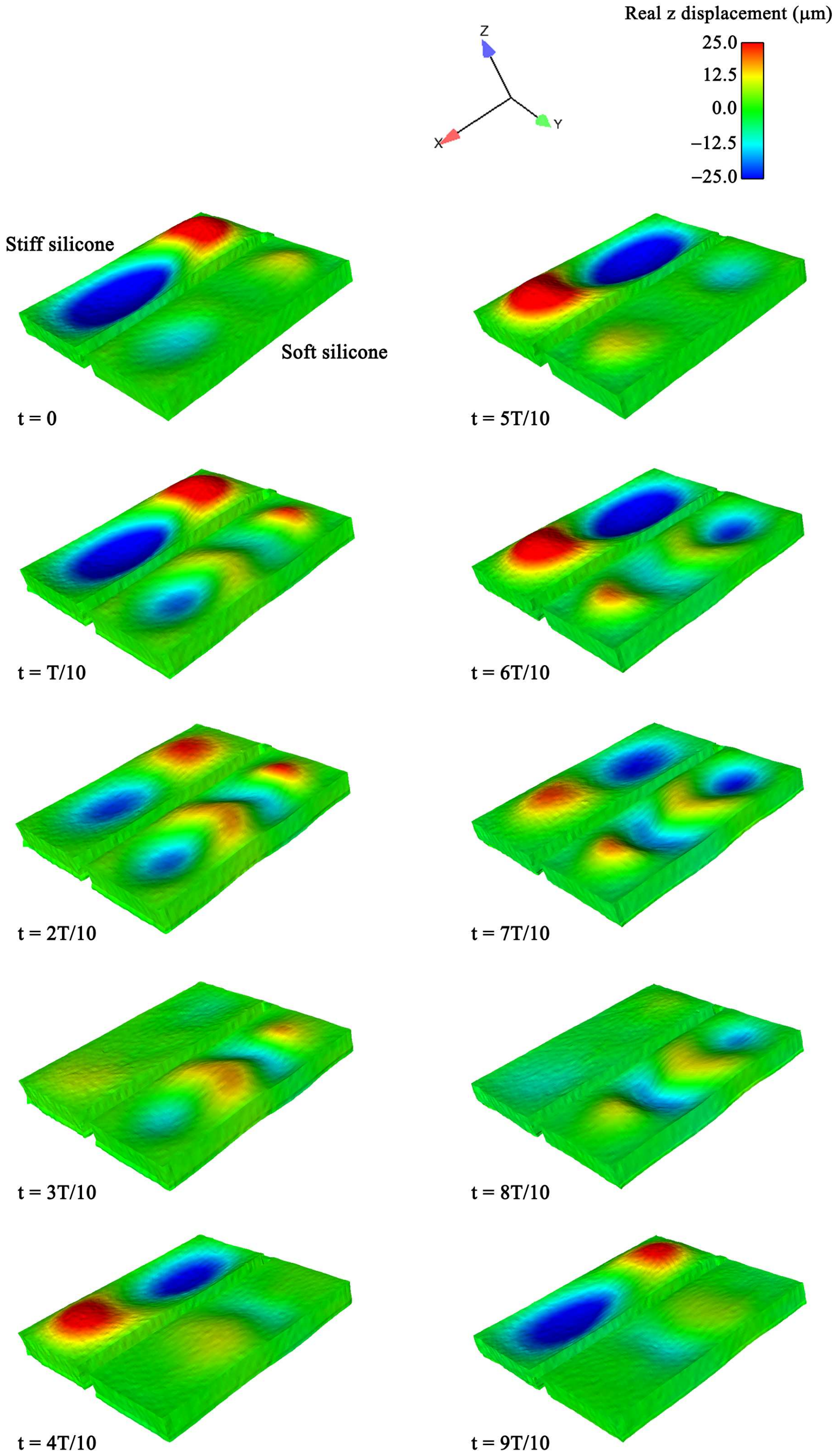

Figure 5.12: As in figure 5.11, the 3D complex transient response of the motion throughout the entire imaged volume is shown. However, the colouring on this figure indicates the motion along the z direction. This colouring allows for visualisation of the flow profile apparent in the soft silicone in particular. Some form of standing wave is visible in the stiff phantom for motion in this direction as well as along $\hat{\boldsymbol{x}}$.

5.4 Inclusions Phantom

In many ways the inclusions phantom behaved similarly to the homogeneous phantom. The most motion was generated along the direction of actuation ($\sim \pm 40\mu$m) and in the through-plane direction ($\sim \pm 50\mu$m). Lateral motion was small ($\sim \pm 10\mu$m), which was to be expected. Appendix B contains figures detailing the three-dimensional wave motion of the phantom.

5.4.1 Inclusions Reconstruction Results

Some elasticity reconstructions were attempted on these data. The best of these results are presented in figure 5.13. The bottom left image used an initial guess of 30kPa for the shear modulus; the bottom right image used an initial guess of 7kPa.

Poor reconstruction arose from the phantom with the cylindrical inclusions. This is not thought to be due to air bubbles trapped within the phantom (recall 3.4.1) but another issue entirely (see 5.6). The images in figure 5.13 show the outlines of the cylinders, but they are difficult to differentiate from the base material. The high level of artifact is indicative of a solution not reaching convergence, yet further iterations yielded no more satisfactory results.

5.4.2 Simulation Tests

Observation of MR displacement field images at some time points shows a very regular steady-state wave pattern (figure 5.14). Previous experience from the work of colleagues with similar phantoms has shown that the presence of a stiffer inclusion should disrupt significantly the regular wave pattern expected in a homogeneous sample [49]. Appendix B has a more complete set of images detailing the full three-dimensional displacement pattern of this phantom at regular time intervals.

It was postulated that the solid boundary conditions imposed on five sides of the gel by the phantom container could impose an undesired regularity on the wave pattern, hence overwhelming any perturbations caused by the inclusions. A more realistic scenario, better modelling a breast with a tumour, might be a similar phantom without the box, being actuated from only one direction. This approach was trialled with the wedge phantom (see 5.5).

To test this hypothesis, simulations were run, whereby a virtual phantom was constructed of the same dimensions as the real phantom and tested under different boundary conditions. Firstly, a homogeneous medium was simulated with rigid boundary conditions on five surfaces, as in the case of the real phantom. Actuation was set to generate shear waves from one side, with the top surface of the simulation free. This was compared to a simulation with the same boundary conditions but a stiff inclusion placed within the soft base medium. The inclusion was placed slightly away from the centre of the phantom. The difference in the wave pattern between the homogeneous case and the inclusion case was

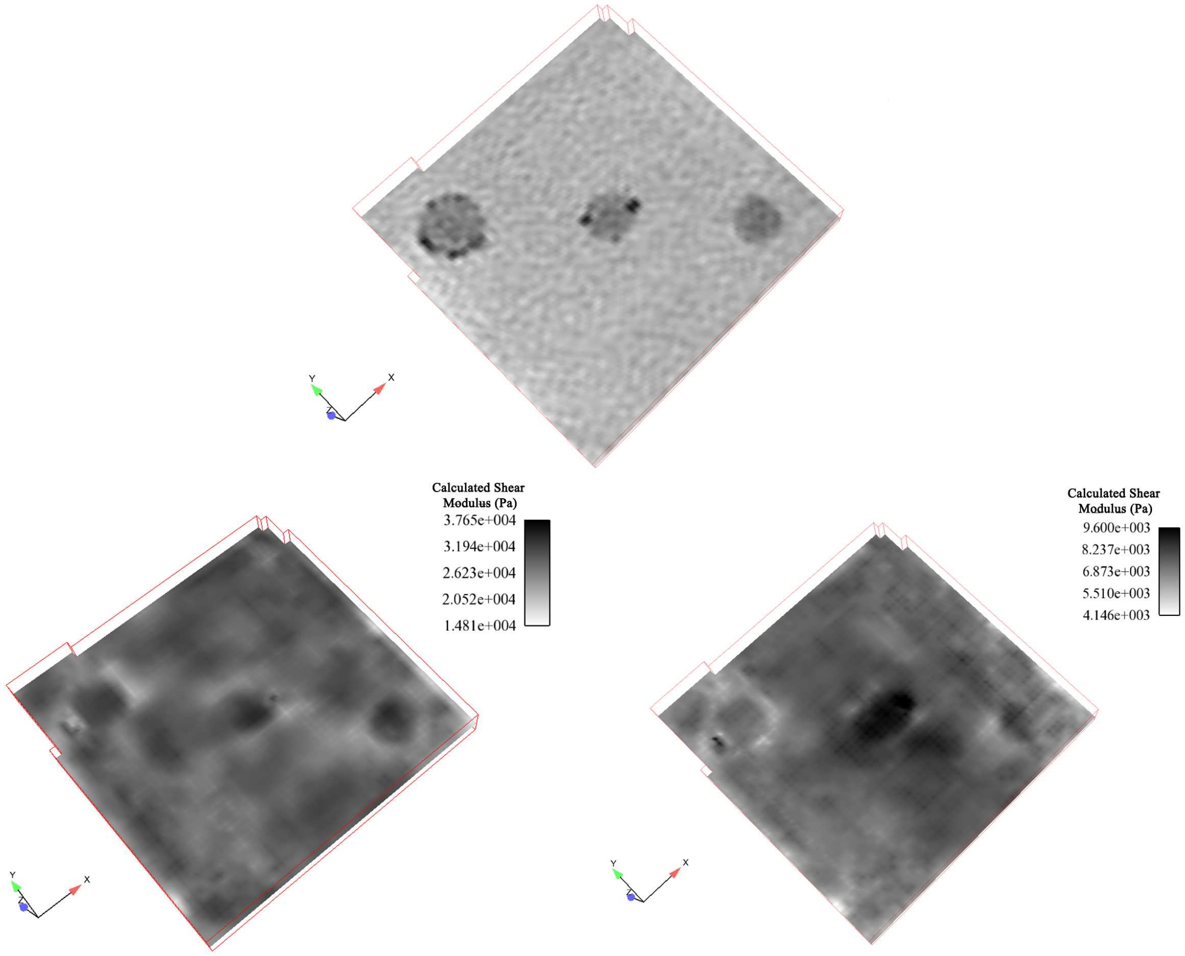

Figure 5.13: The top image shows an MR magnitude image of the phantom. The three cylindrical inclusions are clearly visible. The bottom two images are slices from reconstruction results. The bottom left image used 30kPa as an initial guess for the shear modulus; the bottom right image used 7kPa. The three cylinders are outlined in each case, although neither result is particularly convincing against the high level of artifact, and the lack of distinction between stiffness values of the cylinders and the base material. The centre cylinder in the right-hand image is more visible, although this may be due to noise from air bubbles trapped within the phantom. It must be noted that neither attempt converged to a full solution, which typically takes about 100 iterations. The left-hand image was arrived at after 27 iterations. The right-hand image, only 10. Further iterations did not improve the results. The greyscale-bars indicate the reconstructed shear modulus values.

calculated through a mean squared error method:

$$\% \, error = \frac{(u_h - u_i)^\dagger (u_h - u_i)^\dagger}{(u_h^\dagger u_i)^2} \times 100 \tag{5.4}$$

where u_h is the motion data from the homogeneous simulation, u_i is the motion data from the inclusion simulation, and † represents the conjugate transpose.

This set of tests was repeated for boundary conditions of only one rigid boundary: the bottom of the box. This simulation was to test whether free boundary conditions on the four walls of the phantom would produce a significantly greater perturbation of the displacement field due to the inclusion. These results are presented in figure 5.15.

The difference in motion patterns between the homogeneous and the inclusion simulations for rigid boundaries on five sides was 22.5%. For the free boundary conditions on

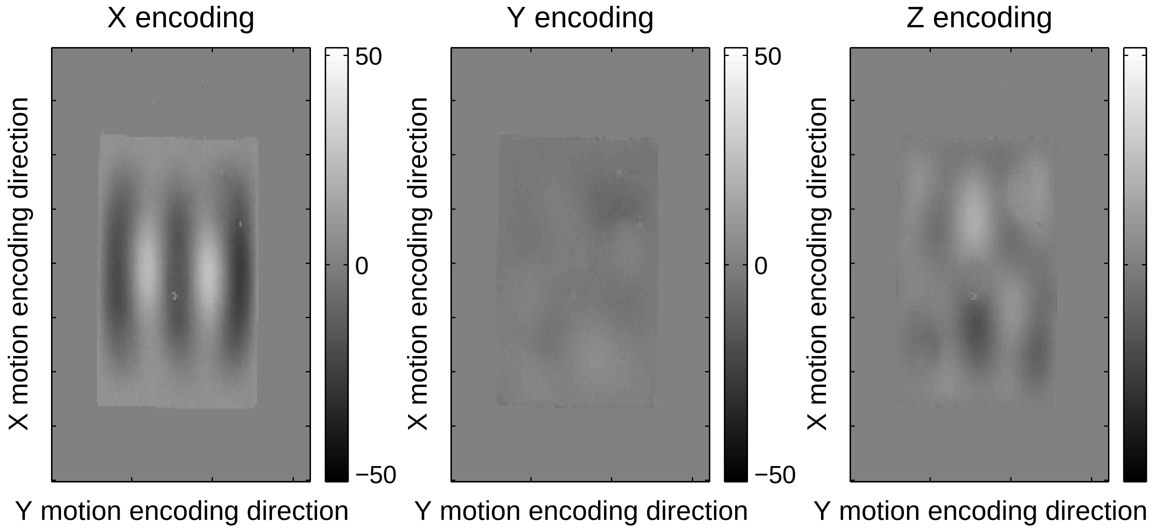

Figure 5.14: A regular wave pattern can be seen in displacement maps of the MR data for the inclusions phantom. Motion encoding along $\hat{\boldsymbol{x}}$ (direction of actuation) is particularly regular in this image. Motion data for $\hat{\boldsymbol{z}}$ shows an approximate 'chequerboard' pattern. There is a lot less motion along $\hat{\boldsymbol{y}}$ and, consequently, a less regular pattern is observed. The direction of actuation was along the vertical axis in these images. This is the same direction as x motion encoding. y motion encoding is thus along the horizontal axis, and z motion encoding is through-plane. The colourbars indicate the magnitude of motion along the particular motion encoding direction. It should be noted that this regularity of pattern was not seen at all time points throughout the actuation cycle.

the walls, the difference was 67.2%. We would expect to see a greater disturbance in the regular wave pattern due to an inclusion with only one hard boundary, on the bottom of the phantom. However the difference between 22.5% and 67.2% is not so significant that it should explain fully the lack of suitable reconstructions. A change in the motion pattern of 22.5% should still be sufficient perturbation to generate suitable reconstructions. It is still unknown as to why successful reconstructions of the elasticity of the phantoms have proved to be so elusive. This is discussed further in 5.6.

5.4.3 Wave Pattern Investigation

An alternative method of examining the data was used. Several line profiles through the phantom were analysed to see if the inclusions could be detected in this manner. The wave pattern for profiles through the base material and the inclusions at 20 different time points throughout the actuation period were compared. The location of the profiles is shown in figure 5.16 and the results of the profiles are presented in 5.17.

The two profiles that pass through the base silicone are comparable in form (figure 5.17, top images). The wave pattern through an inclusion, however, shows some deviation from this pattern, specifically at the location of the inclusions (figure 5.17, bottom images). We would not expect to see a change in wavelength within the inclusions as the size of an inclusion is much smaller than a wavelength. Nevertheless, these figures illustrate that there is some noticeable perturbation to the wave pattern due to the inclusions.

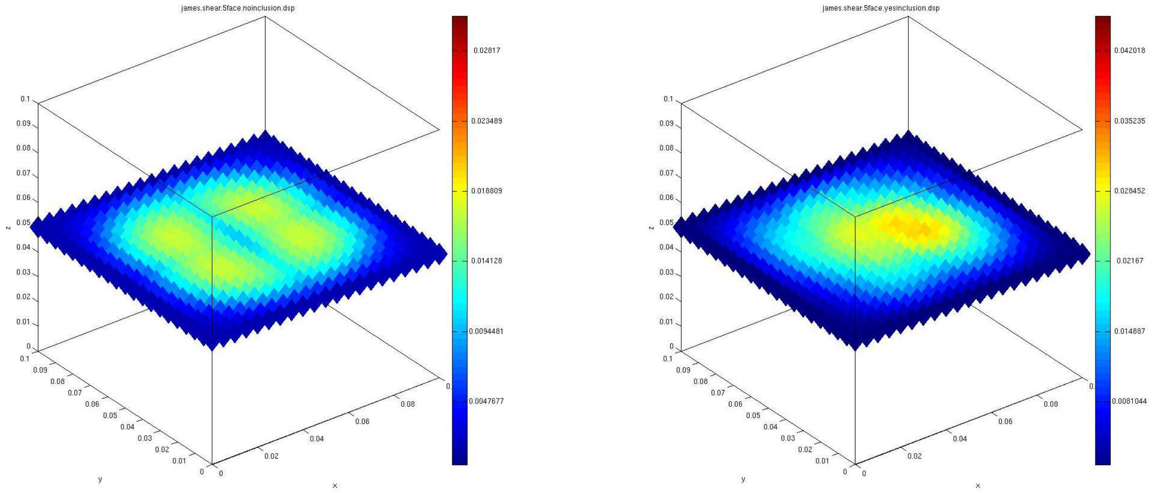

5 side boundary
No inclusion

5 side boundary
Inclusion

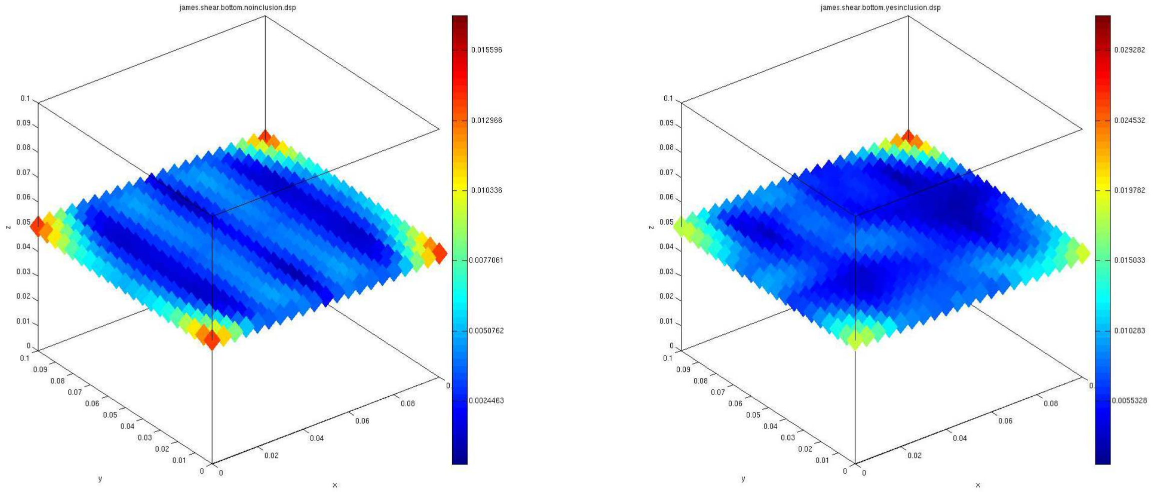

Bottom only boundary
No inclusion

Bottom only boundary
Inclusion

Figure 5.15: The top left image is the displacement map from a single slice of simulated data for a homogeneous material and rigid boundary conditions on five sides. This image can be compared to the top right image, which shows the simulation result for the same boundary conditions but a harder inclusion is present. The difference, calculated through a mean squared error method, between these two results is 22.5%. The bottom two images show the same comparison but for only one rigid boundary condition: on the bottom of the virtual phantom. The difference between these two results is 67.2%. The colourbar indicates an arbitrary measure of displacement. Notice the regular wave pattern occurring with homogeneous simulations is disrupted by the presence of an inclusion. The single boundary case provides more perturbation from the regular wave pattern than the five-sided boundary conditions.

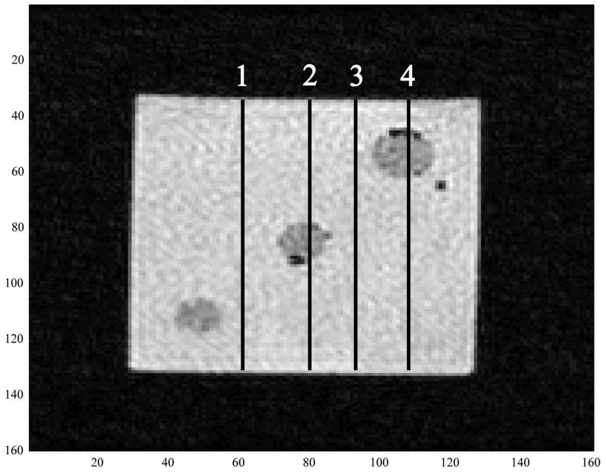

Figure 5.16: The location of four line profiles through the inclusions phantom, shown on a MR magnitude image of the middle slice of the phantom. Two profiles are taken through the soft phantom base (1 and 3); two are taken through stiffer inclusions (2 and 4). Actuation direction is along the vertical axis of the figure.

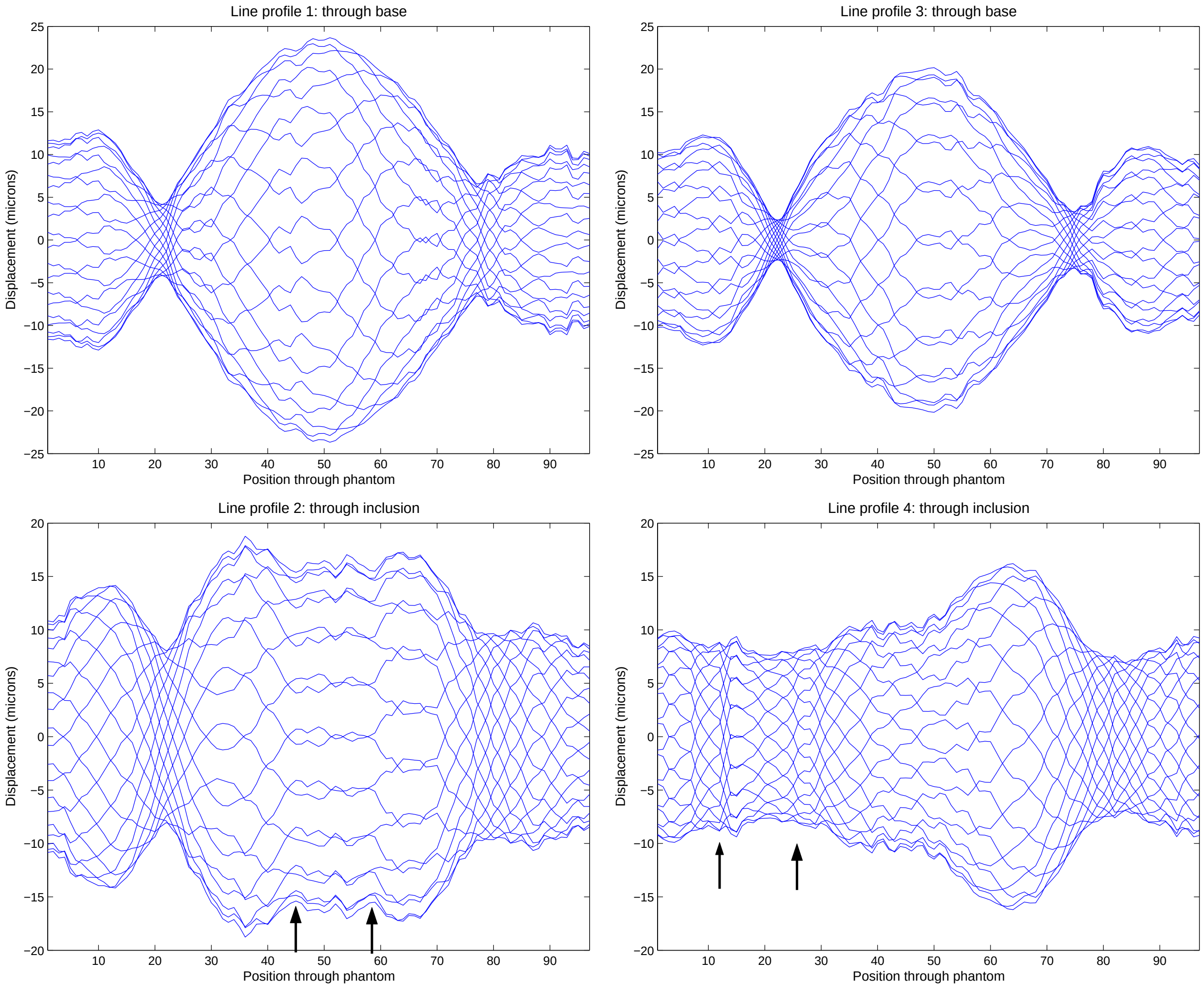

Figure 5.17: Line profiles taken through the inclusions phantom at 20 different time points. The numbers in the titles of these plots correspond to the locations of line profiles in figure 5.16. The results presented are for motion encoding in the direction of actuation (vertical axis of figure 5.16). Plots 1 and 3 (top), through the base of the phantom are very comparable. In plots 2 and 4 (bottom), a perturbation from this regular wave pattern is notable at the locations of the inclusions, indicated by the arrows.

5.5 Wedge Phantom

The wedge phantom was designed as a test for the 3D-orientable phantom box setup. In this regard, the phantom was a success; suitable motion data of this phantom was obtained for actuation along all three axes.

5.5.1 Wedge Reconstruction Results

Problems with elasticity reconstruction also plagued the datasets from this phantom. One of the better reconstruction results is displayed in figure 5.18. This reconstruction was obtained on the unbounded wedge data using an initial stiffness value of 20kPa. The edge of the wedge is visible in the reconstruction, but the stiffer silicone is not very well defined against the base material.

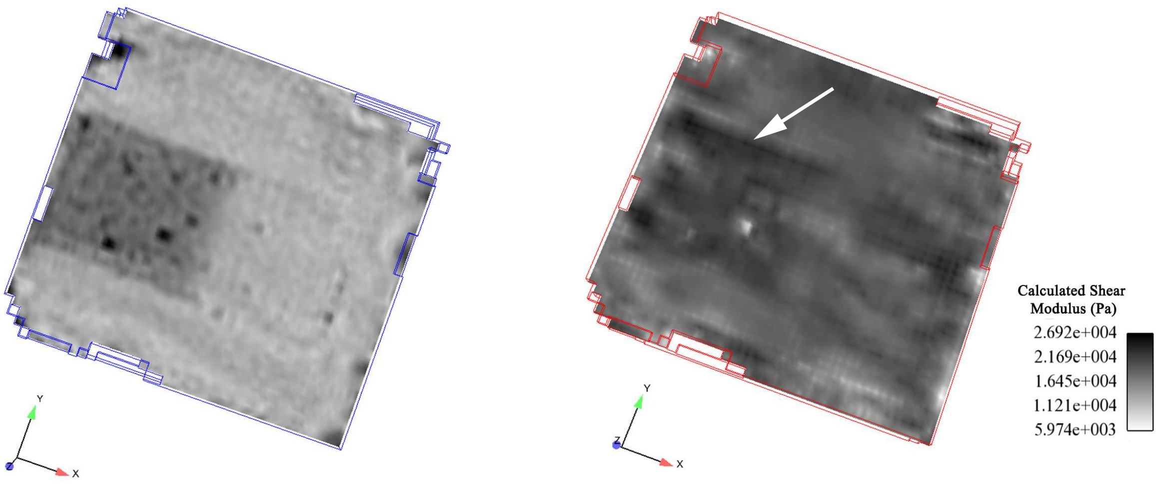

Figure 5.18: The left-hand image shows the MR magnitude of a slice through the unbounded wedge phantom. The cross-section of the wedge is clearly visible. The direction of actuation is along the x axis indicated by the coordinates. The right-hand image shows the same slice of results of a reconstruction attempt. An initial guess of 20kPa was used. The edge of the wedge is visible, indicated by the arrow, however the overall reconstruction is unconvincing with a lot of artifact in the result.

5.5.2 Wave Motion within Wedge Phantoms

The consistent problems with reconstruction would suggest that it is not necessarily due to the actuator setup used for data acquisition. To test further the hypothesis that using one rigid bounded surface rather than five would produce more satisfactory results (recall 5.4.2), the silicone wedge phantom was extracted from its container and imaged as a free cube resting on an actuation tray (recall 3.4.1).

Figure 5.19 shows the position of the wedge in the bounded phantom case, while figure 5.20 shows the three-dimensional motion of the phantom with the x-displacement map overlaid. For comparison, 5.21 shows the position of the wedge in the unbounded phantom case, and 5.22 shows the three-dimensional motion of the phantom with the x-displacement map overlaid. To directly compare the location of the wedge between the two datasets, one was inverted in relation to the other. This was due to the free wedge being imaged upside-down.

Line profiles were also taken through the wedge and the soft base for both the unbounded and bounded case and compared to see if any change in wave pattern could be detected in this manner. These results are presented in figures 5.23 to 5.26.

Certainly a lot more motion was exhibited by the unbounded phantom in the direction of actuation, along with a slightly less structured wave pattern in comparison to the bounded phantom. This is visible in the 3D wave pattern of the two datasets (figures 5.20 and 5.22). The maximum amplitude of motion along the direction of actuation for the unbounded case was $\sim 40\mu$m compared to $\sim 14\mu$m for the bounded case.

However, it is unclear whether the unbounded wedge case would generate a more successful elasticity reconstruction (putting aside noise issues due to inhomogeneities in the phantom caused in the extraction process). Certainly, no better reconstructions have been thus far obtained using the free wedge datasets compared to the bounded wedge case. Until issues preventing successful reconstructions on these datasets have been resolved (see 5.6), we are unable to conclude which method of actuation is the more successful.

Line profiles through the datasets show some lengthening of the wavelength in the stiffer wedge region for the bounded phantom. This is to be expected in a stiffer medium. This change is apparent for the bounded phantom (figures 5.23 and 5.24) but less obvious in the unbounded case (figures 5.25 and 5.26).

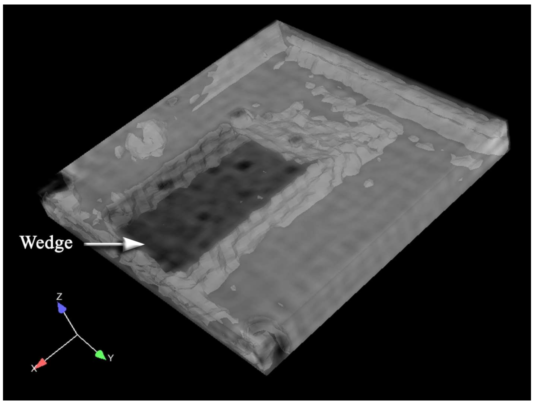

Figure 5.19: The position of the wedge in the bounded phantom is shown in this image. A magnitude image is superimposed on a isosurface image to illustrate the extent of the wedge below the surface of the dataset.

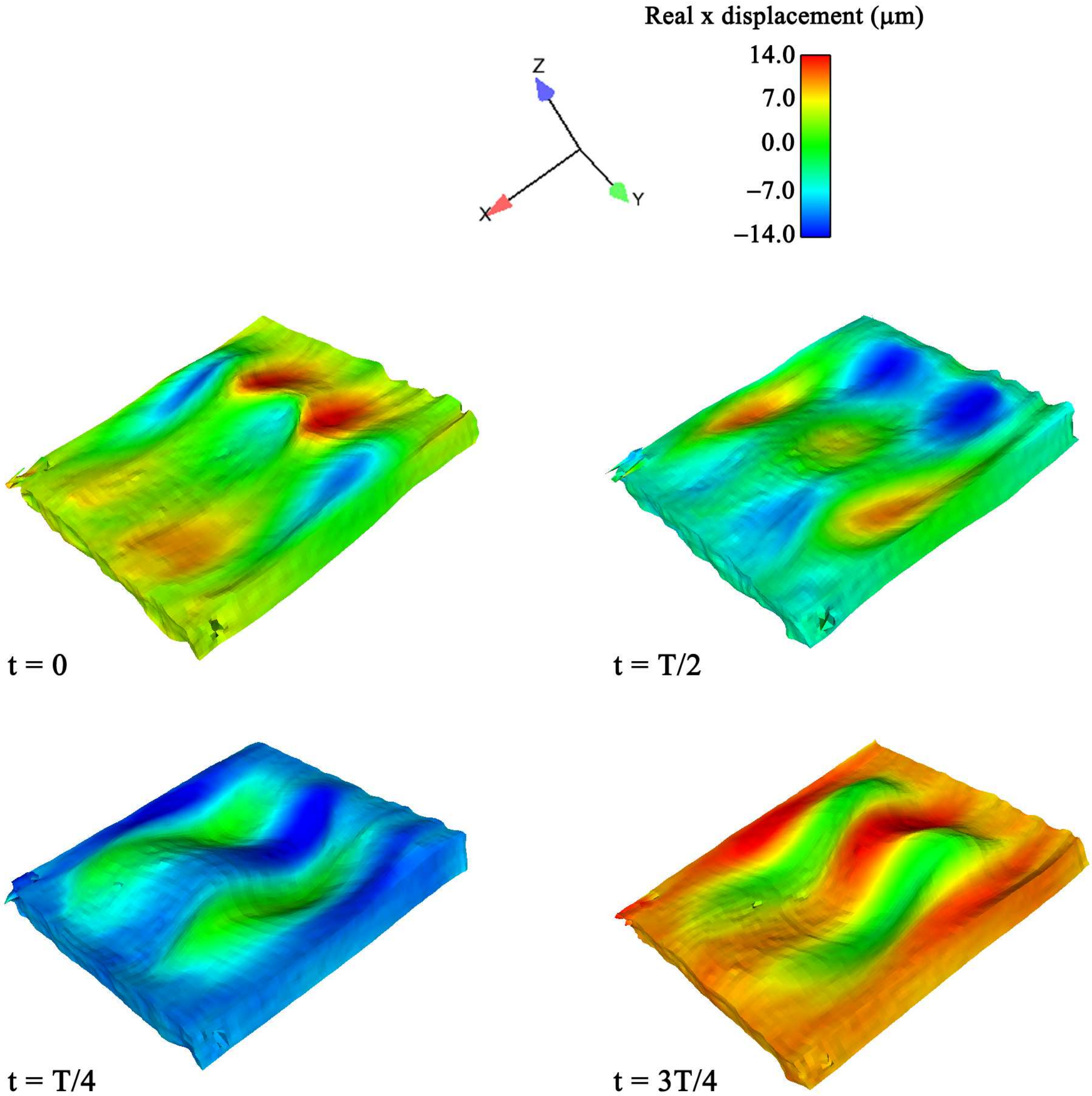

Figure 5.20: A fairly regular motion pattern is visible in this time series showing the full 3D motion of the bounded wedge phantom. The colour corresponds to motion along the x direction, which is the direction of actuation, although the wave pattern visible is the product of the full three dimensional motion data.

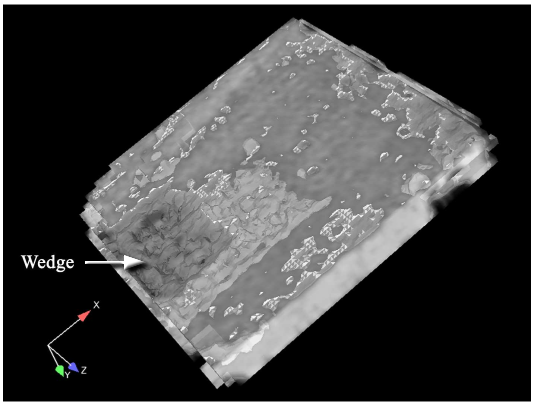

Figure 5.21: The wedge in the unbounded phantom is shown through a superposition of the MR magnitude data and an isosurface image. Note the orientation of these data, compared to that of the bounded wedge, is rotated about the x axis so that the $+y$ and $+z$ directions are opposite. This is so that the position of the wedge in the two datasets can be directly compared. This phantom had to be imaged upside-down in relation to the bounded case so that it rested on the flattest surface available. The direction of actuation is still the same in both sets of data.

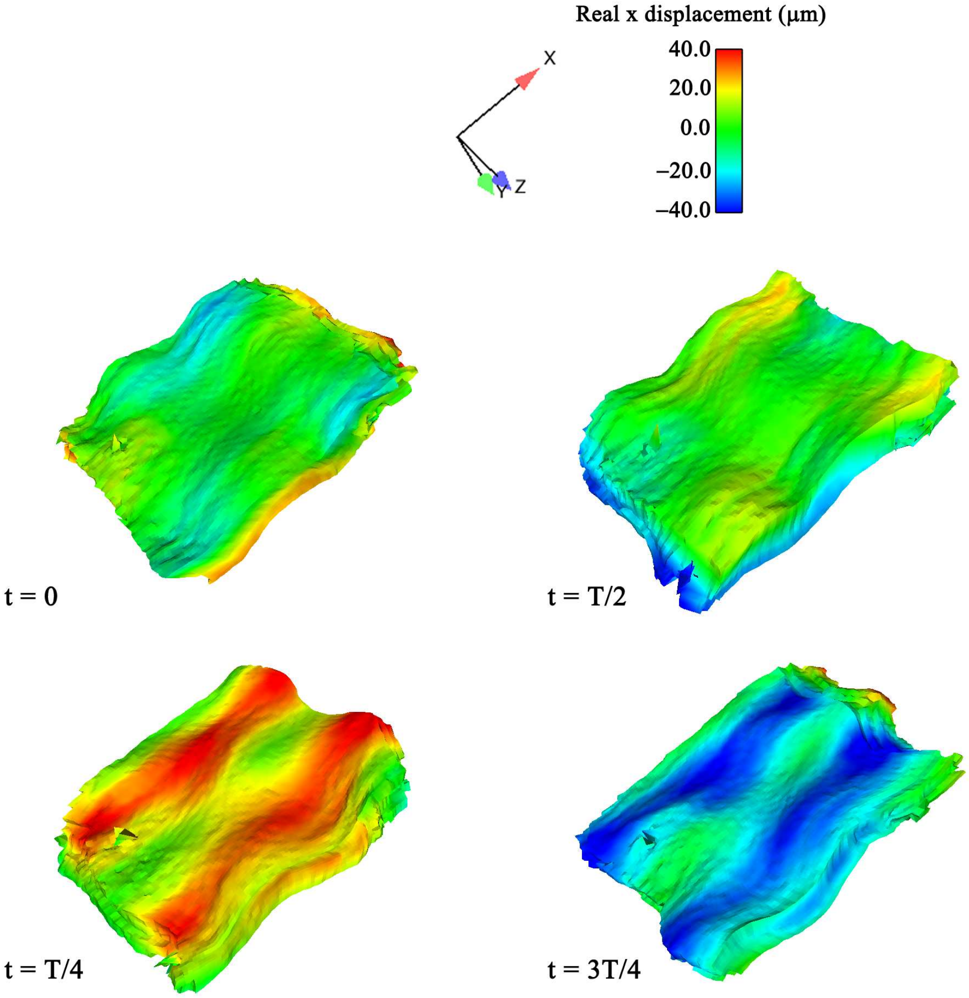

Figure 5.22: A lot more motion along the direction of actuation is noticeable in this time series of the unbounded wedge phantom. A slightly less regular motion pattern is also apparent.

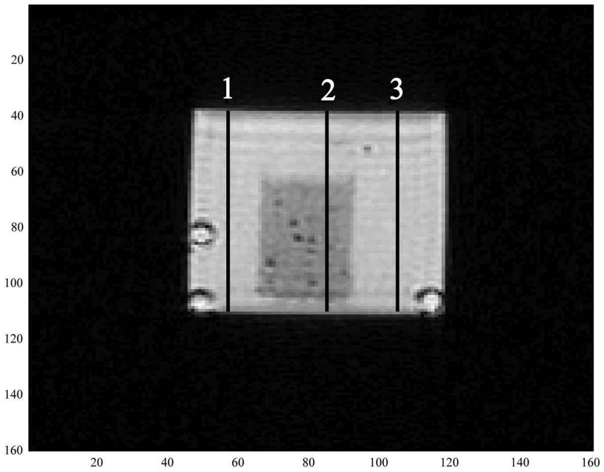

Figure 5.23: A magnitude image of a middle slice from the bounded wedge phantom showing the locations of line profiles presented.

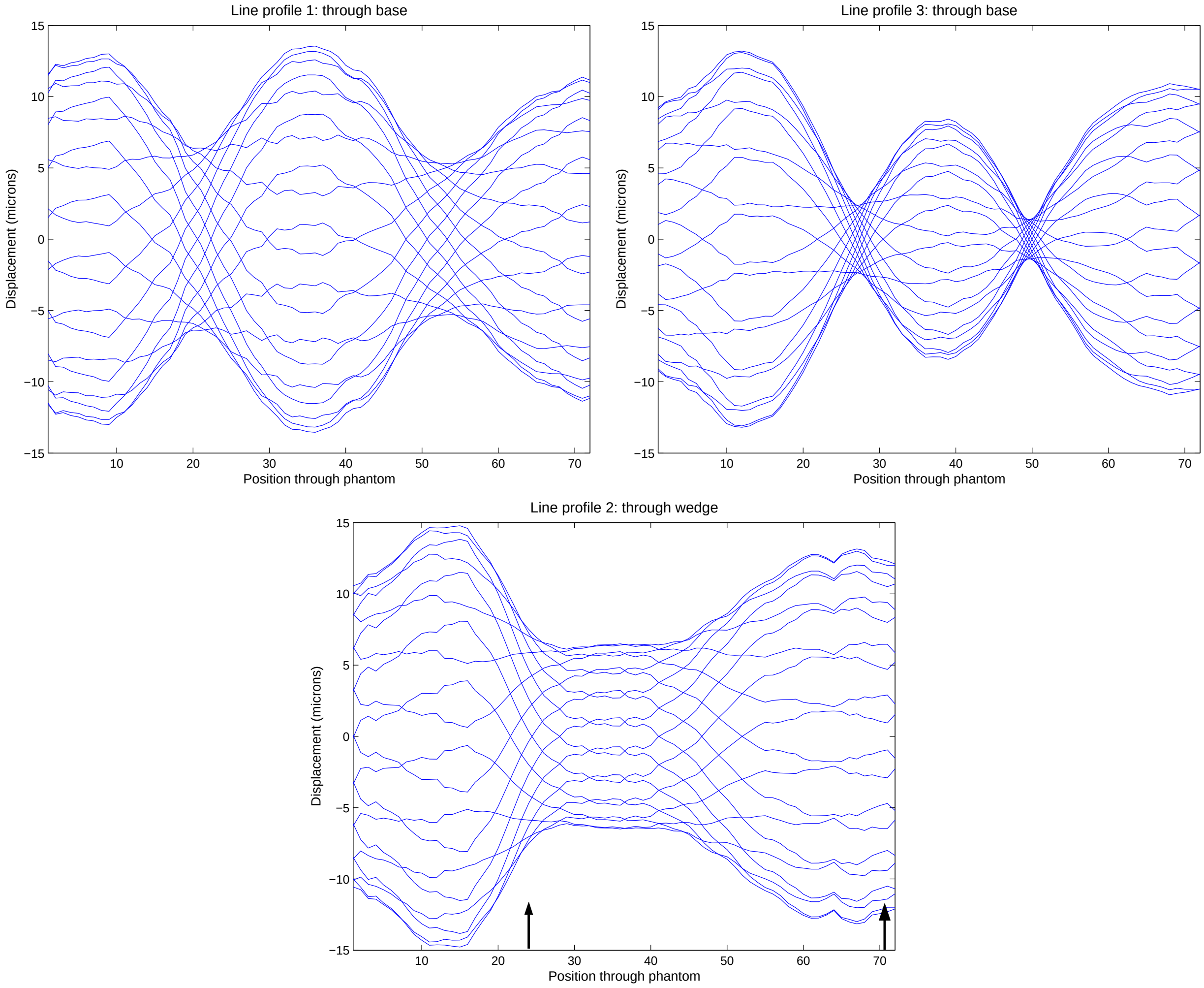

Figure 5.24: Line profiles taken through the bounded wedge phantom at 20 different time points. The numbers in the titles of these plots correspond to the locations of line profiles in figure 5.23. Motion encoding is in the direction of actuation (vertical axis of figure 5.23). The top images (plots 1 and 3), shown a regular wave pattern through the soft base of the phantom. In the bottom image, some attenuation of the wave can be seen, along with a lengthening of the wavelength in the region of the stiffer wedge. The location of the wedge is indicated by the arrows.

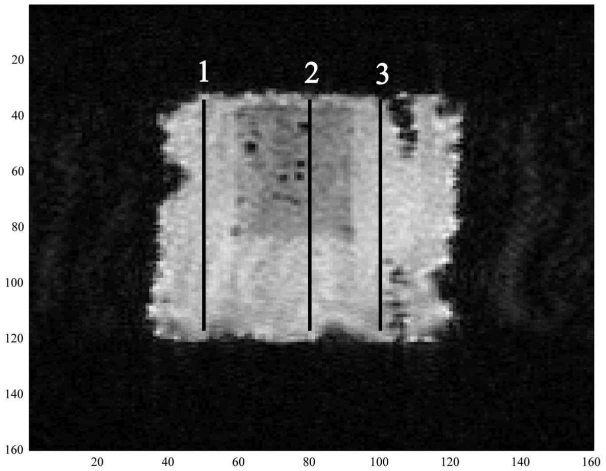

Figure 5.25: A magnitude image of a middle slice from the unbounded wedge phantom showing the locations of line profiles presented.

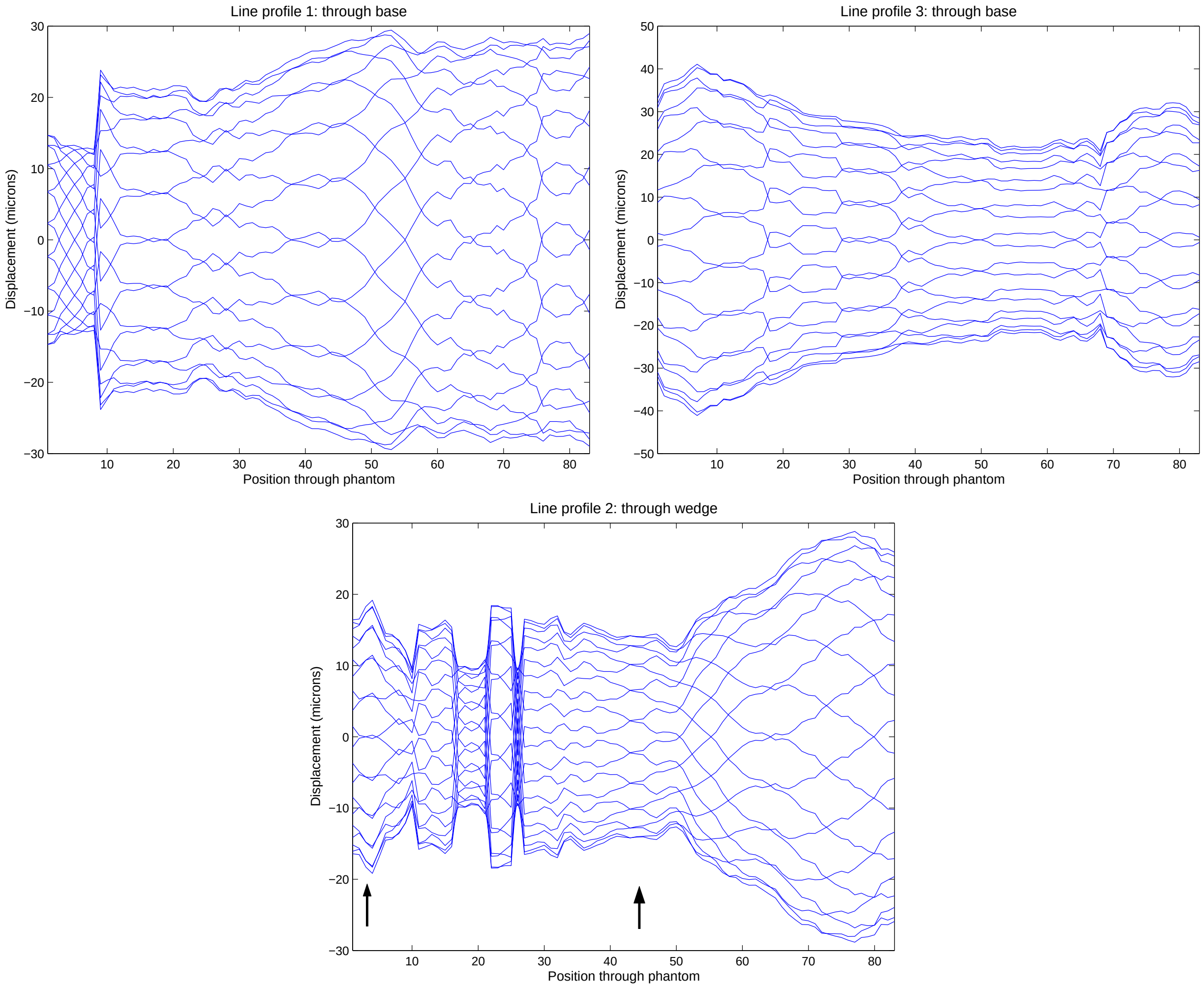

Figure 5.26: Line profiles taken through the unbounded wedge phantom at 20 different time points. The numbers in the titles of these plots correspond to the locations of line profiles in figure 5.25. Motion encoding is again in the direction of actuation (vertical axis of figure 5.25). The lengthening of wavelength in the region of the wedge is less apparent in this phantom. Rather, a marked decrease in the amplitude of motion is visible in the region of the wedge (bottom plot) when compared to line profiles through the base (top plots). The noise in the phantom may be obscuring some wave patterns. The location of the wedge is indicated by the arrows.

5.6 Reconstruction Issues and Future Work

5.6.1 Process of Acquiring Reconstructions

As indicated in the above sections, elasticity reconstructions of silicone phantom datasets have been less than ideal. This matter needs to be resolved before we can be entirely confident of our acquisition method and processing approach. The primary problem is the matching of orientations of the physical phantom to the direction of motions induced within it. However, such issues are not uncommon in the world of MRE. Contact with other groups investigating MRE indicate a huge amount of time and effort is invested into understanding and resolving these orientation issues.

Throughout this thesis, we have taken a number of steps toward resolving this. Firstly, the directional markers were introduced into phantoms to break the symmetry of the dataset. This innovation has meant that we can unambiguously relate the physical orientation of the phantom to the processed data. Another approach involved simulating a homogeneous phantom of the same dimensions and boundary conditions as the actual phantom used in MRE acquisition. This was a method designed to check whether the motions in the phantom were occurring in the correct spatial direction. For instance, 'x' motion needs to be occurring along the spatial 'x' axis.

The motions induced in the real phantom were compared to those that should be seen in the simulation. This was performed for both the stiff and the soft silicone (see figure 5.27). It was found that while the motions in the soft silicone case corresponded to those in the simulation, the motions in the stiff silicone were inverted. This is very difficult to understand as data acquisition must be self-consistent within a slice.

This led us to consider there may be some issues with the way the phase of the motion is calculated. The Fourier fitting of the data was rechecked and found to be satisfactory. Thus, there is still some unknown reason as to why the motion of one sample appears to be inverted to that of the simulation. We cannot rule out entirely that one pair of directions is around the wrong way, as the very small lateral motions recorded in the phantom are not sufficient for comparison.

However, proceeding under the assumption that the directions of motion were aligned with the spatial directions of the dataset coordinate system, the next question is whether these motions occur in the positive or negative direction at a particular time point. It would impossible to determine beyond doubt which physical orientation within the scanner would correspond to positive or negative motion encoding. Therefore reconstructions on the datasets using the four possible rotation matrices were run. This assumes that inverting all directions is equivalent to not inverting any.

Still no definitive reconstructions resulted, however, computing resources were such that it was not possible to run comprehensive tests on all four potential orientations. There are a number of other parameters that must be trialled while searching for a successful reconstruction. These include subzone size, and the value of the initial guess of the shear modulus. Variations in these parameters can lead to non-convergence even if the orientation is correct.

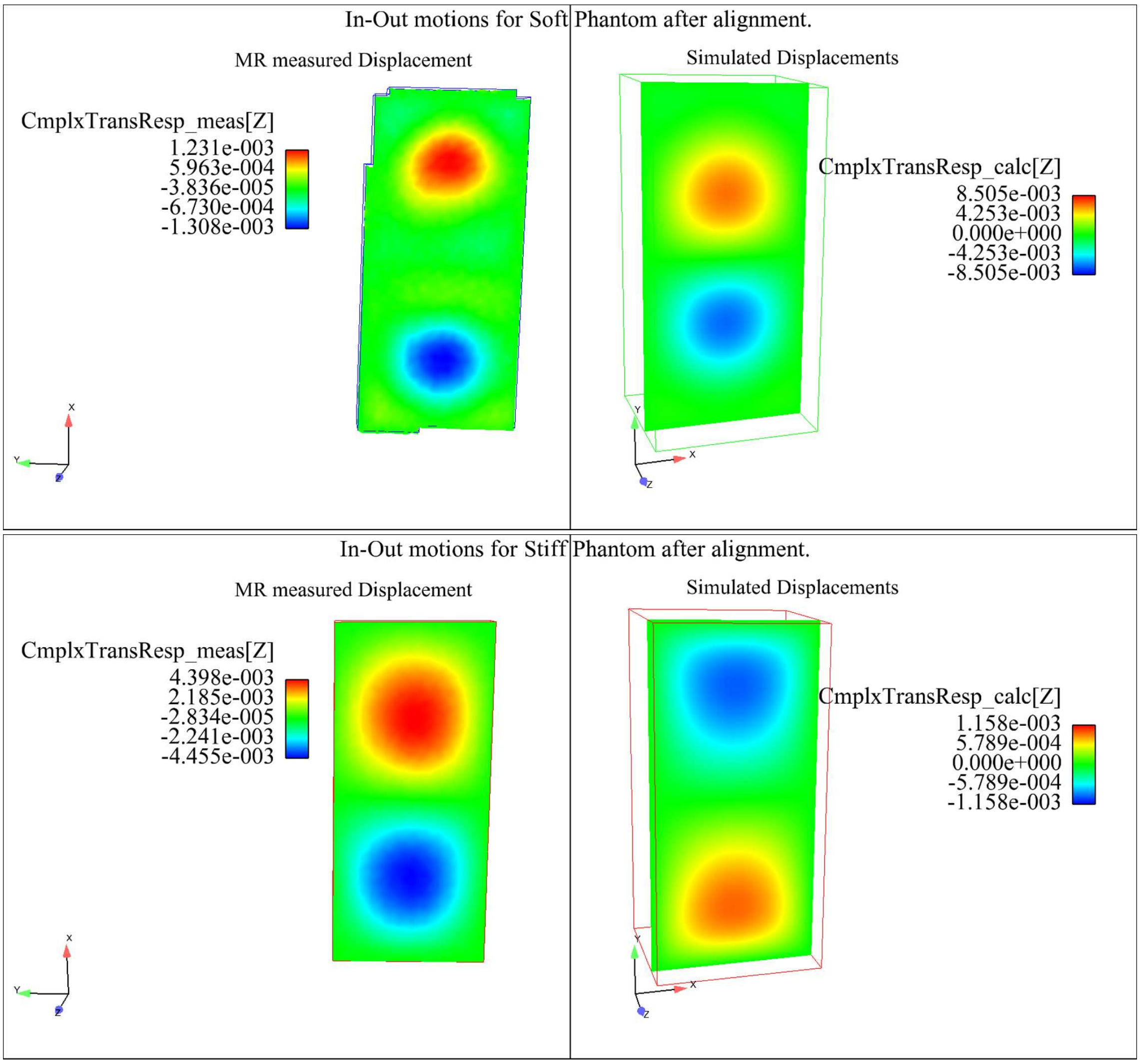

Figure 5.27: In each figure, the left image corresponds to the actual measured motions of the phantom; the right image shows the results of the simulation. The figures show the measured motion (complex transient response) along the z direction as indicated on the axes ('in-out' corresponds to through-plane motion). Red corresponds to motion in the positive z direction; blue to negative. The real data and the simulated data have been matched so that the phase of the motion in each case is the same; the discrepancies in the orientations of the x- and y-axes have been accounted for. It is plain that the soft silicone (top) corresponds well to the simulated data. The hard silicone (bottom), however, shows a flip of in-out motions. The simulations use shear modulus values of 120kPa for the stiff phantom, and 28kPa for the soft. These values were obtained from Peters [79].

5.6.2 Future Work

There are a number of options to be taken in the future to resolve the unsatisfactory reconstructions. Primarily, a very good initial guess of the dynamic shear modulus of silicone would eliminate one of the reconstruction parameters. DMA testing of the silicone should be performed in the future to obtain accurate shear modulus values of both the hard and the soft silicone.

Once this value has been obtained, a second step would be to run reconstructions on a modified wedge dataset. The dataset could be thresholded such that only the stiffer wedge would be analysed. Given a very good initial guess for the shear modulus, if this value diverges over subsequent iterations, we would know there was an issue with the orientation of the data. If the value holds constant, that would eliminate the orientation parameter.

Another approach is to calculate the three-dimensional divergence over the whole dataset. For an incompressible material (which the silicone is assumed to be), the divergence should be zero. Finding the direction in which the divergence is closest to zero would determine the correct direction of motion.

Finally, to investigate what is meant by ‘positive’ and ‘negative’ motion encoding, further MR acquisition experiments could be run. Currently there is an arbitrary, but constant, phase offset between the motion input to the actuator and the triggering pulse that starts the motion encoding gradients. The time value of this phase offset could be determined and then included in the motion encoding pulse sequence. In this way, we would know for sure that ‘positive’ motion encoding did indeed correlate to a positive motion amplitude on the actuator. These developments will require substantial investigation.

Chapter 6

Biological Samples

6.1 Excised Bovine Muscle Phantoms

6.1.1 Method of Actuation

Figure 6.1 shows a magnitude image of a muscle sample embedded in gelatine. Line profiles were taken through this phantom as indicated on the figure, and displayed at 20 time points throughout the motion cycle to investigate the amplitude of motion delivered to the sample. These results are presented in figure 6.2.

Similarly, line profiles were taken through the free-standing muscle phantom. The location of these profiles is shown on a magnitude image in figure 6.3. The results of line profiles at 20 time points are presented in figure 6.4.

For this comparison, both the direction of actuation and motion encoding is along the vertical axis of the magnitude figures.

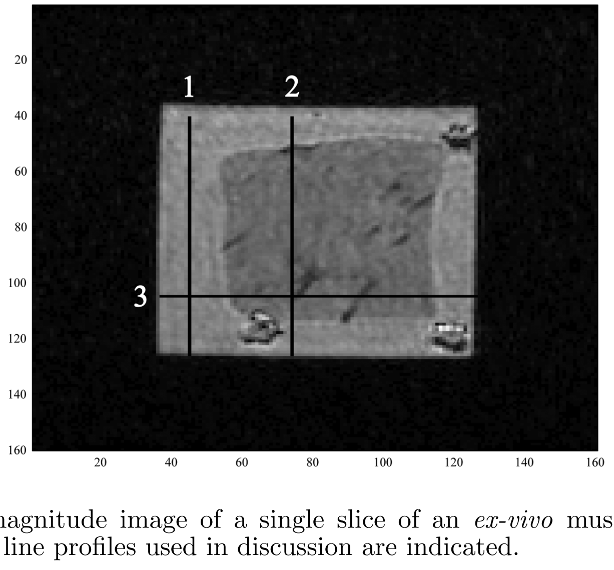

Figure 6.1: The MR magnitude image of a single slice of an *ex-vivo* muscle sample embedded into gelatine. The positions of line profiles used in discussion are indicated.

These figures show that for the muscle sample embedded in gelatine, little motion was transmitted through to the muscle itself. While the amplitude of motion in the gelatine is large ($\sim 30\mu$m) there is a lot less motion transmitted through to the muscle; this motion is of the order of $\sim 10\mu$m, yet most of this motion is due to the actuation: there is little

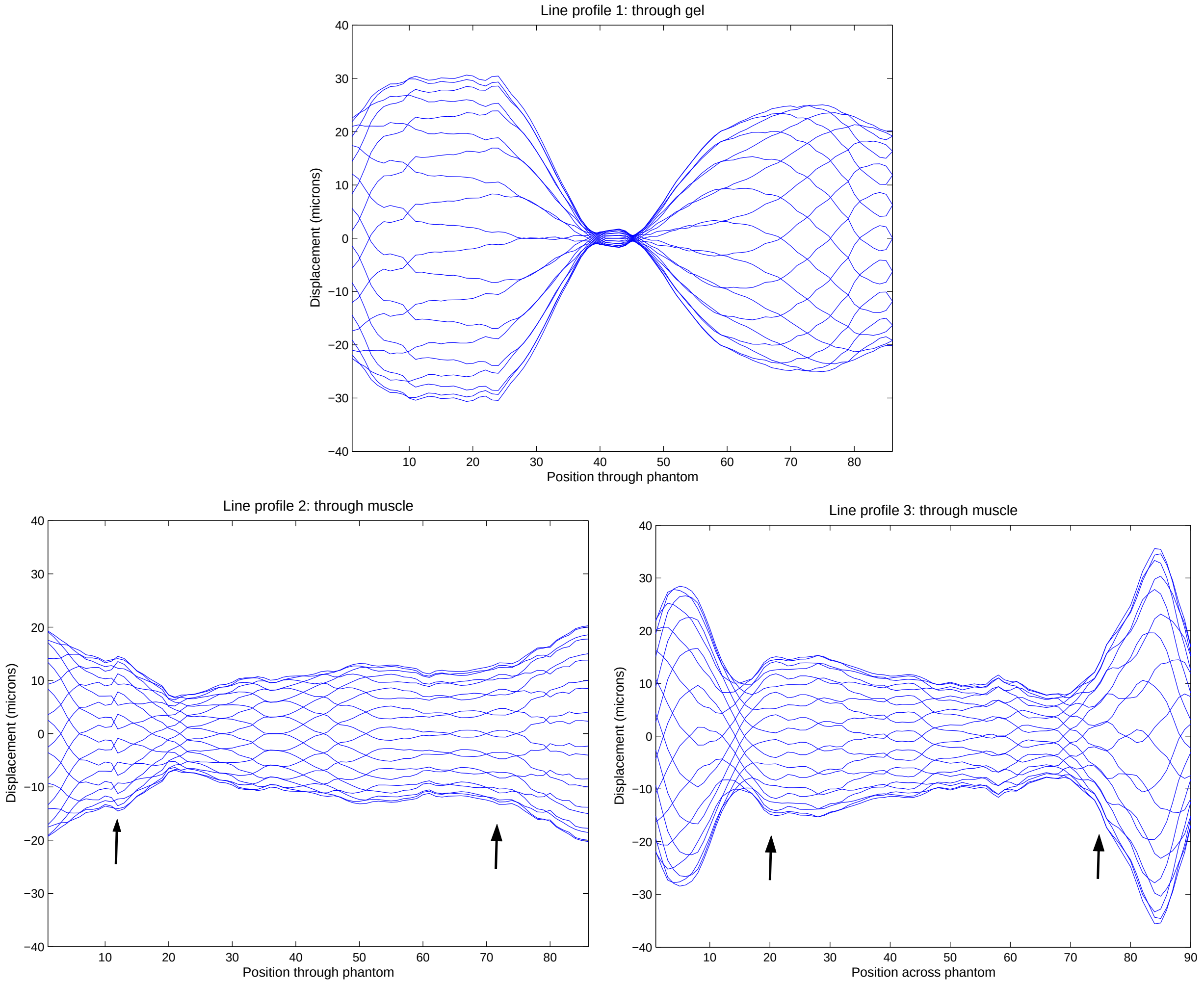

Figure 6.2: The results of line profiles taken at 20 different time points for the muscle sample embedded in gelatine. The top image shows the results solely through the gelatine. A significantly greater amplitude of motion can be observed in this plot in comparison to the bottom images, which pass through the muscle. The bottom right plot in particular shows how the large amplitude of motion detected in the gelatine drops off significantly at the muscle boundary. The positions of the muscle boundaries are indicated by the arrows.

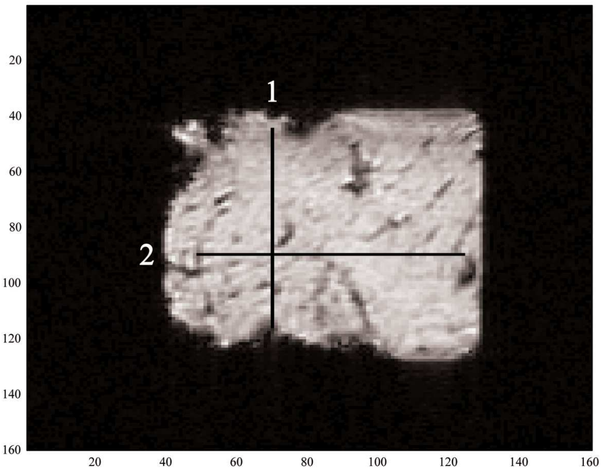

Figure 6.3: The MR image of a single slice of the free-standing *ex-vivo* muscle phantom. As above, the positions of line profile are indicated.

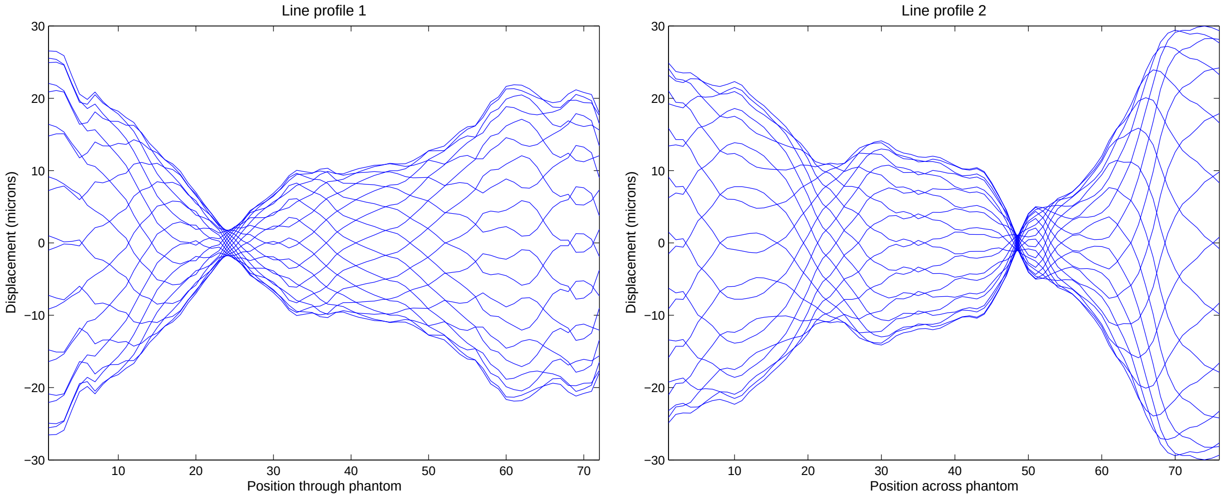

Figure 6.4: The results of line profiles taken at 20 different time points for the free-standing muscle sample. These plots can be directly compared to the lower two images in figure 6.2. The amount of motion seen in the tissue sample through direct actuation is markedly greater than that which is transmitted through the gelatine. Amplitude values of a wave propagating through the muscle sample were around 20 to 30μm.

relative motion within the sample at a given time point. The bottom right plot in figure 6.2 shows that the large amplitude of motion in the gelatine drops off dramatically at the muscle-gel interface.

Thus, we can conclude from this experiment that gelatine, of the concentration used in this phantom, is not suitably impedance-matched to the excised muscle tissue. Shear waves are not transmitted through the muscle-gelatine boundary; instead the waves appear to reflect from the boundary creating significant amplitude of motion only within the gelatine.

By contrast, figure 6.4 shows that where the actuation is applied directly to the *ex-vivo* muscle sample, a significant amount of motion is generated within the tissue (20 to 30μm). A measurable wavelength was also able to be detected (see 6.1.2).

There were, however, some issues with this phantom. A lot more noise was encountered in the data. This was due to air and fat regions within the phantom, along with uneven surface areas, which would have been filled with gelatine in the previous phantom. The uneven surfaces meant that line profiles were unable to be taken to the very edge of the phantom. Also, some parts of the sample rested against the walls of the container. Thus, shear actuation was not solely through the base of the sample, but also unevenly at other locations. This was unavoidable due to the inability to cut the muscle into a perfectly regular shape (refer to 3.4.2). A future acquisition could use either a smaller sample of tissue, or some form of tray actuation which could still be oriented in two directions.

6.1.2 Anisotropy of Muscle Tissue

Data was acquired for the free-standing muscle phantom for actuation along the two in-plane directions. It was hoped to run elasticity reconstructions of these data to get a measure of the anisotropy of the tissue sample. While a true anisotropy reconstruction model is still under development, it would be possible to apply an isotropic model to these data. In this case, we would expect to generate two different values of the shear modulus for the same phantom, depending on the direction of actuation.

However, given the difficulties encountered in processing silicone datasets, this approach has not been possible at this time. Some initial analysis of the wavelength of propagating shear waves in the muscle was undertaken and preliminary results are presented in figure 6.5.

Line profiles through the phantom as indicated on figure 6.3 were examined at one time point to determine an approximate wave length of propagating shear waves. The two directions of actuation are along the horizontal axis of 6.3 (orientation '1', with 'right-left' actuation), and along the vertical axis (orientation '2', with 'superior-inferior' actuation). Line profiles are compared for motion encoding in the direction of actuation in both orientations (figure 6.5). This method of analysis is very similar to that used by a great number of other researchers, such as Bensamoun *et al.* [13], Dresner *et al.* [81], Ringleb *et al.* [72], Sack *et al.* [15], and Uffmann *et al.* [16].

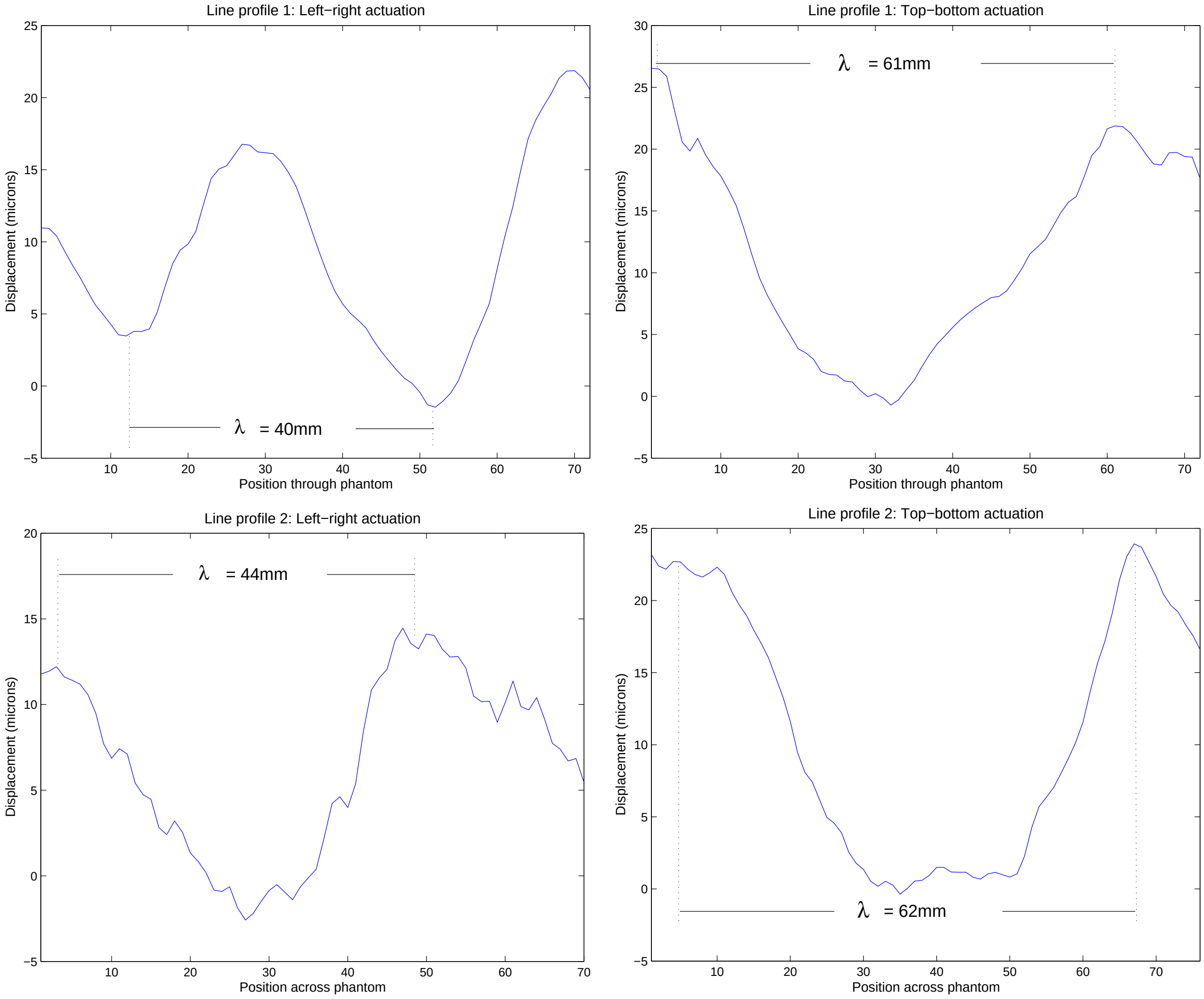

Figure 6.5: Line profiles taken at the same time point for the positions indicated on figure 6.3. The left-hand images show results for left-right actuation; the determined wavelengths along the profiles are 40 and 44mm. The right-hand images show results for top-bottom actuation. There is a notable difference wavelength between the two actuation directions, with the wavelength in these plots determined as 61 and 62mm.

For actuation parallel to the direction of motion encoding, wavelengths measured were about 40mm and 44mm for left-right actuation, compared to wavelengths of about 61mm and 62mm for top-bottom actuation. Thus, between the two actuation directions, we are seeing a change in wavelength from around 40mm, to around 60mm.

Taking these approximate wavelengths, we could conclude an estimate of shear modulus of 17.6kPa for left-right actuation, and 39.6kPa for top-bottom actuation.

Muscle is well known for its mechanical anisotropy, and this has been shown to manifest itself through different propagation speeds of mechanical wave along different orientations of the muscle fibres [13], [15], [16]. Therefore, a difference in wavelength in the same region of muscle, for actuation along a different direction is indication that some degree of anisotropy is being measured.

These initial results, while needing further analysis to determine the degree of accuracy, give a strong indication of a difference in wavelength observed for actuation along orthogonal directions.

MRE literature published to date details a wide variety of stiffness values for muscle tissue. Ringleb *et al.* [72] provide a useful summary table (6.1.2) which details the range of stiffness results for muscle in the relaxed state from 3.7 to 27.3kPa. Some other researchers give even higher values, for example Bishop *et al.* [82] who quote an *ex-vivo* shear modulus of 71kPa. The wide range of values is indicative of the different types of muscle imaged, along with differences in *ex-vivo* and *in-vivo* data. Dresner *et al.* [81] note that for *ex-vivo* data, the stiffness of the tissue can be a function of the amount of time passed since harvesting, even if harvesting occurs well before rigor mortis.

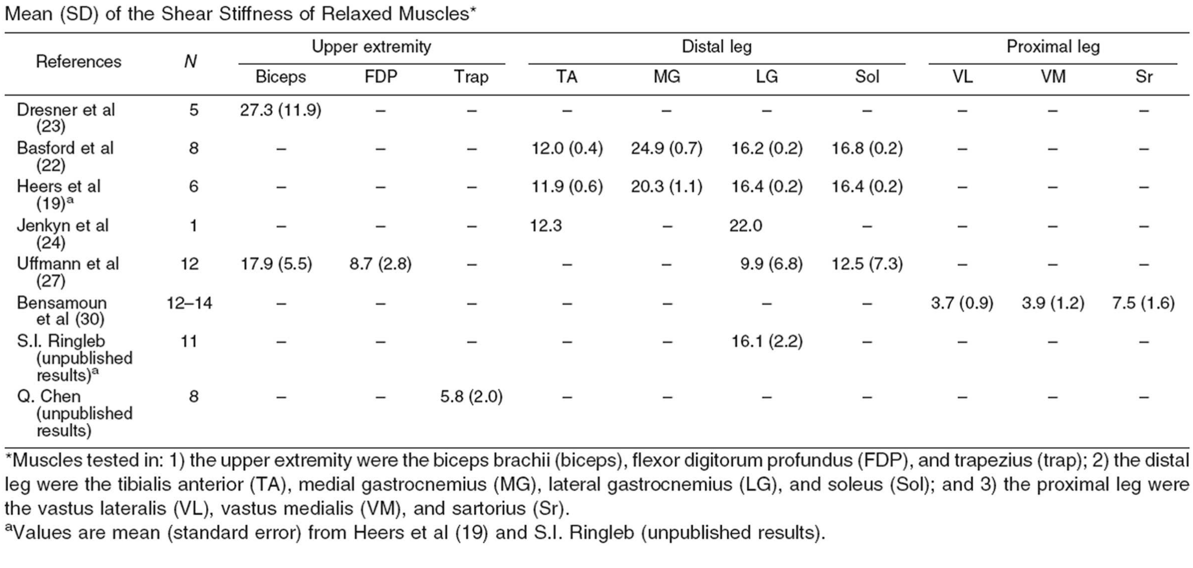

Mean (SD) of the Shear Stiffness of Relaxed Muscles*

References	N	Upper extremity			Distal leg				Proximal leg		
		Biceps	FDP	Trap	TA	MG	LG	Sol	VL	VM	Sr
Dresner et al (23)	5	27.3 (11.9)	–	–	–	–	–	–	–	–	–
Basford et al (22)	8	–	–	–	12.0 (0.4)	24.9 (0.7)	16.2 (0.2)	16.8 (0.2)	–	–	–
Heers et al (19)[a]	6	–	–	–	11.9 (0.6)	20.3 (1.1)	16.4 (0.2)	16.4 (0.2)	–	–	–
Jenkyn et al (24)	1	–	–	–	12.3	–	22.0	–	–	–	–
Uffmann et al (27)	12	17.9 (5.5)	8.7 (2.8)	–	–	–	9.9 (6.8)	12.5 (7.3)	–	–	–
Bensamoun et al (30)	12–14	–	–	–	–	–	–	–	3.7 (0.9)	3.9 (1.2)	7.5 (1.6)
S.I. Ringleb (unpublished results)[a]	11	–	–	–	–	–	16.1 (2.2)	–	–	–	–
Q. Chen (unpublished results)	8	–	–	5.8 (2.0)	–	–	–	–	–	–	–

*Muscles tested in: 1) the upper extremity were the biceps brachii (biceps), flexor digitorum profundus (FDP), and trapezius (trap); 2) the distal leg were the tibialis anterior (TA), medial gastrocnemius (MG), lateral gastrocnemius (LG), and soleus (Sol); and 3) the proximal leg were the vastus lateralis (VL), vastus medialis (VM), and sartorius (Sr).

[a] Values are mean (standard error) from Heers et al (19) and S.I. Ringleb (unpublished results).

Table 6.1: Table reproduced from Ringleb *et al.* [72] summarising recent MRE results for *in-vivo* studies of human muscle. The references in the first column are the authors'.

Taking the maximum and minimum shear modulus values found in the literature, a range of expected wavelengths can be found through equation 5.3. Most researchers use a density value of 1100kgm^{-3} for the density of muscle. For actuation at 100Hz, we might expect wavelengths from 1.8 to 8.4cm. Our findings are well within this range, and correlate well to results from a number of other investigators such as Bensamoun *et al.* [13], Ringleb *et al.* [72], and Uffmann *et al.* [16].

Much of the literature also comments on the attenuation of wave amplitude as a function of propagation distance [13], [81], [72], [15]. This damped pattern was certainly seen in our results, and is most likely caused by the uneven actuation of the sample where the muscle rested on the sides of the container.

6.2 Excised Ovine Brain Phantom

While the brain encased in epoxy resin showed significant motion, of an amplitude of about 20μm, the entire brain appeared to move in phase. Thus little relative motion of one part of the brain to another was seen (figure 6.6).

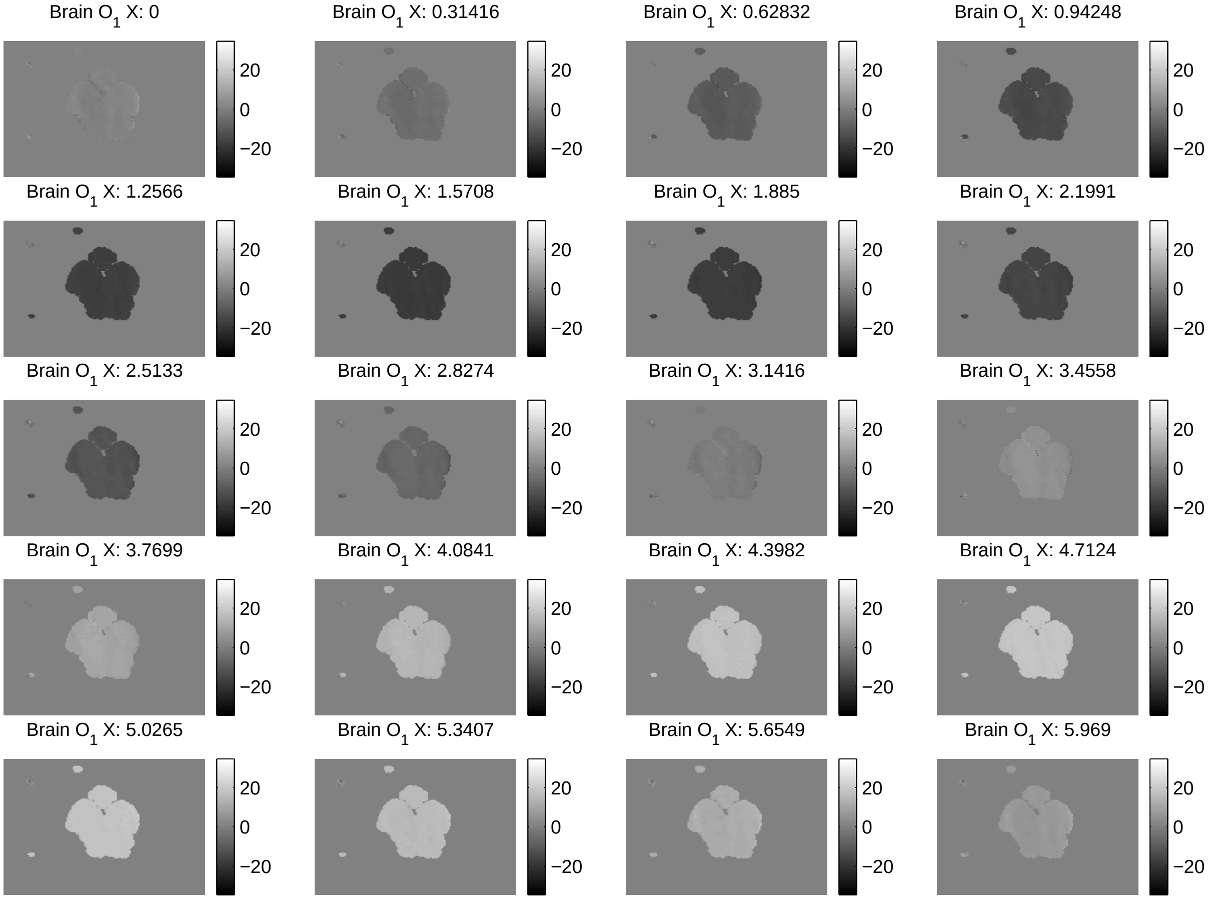

Figure 6.6: The displacement of the phantom is shown at 20 time points throughout the period for one slice. Motion encoding is in the x direction, which is along the vertical axis in these images; this is the same direction as actuation. O_1 stands for orientation 1. The numbers titling each image indicate the position along the period of the motion, expressed as a fraction of 2π. The scale of the motion is indicated by the colourbar and covers $\pm 30\mu$m. While the motion of the phantom as a whole changes throughout the actuation cycle, it is clear from the near constant shade of each individual image that there is little relative motion within the phantom.

The images of the phase of the motion confirm this (figure 6.7), with a more or less constant phase across the entire brain for encoding along all three axes.

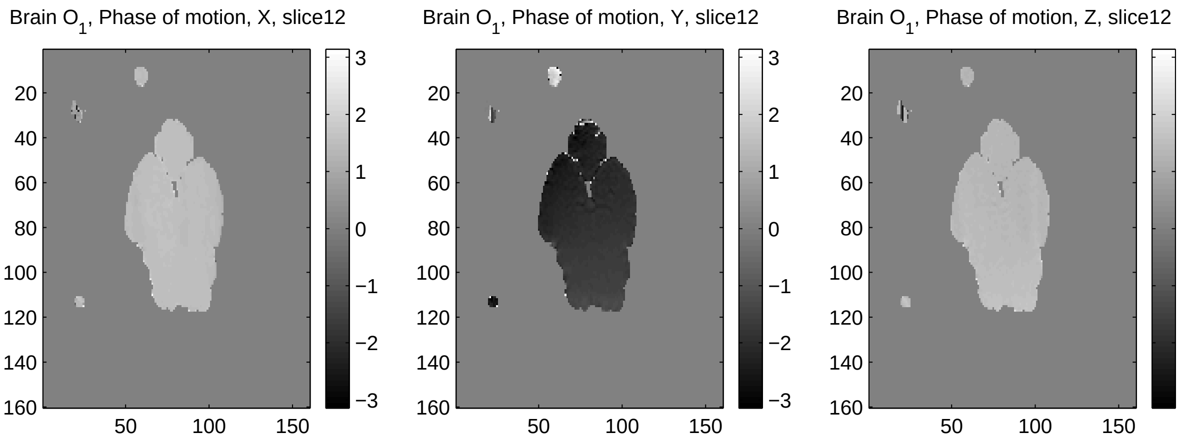

Figure 6.7: Images showing the phase of the motion in the brain phantom for a particular slice. In these images, x motion encoding (left) refers to the vertical axis, y motion encoding (centre) to the horizontal axis, and z motion encoding (right) in the through-plane direction. The phase for motion in each direction is relatively constant throughout the phantom, indicating again that little relative motion is observed. The colourbars indicate the value of the phase from $-\pi$ to π.

Data was acquired with the brain positioned in three orientations. Line profiles through the phantom were compared for actuation in the three orientations to investigate anisotropy (figures 6.8 and 6.9). These results were largely inconclusive as the relative motion along a spatial direction is small (1 to 4μm), compared to the motion of the entire brain ($\sim 20\mu$m). There is perhaps a wave pattern present, and also some potential differences in this wave pattern between orientations, however, the small scale of the motions means that any patterns present could also be due to, or masked by, noise.

Very limited data for *ex-vivo* brain elastography has been found in the literature, thus it is difficult to compare our experimental methods to other sources. It was thought that the solid epoxy would simulate to some degree the boundary of a skull, although, of course in an *in-vivo* situation, the brain is free to move somewhat against the skull. Vappou *et al.* [83] have shown some success in *ex-vivo* brain MRE using a porcine brain suspended in echographic gel, and actuating the brain directly through an attachment between the hemispheres. While echographic gel is unlikely to transmit shear waves if it were to be incorporated into a box set up such as used in our experiments, it may be worth considering a more direct method of brain actuation. Of course, other factors would need to be considered, such as preservation of the brain and the logistical feasibility with the MR resources available. With our particular focus on brain tissue anisotropy, it may very difficult indeed to perform successful *ex-vivo* testing with actuation in more than one direction.

A number of *in-vivo* human brain MRE studies have been performed, however [84], [85], [86], [87], [88], [18], [19], [32], [20], [89], [90]. As yet, no consensus has been reached on the stiffness values of grey and white matter, nor even which tissue type is stiffer. Kruse *et al.* [18] acknowledge that a lot of brain elasticity data comes from *ex-vivo* measurements without consideration for the effects of blood pressure and metabolic activity, thus accounting for some of the discrepancies in data.

Most recent MRE studies into brain elasticity conclude that white matter is stiffer than grey [18], [20], [89]. Work undertaken by Green *et al.* [85], [86] is the exception, where

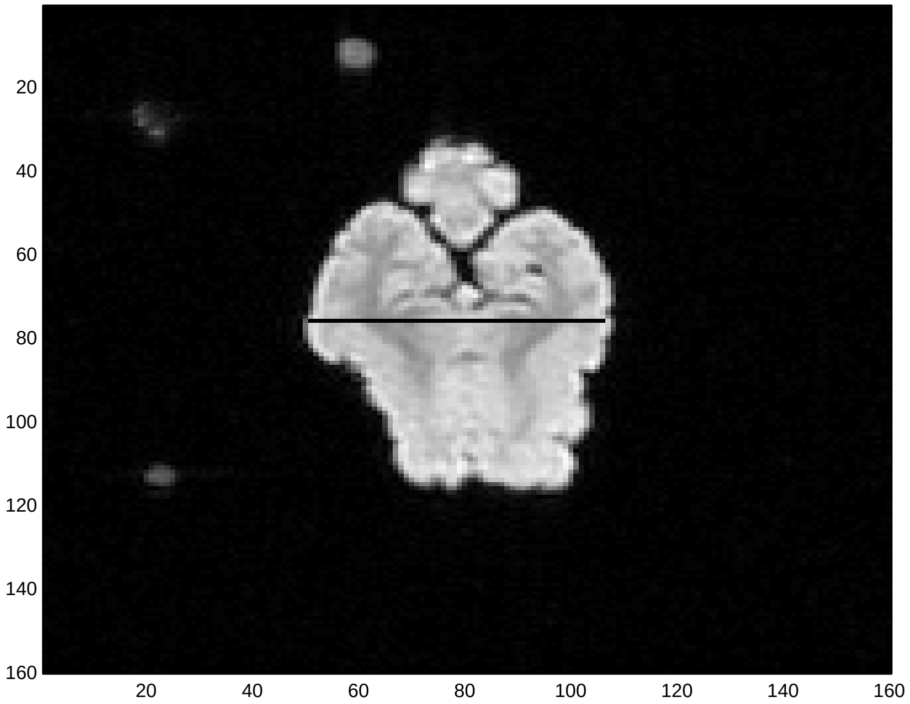

Figure 6.8: A magnitude image of an axial slice of the brain phantom. The black line shows the position of the horizontal line profile used for motion data presented. For comparison of motion for different actuation directions, as close as possible to the same slice, and line profiles were used for each acquisition. This was facilitated through the positioning of the directional markers. Thus, the same line profiles have been used in analysis with the direction of actuation effectively coming superior-inferior (orientation 1), right-left (orientation 2) and anterior-posterior (orientation 3). See results presented in figure 6.9.

the reported value for white matter is significantly lower than that of other researchers. Ladd [19] notes that differences between MRE experiments could be due to differences in reconstruction techniques, the amount of motion data acquired and used for reconstruction, and the assumptions on tissue properties used as a basis for reconstruction. For instance, some groups use a viscoelastic model [86], others do not [87].

Stiffness values for grey matter range from 2.8kPa [86] to 12.9kPa [89], while values for white matter range from 2.1kPa [86] to 15.2kPa [89]. Most groups assume a constant density of 1000kgm^{-3} for brain tissue. Thus, taking the outside values of elasticity quoted in the literature, and with actuation at 100Hz, we should expect to see shear waves of wavelength 1.4 to 4.4cm. It is difficult to say whether any such pattern exists in our results; some periodic variations could be said to exist of a wavelength of about 1cm. However, it is difficult to distinguish anything definitive against the noise. Ladd reports a wave pattern of concentric, elliptic wavefronts emanating from the skull to the centre of the brain. No such pattern is observed in our *ex-vivo* phantom.

It is possible that the phantom fabrication process renders the sheep brain no longer viable as an elasticity phantom. It may also be the case that the hard epoxy casing imposes too great a boundary condition on the surface of the brain for significant relative motion of the tissue to occur. The sheep brain is, of course, a lot smaller than a human brain (about 9cm along the anterior-posterior axis). The incompressibility constraint of soft tissue would also mean that too rigid boundary conditions will generate little internal motion.

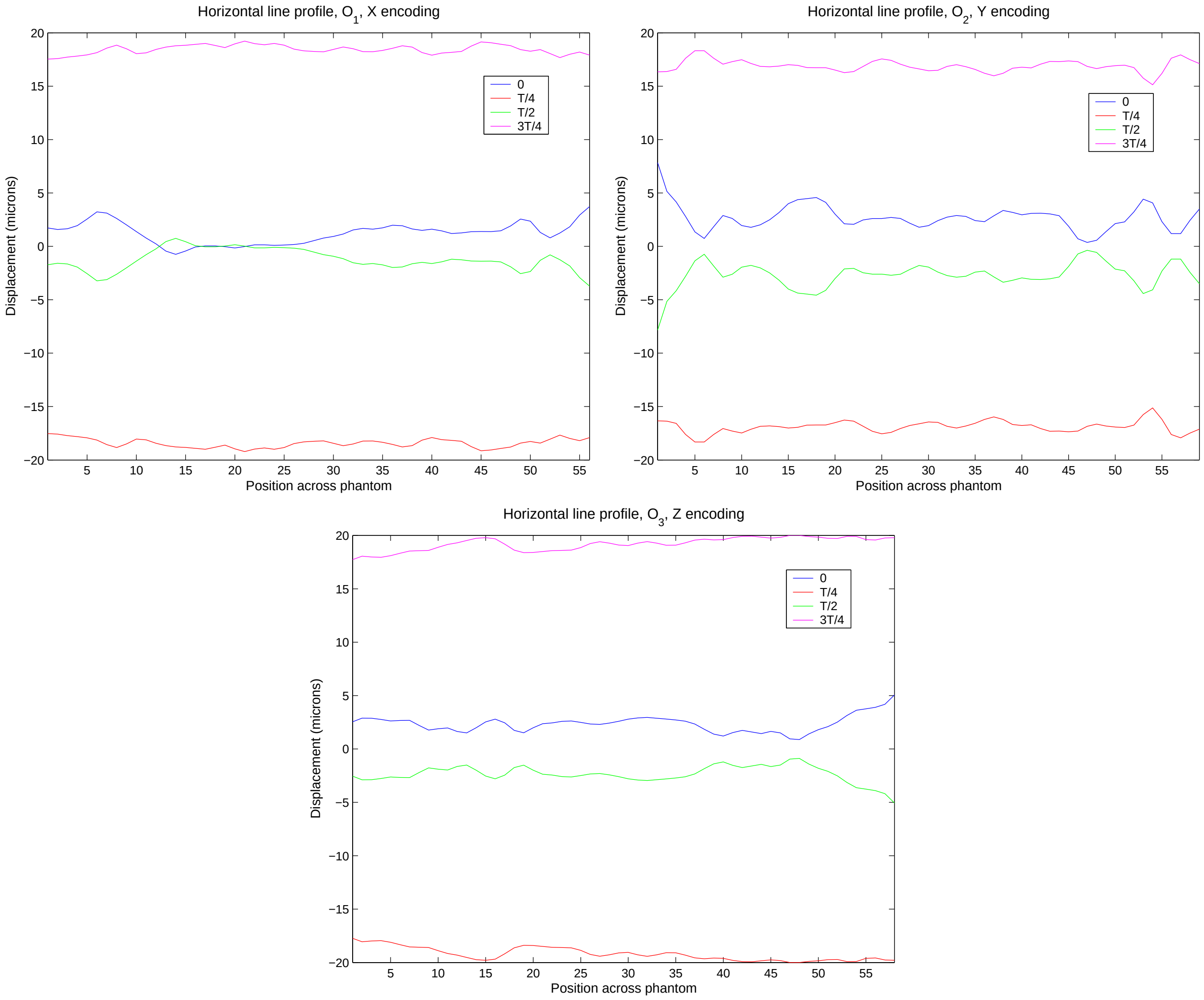

Figure 6.9: The results from the line profile taken through the brain phantom as indicated on figure 6.8 are presented. Data from motion encoding along the direction of actuation for the three orientations are shown at four different time points throughout the actuation cycle. The figures are thus directly comparable. It is clear in all cases that while the total motion of the brain is significant ($\sim \pm 20 \mu$m), there is little relative motion with the brain. It is difficult to determine any potential wavelength, let alone a change in wavelength due to anisotropy, from the noise in the data.

The *in-vivo* human brain studies that detail their actuation amplitude all use a significantly greater amplitude (120μm to 1000μm); recall the peak-to-peak amplitude of our system is estimated to be 40μm. Uffmann *et al.* [89] state that while a 600μm amplitude was used in actuation, maximum displacement within the brain was $\pm15\mu$m. While the majority of this damping would be caused by the fluid between the skull and the brain, Hamhaber *et al.* [87] report significant damping of the brain tissue itself. If the damping of the tissue were significant in our case, with only $\pm20\mu$m motion being induced, we might not expect to see significant motion within the brain.

Most groups operate at an actuation frequency between 80 to 100Hz. While there is no clinical precedent for actuating at a higher frequency, such a test would generate waves of a shorter wavelength which may be visible in the smaller sheep brain. However, Xu *et al.* [90] warn of actuating above 200Hz, stating that attenuation of shear waves becomes marked at higher frequencies.

Chapter 7

Conclusion

7.1 Pulse Sequence Development

The primary focus of this thesis was the development of an acquisition protocol for MR Elastography data suitable for clinical applications. To this end, work was undertaken on developing pulse sequences and a variety of phantoms were designed and fabricated for the testing of these pulse sequences.

A robust imaging protocol was successfully developed based on a 3D gradient echo sequence. This sequence proved to be suitable for imaging silicone phantoms, along with brain and muscle tissue. Given the variation in magnetic relaxation properties of these materials, this sequence should be able to be used for elastography imaging of many tissue types.

The overall scan time for a 16cm ×16cm ×2cm volume with a 2mm isotropic resolution and motion encoding along all three orthogonal directions was about 45 minutes. It should be emphasized that our approach is a 'quantitative' MRE method motion where the 3D motion is recorded at each voxel throughout the entire period of oscillation, rather than a single direction and time. These 'qualitative methods' offer faster scan times, but only because less information is obtained, which compromises the ability to fully describe the motion induced in a sample.

45 minutes is still too long for practical clinical application, however there are a number of simple methods that would greatly reduce the overall scan time, while still retaining a quantitative dataset. Future work would involve implementing some of these methods. Firstly, there is a fundamental limit on the triggering speed that can be applied through the ECG gating. There exists the option for an external triggering system. A more direct triggering may allow any TR to be selected, providing it were still a multiple of the driving period of 10ms. Currently the triggering is limited to 100ms through the physiological monitoring system. The overall acquisition time could thus be at least halved to a more reasonable 20 minute time period without loss of resolution or motion information.

Additionally, the number of delay times acquired could be reduced to a minimum of two. This would reduce the amount of motion data but would still allow for sinusoidal reconstruction through our Fourier fitting process. The number of motion directions could also be reduced, although this would compromise the full quantitative nature of the dataset.

In a number of phantoms imaged in this work, very little lateral motion was seen, thus not adding significantly to the overall motion data. However, this could be a function of the geometry of our setup and the viability of eliminating acquisition along a particular direction would require *in-vivo* investigation of the nature of generated waves.

The EPI sequence developed shows great promise as a very fast method of elastography data acquisition. Preliminary results show that motion in one-dimension can be detected in as little as 200ms per slice. A full three-dimensional acquisition at one delay time took only 3 minutes 20. This was acquired with a triggering time of 500ms. Further development to minimise the TR of the sequence could see this trigger time reduced significantly, thus reducing the overall scan time. More investigation needs be done in minimising and/or compensating for EPI ghosting artifacts. The EPI sequence also offers greater motion sensitivity in that more sets of motion encoding trapezoids could be implemented in the sequence. Currently, the four sets offers a greater sensitivity over the 3D GRE sequence by a factor of two. It may be possible to include even more MEGs without compromising the sequence TR. Other than the artifacts, another downside to the EPI sequence is the relatively long echo time, meaning the sequence is not suitable for imaging muscle and other tissues with short T_2 values.

7.2 Working with Silicone

Several phantoms were developed in order to have a known medium on which to test the pulse sequences. Silicone was found to be a suitable material for magnetic resonance imaging, and has the ability to closely mimic the mechanical properties of soft tissues. While silicone is a relatively easy material to work with, care must be taken in fabrication to avoid air bubbles, which can lead to susceptibility artifacts.

With a view to future clinical testing, the mass of the phantom was approximately that of a human breast. In the setup used for phantom testing, this phantom mass and the base were found to be moving relative to one another. This resulted in a reduced amplitude of motion delivered to the sample. For future clinical trials, clamping of the actuator unit to a solid object (the breast coil for instance) would allow a greater amplitude of motion to be delivered to a sample.

Allowing for the reduced amplitude of motion, the data from the silicone phantoms all showed a successful application of both the actuator apparatus and the motion encoding pulse sequences. The data acquisition process was refined to create a full 3D dataset of the imaged volume recording the magnitude and phase of motions in three dimensions at each voxel. For an interpolated dataset of a typical resolution, this equates to full 3D motion data at over half a million points in space. Issues with unwrapping the phase of the data were resolved by implementing 2D and 3D phase-unwrapping algorithms.

7.3 Elasticity Reconstruction

While outside the specific scope of this thesis, some elasticity reconstructions on the silicone datasets were attempted. Obtaining a successful reconstruction proved to be elusive, with more work still required to determine the exact cause of the problem. Questions remain over whether the correct coordinate system is being used to describe the direction of motions in relation to the spatial orientation of the phantom. Alongside this issue is the need to obtain accurate values for the shear modulus of silicone to initiate iterative reconstructions.

7.4 Tissue Anisotropy

Moving toward more clinically-realistic phantoms, several biological specimens were tested. A particular focus on these samples was the investigation of tissue anisotropy, as many tissues, including malignant tumours along with muscle, are known to be highly anisotropic.

It was first found that embedding samples of excised bovine muscle tissue in gelatine did not result in significant transmission of shear waves to the muscle itself. A direct actuation of a muscle sample proved to be much more efficient. This also moves toward a clinical approach to actuation where the area under investigation (breast, liver, skeletal muscle, etc) will not be confined within a rigid box. In these cases, actuation will have to come from a single boundary.

Initial analysis of *ex-vivo* muscle data suggests that a change in wavelength is detected for actuation along different directions. This successfully demonstrates the expected mechanical anisotropy, however, more analysis needs to be undertaken on these data to fully quantify the results. A reconstruction algorithm based on an anisotropic model is currently under development by others in the research group, and the data acquired in this thesis will provide a good test case for this model.

MR elastography of the brain is gathering increased attention from a number of MRE research groups. It is unknown whether there is a relationship between mechanical anisotropy of brain and the diffusion anisotropy in white matter tracts. An attempt was made to detect any mechanical anisotropy using an *ex-vivo* ovine brain encased in a solid epoxy resin cube. While the brain, as a whole, exhibited significant motion, there was little relative motion within the brain itself. Thus, at this stage, no mechanical anisotropy has been detected. Examination of the phantom at a higher actuation frequency may yield more success. However, the limited literature available suggests that *ex-vivo* brain MRE studies are difficult to undertake, and it may be necessary to modify our method of actuation to produce more favourable results.

Acknowledgements

The following people helped in many ways in this thesis. Without the support of all of them, this research would not have been possible; their assistance is much appreciated.

- Dr Richard Watts, my supervisor, for his support, guidance, feedback, his MR expertise, and for giving up his Friday nights to scan phantoms to the small hours.
- Dr Eli Van Houten, my co-supervisor, for his advice, feedback (all the way from Paris), and engineering expertise.
- Dr Naren Naik, for all his help with the elastography and reconstruction theory, and for his mathematical and image processing expertise.
- Dr Ashton Peters, for assistance with the silicone gels.
- Matthew McGarry, for many, many thankless reconstructions, and for always having something to try next. Matt provided the simulation test for the inclusions phantom and the comparative motion test between the homogeneous phantom and the simulation; those images are from him. Matt showed me how to use the ENSIGHT visualisation software, thus allowing me to obtain many more pretty pictures, and coached my understanding of the reconstruction process, especially when Eli was away.
- Zohreh Barani Lonbani, for her assistance in reconstructions and phantom manufacture. Zohreh undertook the first attempts at reconstruction from the inclusions phantom, and those images in this thesis are from her.
- David Visser for his help with reconstructions and work on the directional issues.
- Graeme Kershaw and the Physics and Astronomy Mechanical Workshop team, for technical wizardry, completing the many modifications to our apparatus in record time, and for helping seal the brain in the box.
- Geoff Graham and the Physics and Astronomy Electronics Workshop team, for help on the independent motion verification of the phantom setup.
- Gareth Leeper and the MR staff at St George's Radiology, for supporting our research through use of the MRI scanner
- Prof. John Dalrymple-Alford, for supplying the brains.
- And of course, Latoya, my wife, for everything else -xx- .

Bibliography

[1] D. Hill, V. White, D. Jolley, and K. Mapperson. Self examination of the breast - is it beneficial - meta-analysis of studies investigating breast self examination and extent of disease in patients with breast-cancer. *British Medical Journal*, 297(6643):271–275, 1988.

[2] A. Manduca, T. E. Oliphant, M. A. Dresner, J. L. Mahowald, S. A. Kruse, E. Amromin, J. P. Felmlee, J. F. Greenleaf, and R. L. Ehman. Magnetic resonance elastography: Non-invasive mapping of tissue elasticity. *Medical Image Analysis*, 5(4):237–254, 2001.

[3] Francis A. Duck. *Physical Properties of Tissue.* Academic Press, London, 1990.

[4] Armando Manduca. Analysis of dynamic magnetic resonance elastography data. In Luigi Landini, Vicenzo Positno, and Maria Santarelli, editors, *Advanced Image Processing in Magnetic Resonance Imaging*, pages 451–477. Taylor & Francis, Boca Raton, 2005.

[5] T. A. Krouskop, T. M. Wheeler, F. Kallel, B. S. Garra, and T. Hall. Elastic moduli of breast and prostate tissues under compression. *Ultrasonic Imaging*, 20(4):260–274, 1998.

[6] A. Samani, J. Bishop, C. Luginbuhl, and D. B. Plewes. Measuring the elastic modulus of *ex vivo* small tissue samples. *Physics in Medicine and Biology*, 48(14):2183–2198, 2003.

[7] O. Rouviere, M. Yin, M. A. Dresner, P. J. Rossman, L. J. Burgart, J. L. Fidler, and R. L. Ehman. MR elastography of the liver: Preliminary results. *Radiology*, 240(2):440–448, 2006.

[8] M. Yin, J. Woollard, X. F. Wang, V. E. Torres, P. C. Harris, C. J. Ward, K. J. Glaser, A. Manduca, and R. L. Ehman. Quantitative assessment of hepatic fibrosis in an animal model with magnetic resonance elastography. *Magnetic Resonance in Medicine*, 58(2):346–353, 2007.

[9] B. C. Goss, K. P. McGee, E. C. Ehman, A. Manduca, and R. L. Ehman. Magnetic resonance elastography of the lung: Technical feasibility. *Magnetic Resonance in Medicine*, 56(5):1060–1066, 2006.

[10] Y. Y. Cheung, M. Doyley, T. B. Miller, F. Kennedy, F. Lynch, J. S. Wrobel, K. Paulson, and J. Weaver. Magnetic resonance elastography of the plantar fat pads - preliminary study in diabetic patients and asymptomatic volunteers. *Journal of Computer Assisted Tomography*, 30(2):321–326, 2006.

[11] J. B. Weaver, M. Doyley, Y. Cheung, F. Kennedy, E. L. Madsen, E. E. W. Van Houten, and K. Paulsen. Imaging the shear modulus of the heel fat pads. *Clinical Biomechanics*, 20(3):312–319, 2005.

[12] N. S. Shah, S. A. Kruse, D. J. Lager, G. Farell-Baril, J. C. Lieske, B. F. King, and R. L. Ehman. Evaluation of renal parenchymal disease in a rat model with magnetic resonance elastography. *Magnetic Resonance in Medicine*, 52(1):56–64, 2004.

[13] S. F. Bensamoun, S. I. Ringleb, L. Littrell, Q. S. Chen, M. Brennan, R. L. Ehman, and K. N. An. Determination of thigh muscle stiffness using magnetic resonance elastography. *Journal of Magnetic Resonance Imaging*, 23(2):242–247, 2006.

[14] S. I. Ringleb, S. F. Bensamoun, Q. S. Chen, A. Manduca, K. N. An, and R. L. Ehman. Applications of magnetic resonance elastography to healthy and pathologic skeletal muscle. *Journal of Magnetic Resonance Imaging*, 25(2):301–309, 2007.

[15] I. Sack, J. Bernarding, and J. Braun. Analysis of wave patterns in MR elastography of skeletal muscle using coupled harmonic oscillator simulations. *Magnetic Resonance Imaging*, 20(1):95–104, 2002.

[16] K. Uffmann, S. Maderwald, W. Ajaj, C. G. Galban, S. Mateiescu, H. H. Quick, and M. E. Ladd. *In vivo* elasticity measurements of extremity skeletal muscle with MR elastography. *NMR in Biomedicine*, 17(4):181–190, 2004.

[17] D. A. Woodrum, A. J. Romano, A. Lerman, U. H. Pandya, D. Brosh, P. J. Rossman, L. O. Lerman, and R. L. Ehman. Vascular wall elasticity measurement by magnetic resonance imaging. *Magnetic Resonance in Medicine*, 56(3):593–600, 2006.

[18] S. A. Kruse, G. H. Rose, K. J. Glaser, A. Manduca, J. P. Felmlee, C. R. Jack, and R. L. Ehman. Magnetic resonance elastography of the brain. *Neuroimage*, 39(1):231–237, 2008.

[19] M. E. Ladd. Applications of MRE - brain. In *ISMRM Workshop*, New York, NY, 2006.

[20] P. J. McCracken, A. Manduca, J. Felmlee, and R. L. Ehman. Mechanical transient-based magnetic resonance elastography. *Magnetic Resonance in Medicine*, 53(3):628–639, 2005.

[21] A. L. McKnight, J. L. Kugel, P. J. Rossman, A. Manduca, L. C. Hartmann, and R. L. Ehman. MR elastography of breast cancer: Preliminary results. *American Journal of Roentgenology*, 178(6), 2002.

[22] D. B. Plewes, J. Bishop, A. Samani, and J. Sciarretta. Visualization and quantification of breast cancer biomechanical properties with magnetic resonance elastography. *Physics in Medicine and Biology*, 45(6):1591–1610, 2000.

[23] R. Sinkus, J. Lorenzen, D. Schrader, M. Lorenzen, M. Dargatz, and D. Holz. High-resolution tensor MR elastography for breast tumour detection. *Physics in Medicine and Biology*, 45(6):1649–1664, 2000.

[24] R. Sinkus, M. Tanter, S. Catheline, J. Lorenzen, C. Kuhl, E. Sondermann, and M. Fink. Imaging anisotropic and viscous properties of breast tissue by magnetic resonance-elastography. *Magnetic Resonance in Medicine*, 53(2):372–387, 2005.

[25] R. Sinkus, M. Tanter, T. Xydeas, S. Catheline, J. Bercoff, and M. Fink. Viscoelastic shear properties of *in vivo* breast lesions measured by MR elastography. *Magnetic Resonance Imaging*, 23(2):159–165, 2005.

[26] E. E. W. Van Houten, M. M. Doyley, F. E. Kennedy, J. B. Weaver, and K. D. Paulsen. Initial *in vivo* experience with steady-state subzone-based MR elastography of the human breast. *Journal of Magnetic Resonance Imaging*, 17(1):72–85, 2003.

[27] T. Xydeas, K. Siegmann, R. Sinkus, U. Krainick-Strobel, S. Miller, and C. D. Claussen. Magnetic resonance elastography of the breast - correlation of signal intensity data with viscoelastic properties. *Investigative Radiology*, 40(7):412–420, 2005.

[28] A. Samani, J. Bishop, and D. B. Plewes. A constrained modulus reconstruction technique for breast cancer assessment. *IEEE Transactions on Medical Imaging*, 20(9):877–885, 2001.

[29] M. H. Chappell, A. M. Ulug, L. Zhang, M. H. Heitger, B. D. Jordan, R. D. Zimmerman, and R. Watts. Distribution of microstructural damage in the brains of professional boxers: A diffusion MRI study. *Journal of Magnetic Resonance Imaging*, 24(3):537–542, 2006.

[30] R. Watts, C. Liston, S. Niogi, and A. M. Ulug. Fiber tracking using magnetic resonance diffusion tensor imaging and its applications to human brain development. *Mental Retardation and Developmental Disabilities Research Reviews*, 9(3):168–177, 2003.

[31] H. U. Voss, R. Watts, A. M. Ulug, and D. Ballon. Fiber tracking in the cervical spine and inferior brain regions with reversed gradient diffusion tensor imaging. *Magnetic Resonance Imaging*, 24(3):231–239, 2006.

[32] P. McCracken, A. Manduca, J. P. Felmlee, and R. L. Ehman. Transient MR elastography: Modeling traumatic brain injury. In *Medical Image Computing and Computer-Assisted Intervention - Miccai 2004, Pt 2, Proceedings*, volume 3217 of *Lecture Notes in Computer Science*, pages 1081–1082. 2004.

[33] Donald W. McRobbie, Elizabeth A. Moore, Martin J. Graves, and Martin R. Prince. *MRI from Picture to Proton.* Cambridge University Press, Cambridge, 2003.

[34] E. Mark Haacke, Robert W. Brown, Michael R. Thompson, and Ramesh Venkatesan. *Magnetic Resonance Imaging: Physical Principles and Sequence Design.* John Wiley & Sons, Inc., New York, 1999.

[35] Maria Filomena Santarelli. Basic physics of MR signal and image generation. In Luigi Landini, Vicenzo Positno, and Maria Santarelli, editors, *Advanced Image Processing in Magnetic Resonance Imaging*, pages 3–37. Taylor & Francis, Boca Raton, 2005.

[36] F. Bloch. Nuclear induction. *Physical Review*, 70(7-8):460–474, 1946.

[37] Jerrold T. Bushberg, J. Anthony Seibert, Jr. Edwin M. Leidholdt, and John M. Boone. *The Essential Physics of Medical Imaging.* Lippincott Williams & Wilkins, Philadelphia, second edition, 2002.

[38] D. K. Sodickson and W. J. Manning. Simultaneous acquisition of spatial harmonics (SMASH): Fast imaging with radiofrequency coil arrays. *Magnetic Resonance in Medicine*, 38(4):591–603, 1997.

[39] K. P. Pruessmann, M. Weiger, M. B. Scheidegger, and P. Boesiger. SENSE: Sensitivity encoding for fast MRI. *Magnetic Resonance in Medicine*, 42(5):952–962, 1999.

[40] P. Kellman, F. H. Epstein, and E. R. McVeigh. Adaptive sensitivity encoding incorporating temporal filtering (TSENSE). *Magnetic Resonance in Medicine*, 45(5):846–852, 2001.

[41] J.C.P. Heggie, N.A. Liddell, and K.P. Maher. *Applied Imaging Technology.* St Vincent's Hospital, Melbourne, fourth edition, 2001.

[42] C. B. Paschal and H. D. Morris. k-space in the clinic. *Journal of Magnetic Resonance Imaging*, 19(2):145–159, 2004.

[43] A. P. Sarvazyan, O. V. Rudenko, S. D. Swanson, J. B. Fowlkes, and S. Y. Emelianov. Shear wave elasticity imaging: A new ultrasonic technology of medical diagnostics. *Ultrasound in Medicine and Biology*, 24(9):1419–1435, 1998.

[44] L. S. Wilson, D. E. Robinson, and M. J. Dadd. Elastography - the movement begins. *Physics in Medicine and Biology*, 45(6):1409–1421, 2000.

[45] K. J. Parker, D.S. Fu, S.M. Graceswki, F. Yeung, and S. F. Levinson. Vibration sonoelastography and the detectability of lesions. *Ultrasound in Medicine and Biology*, 24(9), 1998.

[46] V. Dutt, R. R. Kinnick, R. Muthupillai, T. E. Oliphant, R. L. Ehman, and J. F. Greenleaf. Acoustic shear-wave imaging using echo ultrasound compared to magnetic resonance elastography. *Ultrasound in Medicine and Biology*, 26(3):397–403, 2000.

[47] R. Muthupillai, D. J. Lomas, P. J. Rossman, J. F. Greenleaf, A. Manduca, and R. L. Ehman. Magnetic-resonance elastography by direct visualization of propagating acoustic strain waves. *Science*, 269(5232):1854–1857, 1995.

[48] D. B. Plewes. MRI methods for imaging the mechanical properties of tissue. In *ISMRM Workshop*, New York, NY, 2006.

[49] J. B. Weaver, E. E. W. Van Houten, M. I. Miga, F. E. Kennedy, and K. D. Paulsen. Magnetic resonance elastography using 3D gradient echo measurements of steady-state motion. *Medical Physics*, 28(8):1620–1628, 2001.

[50] J. Braun, K. Braun, and I. Sack. Electromagnetic actuator for generating variably oriented shear waves in MR elastography. *Magnetic Resonance in Medicine*, 50(1):220–222, 2003.

[51] K. Uffmann, C. Abicht, W. Grote, H. H. Quick, and M. E. Ladd. Design of an MR-compatible piezoelectric actuator for MR elastography. *Concepts in Magnetic Resonance*, 15(4):239–254, 2002.

[52] T. E. Oliphant, A. Manduca, R. L. Ehman, and J. F. Greenleaf. Complex-valued stiffness reconstruction for magnetic resonance elastography by algebraic inversion of the differential equation. *Magnetic Resonance in Medicine*, 45(2):299–310, 2001.

[53] E. E. W. Van Houten, K. D. Paulsen, M. I. Miga, F. E. Kennedy, and J. B. Weaver. An overlapping subzone technique for MR-based elastic property reconstruction. *Magnetic Resonance in Medicine*, 42(4):779–786, 1999.

[54] E. E. W. Van Houten, M. I. Miga, J. B. Weaver, F. E. Kennedy, and K. D. Paulsen. Three-dimensional subzone-based reconstruction algorithm for MR elastography. *Magnetic Resonance in Medicine*, 45(5):827–837, 2001.

[55] E. E. W. Van Houten, M. M. Doyley, F. E. Kennedy, K. D. Paulsen, and J. B. Weaver. A three-parameter mechanical property reconstruction method for MR-based elastic property imaging. *IEEE Transactions on Medical Imaging*, 24(3):311–324, 2005.

[56] F. Kallel, M. Bertrand, and J. Ophir. Fundamental limitations on the contrast-transfer efficiency in elastography: An analytic study. *Ultrasound in Medicine and Biology*, 22(4), 1996.

[57] W. Michael Lai, David Rubin, and Erhard Krempl. *Introduction to Continuum Mechanics*. Pergamon Press Inc., New York, 1974.

[58] Perry Sprawls, Jr. *Physical Principles of Medical Imaging*. Medical Physics Publishing, Madison, 2nd edition, 1995.

[59] H. L. Liew and P. M. Pinsky. Recovery of shear modulus in elastography using an ajoint method with B-spline representation. *Finite Elements in Analysis and Design*, 41(7-8):778–799, 2005.

[60] A. A. Oberai, N. H. Gokhale, and G. R. Feijoo. Solution of inverse problems in elasticity imaging using the adjoint method. *Inverse Problems*, 19(2):297–313, 2003.

[61] Robert B. Dennis, Jr. J. E. Schnabel. *Numerical Methods for Unconstrained Optimization and Nonlinear Equations.* Prentice-Hall, Englewood Cliffs, 1983.

[62] Heinz W. Engl, Alfred K. Louis, and William Rundell. *Inverse Problems in Medical Imaging and Nondestructive Testing (Conference Proceedings).* Springer-Verlag, Wien, 1997.

[63] Jorge Nocedal and Stephen J. Wright. *Numerical Optimization.* Springer, New York, second edition, 2006.

[64] Curtis R. Vogel. *Computational Methods for Inverse Problems.* S.I.A.M., Philadelphia, 2002.

[65] Heinz W. Engl, Martin Hanke, and Andreas Neubauer. *Regularization of Inverse Problems.* Kluwer Academic Publishers, Dordrecht, 2000.

[66] James L. Flewellen. Magnetic resonance elastography for breast cancer detection. 480 research report, Department of Physics and Astronomy, University of Canterbury, 2006.

[67] J. N. Rydberg, R. C. Grimm, and R. L. Ehman. Rapid magnetic resonance elastography (MRE) using fast spin-echo (FSE). *Radiology*, 221:329–330, 2001. Suppl. S.

[68] O. Lopez, K. K. Amrami, A. Manduca, P. J. Rossman, and R. L. Ehman. Developments in dynamic MR elastography for *in vitro* biomechanical assessment of hyaline cartilage under high-frequency cyclical shear. *Journal of Magnetic Resonance Imaging*, 25(2):310–320, 2007.

[69] I. Sack, B. Beierbach, U. Hamhaber, D. Klatt, and A. Braun. Non-invasive measurement of brain viscoelasticity using magnetic resonance elastography. *NMR in Biomedicine*, 21(3):265–271, 2008.

[70] Dennis C. Ghiglia and Mark D. Pritt. *Two-Dimensional Phase Unwrapping: Theory, Algorithms and Software.* John Wiley & Sons, New York, 1998.

[71] Rafael C. Gonzalez and Richard E. Woods. *Digital Image Processing.* Pearson Education, Delhi, 2002.

[72] S. I. Ringleb, Q. S. Chen, D. S. Lake, A. Manduca, R. L. Ehman, and K. N. An. Quantitative shear wave magnetic resonance elastography: Comparison to a dynamic shear material test. *Magnetic Resonance in Medicine*, 53(5):1197–1201, 2005.

[73] E. Han, G. Gold, J. Stainsby, G. Wright, C. Beaulieu, and J. Brittain. *In-vivo* T1 and T2 measurements of muskuloskeletal tissue at 3T and 1.5T. *Proceedings of the ISMRM*, 11, 2003.

[74] Peter J. Chen. *Selected Topics in Wave Propagation.* Noordhoff International Publishing, Leyden, 1976.

[75] Karl F. Graff. *Wave Motion in Elastic Solids.* Ohio State University Press, Belfast, 1975.

[76] Iain G. Main. *Vibrations and Waves in Physics.* Cambridge University Press, Cambridge, first edition, 1978.

[77] H. J. Pain. *The Physics of Vibrations and Waves.* John Wiley & Sons, Chichester, sixth edition, 2005.

[78] Y.C. Fung. *Biomechanics: Mechanical Properties of Living Tissues.* Springer-Verlag, New York, second edition, 1993.

[79] Ashton Peters. *Digital Image Elasto-Tomography: Mechanical Property Reconstruction from Surface Measured Displacement Data.* PhD thesis, University of Canterbury, 2007.

[80] Ashton Peters, J. Geoffrey Chase, and Elijah E. W. Van Houten. Digital image elasto-tomography: mechanical property estimation of silicone phantoms. *Medical and Biological Engineering and Computing*, 46(3), 2008.

[81] M. A. Dresner, G. H. Rose, P. J. Rossman, R. Muthupillai, A. Manduca, and R. L. Ehman. Magnetic resonance elastography of skeletal muscle. *Journal of Magnetic Resonance Imaging*, 13(2):269–276, 2001.

[82] J. Bishop, G. Poole, M. Leitch, and D. B. Plewes. Magnetic resonance imaging of shear wave propagation in excised tissue. *Journal of Magnetic Resonance Imaging*, 8(6):1257–1265, 1998.

[83] J. Vappou, E. Breton, P. Choquet, C. Goetz, R. Willinger, and A. Constantinesco. Magnetic resonance elastography compared with rotational rheometry for *in vitro* brain tissue viscoelasticity measurement. *Magnetic Resonance Materials in Physics Biology and Medicine*, 20(5-6):273–278, 2007.

[84] J. Braun, J. Bernarding, T. Tolxdorff, and I. Sack. *In-vivo* magnetic resonance elastography of the human brain using ultrafast acquisition techniques. *Proceedings of the ISMRM*, 10, 2002.

[85] M. A. Green, R. Sinkus, S. Cheng, and L. E. Bilston. 3D MR-elastography of the brain at 3Tesla. *Proceedings of the ISMRM*, 13, 2005.

[86] M. A. Green, R. Sinkus, and L. E. Bilston. High resolution 3D brain MR-elastography. *Proceedings of the ISMRM*, 14, 2006.

[87] U. Hamhaber, I. Sack, S. Papazoglou, J. Rump, D. Klatt, and J. Braun. Three-dimensional analysis of shear wave propagation observed by *in vivo* magnetic resonance elastography of the brain. *Acta Biomaterialia*, 3(1):127–137, 2007.

[88] S. A. Kruse and R. L. Ehman. 2D approximation of 3D wave propagation in MR elastography of the brain. *Proceedings of the ISMRM*, 11, 2003.

[89] K. Uffmann, S. Maderwald, A. De Greiff, and M. E. Ladd. Determination of grey and white matter elasticity with MR elastography. *Proceedings of the ISMRM*, 11, 2004.

[90] L. Xu, Y. Lin, Z. N. Xi, H. Shen, and P. Y. Gao. Magnetic resonance elastography of the human brain: A preliminary study. *Acta Radiologica*, 48(1):112–115, 2007.

Appendix A

Derivations

A.1 Classical Derivation of the Larmor Equation

Starting with equation (2.4), and assuming the external magnetic field has components only along $\hat{\boldsymbol{z}}$, i.e. $\boldsymbol{B} = B_z\hat{\boldsymbol{z}}$:

$$\frac{\mathrm{d}}{\mathrm{d}t}\begin{pmatrix}\mu_x\\ \mu_y\\ \mu_z\end{pmatrix} = \gamma\begin{pmatrix}\mu_x\\ \mu_y\\ \mu_z\end{pmatrix}\times\begin{pmatrix}0\\ 0\\ B_z\end{pmatrix} \tag{A.1}$$

In components:

$$\begin{aligned}\frac{\mathrm{d}\mu_x}{\mathrm{d}t} &= \gamma\mu_y B_z\\ \frac{\mathrm{d}\mu_y}{\mathrm{d}t} &= -\gamma\mu_x B_z\\ \frac{\mathrm{d}\mu_z}{\mathrm{d}t} &= 0\end{aligned} \tag{A.2}$$

Taking the second derivative of the x and y components:

$$\begin{aligned}\frac{\mathrm{d}^2\mu_x}{\mathrm{d}t^2} &= -(\gamma B_z)^2\mu_x\\ \frac{\mathrm{d}^2\mu_y}{\mathrm{d}t^2} &= -(\gamma B_z)^2\mu_y\end{aligned} \tag{A.3}$$

Equation (A.2) reveals μ_z is a constant, and the solution to equation (A.3) is clearly a simple harmonic motion solution, where the resonant frequency is $\sqrt{(\gamma B_z)^2}$. Given the assumption on the nature of the external magnetic field, this plainly reveals the Larmor equation:

$$\omega = \gamma B \tag{A.4}$$

A.2 Quantum Mechanical Derivation of the Larmor Equation

The definition of quantised angular momentum: $\boldsymbol{J} = \hbar J$, and equation (2.1) combine to relate the magnetic moment of the proton to the spin angular momentum quantum number, J:

$$\boldsymbol{\mu} = \gamma\hbar J \tag{A.5}$$

J is equal to $\frac{1}{2}$ for protons; thus for a proton in an external magnetic field, there are two possible states, spin-up and spin-down, corresponding to a value of $J = \pm\frac{1}{2}$. The energy of the state is given by:

$$E = \boldsymbol{\mu} \cdot \boldsymbol{B} = \gamma\hbar JB \tag{A.6}$$

The energy difference between the two energy states is:

$$\Delta E = (\frac{1}{2} - -\frac{1}{2})\gamma\hbar B = \gamma\hbar B \tag{A.7}$$

From the de Broglie wave equation: $\Delta E = \hbar\omega$, we can equate the changes in energy and arrive at the Larmor equation:

$$\begin{aligned} \hbar\omega &= \gamma\hbar B \\ \omega &= \gamma B \end{aligned} \tag{A.8}$$

Appendix B

Motion Data for Inclusions Phantom

The 3D complex transient response for the inclusions phantom data is presented here. These images allow for better visualisation of the wave motion within the phantom. A magnitude image overlaid with an isosurface plot indicates the position of the cylinders (figure B.1). A time series of the wave function in the phantom is shown overlaid with the displacement along $\hat{\boldsymbol{x}}$ (figure B.2) and $\hat{\boldsymbol{z}}$ (figure B.3). As in previous such images, red indicates motion along the positive direction according to the axes coordinates, and blue indicates negative motion. Noise from an air bubble is visible in the centre of each image. Motion data for $\hat{\boldsymbol{y}}$ is not included as the amplitude of motion in this direction was small.

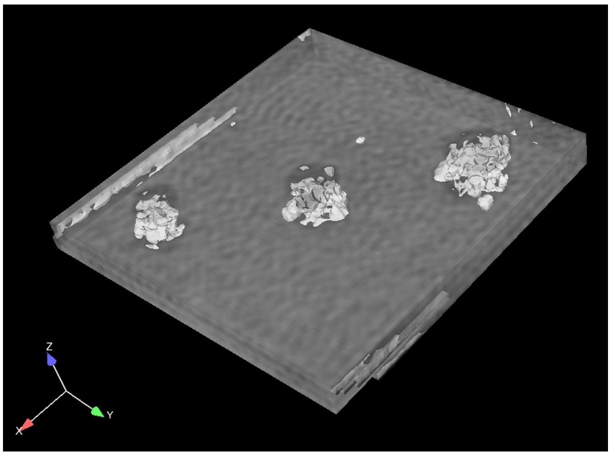

Figure B.1: A magnitude image overlaid with an isosurface plot indicates the position of the cylinders for comparison against wave motion figures.

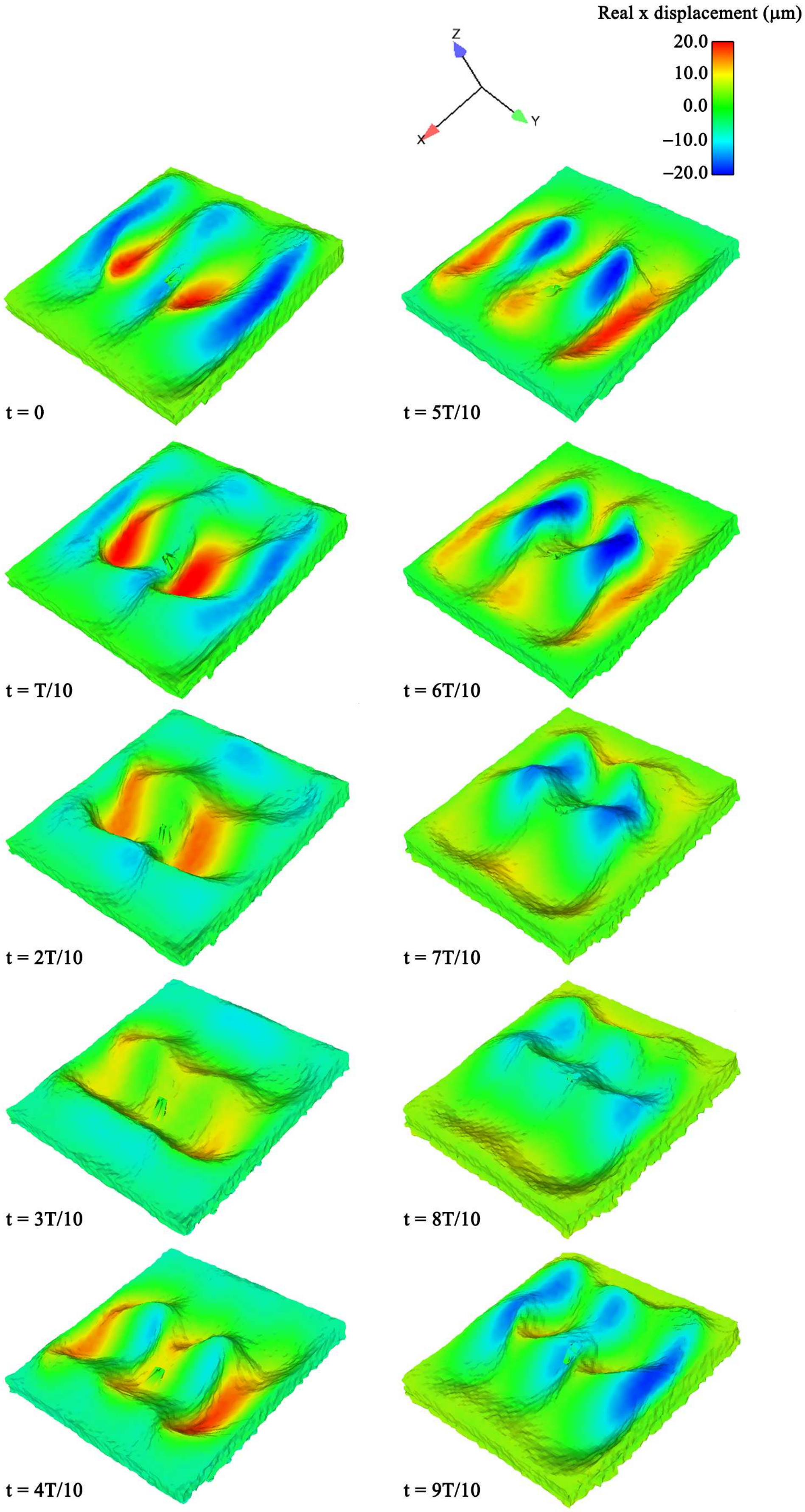

Figure B.2: The 3D motion of the phantom at 10 time points throughout the motion cycle. The colours indicate the motion in the x direction (direction of actuation).

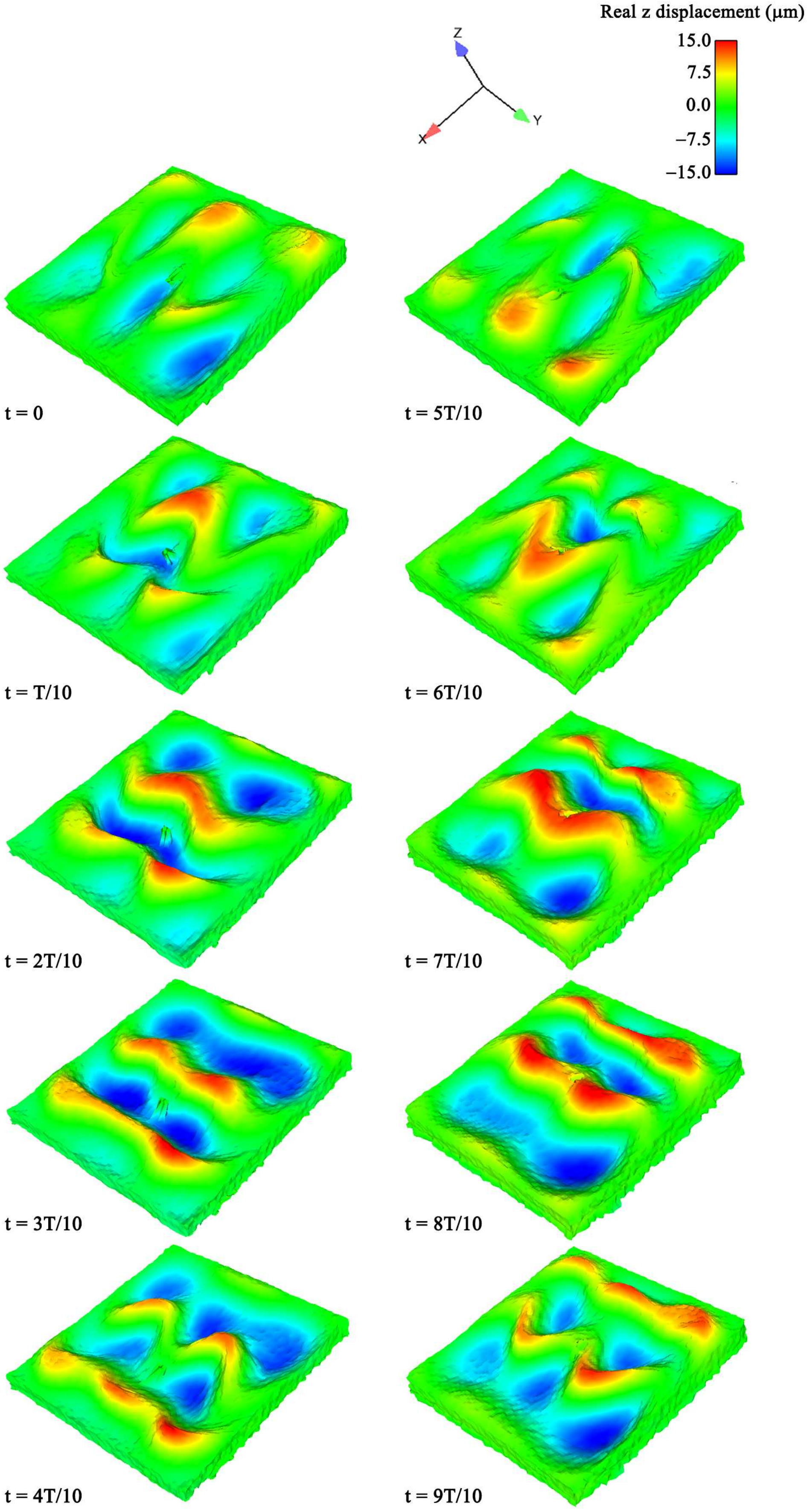

Figure B.3: The 3D motion of the phantom at 10 time points throughout the motion cycle. The colours indicate the motion in the z direction (through-plane direction).